Copper (I) Coordination Networks Synthesized with Solid-Solid Reactions

---

A Dissertation

Presented to

the Faculty of the Graduate School

University of Missouri-Columbia

In Partial Fulfillment

of the Requirements for the Degree

Doctor of Philosophy

---

by

Steven Bockhold

Dr. Steven Keller, Dissertation Supervisor

MAY 2008

The undersigned, appointed by the Dean of the Graduate School,

have examined the dissertation entitled

COPPER(I) COORDINATION NETWORKS SYNTHESIZED

WITH SOLID-SOLID REACTIONS

presented by Steven Bockhold

a candidate for the degree of Doctor of Philosophy

and hereby certify that in their opinion it is worthy of acceptance.

Professor Steven Keller

Professor John Adams

Professor Paul Duval

Professor Silvia Jurisson

Professor Paul Miceli

I would like to dedicate this dissertation to my family and friends, in particular my wife, Kate. They believed in me during my time in grad school and always knew that I could do it. Also to Dr. John Adams for giving me the inspiration to teach.

Acknowledgments

As special thanks to all of those individuals that made my graduate career a fulfilling period of time at the University of Missouri-Columbia. I would like to thank my advisor, Steven W. Keller, for his support and guidance, which have made this project possible. I would also like to thank all the past and present members of the Keller group. The most notable members, Brian Huesgen and Karen Kirby, provided a great deal of assistance in research and teaching. Gratitude also goes to Tony Vaughn and Lindsay Simpson who contributed to the work presented in this dissertation. I would like to thank Charles Barnes for his invaluable crystallographic assistance. Thanks go to Joseph Turner and Bill Vellema and for their assistance with instrumentation and analysis. Eric Weis must also be shown appreciation for allowing the time to discuss issues and ideas I had about my research.

TABLE OF CONTENTS

LIST OF FIGURES

LIST OF TABLES

Copper(I) Coordination Networks Synthesized with Solid-Solid Reactions

Steven Bockhold

Dr. Steven W. Keller, Dissertation Advisor

ABSTRACT

The use of solid-solid reactions in the development of one-. two-, and three-dimensional Cu(I) coordination networks are discussed. The solid-solid reactions were monitored by a variety of instrumental techniques to achieve a better picture of the solid-solid reaction mechanism. The crystalline reagents led to crystalline products with no amorphous phase. The nitrogen containing bridging ligands, 4,7-phenanthroline, 4,4'-dipyridyl, and *trans*-1,2-bis(4-pyridy1)ethylene in addition to 1,3-dithiane were used in the formation of these networks. The resultant crystalline compounds were compared to the solution-based products, showing that on average the same product was formed. Through the bridging ligands and a change in the coordinated solvent, the ultimate goal of showing how these solid-solid reactions could be expanded to cover a large array of reagents was accomplished.

Chapter 1

The Development of Coordination Networks with a Green Chemistry Focus

1.1 Introduction

It has been twenty years since Donald J. Cram, Jean-Marie Lehn, and Charles J. Pedersen received the Nobel Prize in Chemistry for their work in the area of supramolecular chemistry (Figure 1.1).[1-4] Their work covered the development of selective "host-guest" complexes. In these complexes, a host molecule recognizes and selectively binds a certain guest. To function these molecules depend primarily on

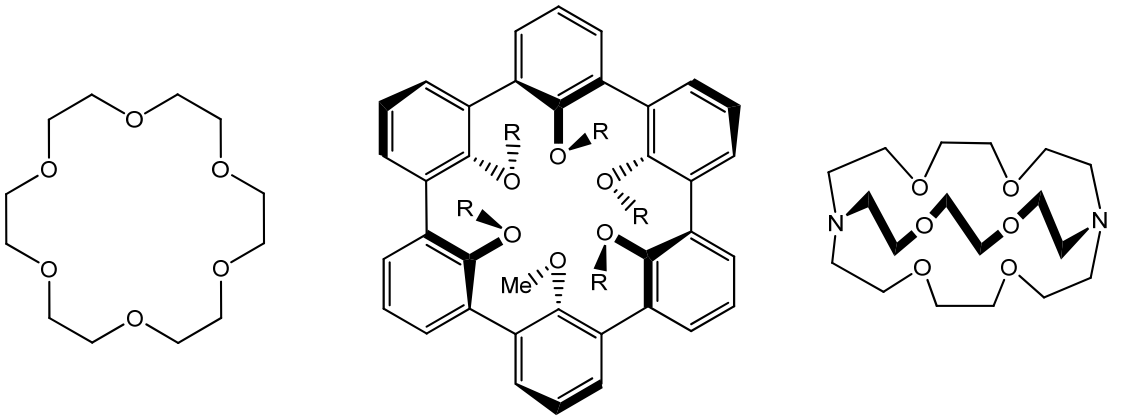

Figure 1.1 – Pictured are the different supramolecular complexes that were developed by Pedersen, Cram, and Lehn. Each of the complexes is molecular and uses oxygen lone pairs in order to form intermolecular interactions with the cations of interest.

non-covalent interactions, including hydrogen bonding, van der Waals forces, π-π interactions, and/or electrostatic effects.[5-7] Although these reactions are weaker than the

stronger intramolecular interactions, put in conjunction they are strong enough to stabilize the structure (Table 1.1). Because of the nature of these interactions, supramolecular chemistry is sometimes referred to as "chemistry beyond molecules."[8] This chemistry has been enriched by using molecules as the building blocks as compared to traditional means in which molecules are formed from the use of atoms as building blocks. The use of these molecular building blocks has been referred to as molecular self-assembly, hierarchical order, or nanoscience in addition to supramolecular chemistry.[9]

Energy comparison for intra- and intermolecular interactions	
Type of interaction	Energy (kJ/mol)
Covalent bonds C-H, C-C, C=C, C-O, C=O, O-H	 413, 348, 614, 358, 799, 463
Coordinate covalent bond	150-300
Ion-ion	100-350
Ion-dipole	50-200
Hydrogen	≤120
Cation-π	≤80
Dipole-dipole	≤50
π-π stacking	≤50
Van der Waals	≤5

Table 1.1 – List of energy comparisons for intra- and intermolecular interactions. The strength of the interactions is listed in ascending order.[5-7]

Supramolecular chemistry has been a growing field in part because of the possibility of mimicking nature. A natural example of supramolecular chemistry can be found with proteins. Proteins are formed from amino acids covalently bonding together to form a chain also known as the primary protein structure (Figure 1.2). Alpha helices or beta sheets form via hydrogen bonding between segments of the same chain. The so-called secondary protein structure forms hydrophobic cores, salt bridges, hydrogen

bonds, and disulfide bonds along with other intermolecular interactions.

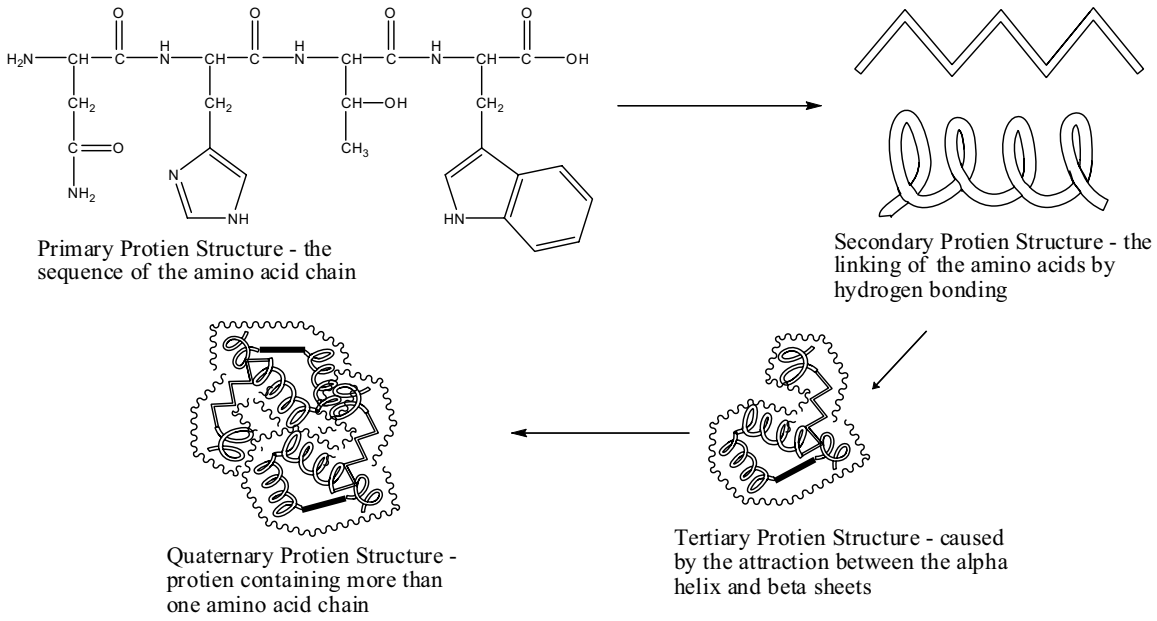

Figure 1.2 – Progression of the structure of proteins. The complexity of the structure begins with the amino acid chain and ends with the overall quaternary protein structure. The enzymatic properties are controlled by the amino acid sequence and how the amino acid influences the structure.

The overall protein structure that develops from these interactions is defined as the tertiary protein structure. Finally, if two of more amino acid chains combine, a quaternary protein structure is formed. The properties of proteins depend not only on the makeup of the chains but on the tertiary protein structure that is evolved from the arrangement of the amino acids.

The idea that the structure of natural products determines their properties leads to research into supramolecular materials. Natural materials are harvested, modified, and applied; however, these materials can be fragile or of limited availability. With supramolecular chemistry, headway is being made toward creating natural mimics that work as well as, if not better than, nature. In this way, nature serves as a template from which design ideas are drawn.

A subset of supramolecular chemistry that holds great promise in mimicking natural structures is coordination chemistry. Coordination chemistry is an area of chemistry that combines the self-assembly and the molecular building block approach of supramolecular chemistry with the use of transition metals and metal-ligand bonding. The ligands act as Lewis bases, donating electron density to the metal cation, creating a bond.[10] A ligand can act as a bridge between the metal cations. If this metal-ligand bridging is continued through out the compound, then a network is formed. The type of network that is developed, depends on the orientation and the number of bridging ligands coordinated to the metal cation. The coordinated ligands can interact with each other further influencing the type of network that develops. The appeal of coordination networks is the variety of the combinations of ligands and metal cations that can be used. Depending on the combination, the compounds have potential applications in areas including gas adsorption,[11-13] ion and solvent exchange,[11,14-17] catalysis,[18,19] magnetism,[20] and nonlinear optics.[21-23]

The coordination geometry around the metal cation is dependent on the electronic structure and oxidation state of the cation. The common metal-ligand coordination geometries are square planar, tetrahedral, or octahedral. For example, Pt(II) normally has a square planar geometry due to its d^8 electronic configuration (Figure 1.3).

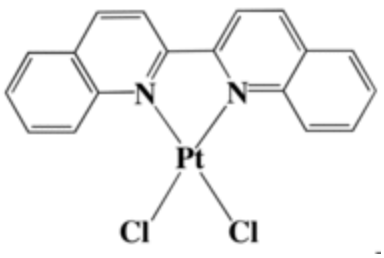

Figure 1.3 – One of the compounds in which Pt(II) has square planar coordination geometry. It is a derivative of *cis*-platin, which has been used as an anti-cancer agent.

Along with the metal choice, ligand selection has an effect on the network that forms. The ligand can either be terminal or act as a bridge between metal cations. The terminal ligands act as capping groups, which prevents the extension of the network in the direction of the terminal ligand. Bridging ligands extend the coordination network that forms by the bonding between neighboring metal cations (Table 1.2). Depending on the coordinated ligands and the coordination geometry around the metal center, the network can extend in one-, two-, or three-dimensions.[10,24-29]

Metal	Possible Coordination Geometry Around the Metal	Possible Bridging Ligands
Cu(I) Cu(II) Ag(I) Pt(II) Ni(II) Au(I) Cd(II) Fe(II) Mn(II)	Linear Trigonal planar Tetrahedral Square planar Octahedral	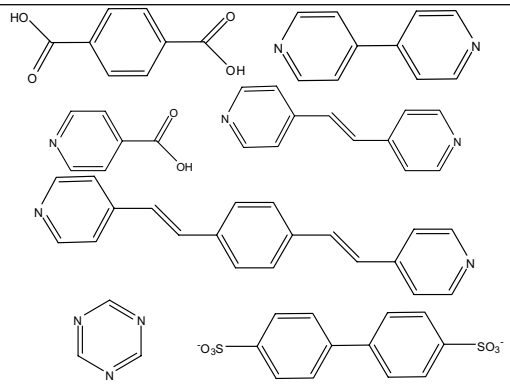

Table 2.2 – List of selected metal cations and ligands used in creating coordination networks. In addition the possible coordination geometries around the metal are also listed.

Another consideration that needs to be made in synthetic planning is whether to use an anionic or neutral ligand. The use of neutral ligands can be beneficial in that noncoordinated anions can fill the voids or cavities, and at times the anion templates the coordination network layout. These materials would be good candidates for use in anion exchange. A good example of anionic templating is observed when using one of the many types of polyoxometalate (POM) anions.[30] POMs are large anionic clusters that

have metal cations such as W or Mo that are surrounded by oxide anions (Figure 1.4). The anions are so large that the networks form around them to accommodate them in the structure.

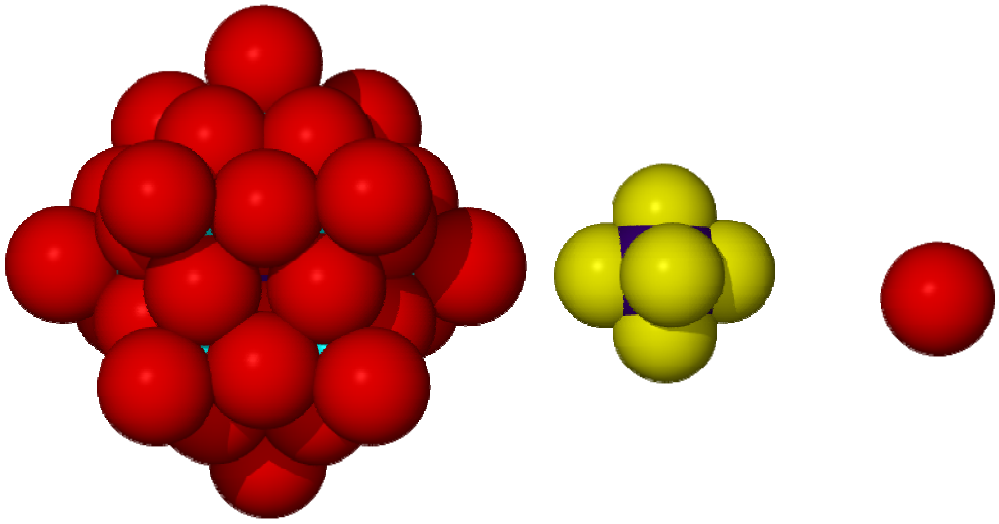

Figure 1.4 – Size comparison between the different anions. The $PW_{12}O_{40}^{-3}$ POM has a relatively large diameter (10.5 Å) compared with other polyatomic and monatomic anions. The polyatomic anion is PF_6^- (3.1 Å), and the monatomic anion is chloride (1.7 Å).

On the other hand, anionic ligands can be used to develop networks in which the cavities contain only solvent, which can be removed. For example, a three-dimensional coordination network, also known as a metal organic framework (MOF), which has been created by Yaghi et. al., is called MOF-5.[31] The MOF is created by having a Zn-O cluster consisting of four Zn(II) cations surrounding an oxygen atom (Figure 1.5). These clusters are bridged by anionic terephthalate ligands, which results in a neutral network. Each cluster is bridged to six different clusters by the terephthalate ligands acting as linear bridges. Each coordinated ligand is orthogonal to the others; from this coordination a three-dimensional framework is developed (Figure 1.6). The empty cavities that develop from the framework can be filled with solvent and gas. MOF-5's

gas sorption ability has led to MOF-5 being one of the most studied MOFs.[32]

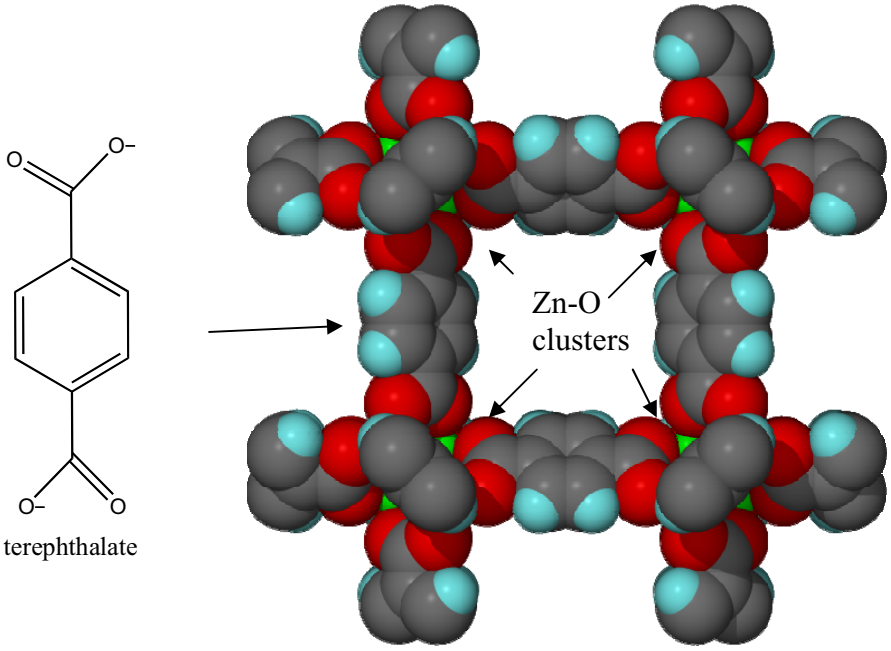

Figure 1.5 – Space-filled model of MOF-5. This unit is extended in any direction to form a three-dimensional network. At the center of each corner is an oxygen anion that is bonded to four zinc cations (in lime green). The terephthalate linkers connect each of these units. The oxygen anions cannot be seen due to their location at the center of the cluster. [31]

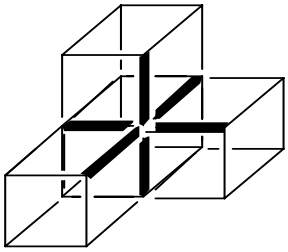

Figure 1.6 – Figure of the cubes formed by the ligand bridging in three dimensions. The dark lines represent the ligands attached to one central Zn cluster.

The knowledge that coordination networks can be constructed simply by choosing a metal cation and ligand combination has led to the approach being called (somewhat derogatorily) "tinker toy" chemistry. Having an understanding of what

limited structural possibilities are available from the combination of ligands, metal cations, and anions has led some to propose that the product's structure can be predicted. However, the prediction of the exact structure is still not in the realm of a "crystal engineer." The chemistry must still be performed and the structure solved. This is not to say that the process is purely trial and error, but that coordination chemistry should be thought of as having certain design principles to follow, be it the selection of the metal cation, based on its coordination network preference, or the ligand due to its length or geometry. Through the general design principles, the goal of making a desired natural network analog might be achieved.

The formation of coordination networks has been a major part of the Keller group's focus. We strive to understand the conditions, (solvent, ligand, and/or metal cation used, and metal:ligand ratio) to produce a certain type of crystal structure, as well as the ways to tune the product structures. We focus on mimicking the natural structure of silicate-containing networks. In silicates, part or all of the structure consists of a silicon atom bonded to four oxygen atoms forming a tetrahedron (Figure 1.7). In quartz, the O atom of each tetrahedron is shared by the corner of another tetrahedron, in other words is "corner-shared." The sharing of O atoms between four neighboring tetrahedra gives the empirical formula of SiO_2 and network neutrality. In addition the bond angle of Si-O-Si for quartz is around 145º (Figure 1.8).

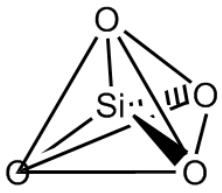

Figure 1.7 – The tetrahedron that is formed from the Si and O bonding in many silicates minerals.

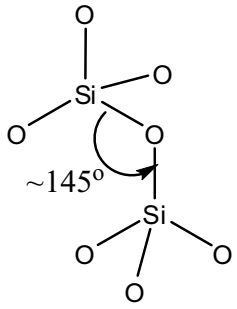

Figure 1.8 – The Si-O-Si bond angle for corner-shared tetrahedra in silicates is approximately 145°.

The extended structure of quartz consists of helical chains in which all the tetrahedra point in the same general direction (Figure 1.9).[33] When physical pressure is applied, the tetrahedra are distorted, creating a dipole. Given the way the tetrahedra are oriented, the dipole is compounded throughout the crystal, causing a voltage to be produced across the crystal. This property is referred to as piezoelectricity; this property can be used in pressure gauges, oscillators, and resonators.[34]

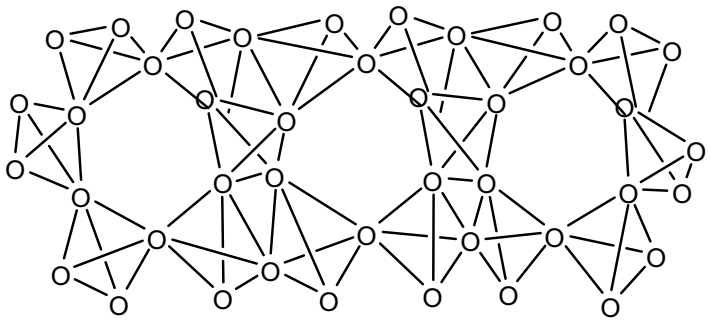

Figure 1.9 – The arrangement of the silicate tetrahedral pictured down the helical chains. The arrangement allows for a voltage to form across the crystal when pressure is applied.

Like quartz, zeolites contain corner-shared SiO_4 tetrahedra. In addition to the silicate tetrahedra, Al^{+3} cations replace some of the Si^{4+} cations. The replacement of Si^{4+} with Al^{+3} in the framework gives the structure an overall negative charge. Instead of the

helical formation, the tetrahedra link together to form channels and pores.[35] These pores usually vary in size from 4 to 7 Å , which open up to cavities of 10 to 13 Å (Figure 1.10).[33] The cavities loosely hold a wide variety of cations, such as Na^+, K^+, and Mg^{2+}, among others, which balance the framework's negative charge. In addition to these cations, water is also located in the cavities. When heated the water is released causing them to dance about, which is why zeolites means "stones that boil" in Greek. These cations can be exchanged because of the large size and/or weak interactions between the cations and the cavity walls.

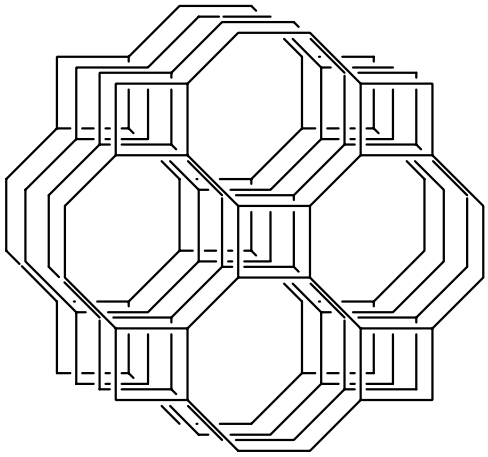

Figure 1.10 – A zeolite framework in which the cavities are shown. The silicon atoms are located where the lines meet. The silicon atoms are bridged by oxygen atoms. If the structure is rotated 90°, the structure looks identical, giving the zeolite a three-dimensional channel system.

More industrially important than cation exchange is the water that is trapped in zeolites, making the zeolites extremely powerful acids. They are such strong acids that H^+ can be easily attached to hydrocarbons. This attachment of H^+ dramatically increases the hydrocarbon reactivity. In the end, the zeolite is able to re-acquire the H^+ from the hydrocarbons, returning the zeolites to the same condition and therefore making the microporous aluminosilicates a catalyst.[33] Industrial processes are used to produce

zeolites with specific pore sizes and shapes. The petroleum industry uses the specificity in order to create the desired types of hydrocarbons.

Another widely used type of silicate is clay. The framework of natural clays is also made of corner-sharing SiO_4 tetrahedra with the addition of AlO_6 octahedra. However, instead of a three-dimensional framework like quartz and zeolites, clays are two-dimensional materials (Figure 1.11). These sheets contribute to the clay's absorptive property since the clay can swell, allowing small molecules and cations to intercalate. Clays are classified depending on the way the sheets pack and the arrangement of tetrahedra and octahedra.[35]

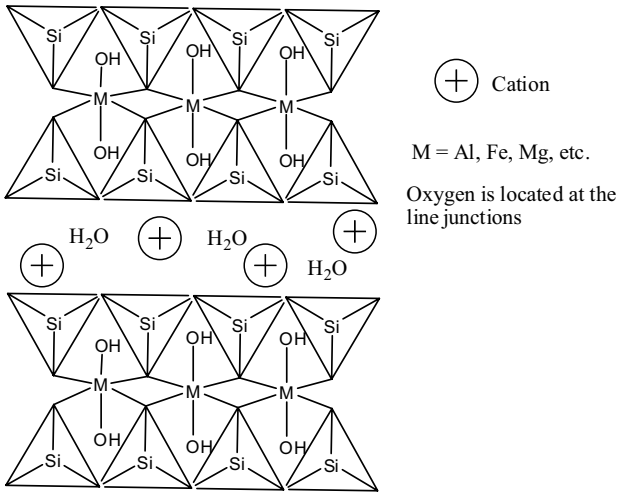

Figure 1.11 –. The structure of clay consists of layers of the alumino-silicate structure with loosely held cations and solvent located between the layers. The cations are usually alkali metals or alkaline earth metals.

We are able to use this knowledge to try and "engineer" silicate mimics. We deal primarily with copper(I), which has an electronic configuration of d^{10}. Copper(I) compounds generally exhibit tetrahedral coordination of ligands around the copper cation. A variety of different structures can be made from copper(I) coordination complexes, ranging from simple discrete molecules, one-dimensional chains, two-

dimensional ladders, three-dimensional networks, or sometimes a combination of these topologies.

We have found initial success with producing a coordination network silicate mimic that is similar to the feldspar structure.[36] In the feldspar mimic, copper(I) is coordinated to four bridging pyrimidine ligands. When pyrimidine bridges copper cations, the Cu-pyrimidine-Cu angle is 120° which is smaller than the Si-O-Si 145° angle discussed earlier (Figure 1.12). The 120° angle leads to hexagonal cavities in which the anions and solvents lie.

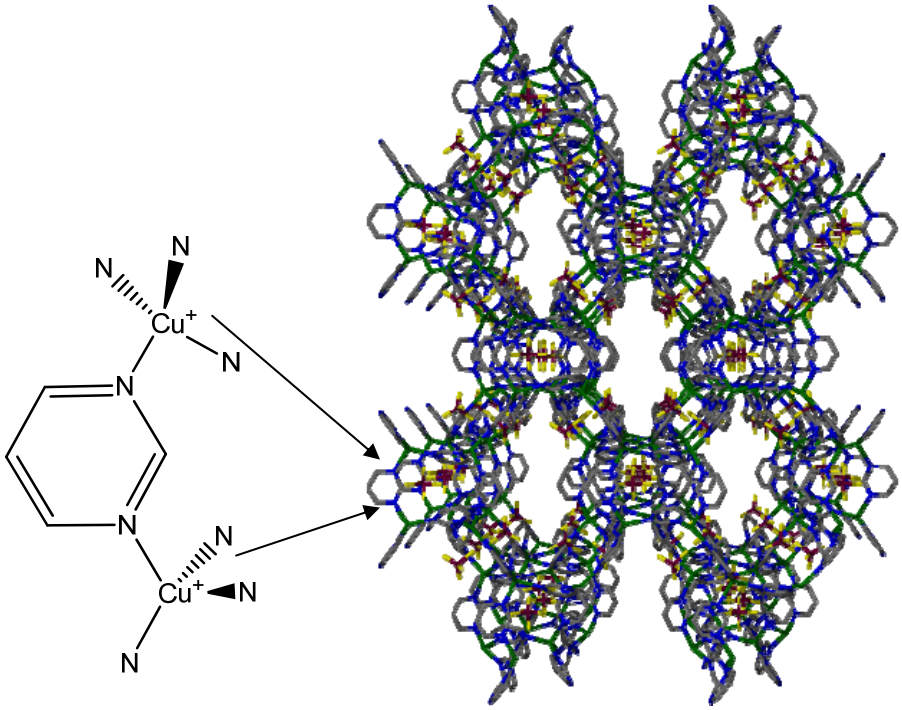

Figure 1.12 – On the left, figure of the bond angle between Cu-pyrimidine-Cu, which is 120°. This bond angle is smaller than the Si-O-Si bond angle, 145°. On the right is extended structure of the feldspar mimic. The color scheme is as follows: C = carbon, Cu = green, N = blue, F = yellow, and B = red. The hydrogen atoms are removed for clarity.[36]

A comparison between the feldspar and copper(I)-pyrimidine structure can be seen in Figure 1.13. One difference between feldspar and this coordination network is the

charge of the framework. Instead of a negatively charged network of feldspar, the copper(I)-pyrimidine network is positively charged when the neutral ligand pyrimidine is used. This provides the possibility of anion exchange. In both cases the cavities are filled with the non-coordinated counter ion.

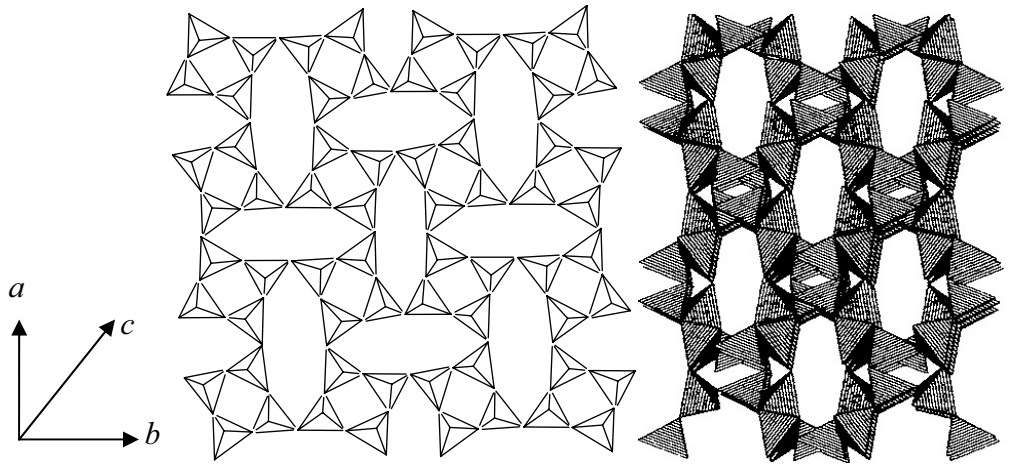

Figure 1.13 – On the left is a representation of the feldspar structure viewed down the *c*-axis. Feldspar has a empirical formula of $(Na,K)AlSi_3O_8$ or $Ca_2Al_2Si_2O_8$. The tetrahedra contain either silicon or aluminum atoms in the center surrounded by oxygen atoms. These tetrahedra form eight-membered rings that loosely hold cations. The copper(I)-pyrimidine feldspar mimic has the copper atoms located at the centers of the tetrahedra. Anions (instead of cations) are held within the cavities.[36]

With the initial success of creating a feldspar mimic, it was decided to use 3,3'-bipyridine because of its similarity to pyrimidine (Figure 1.14).[37] The design rationale was to extend the distance between nitrogen atoms, which would serve to enlarge the cavities of the feldspar mimic. Like the pyrimidine-copper(I) compound, the 3,3'-bipyridine-copper(I) structure has the copper(I) cation coordinated to four different 3,3'-bipyridine ligands. However, the crystal structure turned out to be a two-fold interpenetrating network and not the feldspar mimic (Figure 1.15). The interpenetration was caused by the rotation of the 3,3'-bipyridine's pyridine rings. This rotation allows

for the ligands to pack closer together.

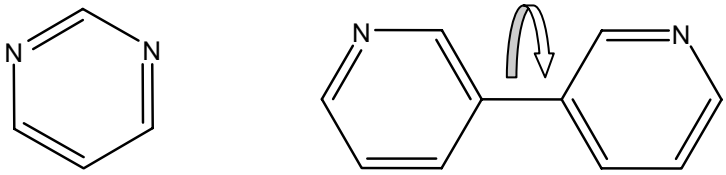

pyrimidine 3,3'-bipyridine

Figure 1.14 – The molecular comparison of pyrimidine and 3,3'-bipyridine.

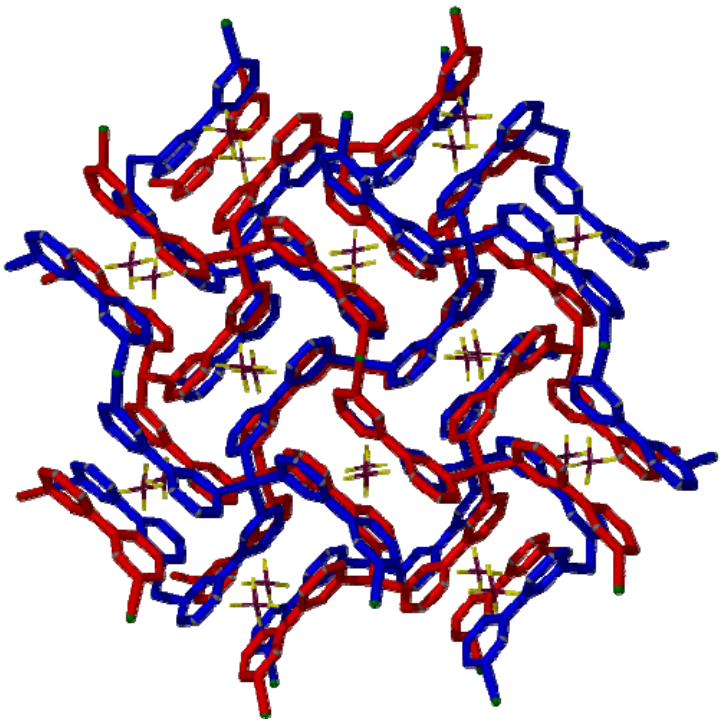

Figure 1.15 – Stick representation of the [Cu(3,3'-bipyridine)$_2$](BF$_4$ or PF$_6$) two-fold interpenetrating network.[37].

The focus of producing silicate mimics is still present in our group. More recently we crystallized a copper(I)-pyrimidine structure that closely resembled the zeolite A structure. With this structure there have been some encouraging results with anion exchange (Figure 1.16). An anion exchange competition between pertechnetate

($^{99m}TcO_4^-$) and its analog ReO_4^- with ClO_4^-, SO_4^{-2}, PO_4^{3-}, and NO_3^- was performed.[38] It was shown that the compound had a strong selectivity toward ReO_4^-, which is a good indication of the expected results for pertechnetate, a fission product of nuclear power plants.[39] The network remained intact and crystalline after several weeks of being left in the solvent-exchange solution. The anion exchange property suggests it might be used in further studies and eventually used as an anion-exchange medium.

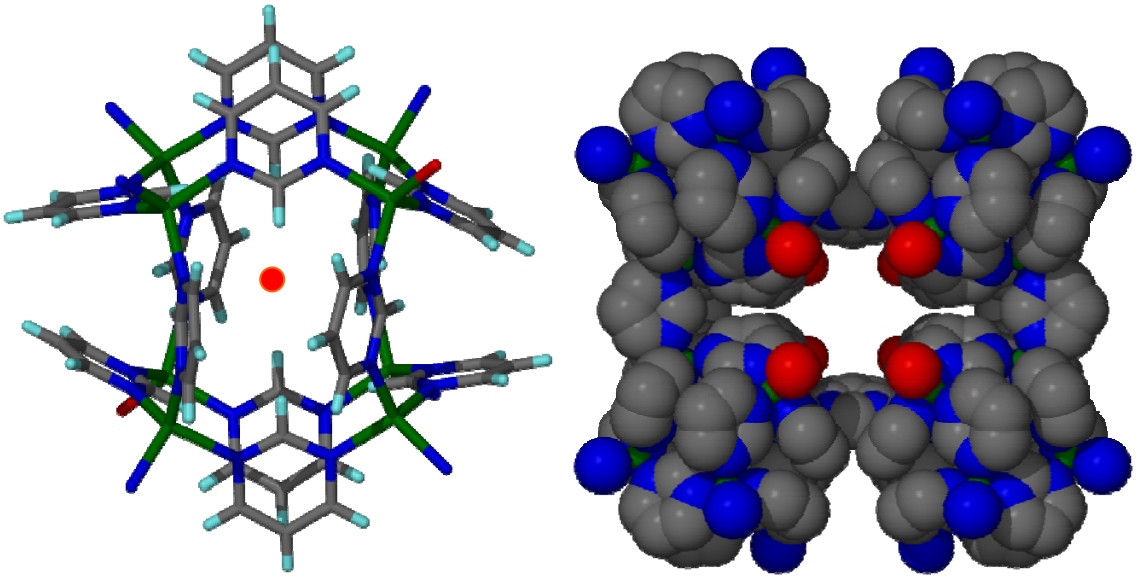

Figure 1.16 – On the right is a single cage in which one of the anions is located. The copper(I) cations, in green, are bridged by the pyrimidine ligands. The anion's location is signified by the red dot. On the left is the extended structure made from connecting cages together via pyrimidine ligands. A terminating hydroxide, in red, contributes to the overall structure from the connected cages continuing in all directions. All hydrogen atoms and anions have been removed for clarity.

1.2 Synthesis and Characterization of Coordination Networks

The basis for synthesizing coordination networks is performed by using solubility differences between reactants and products. The first method used is hydrothermal solvation. In this process the reaction mixture is heated, at times under pressure. In some

cases unstable ligands can be accessed through this technique, therefore increasing the number of structure possibilities.[40] The second method is through a process called solvent vapor diffusion (SVD) and is the primary way to obtain good quality crystals for single crystal X-ray diffraction (XRD).

In SVD, the solvent composition changes slowly, allowing the slow crystallization of coordination networks. The reagents are dissolved in an open reaction vessel, which is then put into a larger vessel. The larger vessel contains a solvent, the outer solvent, in which the coordination network is assumed not to be as soluble. When the open reaction vessel is placed in the large vessel, the outer solvent volume is not enough to spill into the inner container. Over time the outer solvent diffuses into the inner vessel; that solvent's outer concentration slowly increases in the inner vial, causing product to crystallize slowly (Figure 1.17). This slow crystallization leads to good quality single crystal growth. Single crystals are needed in order to determine the coordination network structure.

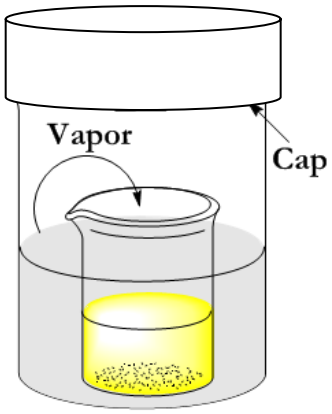

Figure 1.17 – A schematic of the SVD setup, in which the open reaction beaker is inside a larger beaker that is capped. The solvent in the larger beaker surrounds the smaller beaker. The outer solvent slowly diffuses into the inner beaker. The diffusion time depends on the volatility of the solvent.

The resulting single crystals are then inspected for use in XRD. A single crystal

is considered of good quality if the crystal can extinguish polarized light. The crystal is then mounted on a fiber and put in a liquid nitrogen stream in order to keep the crystal at -100 °C. The temperature helps to limit the amount of molecular motion, which in turn improves the results after the pattern is analyzed. A beam of X-rays produced by electrons emitted from a cathode hitting a metal plate (usually Cu or Mo) is directed at the crystal. The crystal diffracts the X-ray beam. The angle of diffraction and X-ray wavelength is related by the formula $n\lambda=2d \sin\theta$, also known as Bragg's Law.[41] The relation between the diffraction angle and X-ray wavelength is based on the position of crystallographic planes from which the X-rays diffract. The diffraction causes a screen sensitive to the diffracted X-rays to phosphoresce at the locations that are hit by X-rays. The arrangement of spots is captured by a charge-coupled device (CCD) camera, which serves as a detector (Figure 1.18). The crystal and/or detector then change position as directed by a computer in order to capture another piece of diffraction data. This process is continued until enough data is collected to solve the crystal structure through data analysis. The data is refined with software in order to determine the three-dimensional placement of atoms. This refinement is performed by or with help from an experienced crystallographer in order to determine the legitimacy of the structure.

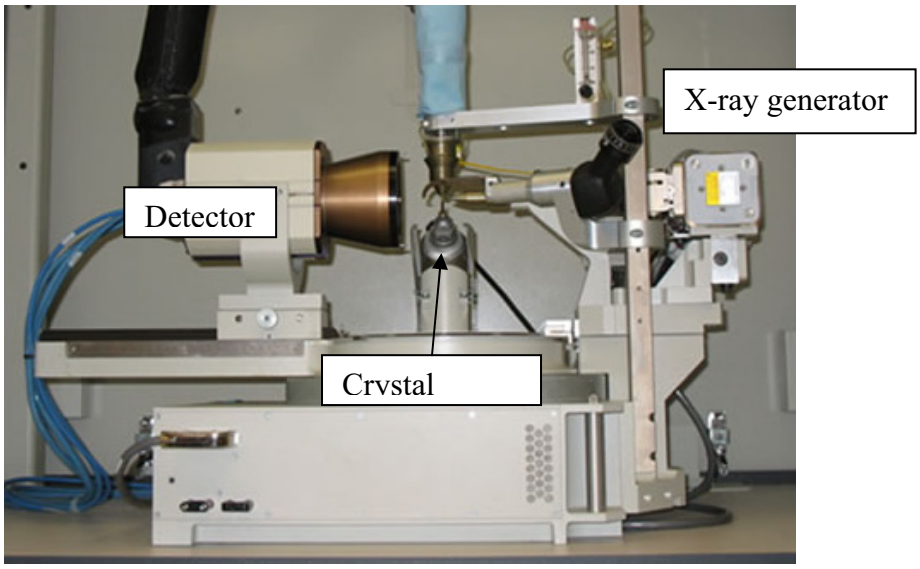

Figure 1.18 – Picture of the Siemens SMART system (Mo(K_α) = 0.71073 Å) with a CCD area detector at the University of Missouri-Columbia. With each sample a full hemisphere of crystallographic data was collected.

The structure of a powder sample can be determined by using powder X-ray diffraction (PXRD). Instead of the powder sample being rotated, the detector and the emitter proceed through a desired angle range (Figure 1.19). Diffraction of the X-ray beam occurs at different angles.

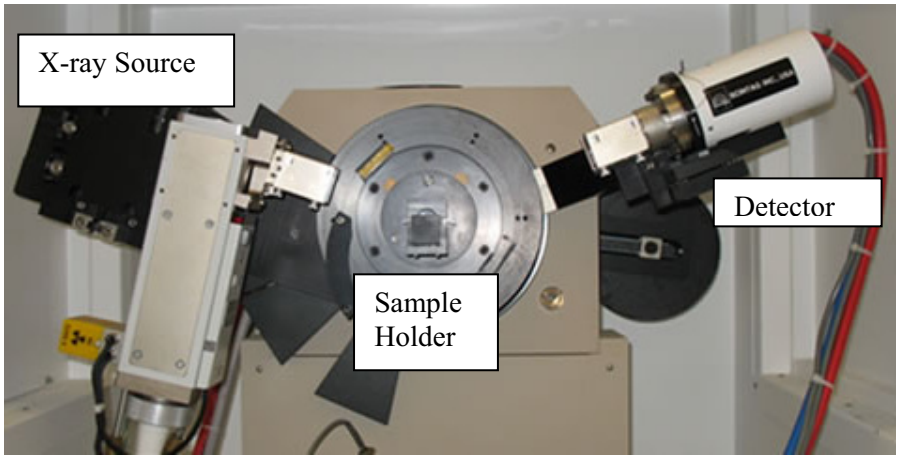

Figure 1.19 – Picture of the Scintag X2 system at the University of Missouri-Columbia. The instrument collected PXRD patterns at 40 kV and 30 mA for Cu K_α (λ=1.540562 Å).

The detector then relates the angle of that diffraction and intensity to the computer that relates the information graphically developing the PXRD pattern. The resultant data is different for PXRD than for single crystal XRD; instead of spots, a ring pattern forms (Figure 1.20). This is because the powder is a polycrystalline material. This difference can be understood when looking at the simple case of twinned crystals.

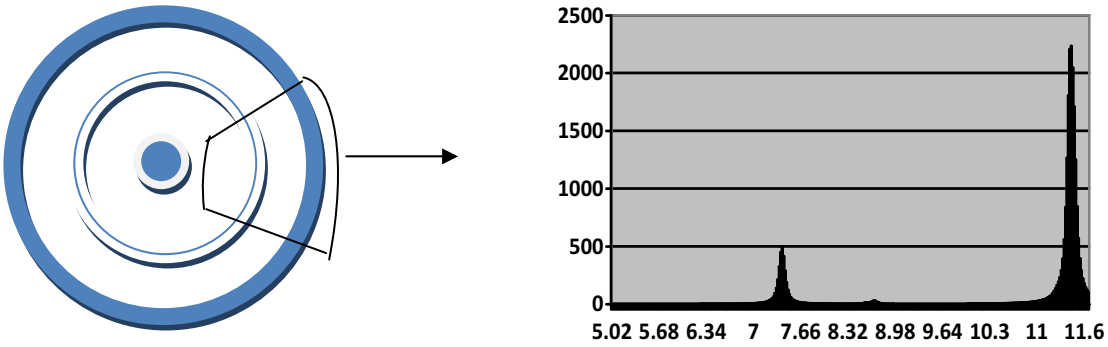

Figure 1.20 – Diffraction pattern for polycrystalline material on the right. The computer output can be seen on the right. On the graph, the x-axis is the degree at which diffraction takes place and the y axis is the intensity of the diffraction.

A twinned crystal is two crystals that are thought to be a single crystal, but the two crystals do not align perfectly (Figure 1.21).

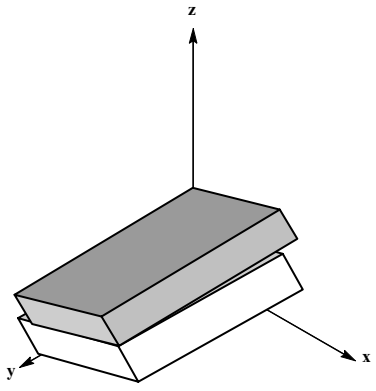

Figure 1.21 – In this example the two single crystals are shifted slightly from one another. This shifting causes the two phosphorescent spots to appear directly next to each other.

This misalignment causes the diffraction pattern to show two spots directly next to each other (Figure 1.22). A polycrystalline material consists of a multitude of single crystals that are randomly oriented. The random orientation of the crystals can be thought of as an extension of the twined crystals. Since the powder is made up of so many crystals and each crystal contributes a spot array, rings form from all the contributions.

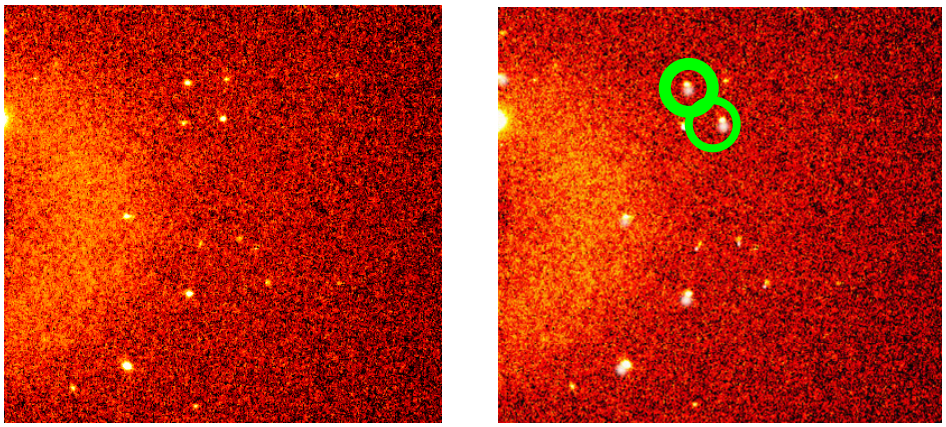

Figure 1.22 – Figure of the comparison between the diffraction patterns of a single crystal (on right) and a twinned crystal (on left). The double spots are circled in green.

The usual structural identification method of a powder sample is to use known single crystal XRD data in order to calculate a PXRD pattern. Any crystalline material that is at least 5% of the overall powder composition will have peaks that correspond to that material. The time-tested software program used in this endeavor is Lazy-Pulverix.[42] This calculated PXRD pattern is then compared to the experimental PXRD pattern. If the patterns match, then an experienced crystallographer determines whether the powder is indeed the same crystal structure as the one found for the single crystal. Indexing the PXRD pattern by Treor 90[43] or DICVOL[44] software programs in order to determine the unit cell parameters also can be used as further support. However, if the patterns do not match, one might need to produce single crystals for XRD to resolve the true crystal

structure of the powder sample. It is possible to dissolve a powder sample in order to seed the growth of X-ray quality single crystals.[45]

One problem with matching and indexing PXRD patterns is the fact that thermal expansion can shift the PXRD pattern peaks, which signifies a change in the unit cell dimensions. As mentioned, single crystal data are usually collected at -100 °C, whereas PXRD is normally performed at room temperature. The change in the diffraction pattern can be dramatic especially when the crystal packing contains a lot of weak intermolecular forces. A good example of this can be found with urea. Urea crystals are dominated by hydrogen bonding between each urea having four hydrogen bonds along the *c*-axis and two hydrogen bonds along the *a*-*b* plane (Figure 1.23).[46] The unit cell expands from a = 5.59 Å and c = 4.69 Å to a = 5.67 Å and c =4.71 Å at 150 K and 293 K, respectively.[47] Note that the *a*-axis expanded to a greater extent (0.08 Å) than *c* (0.02 Å) because of the stronger interactions along the *c*-axis. This expansion would therefore shift the PXRD pattern peaks to lower 2θ value. This shift would not be the same for all peaks since the plane distances would change differently depending on the orientation of the hydrogen bonding.

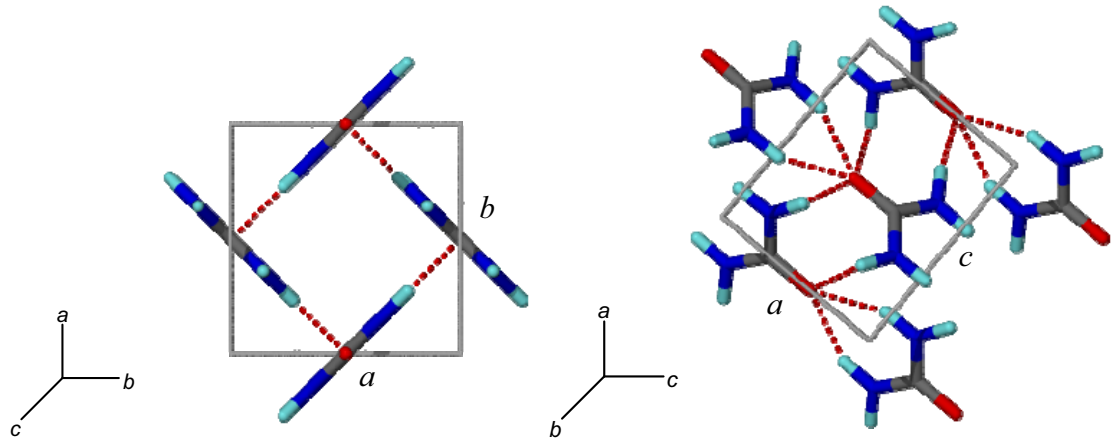

Figure 1.23 – On the left is the view of the *a*-*b* plane for urea. On the right is the view of the *a*-*c* plane for urea. The strongest intermolecular interactions can be seen along the *c*-axis. Hydrogen bonding is indicated by the red dashed lines. The color scheme is as follows: N = blue, C = gray, O = red, and H = aqua.[46]

The other issue with comparing the calculated to the experimental PXRD patterns is that the shape of the crystals, especially observed with needles and plates, can also have an effect on the observed intensities. This effect is referred to as preferred orientation. The reason for preferred orientation is the way the crystals lie against each other. For example, crystal plates more favorably lie on one another with the wide face of the crystal. This causes the powder to not maintain a true random orientation. The effect of preferred orientation can lead to intensities of certain peaks to lower, even to the point of peak disappearance. In Figure 1.24, the effect of preferred orientation can be seen in the disappearance of the peak at around 12.5° and the increase of the peak intensity at 30° for the preferred orientation pattern vs. the random orientation. Preferred orientation must be considered when comparing an experimental PXRD pattern and the calculated PXRD pattern from the single crystal data. The calculated PXRD pattern from the single crystal XRD data is assumed to be under random conditions.

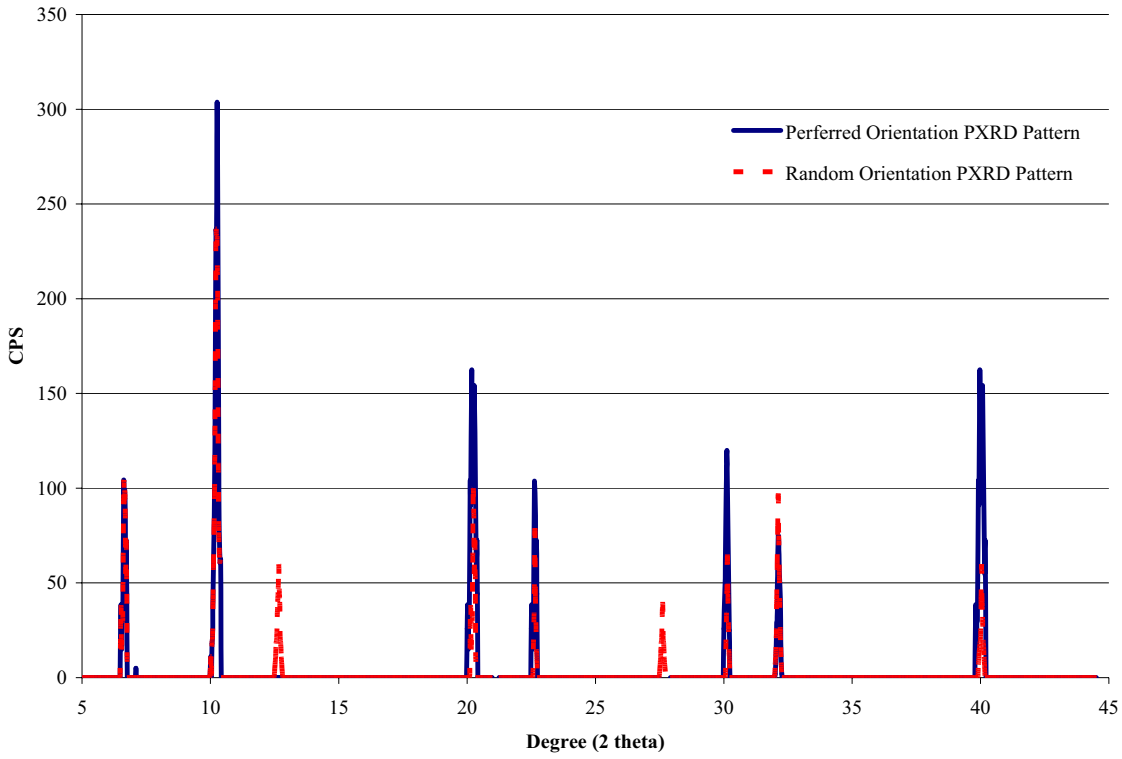

Figure 1.24 – Comparison between a random ordered polycrystalline material and one with preferred orientation. The pattern with preferred orientation has different peak intensities. The relative intensity has changed between the peaks.

1.3 Solid-Solid Reactions as a Route to Green Chemistry

The structure determination of powder compounds is important not only because it saves time and work, but it can contribute to the area green chemistry. This contribution is represented by analyzing products from solid-solid reactions in order to determine the products structure. Solid-solid reactions can assist with the goal of green chemistry which is to use chemical processes and reactants to minimize any adverse impact on the environment. Like achieving 100% efficiency, the goal of perfecting a synthesis to make it perfectly green is not plausible, but we always strive to achieve the

maximum goal. According to the Environmental Protection Agency (EPA) there are twelve principles of green chemistry, which are as follows:[48]

1. **Prevent waste:** Design chemical syntheses to prevent waste, leaving no waste to treat or clean up.
2. **Design safer chemicals and products:** Design chemical products to be fully effective, yet have little or no toxicity.
3. **Design less-hazardous chemical syntheses:** Design syntheses to use and generate substances with little or no toxicity to humans and the environment.
4. **Use renewable feedstocks:** Use raw materials and feedstocks that are renewable rather than depleting. Renewable feedstocks are often made from agricultural products or are the wastes of other processes; depleting feedstocks are made from fossil fuels (petroleum, natural gas, or coal) or are mined.
5. **Use catalysts, not stoichiometric reagents:** Minimize waste by using catalytic reactions. Catalysts are used in small amounts and can carry out a single reaction many times. They are preferable to stoichiometric reagents, which are used in excess and work only once.
6. **Avoid chemical derivatives:** Avoid using blocking or protecting groups or any temporary modifications if possible. Derivatives use additional reagents and generate waste.
7. **Maximize atom economy:** Design syntheses so that the final product contains the maximum proportion of the starting materials. There should be few, if any, wasted atoms.
8. **Use safer solvents and reaction conditions:** Avoid using solvents, separation agents, or other auxiliary chemicals. If these chemicals are necessary, use innocuous chemicals.
9. **Increase energy efficiency:** Run chemical reactions at ambient temperature and pressure whenever possible.
10. **Design chemicals and products to degrade after use:** Design chemical products to break down to innocuous substances after use so that they do not accumulate in the environment.
11. **Analyze in real time to prevent pollution:** Include in-process real-time monitoring and control during syntheses to minimize or eliminate the formation of byproducts.
12. **Minimize the potential for accidents:** Design chemicals and their forms (solid, liquid, or gas) to minimize the potential for chemical accidents including explosions, fires, and releases to the environment.

Throughout the past decade there has been a great deal of interest in green chemistry, leading to the development of "solvent-free" reactions. In this way, some of the green principles could be accomplished, most notably *prevention of waste* and *use of safer solvents*. These reaction types include but are not exclusive to photochemical,[49] supercritical CO_2,[50,51] grinding, [52-57] high-speed ball milling,[58,59] ultrasound,[60] microwave irradiation,[61,62] ionic liquids,[63,64] or simply mixing. These reactions are considered solvent-free because a traditional external solvent is not being added to the reaction mixture. The lack of an external solvent increases the "greenness" of these reactions. A majority of these reactions are in fact not truly solvent-free, but instead one of the reactants serves as the solvent during the reaction progression, therefore aiding diffusion.[65,66] Perhaps the simplest case is a reaction in which one of the reagents is in the liquid phase, making the liquid reagent in effect the solvent.

Solid reagents can also be ground together giving these green reactions the benefit of generating products in a much higher yield. In some cases enantioselectivity is achieved, which is of vital importance in pharmaceuticals. [53] In some cases only one of the enantiomers is desired, with the other having a profoundly negative effect on a biological system. In the majority of organic solid reagent mixtures, the eutectic point is reached.[66] When the eutectic point is reached, both reactants melt allowing for a higher diffusion rate of the material. If the product is insoluble in the melt, it will of course precipitate out of the melt and thus lead to higher yields.

As a specific example, aldol condensation can be achieved by solid-solid reactions. Normally, noxious reagents are required for these types of reactions. [53] However, in the green form of the reaction, the reagents are ground together with solid

NaOH (Figure 1.25). The NaOH serves as a catalyst. Water is released and absorbed by the mixture, which increases diffusion. In a sense, the reaction is producing its own solvent which achieves the percent yield postcrystallization is 98%.[53]

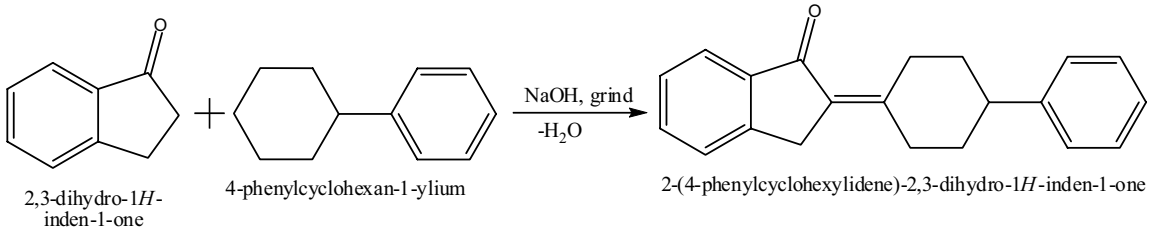

Figure 1.25 – Aldol condensation reaction using NaOH as a catalyst.

In the realm of coordination chemistry there have been some developments in solid-solid reactions. An example of this is the reaction of Pt(ethylenediamine)$(NO_3)_2$ and 4,4'-bipyridine (Figure 1.26). In this case, the reagents were ground together, forming a gummy mixture. It is interesting to note that the ethylenediamine in its pure form is a liquid at room temperature. This suggests that when the ethylenediamine becomes uncoordinated it is acting as a solvent that in turn increases the diffusion rate and therefore the reaction rate. This reaction is complete within ten minutes, as compared to a reaction in solution that requires a week at 100 °C.[56]

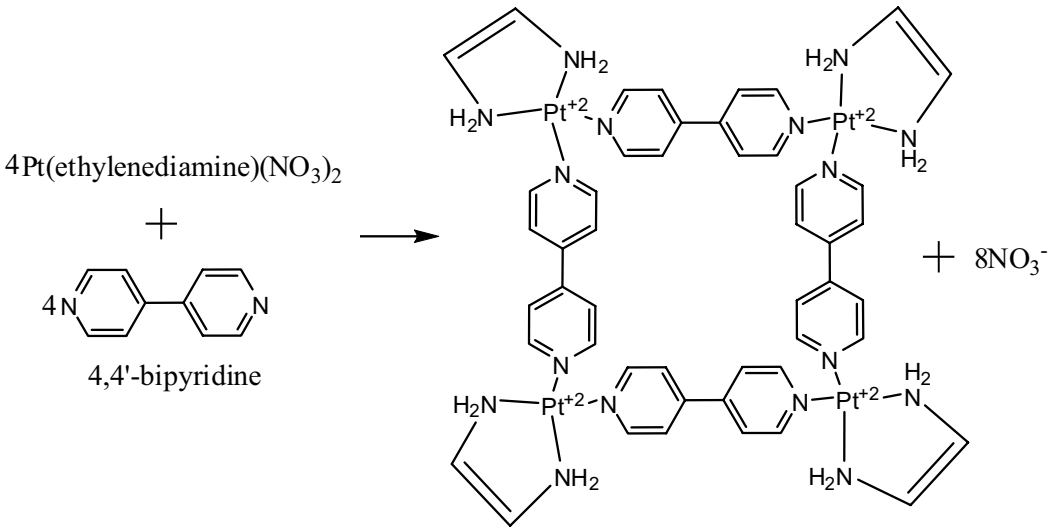

Figure 1.26 – Metal coordination chemistry without the use of an external solvent.

These solid-solid reactions address several principles of green chemistry. (Each principle addressed is in italics.) First, the *waste* created by using a solvent is lessened or prevented, with only a little needed for purification purposes. In addition to the waste, in some cases *noxious chemicals* needed for synthesis are eliminated. As seen in one of the examples, *catalysts* can still be used during these reactions. Products can be made that are stereoselective, and thus the need for *chemical derivatives* can be avoided. The *lack of a traditional solvent* increases the *energy efficiency* in three ways: refluxing the product is not needed, the amount of heat needed to drive off the solvent is lessened, and the reactions can be run at *ambient temperature and pressure*. The *percent yield* can be above 90% for this reaction, which at times can be dramatically higher than those produced in solution phase reactions. All of these reasons minimize the *potential for accidents*.

1.4 The Goal of Dissertation Research

In the following chapters, we will look to design principles in order to design synthetic solid-solid routes in which a crystalline product is created. In the cases noted in the introduction for solid-solid reactions, the material changes from a crystalline material to an amorphous product. Through this dissertation's research, novel solid-solid synthetic pathways are achieved in which the reactants and product are crystalline in nature without the need for prolonged grinding or annealing. The reactions are characterized in a number of ways in order to develop a picture of what is happening at the molecular level, i.e. mechanism.

The solid-solid reaction products were analyzed in order to identify the structure of the coordination networks created. The crystal structure of solid-solid reaction products is compared with solution-based products to serve as a route to identification. The solid-solid reactions progression to products are monitored through a variety of instrumental analyses. In this fashion, the mechanism by which these structures are created can be further refined. Through this understanding, we hope to design more complex coordination networks using solid-solid reactions. An example would be to create a mixed ligand network in which the design of the network could incorporate two or more different bridging ligands. The green chemistry principles will be used as a guide to further the improvement of coordination network synthesis.

This dissertation covers ligands that have been used in prior coordination networks. The ligands were chosen due to the likelihood of coordination network formation and the existence of known coordination networks of which they are a part.

4,7-phenanthroline is the ligand from which this dissertation begins due to the discovery of its reactivity with tetraacetonitrilecopper(I) tetrafluoroborate in the solid state. The expansion into other nitrogen-containing ligands similar to 4,7-phenanthroline was a natural progression. In the majority of the solid-solid reactions, a previously known solution-based coordination networks formed. However, in a few cases a newly created coordination network was found. In order to obtain the crystal structure of the new polycrystalline compounds, the material served to seed single crystal growth. The single crystals of good quality XRD were used to obtain the crystal structure. The single crystal XRD data was then compared to the polycrystalline XRD data to determine the structure of the compound. In some cases the structure remained undetermined.

This dissertation shows that the area of solid-solid reactions can be expanded into an area that can encompass a variety of ligands and coordinated solvents. These solid-solid reactions are rather unique; instead of continuously grinding to produce a crystalline product, the reaction progressed with or without mixing given the right conditions. In the end a polycrystalline product was formed, adding to the sphere of solid-solid reactions and green chemistry.

References

(1) Pederson, C. J. *J. Am. Chem. Soc.* **1967**, *89*, 2459-2496.

(2) Pederson, C. J. *J. Am. Chem. Soc.* **1967**, *89*, 7017-7036.

(3) Lehn, J. M. *Acc. Chem. Res.* **1978**, *11*, 49-57.

(4) Cram, D. J. *Science* **1988**, *240*, 760-767.

(5) Steed, J. W.; Atwood, J. L. *Supramolecular Chemistry*; Wiley, West Sussex, 2000.

(6) Brown, T. L.; LeMay, H. E. *Chemistry: The Central Science*; Prentice Hall: NJ, 2003.

(7) Dance, I. *New J. Chem.* **2003**, *27*, 22-27.

(8) Lehn, J. M. *Angew. Chem. Int. Ed. Engl.* **1990**, *29*, 1304-1319.

(9) Whitesides, G. M.; Grzybowski, B. *Science* **2002,** *295,* 2418-2421.

(10) Braga, D.; Grepioni, F. *Acc. Chem. Res.* **2000**, *33*, 601-608.

(11) Yaghi, O. M.; Li, G.; Li, H. *Nature* **1995**, *378*, 703-706.

(12) Eddaoudi, M.; Kim, J.; Rosi, N.; Vodak, D.; Wachter, J.; O'Keeffe, M.; Yaghi, O. M. *Science* **2002,** *295,* 469-472.

(13) Eddaoudi, M.; Moler, D. B.; Li, H.; Chen, B.; Reineke, T. M.; O'Keeffe, M.; Yaghi, O. M. *Acc. Chem. Res.* **2001**, *34*, 319-330.

(14) Yaghi, O. M.; Li, H. *J. Am. Chem. Soc.* **1996**, *118*, 295-296.

(15) Noro, S.; Kitaura, R.; Kondo, M.; Kitagawa, S.; Ishii, T.; Matsuzaka, H.; Yamashita, M. *J. Am. Chem. Soc.* **2002**, *124*, 2568-2583.

(16) Yaghi, O. M.; Li, H. *J. Am. Chem. Soc.* **1995**, *117*, 10401-10402.

(17) Gardner, G. B.; Kiang, Y. H.; Lee, S.; Asgaonkar, A.; Venkataraman, D. *J. Am. Chem. Soc.* **1996**, *118*, 6946-6953.

(18) Seo, J. S.; Whang, D.; Lee, H.; Jun, S. I.; Oh, J.; Jeon, Y. J.; Kim, K. *Nature* **2000**, *404*, 982-986.

(19) Aoyama, Y. *Top. Curr. Chem.* **1998**, *198*, 132-161.

(20) Manson, J. L.; Ressouche, E.; Miller, J. S. *Inorg. Chem* **2000**, *39*, 1135-1141.

(21) Songping, D. H.; Xiong, R. G. *Polyhedron* **1997**, *16*, 3929-3939.

(22) Evans, O. R.; Xiong, R. G.; Wang, Z.; Wong, G. K.; Lin, W. *Angew. Chem. Int. Ed. Engl.* **1999**, *38*, 536-538.

(23) Lin, X. J.; Shen, Z.; Li, Y. Z.; Uno, H.; Song, Y.; Xu, H. J.; You, X. Z. *J. Coord. Chem.* **2005**, *58*, 1139-1144.

(24) Desiraju, G. R. *Science* **1997**, *278*, 404-405.

(25) Desiraju, G. R.; Parshall, G. W. *Mater. Sci. Monogr.* **1989**, *54,* 85-113.

(26) Melendez, R. E.; Hamilton, A. D. *Top. Curr. Chem.* **1998**, *198*, 97-129.

(27) Zaworotko, M. J. *Chem. Soc. Rev.* **1994**, *23*, 283-288.

(28) Desiraju, G. R. *Acc. Chem. Res.* **2002**, *35*, 565-573.

(29) Lehn, J. M. *Proc. Natl. Acad. Sci. U.S.A.* **2002**, *99*, 4763-4768.

(30) Inman, C.; Knaust, J. M.; Keller, S. W. *Chem. Commun. (Camb.)* **2002**, *2*, 156-157.

(31) Yaghi, O. M.; Li, H.; Davis, C.; Richardson, D.; Groy, T. L. *Acc. Chem. Res.* **1998**, *31*, 474-484.

(32) Rosi, N. L.; Eckert, J.; Eddaoudi, M.; Vodak, D. T.; Kim, J.; O'Keeffe, M.; Yaghi, O. M. *Science* **2003**, *300*, 1127-1129.

(33) Ball, P. *Made to Measure: New Materials for the 21st Century*; Princeton University Press: Princeton, NJ, 1997.

(34) Mottana, A.; Crespi, R.; Liborio, G. *Simon and Schuster's Guide to Rocks and Minerals*; Simon and Schuster, Inc.: NY, 1978.

(35) Ball, P. *Designing the Molecular World: Chemistry at the Frontier*; Princeton University Press: Princeton, NJ, 1994.

(36) Keller, S. W. *Angew. Chem. Int. Ed. Engl.* **1997**, *36*, 247-248.

(37) Lopez, S.; Kahraman, M.; Harmata, M.; Keller, S. W. *Inorg. Chem.* **1997**, *36*, 6138-6140.

(38) Knight, D. A. Dissertation, University of Missouri-Columbia, Columbia, MO, 2005.

(39) Gawenis, J. A.; Holman, K. T.; Atwood, J. L.; Jurisson, S. S. *Radiochim. Acta.* **1993**, *60*, 203.

(40) Elsevier, C. J.; Reedijk, J.; Walton, P. H.; Ward, M. D. *Dalton Trans.* **2003**, *10*, 1869-1880.

(41) Hammond, C. *The Basics of Crystallography and Diffraction*; Oxford University Press, Oxford, UK, 2001.

(42) Yvon, K.; Jeitschko, W.; Parthe, E. *J. Appl. Crystallogr.* **1977**, *10*, 73-74.

(43) Werner, P. E.; Eriksson, L.; Westdahl, M. *J. Appl. Crystallogr.* **1985**, *18*, 367-370.

(44) Boultif, A.; Louër, D. *J. Appl. Cryst.* **2004**, *37*, 724-731.

(45) Braga, D.; D'Addario, D.; Maini, L.; Polito, M.; Giaffreda, S.; Rubini, K.; Grepioni, F. *Top. Curr. Chem.* **2005,** *245,* 1562-1578.

(46) Docherty, R.; Roberts, K. J.; Saunders, V.; Black, S.; Davey, R. J. *Faraday Discuss.* **1993**, *95*, 11-25.

(47) Hammond, R.; Pencheva, K.; Roberts, K. J.; Mougin, P.; Wilkinson, D. *J. Appl. Crystallogr.* **2005**, *38*, 1038-1039.

(48) Agency, U. S. E. P. Washington, D.C., 2006; Vol. 2007.

(49) Gao, X.; Friscic, T.; MacGillivray, L. R. *Angew. Chem. Int. Ed. Engl.* **2004**, *43*, 232-236.

(50) Cooper, A. I. *Green Chem.* **1999**, *1*, G167.

(51) Rohr, M.; Geyer, C.; Wandeler, R.; Schneider, M.; Murphy, E.; Baiker, A. *R. Soc. Chem.* **2001**, *3*, 123-125.

(52) Bose, D. S.; Fatima, L.; Mereyala, H. B. *J. Org. Chem.* **2003**, *68*, 587-590.

(53) Cave, G. W.; Raston, C. L.; Scott, J. L. *Chem. Comm. (Camb.)* **2001**, *21*, 2159-2169.

(54) Cave, G. W. V.; Raston, C. L. *J. Chem. Soc. Perkin Trans.* **2001**, *1,* 3258-3264.

(55) Cave, G. W. V.; Raston, C. L. *Tet. Lett.* **2005**, *46*, 2361-2363.

(56) Orita, A.; Jiang, L.; Nakano, T.; Ma, N.; Otera, J. *Chem. Commun. (London 1996 Print)* **2002**, *14,* 1362-1363.

(57) Raston, C. L.; Scott, J. L. *Green Chem.* **2000**, *2*, 49-52.

(58) Kaupp, G.; Schmeyers, J.; Boy, J. *Chemosphere* **2001**, *43*, 55-61.

(59) Kaupp, G.; Schmeyers, J.; Naimi-Jamal, M. R.; Zoz, H.; Ren, H. *Chem. Eng. Sci.* **2002**, *57*, 763-765.

(60) López-Pestaña, J. M.; Ávila-Rey, M. J.; Martín-Aranda, R. M. *Green Chem.* **2002**, *4*, 628-630.

(61) Díaz-Ortiz, A.; de la Hoz, A.; Langa, F. *Green Chem.* **2000**, *2*, 165-172.

(62) Kad, G. L.; Bhandari, M.; Kaur, J.; Rathee, R.; Singh, J. *Green Chem.* **2001**, *3*, 275-277.

(63) Harjani, J. R.; Friscic, T.; MacGillivray, L. R.; Singer, R. D. *Inorg. Chem.* **2006**, *45*, 10025-10027.

(64) Huang, J.; Jiang, T.; Gao, H.; Han, B.; Liu, Z.; Wu, W.; Chang, Y.; Zhao, G. *Angew. Chem. Int. Ed.* **2004**, *43*, 1397-1399.

(65) Braga, D.; D'Addario, D.; Giaffreda, S. L.; Maini, L.; Polito, M.; Grepioni, F. *Top. Curr. Chem.* **2005**, *254*, 71-94.

(66) Rothenberg, G.; Downie, A. P.; Raston, C. L.; Scott, J. L. *J. Am. Chem. Soc.* **2001**, *123*, 8701-8708.

Chapter 2

Solid-State Reaction between $[Cu(MeCN)_4]X$ and 4,7-phenanthroline ($X = PF_6^-$, BF_4^-, and $SO_3CF_3^-$)

2.1 Introduction

The Keller group strives to understand the conditions, be they solvent, ligand, or metal, to produce a certain type of crystal structure. With this understanding, it may be possible to "engineer" a particular crystal structure. This can lead to the ultimate ability to predict the structure of and therefore accomplish reticular chemistry. "Crystal engineering" would achieve the ultimate goal of our group in which we use this predictive ability to synthesize structures that mimic silicates and specify cavity size.

As mentioned in Chapter 1, 3,3'-bipyridyl was used instead of pyrimidine with $[Cu(MeCN)_4]X$ ($X = BF_4^-$ and PF_6^-) in order to change the cavity size of the feldspar mimic created by the copper(I)-pyrimidine coordination network.[1] However, due to the rotation of the pyridine rings, a two-fold interpenetrating diamonoid network was created. We first used the 4,7-phenanthroline ligand because of its similarity to 3,3'-bipyridyl, but with the added benefit of the nitrogen atoms being in a fixed position (Figure 2.1). Because of the 4,7-phenanthroline molecule's structure, a feldspar mimic was not created due to the steric bulk of 4,7-phenanthroline molecules. Based on the structural synthesis results, the bulkiness of the 4,7-phenanthroline molecule allows at most three 4,7-phenanthroline molecules to be coordinated to the copper(I) cation.[2]

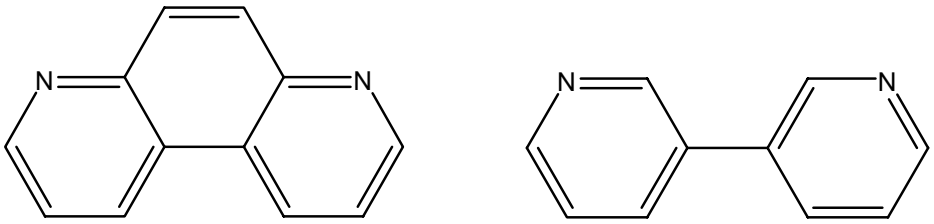

4,7-phenanthroline 3,3'-bipyridyl

Figure 2.1 – Comparison of the molecular structures of 4,7-phenanthroline and 3,3'-bipyridyl.

The previously reported case used a solution-based synthesis in which the reactants were dissolved in acetonitrile and nitrobenzene, into which diethyl ether (Et_2O) was diffused. It was found that by grinding $[Cu(MeCN)_4]BF_4$ with 4,7-phenanthroline the material changed from an off-white reaction mixture to a bright yellow. This was the launching pad for this dissertation.

Each of the tetraacetonitrilecopper(I) starting materials, $[Cu(MeCN)_4]BF_4$, $[Cu(MeCN)_4]PF_6$, and $[Cu(MeCN)_4]SO_3CF_3$, has essentially the same structure.[3-5] The anions are non-coordinating, with the copper(I) cation being coordinated to four acetonitrile molecules. The coordination environment gives the copper a distorted tetrahedral geometry. When equimolar amounts of starting material were used in solution-based synthesis, the structures produced were of the one-dimensional chain variety (Figure 2.2). The product of $[Cu(MeCN)_4]PF_6$ and 4,7-phenanthroline was zigzag chains with non-coordinated PF_6^- anions.[6] The bond angle between the coordinated 4,7-phenanthroline is 128° giving a distorted tetrahedral geometry around the copper cation (Figure 2.3). The wide angle is due to the interchain interactions, primarily π-π stacking (Figure 2.4). The π-π stacking of the different chains causes the aforementioned bond angle to enlarge to have the 4,7-phenanthroline molecules essentially lying on the same plane.

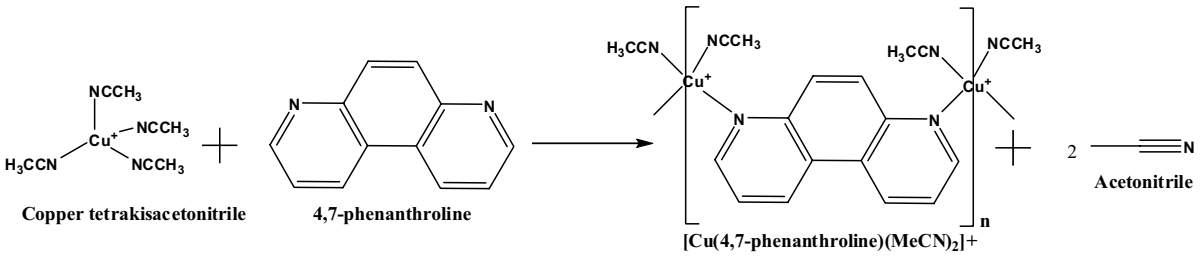

Figure 2.2 – Chemical reaction between tetraacetonitrilecopper(I) salt and 4,7-phenanthroline to create linear chains.

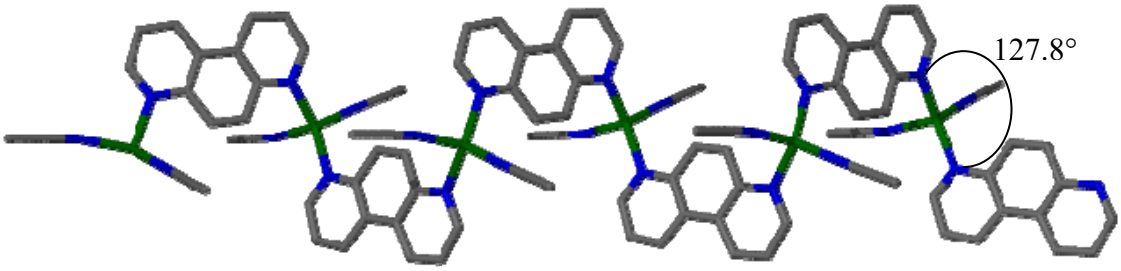

Figure 2.3 – Stick representation of the linear chains of $\{[Cu(4,7\text{-phenanthroline})(MeCN)_2]PF_6\}_n$. Each copper is coordinated to two 4,7-phenanthroline molecules and two acetonitrile molecules. The hydrogen atoms and PF_6^- anions are removed for clarity. The Cu is in green, C in gray, and N in blue.[6]

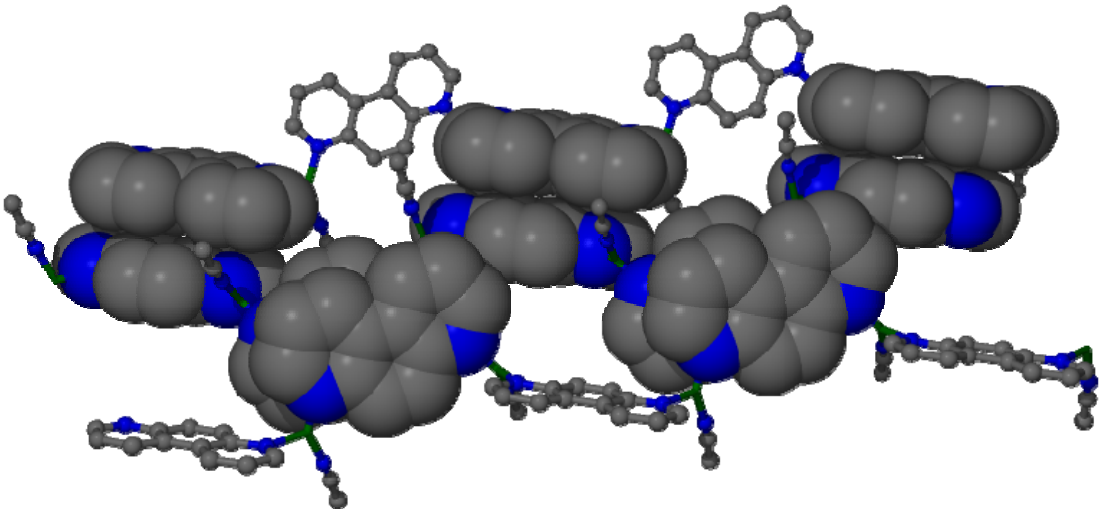

Figure 2.4 – Figure showing the interaction between three of the chains. The π-π interactions occur with each of the 4,7-phenantholines in the chains. The figure shows select interactions that cause the 4,7-phenanthroline-Cu-4,7-phenanthroline bond angle to be a rather large 128°.[6]

The equimolar reaction of $[Cu(MeCN)_4]BF_4$ and 4,7-phenanthroline created a different chain configuration than $\{[Cu(MeCN)_2(4,7\text{-phenanthroline})]PF_6\}_n$ crystal

structure.[6] Instead of two coordinated acetonitrile molecules, there is only one coordinated to the copper cation. The 4,7-phenanthroline molecules still acts as a linker between the copper(I) centers producing a one-dimensional chain. The copper(I) cation has a distorted trigonal coordination environment with the N-Cu-N angle of 107° (Figures 2.5 and 2.6). The BF_4^- anion is also not coordinated to the copper, even though the copper is only three coordinate.

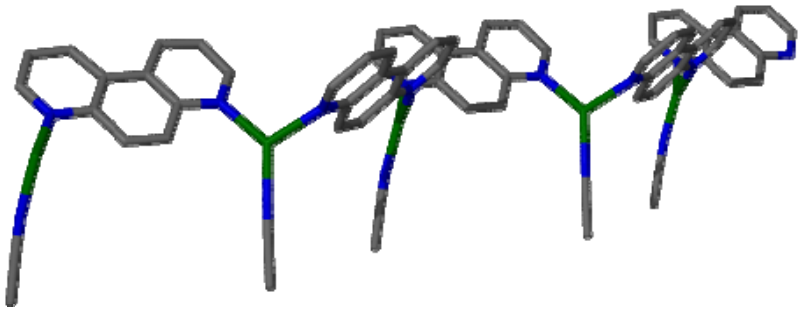

Figure 2.5 – Stick representation of the linear chains of $\{[Cu(4,7\text{-phenanthroline})(MeCN)_2]BF_4)_n$. Each copper is coordinated to two 4,7-phenanthroline molecules and one acetonitrile molecule. The hydrogen atoms and BF_4^- anions are removed for clarity.[6]

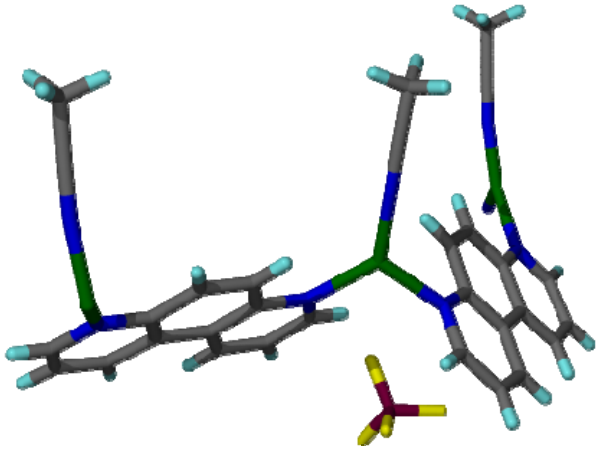

Figure 2.6 – This figure shows the closest contact between the fluorine in the BF_4^- and the copper cation. The distance between the copper cation and a fluorine on the BF_4^- is 4.52 Å, signifying non-coordination.[6]

In the case of the $[Cu(MeCN)_4]SO_3CF_3$ and 4,7-phenanthroline reaction product the $SO_3CF_3^-$ anion is coordinated to the copper(I) cation.[2] Its structure is similar to that of $\{[Cu(4,7\text{-phenanthroline})(MeCN)_2]PF_6\}_n$, where the triflate anion replaces one of the coordinated acetonitrile molecules (Figure 2.7). The bond angle between the two 4,7-phenanthroline ligands is 129.2°, close to the 127.8° for $\{[Cu(4,7\text{-phenanthroline})(MeCN)_2]PF_6\}_n$.

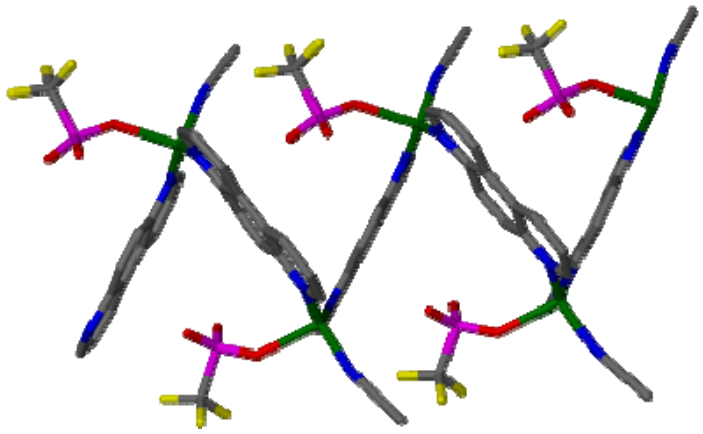

Figure 2.7 – Stick representation of the one-dimensional chains formed during the solid-solid reaction for $\{Cu(4,7\text{-phenanthroline})(MeCN)(SO_3CF_3)\}_n$. Each copper has a triflate anion coordinated to it.[2]

Previous accounts noted that acetonitrile vapor would readily evolve from $[Cu(MeCN)_4]PF_6$, which leads to the oxidation of copper.[7] One can readily see the difference when making $[Cu(MeCN)_4]SO_3CF_3$ powder. The color changes from white to blue within a minute of contact with ambient air, indicating oxidation of the starting material; this is why special handling is needed for the material. In comparison, $[Cu(MeCN)_4]PF_6$ is relatively air stable, lasting upwards of a day in an open container before oxidation is visually apparent. The $[Cu(MeCN)_4]BF_4$ stability in air lies somewhere in between. This loss of acetonitrile will be studied, in order to delineate

between the different compounds. Like the reactions to be studied, the material will be monitored at room temperature to imitate those conditions.

2.2 Experimental

Materials and Methods

Copper(I) oxide (Fisher), tetrafluoroboric acid (Aldrich), hexafluorophosphoric acid (Aldrich), Trifluoromethanesulfonic acid (Aldrich), 4,7-phenanthroline (GFS Chemicals and Aldrich), acetonitrile (Fisher), and Et_2O (Fisher) were used without further purification unless otherwise noted in the synthesis.

Powder X-ray diffraction (PXRD) patterns were collected using a Scintag X2 system at 40 kV and 30 mA for Cu K_α radiation(λ=1.540562 Å). Continuous scans were taken at 0.60°/min from 5° to 37° 2θ, unless otherwise noted. All patterns were indexed with Treor 90[8] or DICVOL[9] software programs. A figure of merit of 10 was used for Treor 90. Single crystal X-ray diffraction (XRD) data of previously solved structures were used in conjunction with LAZY-PULVERIX[10] to generate the calculated powder patterns used for comparison.

Gas chromatography mass spectrometry (GC-MSD) was performed using an Agilent 6890 (Agilent, San Jose) split-less mode at an oven temperature of 60 °C. A 1-μL gas-tight syringe taking a 0.2-μL sample size was used, unless otherwise noted. The samples were taken with an autosampler to ensure sample size precision. Each vial was 2 mL in size and had a Teflon-silicone-Teflon septum. The data were analyzed using WSearch32,[11] where the total ion count (TIC) of the acetonitrile parent ion was taken at the peak of the spectrum.

UV-Visible (UV-Vis) spectra were recorded using a Cary 3 (Varian, Melrose, Australia) with a diffuse reflectance attachment. A home-built sample holder used a polyethylene gasket with a rubber core between two 40 mm diameter optically inactive fused silica discs (Figure 2.8). A Teflon sheet was then inserted to serve as a neutral backing. In order to provide a gas-tight seal, the assembly was clamped together via four bolts. Each run was limited to 350-800 nm as a result of the noise beyond those wavelengths.

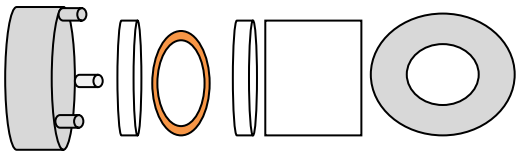

Figure 2.8 – Schematic of the homebuilt UV-Vis diffuse reflectance sample holder. Left to right: metal sample holder, 40 mm diameter fused silica disc, polyethylene gasket with rubber core, 40 mm diameter fused silica disc, Teflon sheet, and metal backing. The holder was sealed by tightening four bolts.

Thermogravimetric analysis (TGA) was performed using a TA 50. The samples were placed in an aluminum pan in order to prevent spillage. The methods used were isothermal and stepwise isothermal with a nitrogen flow. For the isothermal runs the material was held at a constant temperature of 25 °C for a given amount of time. In the stepwise isothermal runs, the temperature was ramped at 20 °C/min until a 1 %/min mass loss was detected, at which point the temperature was held constant. Isothermal conditions would be exited when the mass loss was less than 0.05 %/min. The N_2 flow rate was 40/60 ml/min sample to balance ratio. This process was then repeated until a temperature of 400 °C was reached.

Elemental analysis was performed by Desert Analytics Transwest Geochem (Phoenix, AZ). Samples were transferred under nitrogen. They did not observe changes in the color or texture of samples before or after analysis.

Synthesis

The syntheses of $[Cu(MeCN)_4]BF_4$, **2.1**,[12] $[Cu(MeCN)_4]PF_6$, **2.2**,[12] and $[Cu(MeCN)_4]SO_3CF_3$, **2.3**,[2] are based on previously reported methods. The new structure created is included in the table of selected crystallographic data.

Tetraacetonitrilecopper(I) tetrafluoroborate, 2.1 ($[Cu(MeCN)_4]BF_4$)

In a 250 mL Erlenmeyer flask, copper(I) oxide (2.00 g, 13.98 mmol) was added to 80 mL of acetonitrile (MeCN) and stirred to form a slurry. Tetrafluoroboric acid was added in 0.5 mL aliquots until a total volume of 2 mL was added with continuous stirring on a warm hotplate. The hotplate temperature was raised slightly to bring the mixture to a light boil until the majority of the copper(I) oxide (Cu_2O) had dissolved. The hot solution was then gravity filtered, removing any residual particulates. The resulting transparent, light yellow solution was removed from the hotplate and allowed to cool to room temperature. The solution was then added drop-wise into a Schlenk flask containing an argon atmosphere and 300 mL of Et_2O, at which time a white precipitate formed. The precipitate was allowed to settle, and excess Et_2O was decanted from the flask. The white precipitate was triply washed with Et_2O. The yield was 85%. The precipitate was then dried under vacuum and moved to a 20 mL scintillation vial, flushed with argon and stored in a desiccator.

Tetraacetonitrilecopper(I) hexafluorophosphate, 2.2, ($[Cu(MeCN)_4]PF_6$)

In a 250 mL Erlenmeyer flask, Cu_2O (2.00 g, 13.98 mmol) was added to 80 mL

of MeCN and stirred to form a slurry. Hexafluorophosphoric acid was added in 0.5 mL aliquots until a total volume of 2 mL was added with continuous stirring on a warm hotplate. The hotplate temperature was raised slightly to bring the mixture to a light boil until the majority of the Cu_2O had dissolved. The hot solution was then gravity filtered, removing any residual particulates. The resulting transparent, light yellow solution was removed from the hotplate and allowed to cool to room temperature. The solution was then added drop-wise into a Schlenk flask containing an argon atmosphere and 300 mL of Et_2O, at which time a white precipitate formed. The precipitate was allowed to settle, and excess Et_2O was decanted from the flask. The white precipitate was triply washed with Et_2O. The precipitate was then dried under vacuum and moved to a 20 mL scintillation vial, then flushed with argon and stored in a desiccator. Upon later weighing the yield was 85%.

Tetraacetonitrilecopper(I) trifluoromethanesulfonate, 2.3, ($[Cu(MeCN)_4]SO_3CF_3$)

In a 250 mL Erlenmeyer flask, Cu_2O (2.00 g, 13.98 mmol) was added to 80 mL of MeCN and stirred to form a slurry. Triflic acid was added in 0.5 mL aliquots until a total volume of 2 mL was added with continuous stirring on a warm hotplate. The hotplate temperature was raised slightly to bring the mixture to a light boil until the majority of the Cu_2O had dissolved. The hot solution was then gravity filtered, removing any residual particulates. The resulting transparent, light yellow solution was removed from the hotplate and allowed to cool to room temperature. The solution was then added drop-wise into a Schlenk flask containing an argon atmosphere and 300 mL of Et_2O, at which time a white precipitate formed. The precipitate was allowed to settle, and excess

Et_2O was decanted from the flask. The white precipitate was triply washed with Et_2O. The precipitate was then dried under vacuum and moved to a 20 mL scintillation vial, then flushed with argon and stored in a desiccator.

***catena*-poly[[diacetonitrilecopper(I)-μ-(4,7-phenanthroline)] tetrafluoroborate], 2.4, ($\{[Cu(4,7\text{-phenanthroline})(MeCN)_2]BF_4\}_n$)**

With a mortar and pestle, **2.1** (157 mg, 0.5 mmol) was gently ground with 4,7-phenanthroline (90 mg, 0.5 mmol) for approximately 30 sec until the mixture was a homogeneous off-white color. The mixture was then placed in a 4 mL vial, sealed with parafilm, and capped. After 1 h the off-white color changed to a bright yellow. Based on PXRD the yield was +95%. Elemental analysis calculated (found) for $CuC_{16}N_4H_{14}BF_4$: C, 46.53 (45.451); H, 3.420 (3.350); N 13.58 (12.34).

In a 4 mL vial, 50 mg of the **2.4** product was dissolved in MeCN via sonication. The 4 mL vial was placed in a 20 mL scintillation vial that contained 5 mL of Et_2O. The 20 mL vial was then capped. Diffusion of Et_2O into the 4 mL vial resulted in yellow plate crystals after 1 week. The previously unreported single crystal structure will be referred to as **2.7**, to distinguish it from the polycrystalline form.

***catena*-poly[[diacetonitrilecopper(I)-μ-(4,7-phenanthroline)] hexafluorophosphate], 2.5, ($\{[Cu(4,7\text{-phenanthroline})(MeCN)_2]PF_6\}_n$)**

With a mortar and pestle, **2.2** (186 mg, 0.5 mmol) was gently ground with 4,7-phenanthroline (90 mg, 0.5 mmol) for approximately 30 sec until the mixture was a homogeneous off-white color. The mixture was then placed in a 4 mL vial, sealed with

parafilm, and capped. After 2 h the off-white color changed to a bright yellow. Based on PXRD the yield was +95%. Elemental analysis calculated (found) for $CuC_{16}N_4H_{14}PF_6$: C, 40.84 (40.29); H, 2.970 (2.990); N 11.90 (11.51).

***catena*-poly-[acetonitrile-trifluoromethanesulfonate-copper-μ-(4,7-phenanthroline)], 2.6 [Cu(4,7-phenanthroline)(MeCN)(SO_3CF_3)]$_n$**

With a mortar and pestle, **2.3** (188 mg, 0.5 mmol) was gently ground with 4,7-phenanthroline (90 mg, 0.5 mmol) for approximately 30 sec until the mixture was a homogeneous off-white color. The mixture was then placed in a 4 mL vial, sealed with parafilm, and capped. After 15 min the off-white color changed to a bright yellow. Based on PXRD the yield was +95%. Oxidation occurred during sample shipment, preventing accurate elemental analysis results from being achieved.

Crystal Structure Analysis

Single crystals for XRD were placed in inert oil and selected using an optical microscope. Each crystal chosen uniformly extinguished plane polarized light upon rotation of 90°. The selected crystals were then mounted on thin glass fibers with a small amount of silicone grease. Using a Siemens SMART system (Mo(K_α) = 0.71073 Å) with a charge-coupled area detector, a full hemisphere of crystallographic data was collected. Absorption corrections were applied after integration[13]. All structures were solved using SHELXS Direct Methods[14] and refined using a full least squares treatment on F^2.[15] All non-hydrogen atoms were refined with anisotropic thermal parameters. Crystallographic details for **2.7** are listed in Table 2.1.

	2.7
Empirical formula	$Cu_2C_{16}H_{14}N_4B_2F_4$
Formula weight (g/mol)	412.66
Crystal system, space group	Monoclinic, $P2_1/c$
Temperature (K)	173(2)
Unit cell dimensions (Å, deg)	a = 9.564(2) b =12.031(3) c =14.823(3) β = 92.709(4)
Volume ($Å^3$)	1703.8(6)
Z, ρ calc (g/cm^3)	4, 1.6085
Absorption coefficient (mm^{-1})	1.330
F(000)	832
Crystal size (mm)	0.4× 0.2 × 0.1
Θ Range for data collection (deg)	2.13 to 27.12
Reflections collected/unique	10102 / 3739 [R_{int}=0.0298]
Max. and min. transmission	0.8280 and 0.5309
Data / restraints / parameters	3739 / 0 / 238
Final R indices [I>2σ(I)] [a,b]	R_1= 0.0576, wR_2=0.0468
R indices (all data)	R_1= 0.1372, wR_2=0.1294
Largest diff. peak / hole ($e.A^{-3}$)	0.93 / - 0.79
GoF on F^2	1.067
Structures were refined on F_o^2 using all data. [a] $R = \Sigma(\|F_o\|-\|F_c\|)/\Sigma\|F_o\|$; [b] $wR_2 = [\Sigma(\|F_o\|-\|F_c\|)^2/\Sigma\|F_o\|^2]^{1/2}$	

Table 2.1 – Selected crystallographic details for the new structure, **2.7**.

2.3 Results and Discussion

Description of the Crystal Structure

The structure of $\{[Cu(4,7\text{-phenanthroline})(MeCN)_2]BF_4\}_n$ has two acetonitrile molecules and two 4,7-phenanthroline molecules coordinated to each copper (Figure 2.9). This leads to a coordination environment around the copper(I) that is distorted tetrahedral. The largest N-Cu-N angle is not between the 4,7-phenathroline (104.52(9)°) but between N3 as part of an MeCN and 4,7-phenanthroline (122.8(1)° and 111.8(9)°). There is a distinct difference between the C-N-Cu angles for the coordinated MeCN (144.6(3)° and 166.3(2)°). The bond angles, like the previously reported $\{[Cu(4,7\text{-phenanthroline})(MeCN)]BF_4\}_n$ structure described, are caused by interchain interactions.

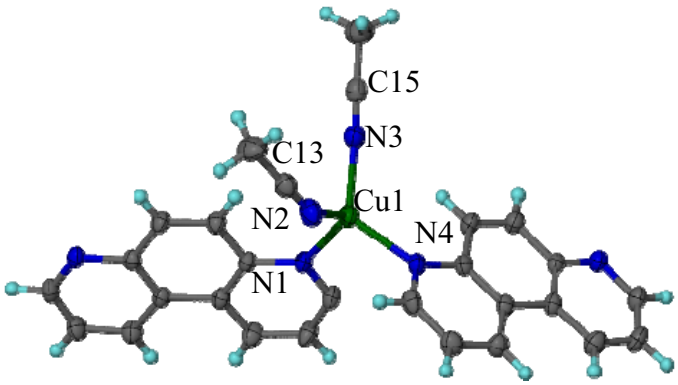

Cu(1) - N(1)	2.071(2) Å	N(1)-Cu(1)-N(2)	100.2(1)°
Cu(1) - N(2)	2.140(3) Å	N(3)-Cu(1)-N(1)	120.7(1)°
Cu(1) - N(3)	1.945(3) Å	N(4)-Cu(1)-N(1)	104.52(9)°
Cu(1) - N(4)	2.043(2) Å	N(3)-Cu(1)-N(2)	93.6(1)°
C(15)-N(2)-Cu(1)	144.6(3)°	N(4)-Cu(1)-N(2)	111.77(9)°
C(13)-N(3)-Cu(1)	166.3(2)°	N(3)-Cu(1)-N(4)	122.8(1)°

Figure 2.9 – Copper coordination environment in **2.7** with selected bond lengths and angles. All nonhydrogen atoms are shown as 50% probability thermal ellipsoids. The color scheme is as follows: Cu = dark green, C = gray, N = dark blue, and H = aqua. This scheme will be kept throughout. All bond distances are shorter or within the range of acceptable Cu-N bond lengths, 2.07 ± 0.07, for pyridine.[16]

The extended structure of **2.7** is a linear 1D chain where 4,7-phenanthroline molecules act as a bridges between the copper(I) cations (Figure 2.10). The difference in the N-Cu-N bond angles can be contributed to the packing of the one-dimensional chains where there is π-π stacking of the 4,7-phenanthroline rings (Figure 2.11). The coordinated MeCN with the narrowest C-N-Cu angle (144.6 (3)°) is located over a 4,7-phenanthroline that is part of another chain. The interchain interactions cause the angle to be bent in order to accommodate this orientation.

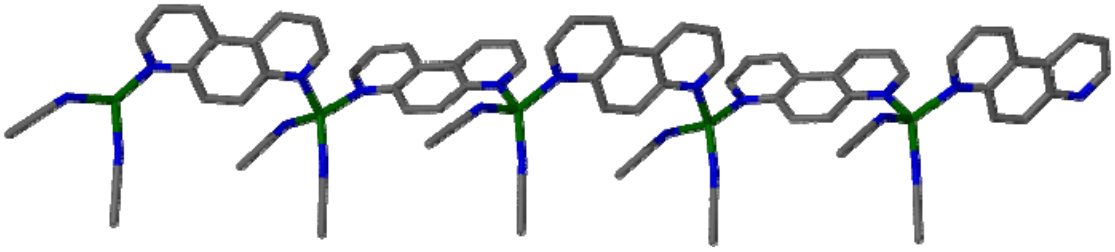

Figure 2.10 - Stick representation of the linear chains of **2.7**. The hydrogen atoms and BF_4^- anions are removed for clarity.

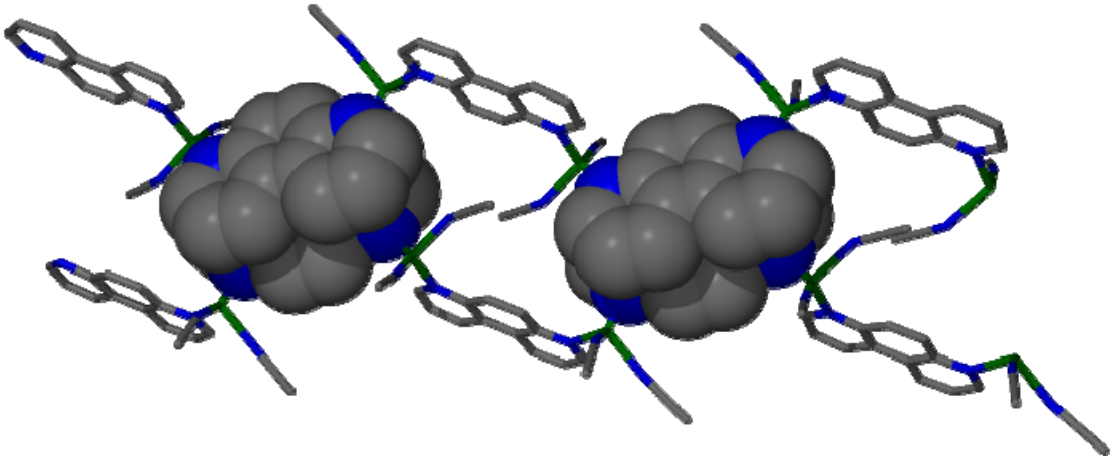

Figure 2.11 – Space-filling representation of the π-π interactions between the 4,7-phenanthrolines from neighboring chains in **2.7**.

Contrast $\{[Cu(4,7\text{-phenanthroline})(MeCN)_2]BF_4\}_n$ with the previously reported structure which has only one acetonitrile molecule coordinated to each copper (Figure

2.12).[6] The previously reported structure, {[Cu(4,7-phenanthroline)(MeCN)]BF_4}$_n$, had an N-Cu-N angle between 4,7-phenanthroline molecules of 106.98° compared to 104.48° for **2.7**. This is somewhat surprising, as one might expect an angle of 120° representing trigonal planar coordination around the copper; however, there are examples of Y-shaped copper(I) coordination complexes in the literature.[6,17-20] When looking down the chains lengthwise, the structures look similar. In this view the copper atoms and 4,7-phenanthroline molecules alternate sides in both structures. The similarity of the crystal packing would cause one of the acetonitrile molecules in {[Cu(4,7-phenanthroline)$(MeCN)_2$]BF_4}$_n$ to bend inward in order to sustain the configuration. This bending leads to an acetonitrile Cu-N-C bond angle of 144.6(3)º, which is quite dramatic when compared to the acetonitrile Cu-N-C bond angle of 172.4º for the previously reported structure.

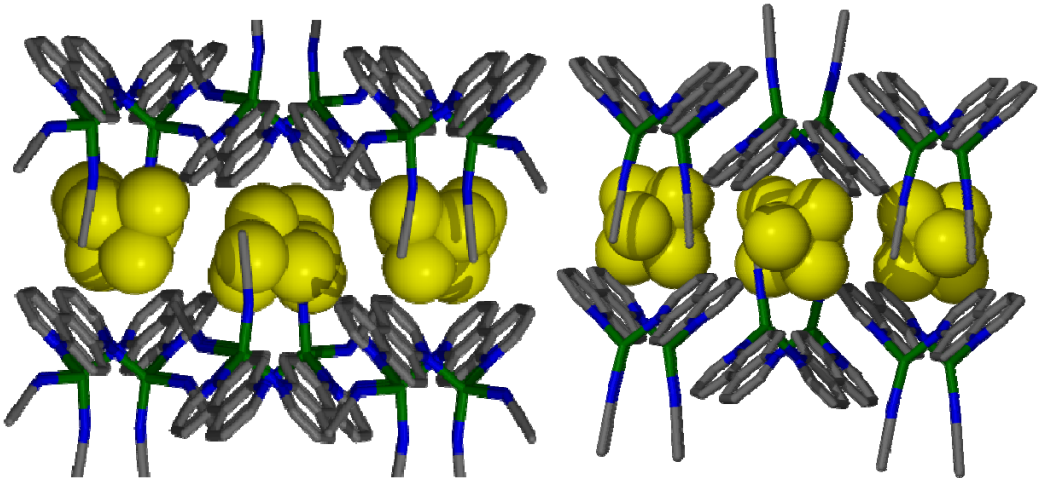

Figure 2.12 – Side-by-side view of looking down the two one-dimensional chains. **2.7** {[Cu(4,7-phenanthroline)$(MeCN)_2$]BF_4}$_n$ is on the left, and the previously reported {[Cu(4,7-phenanthroline)(MeCN)]BF_4}$_n$ structure is on the right. The BF_4^- anions are located between layers of the one-dimensional chains.[6]

The one difference of note in the synthesis of the compounds, besides the solid-solid reaction, is that nitrobenzene was used as a primary solvent for the structure

containing only one acetonitrile. This suggests that nitrobenzene might play an important role in directing the formation of $\{[Cu(4,7\text{-phenanthroline})(MeCN)]BF_4\}_n$. However, no nitrobenzene molecules are in the structure itself.

Monitoring the Reaction

In order to fully understand the process by which the reaction between the solid materials occurs, analysis was performed using UV-Vis spectroscopy, gas chromatography mass spectroscopy detection (GC-MSD), and PXRD. The reaction between the copper salts (**2.4, 2.5,** and **2.6**) and 4,7-phenanthroline occurs only when the container is sealed or MeCN vapor is added to the system. If one leaves the reaction in the open, no reaction is apparent either by color change or by PXRD analysis. Oxidation of the copper starting material is evident by the blue hue of the material. Even if argon or nitrogen gas is streamed across the surface of the reaction mixture to prevent the oxidation, no product is formed. The size of the vial and therefore the headspace volume is also important, because if the headspace volume is too great no reaction occurs. The headspace volume constraint leads one to conjecture that acetonitrile vapor is vital to each of these reactions. The loss of acetonitrile vapor has led to issues with GC-MSD and UV-Vis analyses. The acetonitrile vapor was determined to be escaping from the sample holders causing the reaction not to proceed as it had in a sealed container therefore hindering analyses.

GC-MSD was performed in order to analyze the amount of acetonitrile vapor in the headspace of the sample. For the production of **2.4**, the MeCN headspace vapor increased in a sigmoid overtime for a 0.05 μL headspace sample (Figure 2.13). The TIC

for acetonitrile vapor slowly increases for the first 13 min and then a sharp increase in acetonitrile vapor occurs, followed by a second gradual increase. The reactant material immediately after the three-fold increase is bright yellow, and on PXRD analysis the product is confirmed to indeed be **2.7** (Figure 2.14). There is a shift of the PXRD pattern peaks to a smaller 2θ due to the thermal expansion of the crystal at room temperature, which can be seen in Table 2.2.

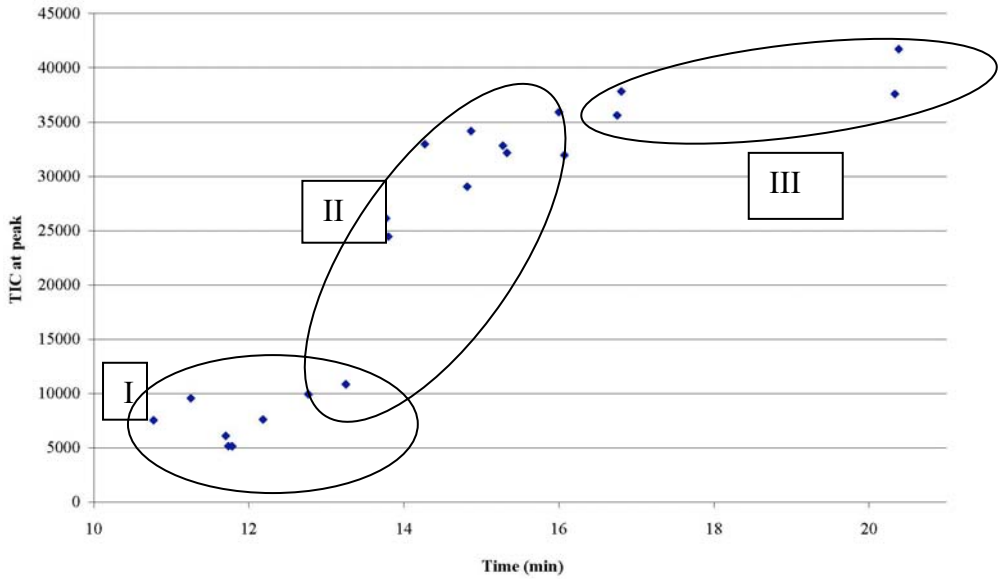

Figure 2.13 – GC-MSD plot of the TIC at the signal peak for acetonitrile headspace vapor monitored over time. Three distinct segments are indicated by the ovals encompassing them.

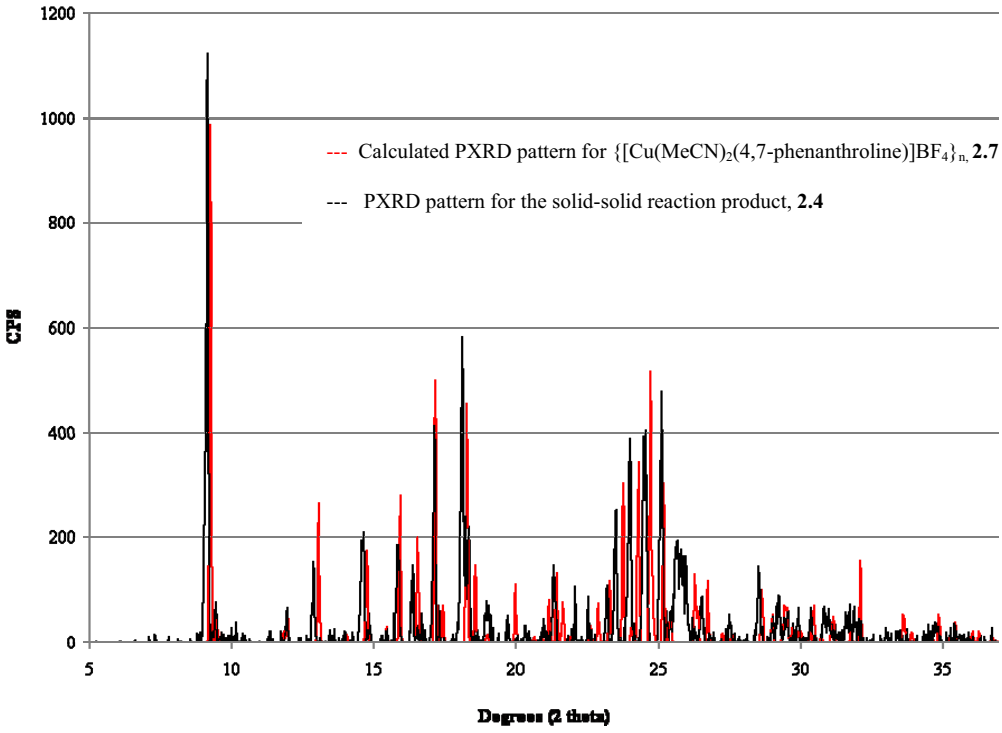

Figure 2.14 – PXRD pattern comparison between the Lazy-Pulverix calculated PXRD pattern for $\{[Cu(MeCN)2(4,7\text{-phenanthroline})]BF_4\}_n$, **2.7,** in red, and experimental PXRD pattern for the solid-solid reaction product for $[Cu(MeCN)_4]BF_4$ and 4,7-phenanthroline, **2.4,** in black.

Name	*a*, Å	*b*, Å	*c*, Å	α, deg.	β, deg.	γ, deg.
2.4 indexed pattern	9.69	12.08	14.85	90	93.56	90
2.7 single crystal (173 K)	9.564(2)	12.031(3)	14.823(3)	90	92.709(6)	90
2.7 single crystal (298 K)	9.688(2)	12.108(6)	14.866(5)	90	93.01(4)	90

Table 2.2 – Comparison of the indexed **2.4** PXRD pattern and **2.7** single crystal unit cell parameters at two different temperatures. The **2.4** PXRD pattern was indexed using Treor 90 with a figure of merit of 10.

Figure 2.13 can be divided into three distinct time intervals: I, II, and III. Interval I is when solid-state diffusion occurs and there is a release of acetonitrile vapor due to coordination of 4,7-phenanthroline molecules to copper(I) cations. This release increases slowly due to the diffusion rate being slow in solids (Figure 2.15). More acetonitrile is

being released as the 4,7-phenanthroline is coordinating to the copper. At a certain point the acetonitrile vapor condenses in regions of the powder. The regional condensation in essences traps the liquid preventing a detectible release of acetonitrile vapor. The acetonitrile condensation causes the diffusion to increase dramatically, which is why interval II develops. The mixture's color does appear to change over interval II. Interval II leads to interval III in which the off-white powder is now a clumpy bright yellow paste. At this point all of the 4,7-phenantholine and $[Cu(MeCN)_4]BF_4$ have been used. Concentration of the acetonitrile vapor in the headspace is not as high as pure acetonitrile liquid (59400 ± 300 TIC) due to the fact that any liquid is saturated and therefore the vapor pressure would not be as high as pure liquid. That said, liquid acetonitrile can be recovered by pressing on the product.

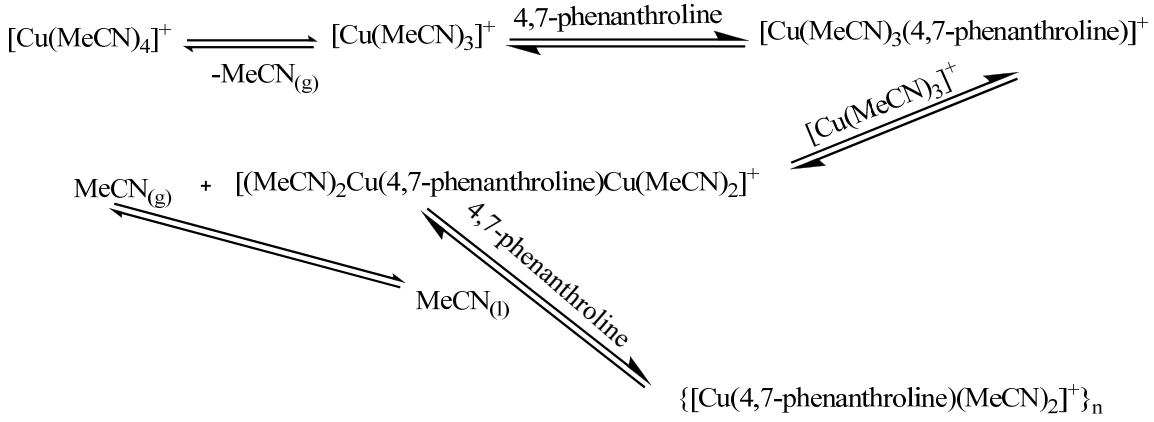

Figure 2.15 – Suggested mechanism of the solid-solid reaction between $[Cu(MeCN)_4]X$ ($X = BF_4^-$ or PF_6^-) and 4,7-phenanthroline.

The formation of **2.5** through the solid-solid reaction of 4,7-phenanthroline and $[Cu(MeCN)_4]PF_6$ was also analyzed via GC-MSD and PXRD. The GC-MSD is quite similar to that of the $[Cu(MeCN)_4]BF_4$ and 4,7-phenanthroline equimolar reaction under the same conditions (Figures 2.16 and 2.17). The main difference is the TIC at the peak

of the first sampling is higher for the $[Cu(MeCN)_4]BF_4$ and 4,7-phenanthroline reaction. This indicates the formation of $\{[Cu(4,7\text{-phenanthroline})(MeCN)_2]BF_4\}_n$ is faster than $\{[Cu(4,7\text{-phenanthroline})(MeCN)_2]PF_6\}_n$. The TIC for the last sampling is approximately the same value.

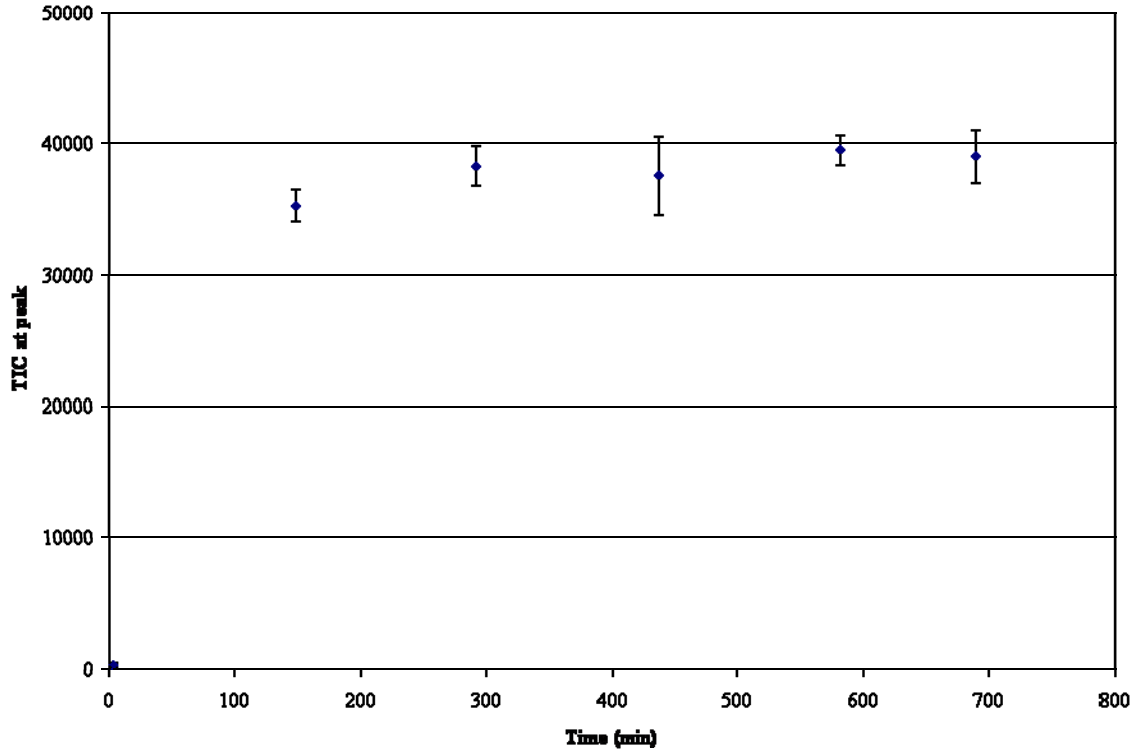

Figure 2.16 – Monitoring the equimolar reaction of $[Cu(MeCN)_4]PF_6$ and 4,7-phenanthroline over time creating $\{[Cu(4,7\text{-phenanthroline})(MeCN)_2]PF_6\}_n$. n = 3 with a standard error of estimate of ±173.

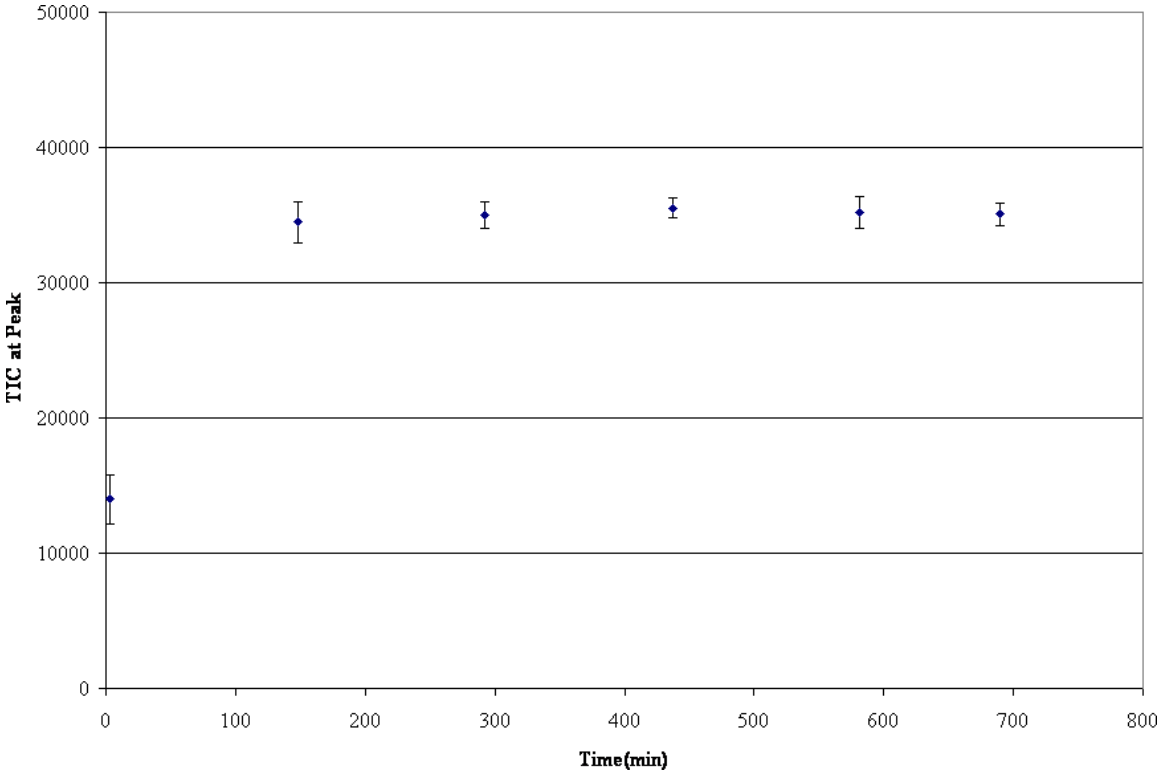

Figure 2.17 – Monitoring the equimolar reaction of $[Cu(MeCN)_4]BF_4$ and 4,7-phenanthroline over time creating $\{[Cu(4,7\text{-phenanthroline})(MeCN)_2]BF_4\}_n$. The TIC is already increasing by the time the first sampling is taken. n = 3 with a standard error of estimate of ±36.

The PXRD pattern of **2.5** compared to the calculated PXRD pattern of $\{[Cu(MeCN)_2(4,7\text{-phenanthroline})]PF_6\}_n$ shows that they are the same structure (Figure 2.18). Due to thermal expansion the peaks at around 13° and 15° 2θ do not overlap. $\{[Cu(MeCN)_2(4,7\text{-phenanthroline})]PF_6\}_n$ single crystals were grown and analyzed via XRD to confirm that the unit cell parameters at 173 K were the same as the previously reported structure. The single crystals were then crushed into a powder with a mortar and pestle, and PXRD analysis was performed at room temperature. The peaks that did not overlap with the calculated powder pattern now match the PXRD pattern for the product of the solid-solid reaction between 4,7-phenanthroline and $[Cu(MeCN)_4]PF_6$, **2.5**. The same crystals were analyzed at 233 K and 298 K to obtain the unit cell parameters at those temperatures (Table 2.3). The change in the unit cell over the temperature range is

not surprising considering the case of urea discussed in Chapter 1.

The interchain interactions of {[Cu(4,7-phenanthroline)(MeCN)]PF_6}$_n$ become weaker with higher temperature. The indexed PXRD pattern of **2.5** by the DICVOL program matches closely to the room temperature unit cell data for {[Cu(4,7-phenanthroline)$(MeCN)_2$]PF_6}$_n$ single crystal. The thermal expansion can be seen in all PXRD comparison cases. Some peaks are more dramatically shifted than others.

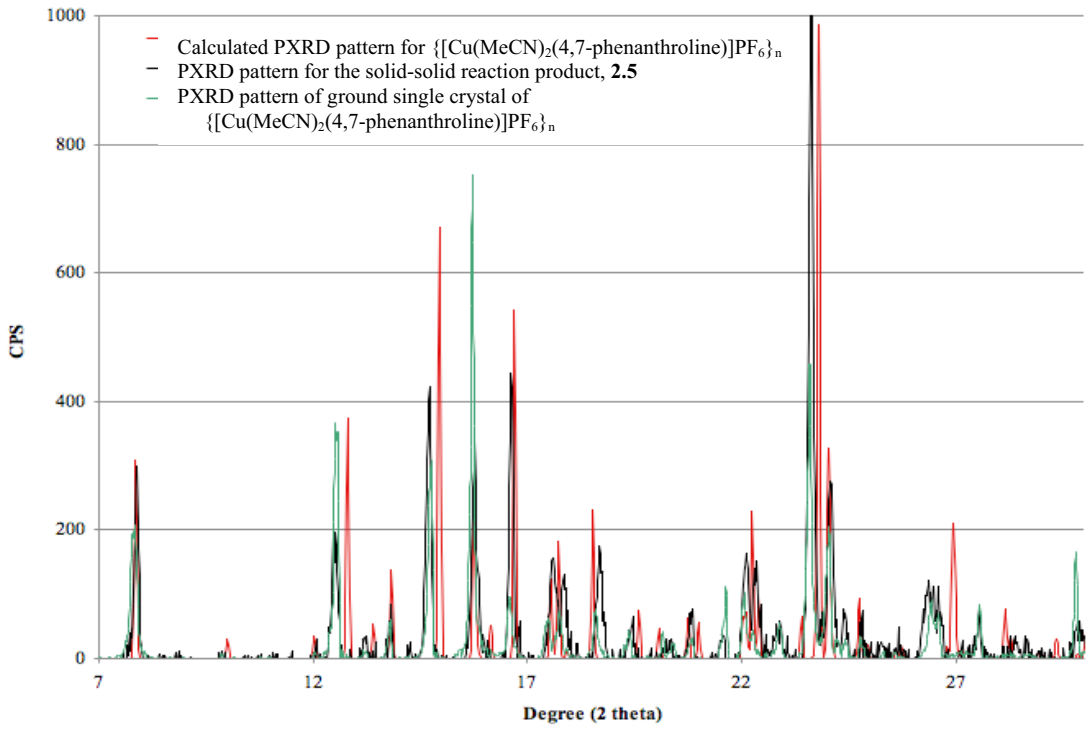

Figure 2.18 – Powder X-ray pattern comparison between the Lazy-Pulverix calculated powder pattern of {[Cu$(MeCN)_2$(4,7-phenanthroline)]PF_6}$_n$, in red, experimental powder pattern for the solid-solid reaction product of [Cu$(MeCN)_4$]PF_6 and 4,7-phenanthroline **2.5,** in black, and PXRD powder pattern for crushed single crystals of {[Cu$(MeCN)_2$(4,7-phenanthroline)]PF_6}$_n$ taken at room temperature.

Name	*a*, Å	*b*, Å	*c*, Å	α, deg.	B, deg.	γ, deg.
2.5 indexed pattern	11.39	11.52	14.25	90	98.592	90
Single crystal (298 K)	11.394(2)	11.539 (3)	14.252(2)	90	98.62(2)	90
Single crystal (233 K)	11.402(2)	11.506(2)	14.092(2)	90	99.48(1)	90
Single crystal (173 K)	11.430(6)	11.495(6)	14.044(7)	90	99.948(1)	90

Table 2.3 – Comparison of the indexed **2.5** PXRD pattern and {[$Cu(MeCN)_2$(4,7-phenanthroline)]PF_6}$_n$ single crystal unit cell parameters taken at different temperatures. The **2.5** PXRD pattern was indexed using DICVOL.

The indexed PXRD pattern of **2.6** by Treor 90 indicated unit cell parameters close to the [Cu(MeCN)(4,7-phenanthroline)(SO_3CF_3)]$_n$ single crystal cell at 298 K (Table 2.4). The unit cell parameters change over a temperature range like the cases of **2.4** and **2.5**. The **2.6** PXRD pattern closely matches the calculated PXRD pattern from previously reported single crystal XRD data for [Cu(MeCN)(4,7-phenanthroline)(SO_3CF_3)]$_n$ (Figure 2.19). The peak shift can also be seen in these cases but is not as dramatic.

Name	*a*, Å	*b*, Å	*c*, Å	α, deg.	β, deg.	γ, deg.
2.6 indexed pattern	13.48	8.13	15.24	90	104.48	90
Single crystal (173 K)	13.421(9)	8.007(6)	15.31(1)	90	103.8(1)	90
Single crystal (298 K)	13.506(3)	8.18(2)	15.33(2)	90	103.9(1)	90

Table 2.4 – Comparison of the indexed **2.6** PXRD pattern and [Cu(MeCN)(4,7-phenanthroline)(SO_3CF_3)]$_n$ single crystal unit cell parameters. The **2.6** PXRD pattern was indexed using Treor 90 with a figure of merit of 10.

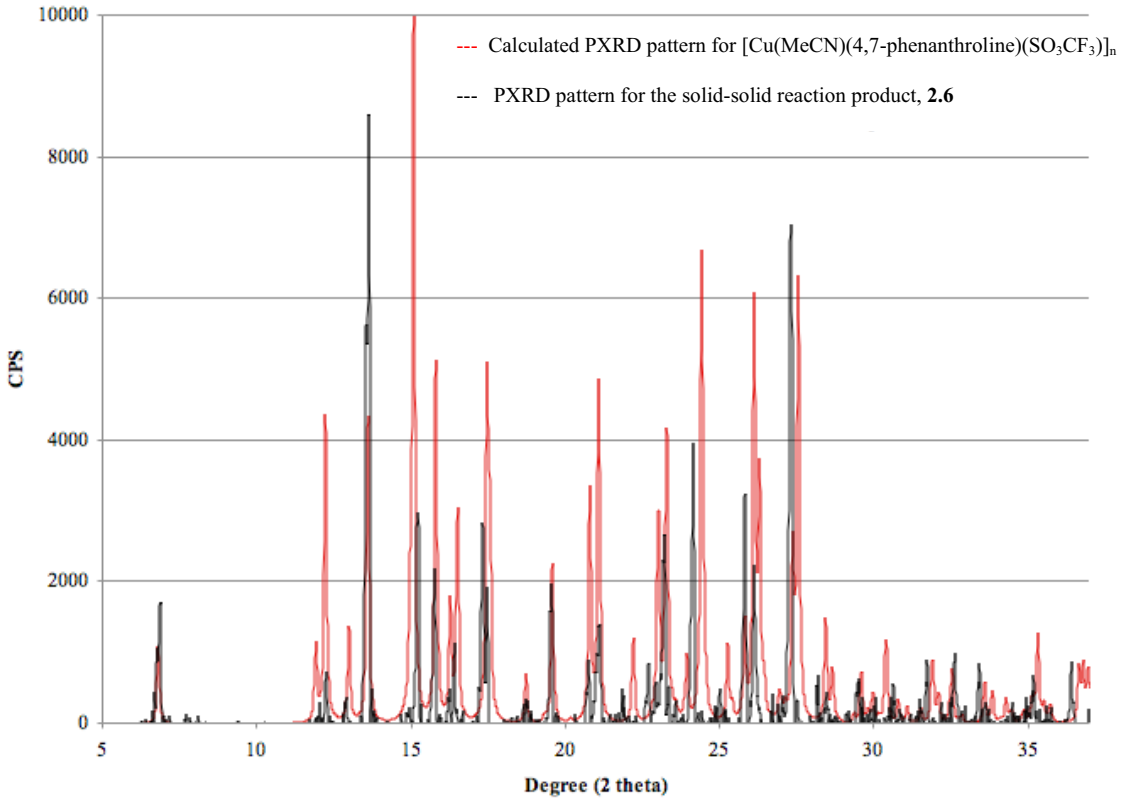

Figure 2.19 – PXRD pattern comparison between the Lazy-Pulverix calculated PXRD pattern of $[Cu(MeCN)(4,7\text{-phenanthroline})(SO_3CF_3)]_n$, in red, and experimental powder pattern of the solid-solid reaction product between $[Cu(MeCN)_4]SO_3CF_3$ and 4,7-phenanthroline, **2.6,** in black.

As for the solid-solid reaction progression, it appears consistent for all the copper starting material, $[Cu(MeCN)_4]X$ (X = BF_4^-, PF_6^-, and $SO_3CF_3^-$). The concentration of acetonitrile vapor must reach a certain point or the reaction is suppressed. This is most likely because only a certain amount of 4,7-phenanthroline can actually replace coordinated acetonitrile molecules via solid diffusion. When a reaction was halted, PXRD analysis showed only the peaks associated with the starting material. It must be noted that the GC-MSD analysis method gave good results if the time between injections did not remove too much acetonitrile vapor which suppresses the reaction, but close enough in time to observe the reaction progress.

Based on visual monitoring of sealed vials, the tetraacetonitrilecopper(I) and 4,7-phenanthroline solid-solid reaction rates differed depending on the anion. The reaction time for the mixture color change went as follows: $[Cu(MeCN)(4,7\text{-phenanthroline})(SO_3CF_3)]_n$ > $\{[Cu(MeCN)_2(4,7\text{-phenanthroline})]BF_4\}_n$ > $\{[Cu(MeCN)_2(4,7\text{-phenanthroline})]PF_6\}_n$.

The acetonitrile vapor concentration levels off around the same TIC at the peak for each of the tetraacetonitrilecopper(I) salts, which suggests that the material does indeed act like a saturated solution and lowers the vapor pressure of MeCN. As stated before, the TIC over pure acetonitrile liquid is 59400 ± 300 If it were solely measuring the amount of acetonitrile vapor given off then $[Cu(4,7\text{-phenanthroline})(MeCN)(SO_3CF_3)]_n$ should be a larger value when the plateau is reached. This is due to the three coordinated acetronitrile molecules released during this reaction versus the two acetonitrile molecules for $\{[Cu(MeCN)_2(4,7\text{-phenanthroline})]BF_4\}_n$ and $\{[Cu(MeCN)_2(4,7\text{-phenanthroline})]PF_6\}_n$ formation.

UV-Vis diffuse reflective spectroscopy was used in order to monitor the solid-solid reactions based on the colors of the reactants and the products. **2.4, 2.5,** and **2.6** are bright yellow in contrast to the off-white of the reactants. The change in the spectra was similar to that seen in the acetonitrile vapor evolved monitored with GC-MSD. (Figure 2.20). For the equimolar reaction of $[Cu(MeCN)_4]SO_3CF_3$ and 4,7-phenanthroline, a change in absorbance at around 435 nm can be seen gradually at first. The 435 nm absorbance changes dramatically in about a minute's time. The absorbance is tripled at this point and then plateaus. Another indication that the acetonitrile vapor is condensing is the baseline shift seen in the non-normalized spectra (Figure 2.21). The baseline shift

signifies scattering due to the presence of liquid due to difference between the index of refraction of the blank and liquid acetonitrile.[21,22] This further exemplifies the overall reaction progression, where the acetonitrile vapor condenses, helping the diffusion of the reactants and therefore increasing the rate.

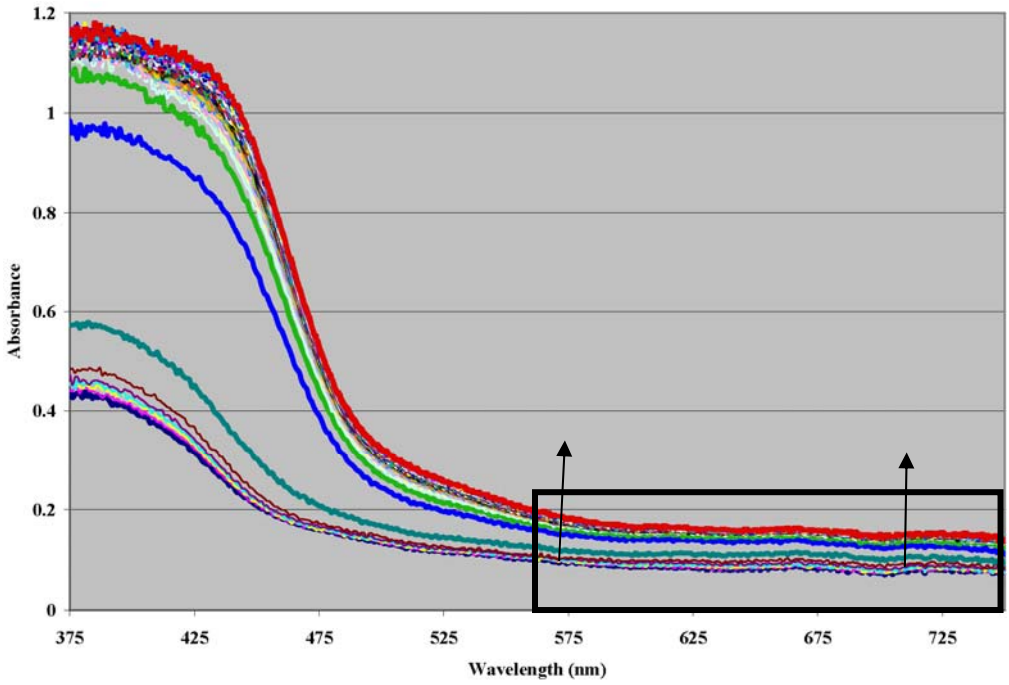

Figure 2.20– The raw UV-Vis diffuse reflectance spectra of [Cu(4,7-phenanthroline)(MeCN)(SO_3CF_3)]$_n$ production monitored over time. Each spectrum represents ~30 sec. There is a baseline shift that can be seen from 575 nm to 725 nm, indicating the condensation of acetonitrile vapor. The arrows indicate the direction of the shift, with the arrows' tails the location of the beginning spectrum which is in blue. The baseline shift is seen with each spectra for the solid-solid reactions.

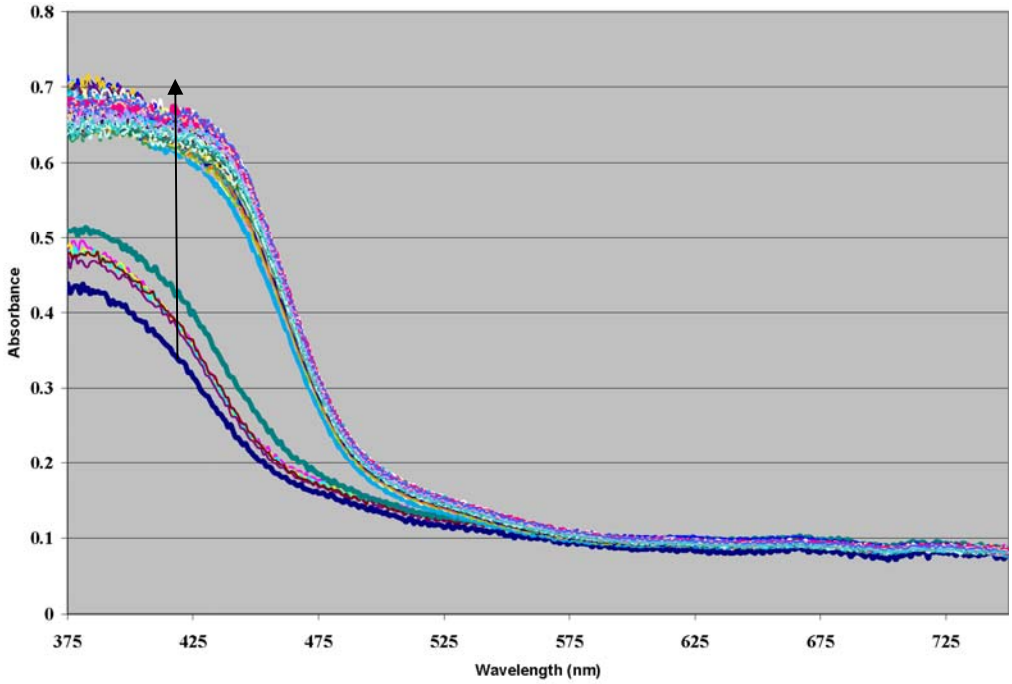

Figure 2.21 - The UV-Vis diffuse reflectance spectra of [Cu(4,7-phenanthroline)(MeCN)(SO_3CF_3)]$_n$ production monitored over time. Each spectrum represents ~30 sec and has been normalized at 750 nm. The arrow indicates the direction of the absorbance change, with its' tail being located on the first spectrum. n = 3

The difference in the rate of product formation for **2.4, 2.5,** or **2.6** is clear from monitoring the absorbance over time (Figure 2.22). Again this helps to support the difference in rate at which **2.4, 2.5,** and **2.6** formed, which was observed visually. Interestingly, the only difference between the reactions is the anion.

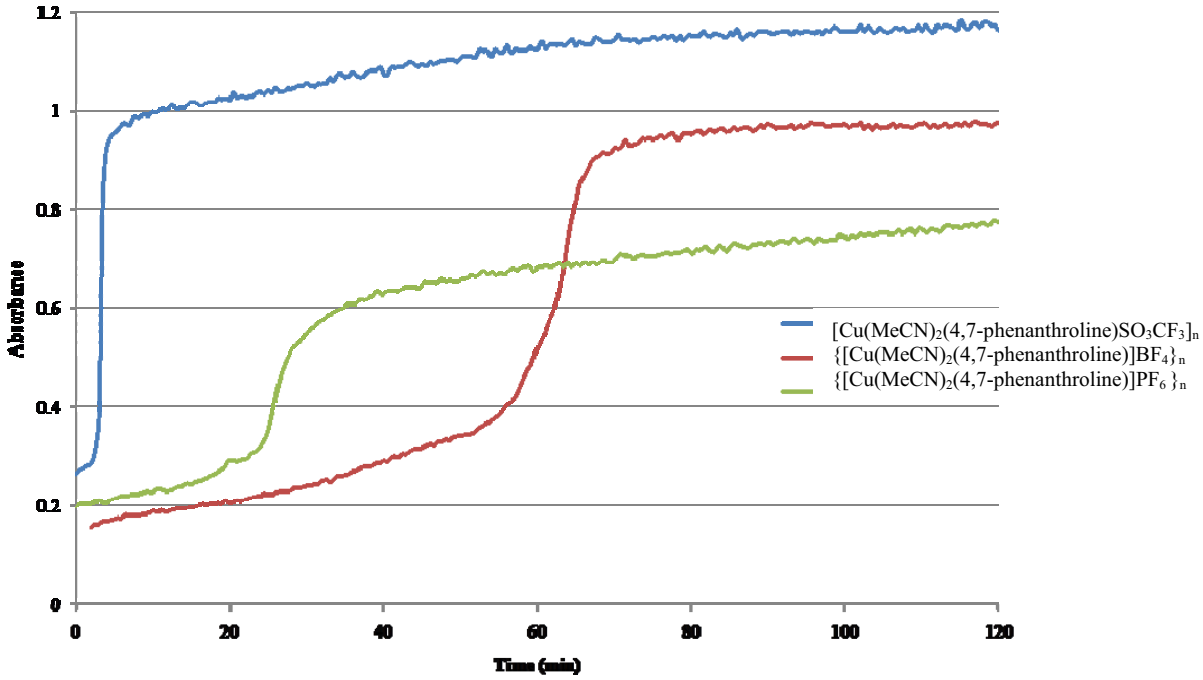

Figure 2.22 – Comparison of the reaction rate for different $[Cu(MeCN)_4]X$ (X = BF_4^-, PF_6^-, or $SO_3CF_3^-$) and 4,7-phenanthroline solid-solid reactions based on the absorbance at 435 nm. All spectra have been normalized at 750 nm. The legend indicates the formation of the different products, each with a different anion. n = 3.

In addition to GC-MSD and UV-Vis, PXRD was performed on the material in 5-min intervals over a small degree range, 18°-27°. This analysis was performed through the use of a temperature stand that had a cap with a beryllium window. This setup allowed for the environment around the starting mixture to be saturated with acetonitrile vapor. This is believed to be a good representation of the system at the time of condensation. Without the acetonitrile vapor the reaction does not proceed because of the cap's large headspace.

The change in the PXRD pattern over time for the production of $\{[Cu(4,7\text{-phenanthroline})(MeCN)_2]BF_4\}_n$ is seen in Figure 2.23. The product can be seen growing in around 23° to 25°, showing a distinct pattern of a hand reaching up. The PXRD peaks from $[Cu(MeCN)_4]BF_4$ are seen decreasing around 26° and 18°. As the reaction

proceeds,,a distinct transition from $[Cu(MeCN)_4]BF_4$ and 4,7-phenanthroline material to $\{[Cu(4,7\text{-phenanthroline})(MeCN)_2]BF_4\}_n$ is observed with no other phases being present and at no time is there a diffraction pattern that is amorphous.

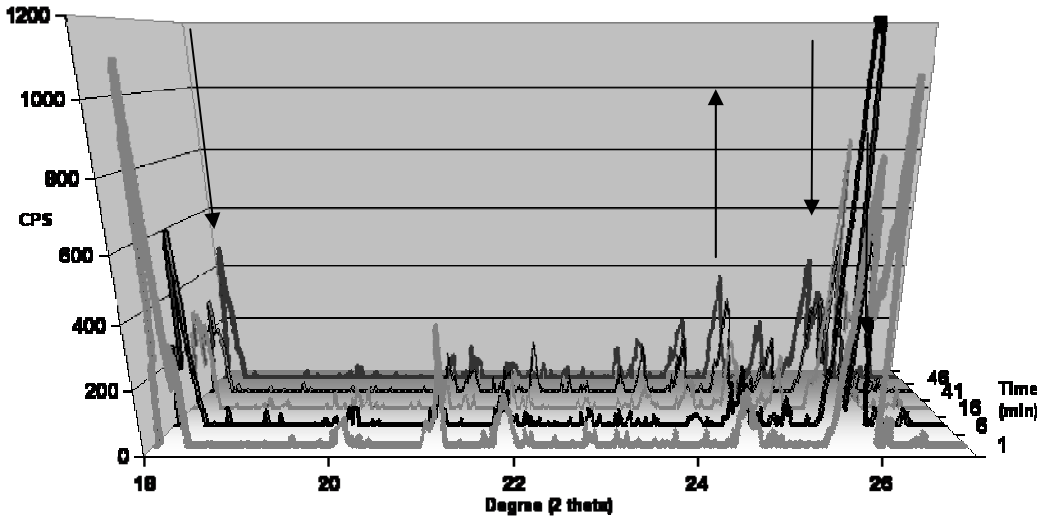

Figure 2.23 – Monitoring the phase change from 4,7-phenanthroline and $[Cu(MeCN)_4]BF_4$ to $\{[Cu(4,7\text{-phenanthroline})(MeCN)_2]BF_4\}_n$ done via PXRD. The time axis indicates the time each scan was started in relation to the time after grinding was finished. The time for each run is approximately 5 min. n = 2

The production of $\{[Cu(4,7\text{-phenanthroline})(MeCN)_2]PF_6\}_n$ gave similar results to those just described (Figure 2.24). There is a distinct change in the diffraction patterns from $[Cu(MeCN)_4]PF_6$ and 4,7-phenanthroline to $\{[Cu(4,7\text{-phenanthroline})(MeCN)_2]PF_6\}_n$. The progression can be seen in the growth around 18° and 23.72° indicating formation of $\{[Cu(4,7\text{-phenanthroline})(MeCN)_2]PF_6\}_n$. A decrease intensity of the peak around 21.5° signifies the depletion of the 4,7-phenanthroline.

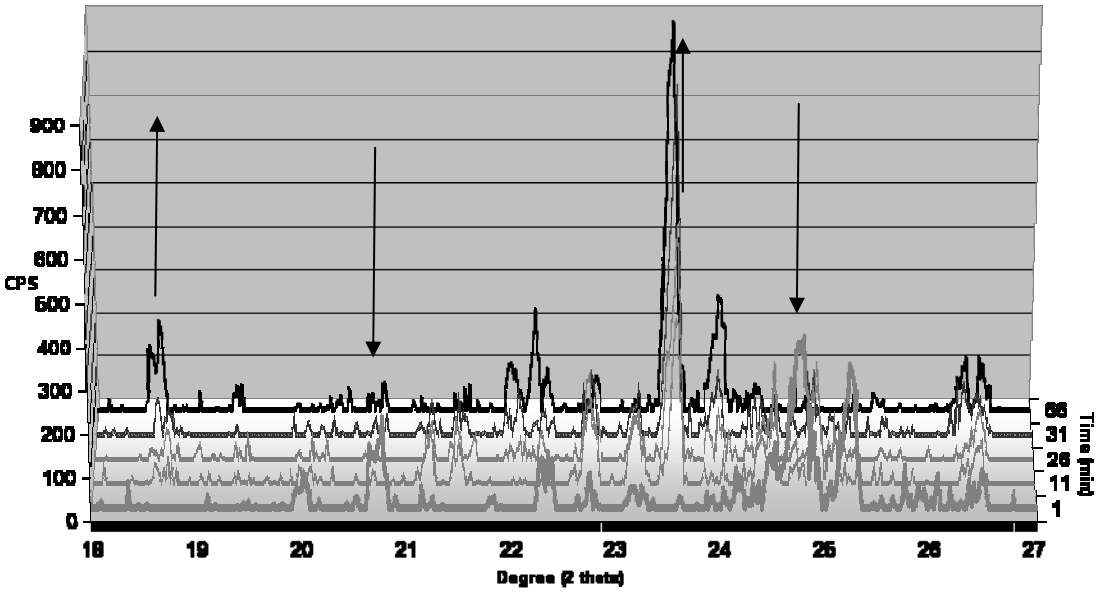

Figure 2.24 – Monitoring the reaction between 4,7-phenanthroline and $[Cu(MeCN)_4]PF_6$ producing $\{[Cu(4,7\text{-phenanthroline})(MeCN)_2]PF_6\}_n$ done via PXRD. The time axis indicates the time each scan was started in relation to the time after grinding was finished. The time for each run is approximately 5 min. n = 2

Only the solid-solid reactions of $[Cu(MeCN)_4]PF_6$ and $[Cu(MeCN)_4]BF_4$ with 4,7-phenanthroline were able to be analyzed by this type of PXRD monitoring. The solid-solid reaction of $[Cu(MeCN)_4]SO_3CF_3$ with 4,7-phenanthroline went to completion within two scans. The PXRD patterns did not show a distinct phase transition as with the previously mentioned reaction mixtures.

Monitoring the Acetonitrile Loss of Tetraacetonitrilecopper(I) Salts

Typically TGA is performed through a range of temperatures. In these cases, the runs were performed at a constant temperature of 25 °C for 1200 min for these salts. The knowledge that acetonitrile vapor was being released from the [Cu(MeCN)]X led to the decision to use TGA. The rate of mass loss for each of the starting material powder samples is related to the visual oxidation of the crystals becoming tan or blue (Figure

2.25). As one can see, the mass loss is rather drastic for $[Cu(MeCN)_4]SO_3CF_3$ powder as compared to $[Cu(MeCN)_4]BF_4$ and $[Cu(MeCN)_4]PF_6$.

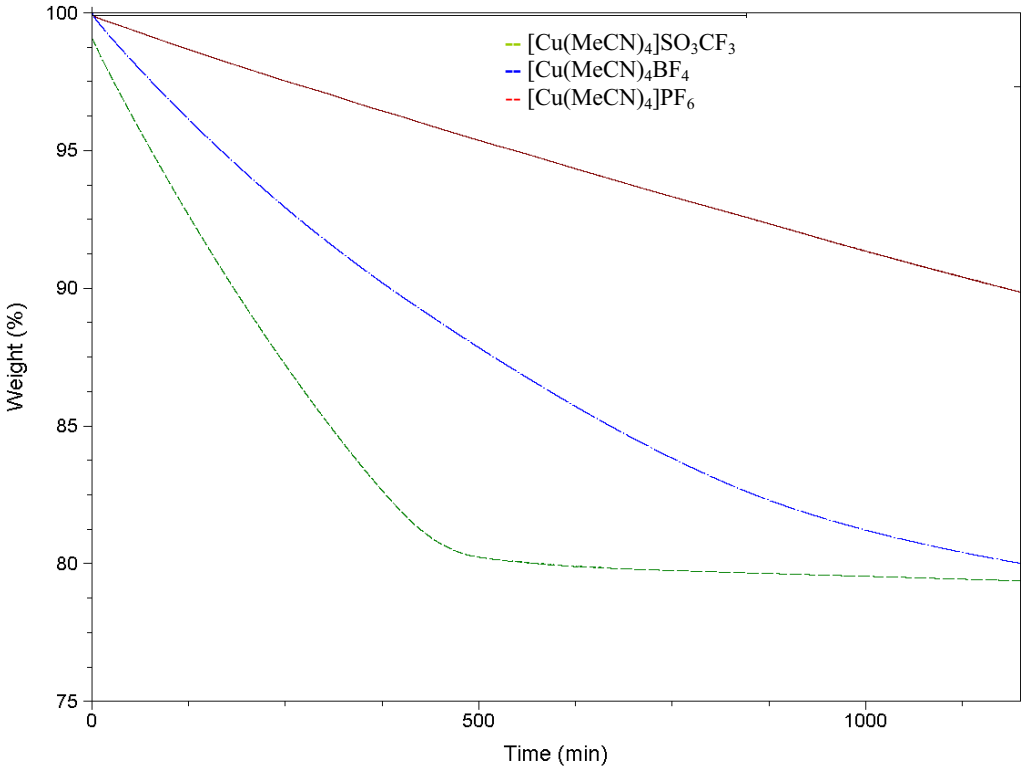

Figure 2.25 – Mass loss comparison between the tetrakisacetonitrilecopper(I) salt powders at 25°C over a period of 1200 min. The legend gives the color scheme and line choice for each of the salts.

Notice how the $[Cu(MeCN)_4]SO_3CF_3$ powder changes mass loss rate at around 450 min. At this point approximately two acetonitrile equivalents are lost (21.78% calculated, 21.08% actual) (Figure 2.26). After this, the slope transitions and no more than 1% of mass loss is seen for up to 3000 min. The acetonitrile loss is further supported with infrared spectroscopy of the exhaust during the 21.78% mass loss, which shows the characteristic fingerprint of acetonitrile vapor. The two acetonitrile equivalents are important because the result indicates that two coordinated acetonitrile molecules are released. This might explain why the tetraacetonitrilecopper(I) salts form

linear chains via solid-solid reactions. The rate of tetraacetonitrilecopper(I) salt decomposition is perhaps the reason for the difference in the solid-solid reaction rates. This is consistent with the idea that the first step would be the release of acetonitrile from the tetraacetronitrilecopper(I) salts. The rate would therefore be controlled by this slow step.

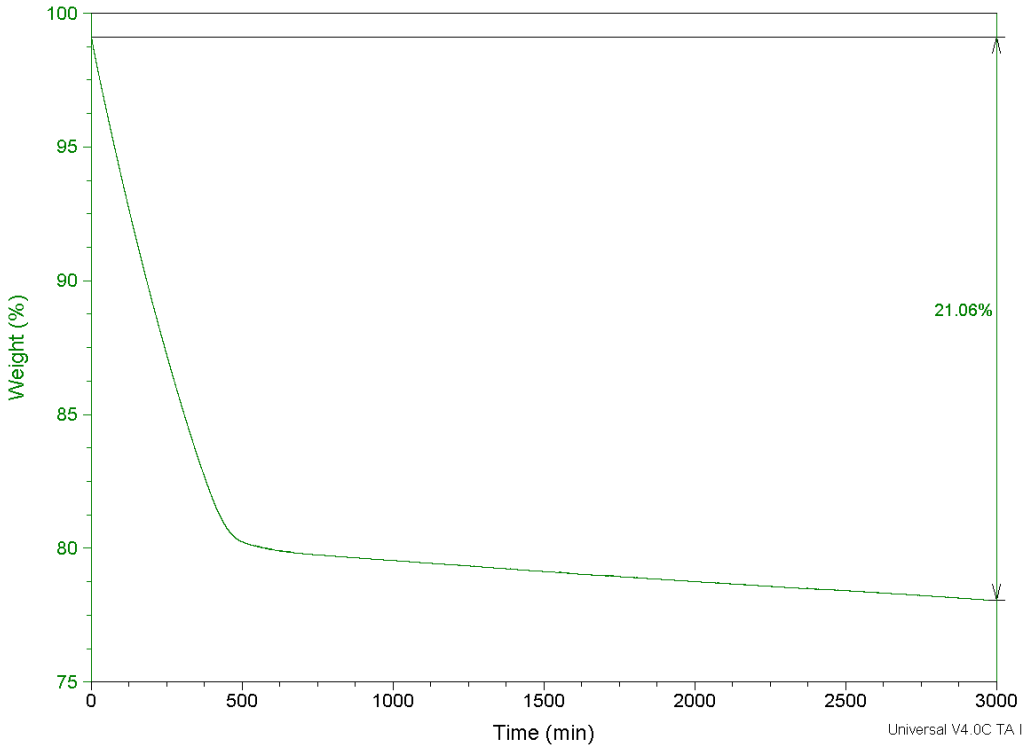

Figure 2.26 – The mass loss of two MeCN equivalents for $[Cu(MeCN)_4]SO_3CF_3$ powder at 25 °C for 3000 min. There is a total of 77% of the material that is left over.

Single crystals of $[Cu(MeCN)_4]X$ ($X=BF_4^-$, PF_6^-, and $SO_3CF_3^-$) were grown to approximately 2.5 mm and isothermal TGA analysis was performed for each. Surprisingly the single crystal isothermal run showed a difference in the order of acetonitrile vapor loss for the tetraacetonitrilecopper(I) salts (Figure 2.27). The single crystal forms of $[Cu(MeCN)_4]BF_4$ and $[Cu(MeCN)_4]PF_6$ lose acetonitrile vapor at a slower rate relative to the powder. The $[Cu(MeCN)_4]PF_6$ single crystal loses mass at a

rate twice as fast as the $[Cu(MeCN)_4]BF_4$ single crystal, 5% and 2% mass loss over 3000 min, respectively. The reason for this discrepancy between the powder and the single crystal is simply because of a passive oxidized layer that forms on the surface of the crystal. The single crystals start as transparent, after each run the single crystals were still intact and a cloudy, tan color. The passive layer acts to prevent acetonitrile from escaping as fast from the inner regions of the single crystal. Based on the powder results, $[Cu(MeCN)_4]BF_4$ would form a passive layer faster than $[Cu(MeCN)_4]PF_6$ due to $[Cu(MeCN)_4]BF_4$ faster release of acetonitrile. On the other hand, the $[Cu(MeCN)_4]SO_3CF_3$ single crystal run appears similar to the powder, with both having a rapid mass loss until approximately two acetonitrile equivalents are released. The rapid mass loss is not as fast for the single crystal simply because the powder has more surface area. After each run, the $[Cu(MeCN)_4]SO_3CF_3$ single crystal has lost the original shape and is in the same post-run condition as the powder. The acetonitrile loss is faster than the passive layer can form, which destroys the integrity of the crystal.

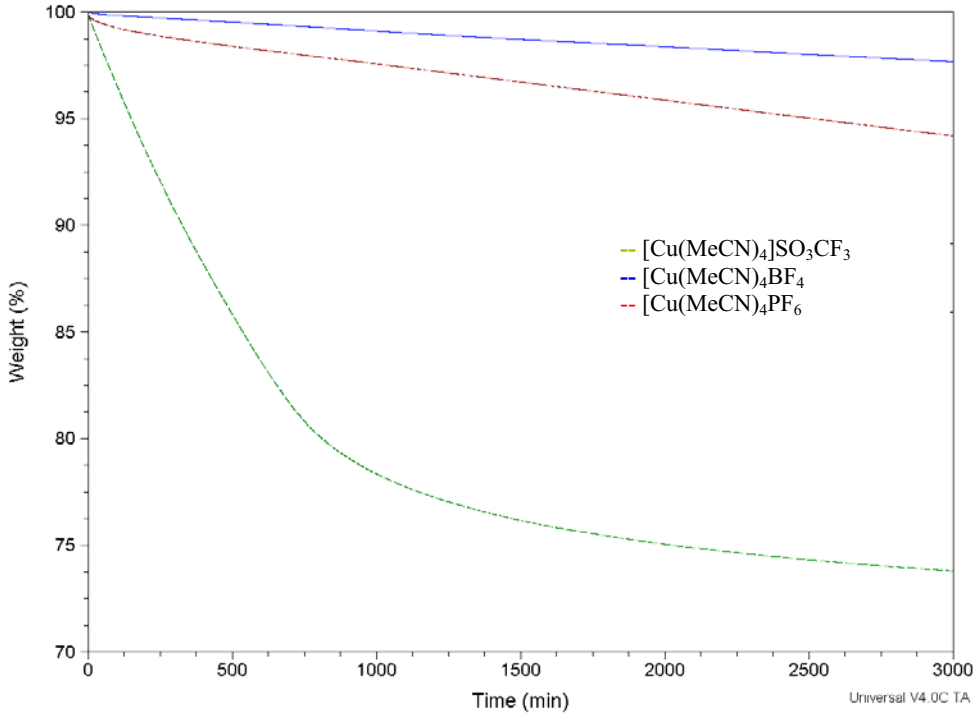

Figure 2.27 – The mass loss comparison between the single crystal copper salts. Like the powder case, $[Cu(MeCN)_4]SO_3CF_3$ loses acetonitrile vapor at a faster rate than $[Cu(MeCN)_4]BF_4$ or $[Cu(MeCN)_4]PF_6$.

The idea of a passive layer is reinforced when comparing the stepwise isothermal results for the $[Cu(MeCN)_4]BF_4$ single crystal and the powder (Figure 2.28). During the runs, both single crystal and powder lose the same mass percentage at approximately the same temperature. The similarity in results indicates that the single crystal form does not trap excess acetonitrile at higher temperatures as with the isothermal runs. At the higher temperatures, the acetonitrile vapor is released more readily than the passive layer forms. The results indicate that the difference in mass loss between the single crystal and the polycrystalline forms is one of surface area.

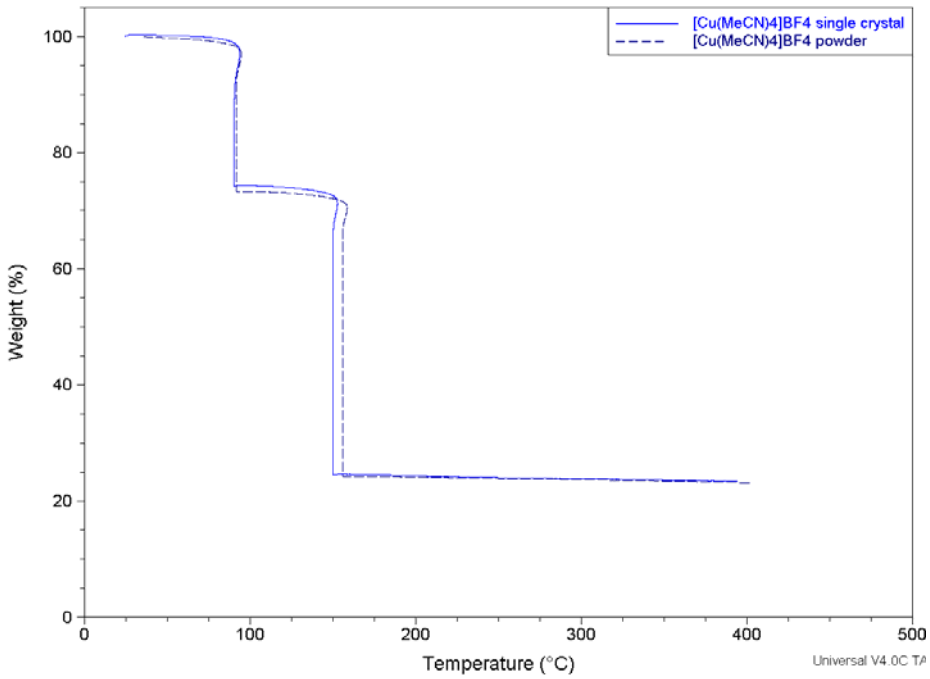

Figure 2.28 – Stepwise isothermal mass loss comparison between $[Cu(MeCN)_4]BF_4$ single crystal and powder.

2.4 Conclusion

The research shows that the reaction between $[Cu(MeCN)_4]X$ (X = BF_4, PF_6, or SO_3CF_3) and 4,7-phenanthroline occurs readily when just the solid reactants are combined. These novel reactions produce their own solvent, which helps facilitate the reaction. These solid-solid reactions create one-dimensional chains of 4,7-phenanthroline molecules bridging copper cations. Those structures proved to be unique to each anion. The variations in these structures were the orientation of the 4,7-phenanthroline and the coordination of one of the anions.

The rate in which the acetonitrile vapor is released by the tetraacetonitrilecopper(I) salts at room temperature is consistent with the reaction rates seen with 4,7-phenanthroline and tetraacetonitrilecopper(I) salt solid-solid reactions. The

distinct difference in the rate at which $[Cu(MeCN)_4]SO_3CF_3$ loses acetonitrile vapor compared to the other tetrakisacetonitrilecopper(I) salts was discussed. The difference in rate is most likely due to the triflate anion coordination to the copper cation.

The same information for a different coordinated solvent could be used in order to determine whether the material is a viable candidate for this type of solid-solid reaction. If the coordinated solvent is being released at room temperature, the relatively fast rate at which the loss occurs could enable the chemist to determine the best starting material for a required system. This type of pseudo-solid-state reaction does lend itself well to green chemistry.

References

(1) Lopez, S.; Kahraman, M.; Harmata, M.; Keller, S. W. *Inorg. Chem.* **1997**, *36*, 6138-6140.

(2) Lopez, S.; Keller, S. W. *Crystal Eng.* **1999**, *2*, 101-114.

(3) Knaust, J. M.; Knight, D. A.; Keller, S. W. *J. Chem. Crystallogr.* **2003**, *33*, 813-823.

(4) Jones, P. G.; Crespo, O. *Acta Crystallogr. C* **1998**, *54*, 18-20.

(5) Black, J. R.; Levason, W.; Webster, M. *Acta Crystallogr. C* **1995**, *51*, 623-625.

(6) Lopez, S.; Keller, S. W. *Inorg. Chem.* **1999**, *38*, 1883-1888.

(7) MacGillivray, L. R.; Subramanian, S.; Zaworotko, M. J. *J. Chem. Soc. Chem. Commun.* **1994**, *11*, 1325-1326.

(8) Werner, P. E.; Eriksson, L.; Westdahl, M. *J. Appl. Crystallogr.* **1985**, *18*, 367-370.

(9) Boultif, A.; Louër, D.; *J. Appl. Cryst.* **2004**, *37*, 724-731.

(10) Yvon, K.; Jeitschko, W.; Parthe, E. *J. Appl. Crystallogr.* **1977**, *10*, 73-74.

(11) Antolasic, F. Wsearch 32 ed. Melbourne, Victoria, Australia, 2005, p Mass Spec analysis tool.

(12) Kubas, G. J. *Inorg. Syntheses* **1979**, *19*, 90-92.

(13) Bruker Analytical X-ray: 1997.

(14) Sheldrick, G. M. University of Gottingen, Germany, 1997.

(15) Barbour, L. University of Missouri-Columbia, Columbia, MO, 2001.

(16) Orpen, A.; Brammer, L.; Allen, F.; Kennard, O.; Watson, D.; Taylor, R. *J. Chem. Soc. Dalton Trans.* **1989**, S1-S83.

(17) Kappenstein, C.; Hugel, R. P. *Inorg. Chem.* **1977**, *16*, 250.

(18) Kappenstein, C.; Hugel, R. P. *Inorg. Chem.* **1978**, *17*, 1945-1949.

(19) Thomas, J. C.; Peters, J. C. *Polyhedron* **2004**, *17*, 2901-2913

(20) Fujisawa, K.; Noguchi, Y.; Miyashite, Y.; Okamoto, K.; Lehnert, N. *Inorg. Chem.* **2007**, *46,* 10607-10623

(21) Haidekker, M. A.; Akers, W. J.; Fischer, D.; Theodorakis, E. A. " *Opt. Lett.* **2006**, *31*, 2529-2531

(22) Fricker, M.D.; Chow, C.M.; Errington, R.J.; May, M. *Exp. Biol. Online* **1997**, *2*, 1-23

Chapter 3

Solid-Solid Reactions between $[Cu(MeCN)_4]X$ and 4,4'-dipyridyl (X= PF_6, BF_4, and SO_3CF_3)

3.1 Introduction

We have expanded solid-solid reactions past the use of 4,7-phenanthroline and $[Cu(MeCN)_4]X$ (X= PF_6^-, BF_4^-, and $SO_3CF_3^-$) with 4,4'-dipyridyl replacing 4,7-phenanthroline as the bridging ligand. A structural comparison of 4,4'-dipyridyl and 4,7-phenanthroline is shown in Table 3.1. 4,4'-dipyridyl has been used in a wide variety of coordination networks as a linker between metal cations. It is in fact one of the most prevalent nitrogen-containing ligands used, with over 683 structures present in the Cambridge Structural Database.[1] One reason for the plethora of structures that contain 4,4'dipyridyl is the two potential nitrogen bonding sites located on opposite ends of the molecule. The arrangement of the nitrogen atoms allows a 4,4'-dipyridyl molecule to serve as a stiff, linear linker. The length of a 4,4'-dipyridyl molecule allows for a respectable cavity size for metal organic frameworks (MOFs) created using this molecule. As mentioned previously, 4,7-phenanthroline was used because of it rigidity; this is the case for 4,4'-dipyridyl even though there is rotation of the pyridine rings. The rigidity coupled with the molecule's size is the reason the 4,4'-dipyridyl molecule readily forms a variety of structural types, including zigzag polymers,[2-6] ladder networks,[7-11] two-dimensional networks such as square grids,[11-18] and three-dimensional diamonoid networks.[19-21]

Name	Structure	Melting Point
4,7-phenanthroline	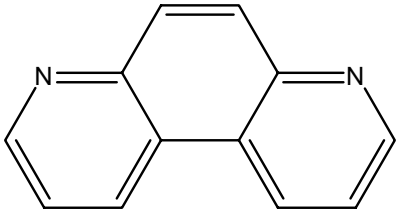	172-174 °C
4,4'-dipyridyl	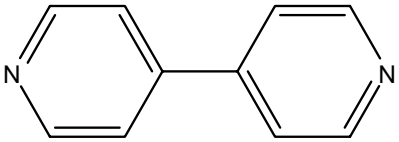	109-112 °C

Table 3.1 – Comparison between 4,7-phenanthroline and 4,4'-dipyridyl molecular structures and melting points.

Copper(I) and 4,4'-dipyridyl were used in previous studies, from which diamonoid network formed with PF_6^- lying within network cavities (Figure 3.1).[19] The copper(I) cations are coordinated to four 4,4'-dipyridyl ligands. Each of the coordinated 4,4'-dipyridyl molecules bridge to two different copper(I) cations. The copper(I)-4,4'-dipyridyl networks can be viewed as four interpenetrating one-dimensional chains that wrap around to form a cylinder (Figure 3.2). The PF_6^- anions reside in the cavities, however BF_4^- and CN^- were found not to exchange with the PF_6^- in solution.[19]

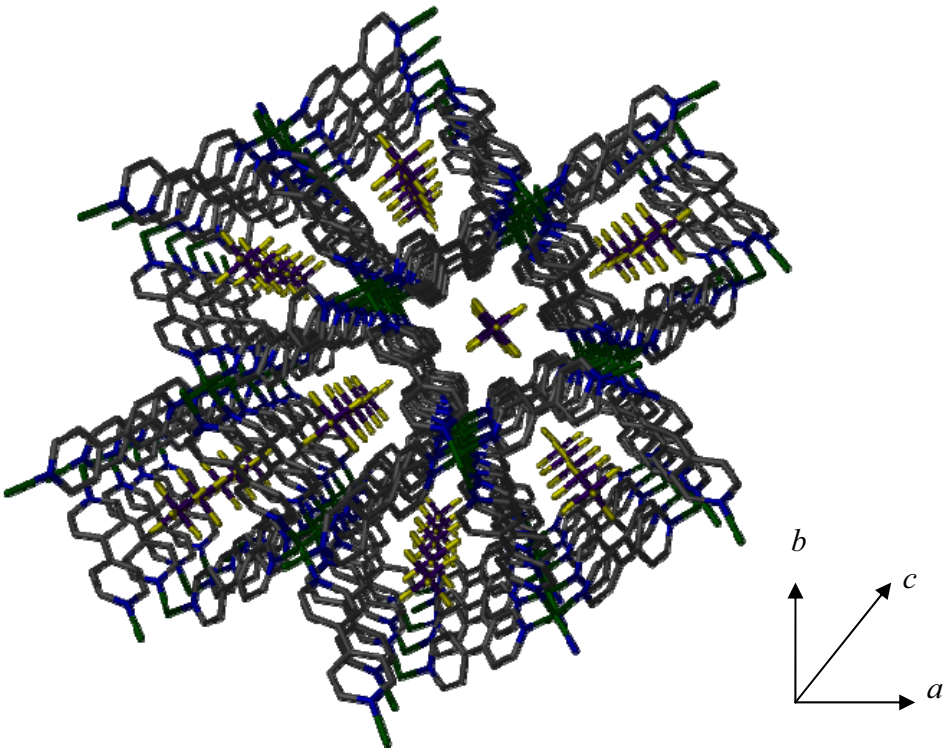

Figure 3.1 – View of $\{[Cu(4,4'\text{-dipyridyl})_2]PF_6\}_n$ packing looking down the *c*-axis. Each cavity is approximately 6 Å x 6 Å. All hydrogen atoms have been omitted for clarity. The color scheme is as follows: Cu = green, N = blue, C = gray, F = yellow, and P = purple.[19]

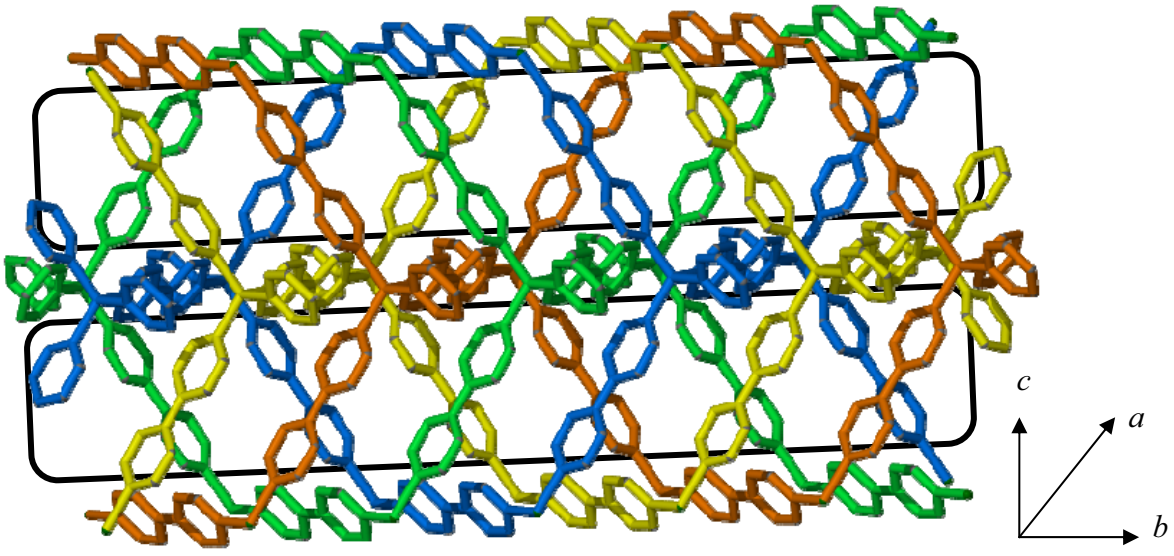

Figure 3.2 – Pictured is the side view of two cavities on top of one another. The cavities are indicated by the black lines. Each of the four interpenetrating chains is given a different color. Hydrogen atoms and anions have been removed for clarity. [19]

Another consideration is whether 4,4'-dipyridyl, like 4,7-phenanthroline, can be used in the solid-solid reactions. The major question was whether *three-dimensional* copper(I)-containing coordination networks could be produced with solid-solid reactions. A linear structure similar to that of $\{[Cu(MeCN)_2(4,7\text{-phenanthroline})]BF_4\}_n$ was produced using 4,4'-dipyridyl, copper(I), and acetonitrile with solution-based techniques (Figures 3.3 and 3.4).[6] The coordination network is made up of 4,4'-dipyridyl bridging the copper(I) cations, which have two additional acetonitrile molecules to complete the distorted tetrahedral coordination sphere.

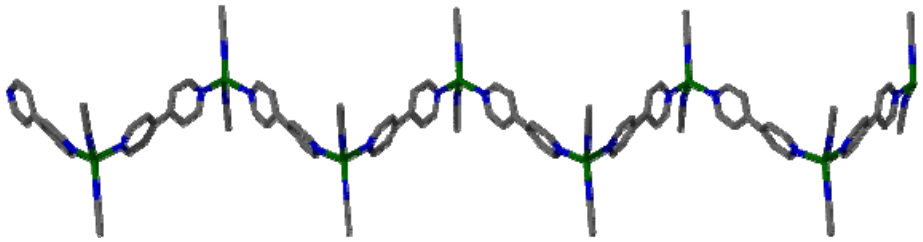

Figure 3.3 – A one-dimensional copper(I) 4,4'-dipyridyl chain in $\{[Cu(4,4'\text{-dipyridyl})(MeCN)_2]^+\}_n$.[6]

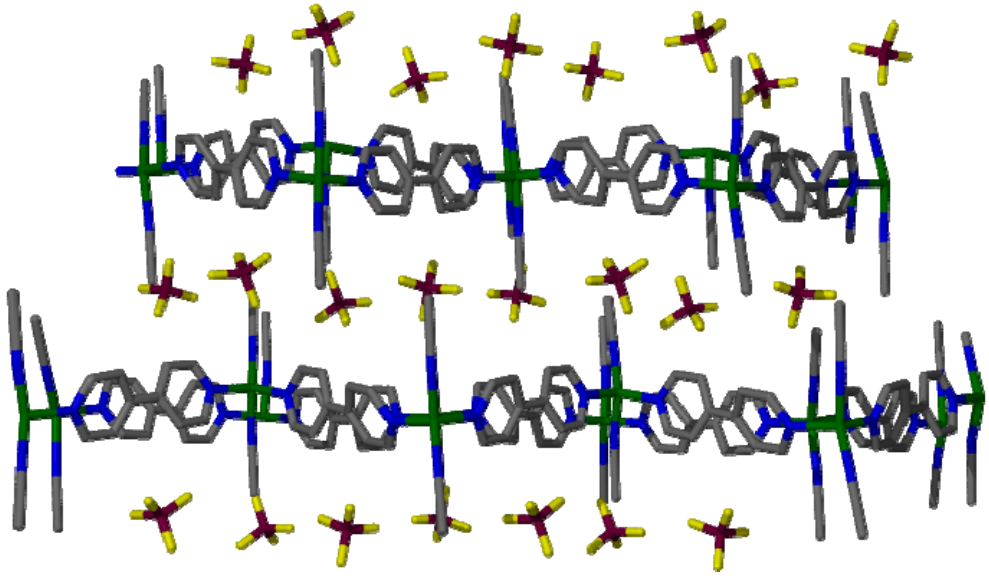

Figure 3.4 – Pictured is the packing of the one-dimensional $\{[Cu(4,4'\text{-dipyridyl})(MeCN)_2]BF_4\}_n$ chains. The chains pack on top of one another forming sheets between which the anions lie.[6]

Another copper containing coordination network is a two-dimensional sheet created with a PF_6^- anion located between the sheets (Figure 3.5).[11] The copper in this structure has an oxidation state of +2 and is coordinated by four 4,4'-dipyridyl ligands and one MeCN molecule. Each 4,4'-dipyridyl ligand coordinated to one copper(II) center lie on the same plane. The coordinated MeCN molecules along with the noncoordinated PF_6^- anions are located between neighboring sheets. The PF_6^- anions balance the charge of the copper(II) cation.

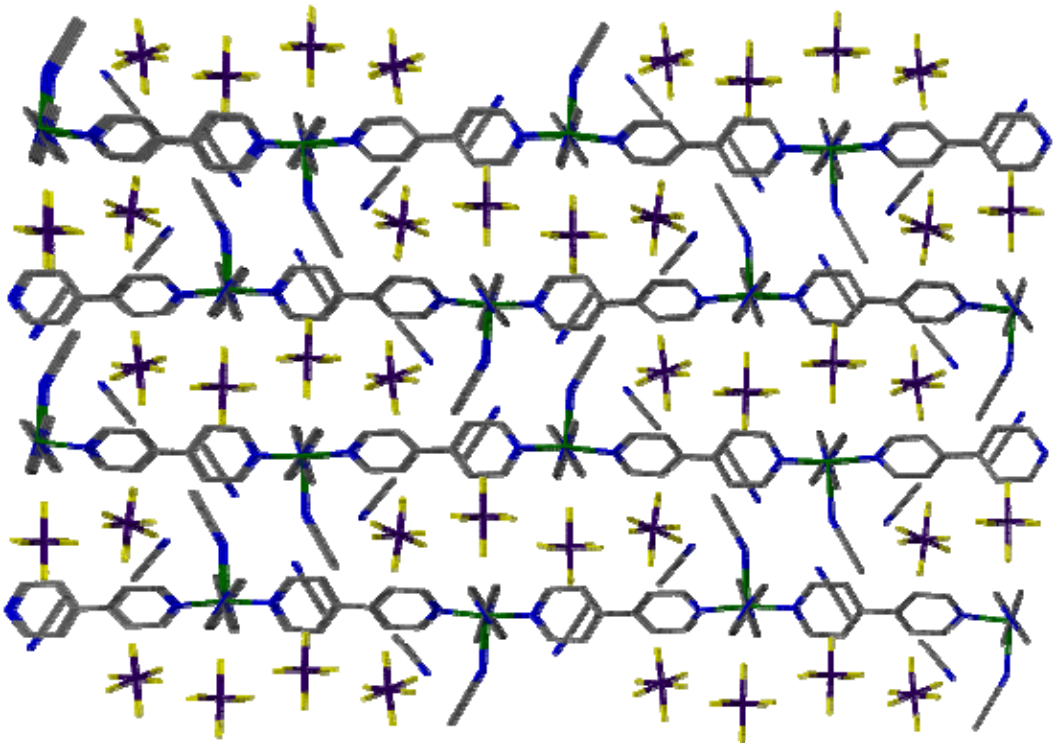

Figure 3.5 – Two-dimensional layer structure for $\{[Cu(MeCN)(4,4'\text{-dipyridyl})_2](PF_6)_2\}_n$.[11]

The numerous structural variations that can be found by using 4,4'-dipyridyl in the synthesis of coordination networks make it a good candidate for use in solid-solid reactions. The results of this study will give a better idea of what variation, if any, these reaction have verses solution based reactions.

3.2 Experimental

Materials and Methods

Copper(I) oxide (Fisher), tetrafluoroboric acid (Aldrich), hexafluorophosphoric acid (Aldrich), trifluoromethanesulfonic acid (Aldrich), 4,4'-dipyridyl (GFS Chemicals and Aldrich), acetonitrile (Fisher), and diethyl ether (Fisher) were used without further purification unless otherwise noted in the synthesis. Starting materials **2.1, 2.2,** and **2.3** were synthesized as described in Chapter 2. The new structures created are included in the table of selected crystallographic data (Table 3.2).

Powder X-ray diffraction (PXRD) patterns were collected using a Scintag X2 system at 40 kV and 30 mA for Cu K_α radiation (λ=1.540562 Å). Continuous scans were taken at 0.60° per min from 5° to 37° 2θ, unless otherwise noted. All patterns were indexed via Treor 90 software program.[22] Single crystal X-ray diffraction (XRD) data of previously solved structures were used in conjunction with LAZY-PULVERIX[23] to generate the calculated powder patterns used for comparison.

Gas chromatography mass spectrometry (GC-MSD) was performed using an Agilent 6890 (Agilent, San Jose) split-less mode at an oven temperature of 60 °C. A 1-µL gas-tight syringe was used to take a 0.2-µL sample size, unless otherwise noted. The samples were taken with an autosampler to ensure sample size precision. Each vial was 2 mL in size and had a Teflon-silicone-Teflon septum. The data were analyzed using WSearch32,[24] where the total ion count (TIC) for the acetonitrile parent ion was taken at the peak of the spectrum.

UV-Visible (UV-Vis) spectra were recorded using a Cary 3 (Varian, Melrose Australia) with a diffuse reflectance attachment. A home-built sample holder used a

polyethylene gasket with a rubber core between two 40 mm diameter optically inactive fused silica discs. A Teflon sheet was then inserted to serve as a neutral backing. In order to provide a gas-tight seal the assembly was clamped together via four bolts. Each run was limited to 350-800 nm as a result of the noise beyond those wavelengths. A schematic of the sample holder can be viewed in Chapter 2 (Figure 2.8).

Elemental analyses were performed by Desert Analytics Transwest Geochem (Phoenix, AZ). Samples were transferred under nitrogen. The analysts did not observe changes in the color or texture of the samples before or after analysis.

Synthesis of Reaction Products

***net*-{[poly[(4,4'-dipyridyl)copper(I)]-*v*-(4,4'-dipyridyl)$_2$] tetrafluoroborate}, {[Cu(4,4'-dipyridyl)$_2$]BF_4}$_n$, 3.1**

With a mortar and pestle, **2.1**, $[Cu(MeCN)_4]BF_4$, (157 mg, 0.5 mmol) was gently ground with 4,4'-dipyridyl (156 mg, 1 mmol) for approximately 15 sec until the mixture was of homogeneous off-white color. The mixture was then placed in a 4 mL vial, sealed with parafilm, and capped. After 30 min, the off-white color changed to yellow and then a bright orange. Elemental analysis calculated (found) for $C_{20}H_{16}B_1Cu_1F_4N_4$: C, 51.91 (49.01); H, 3.490 (3.520); N 12.11 (12.17).

In a medium test tube, 2 mL of a saturated solution of 4,4'-dipyridyl in MeCN was layered on top of a 2 mL saturated solution of $[Cu(MeCN)_4]BF_4$ in MeCN. Diethyl ether was then layered on top of the orange solution. After four weeks, orange blocky XRD quality crystals formed. The single crystal form will be referred to as **3.4**.

***net*-{[poly[(4,4'-dipyridyl)copper(I)]-*v*-(4,4'-dipyridyl)$_2$] hexafluorophosphate}, {[Cu(4,4'-dipyridyl)$_2$]PF_6}$_n$, 3.2**

With a mortar and pestle, **2.2**, $[Cu(MeCN)_4]PF_6$, (186 mg, 0.5 mmol) was gently ground with 4,4'-dipyridyl (156 mg, 1 mmol) for approximately 15 sec until the mixture was of homogeneous off-white color. The mixture was then placed in a 4 mL vial, sealed with parafilm, and capped. After 45 min, the off-white color changed to dull yellow and then a bright orange. Elemental analysis calculated (found) for $C_{20}H_{16}PCuF_4N_4$: C, 46.12 (45.13); H, 3.10 (3.090); N 10.76 (10.50).

***net*-{[poly[(4,4'-dipyridyl)copper(I)]-*v*-(4,4'-dipyridyl)$_2$] trifluoromethanesulfonate} {[Cu(4,4'-dipyridyl)$_2$]SO_3CF_3}$_n$, 3.3**

With a mortar and pestle, **2.3**, $[Cu(MeCN)_4]SO_3CF_3$, (188mg, 0.5 mmol) was gently ground with 4,4'-dipyridyl (156 mg, 1 mmol) for approximately 15 sec until the mixture was of homogeneous off-white color. The mixture was then placed in a 4 mL vial, sealed with parafilm, and capped. After 5 min, the off-white color changed to a bright yellow and then a bright orange. Elemental analysis calculated (found) for $C_{20}H_{17}SO_3CuF_3N_4$: C, 48.05 (48.14); H, 3.07 (3.160); N 10.67 (10.80).

In a 4 mL vial, ~50 mg of **3.3** was dissolved in MeCN via sonication. The liquid was then decanted off into another 4 mL vial. This vial was placed in a 20 mL scintillation vial that contained 5 mL of diethyl ether. After two weeks, deep orange crystals formed. The single crystals formed will be referred to as **3.5**.

Crystal Structure Analysis

Single crystals for XRD were placed in inert oil and selected using an optical microscope. Each crystal chosen uniformly extinguished plane polarized light upon rotation of 90°. The selected crystals were then mounted on thin glass fibers with a small amount of silicone grease. Using a Siemens SMART system (Mo(K_α) = 0.71073 Å) with a charge-coupled area detector, a full hemisphere of crystallographic data was collected. Absorption corrections were applied after integration.[25] All structures were solved using SHELXS Direct Methods[26] and refined using a full least squares treatment on F^2.[27] All non-hydrogen atoms were refined with anisotropic thermal parameters. Crystallographic details for **3.4** and **3.5** are listed in Table 3.2. Neither structure has been previously included in the Cambridge Crystal Database.

Atoms S1 and C6 in **3.5** are both located directly on a four-fold rotation axis, and therefore each have a site occupancy of 0.25, which adds up to, one sulfur atom and one carbon atom in the asymmetric unit. Atoms O1 and F1 each have site occupancies of 0.75. Four oxygen atoms and four fluorine atoms are generated by the four-fold rotation axis. Four multiplied by 0.75 equals three, so there are really a total of three oxygen atoms and three fluorine atoms in the asymmetric unit., This, makes a total of one complete triflate anion per asymmetric unit.

	3.4	**3.5**
Empirical formula	$Cu_1C_{20}H_{16}N_4B_1F_4$	$CuC_{21}H_{16}N_4O_3SF_3$
Formula weight (g/mol)	462.72	524.98
Crystal system, space group	Monoclinic, $P2_1/c$	Tetragonal, P4/n
Temperature (K)	173(2)	173(2)
Unit cell dimensions (Å, deg)	a = 7.161(1) b = 16.282(2) c = 17.260(2) β = 100.849(2)	a = 13.462(3) c=5.976(10)
Volume ($Å^3$)	1976.5(5)	1083.1(3)
Z, ρ calc (g/cm^3)	4, 1.555	8, 1.609
Absorption coefficient (mm^{-1})	1.156	4.649
F(000)	936	2128
Crystal size (mm)	0.2 × 0.2 × 0.1	0.4 × 0.4 × 0.1
Θ Range for data collection (deg)	2.40 to 26.00	3.03 to 24.62
Reflections collected/unique	13384 / 4344 [R_{int}=0.0902]	7146 / 1211 [R_{int}=0.0503]
Max. and min. transmission	0.8932 and 0.6773	0.6536 and 0.4851
Data / restraints / parameters	4344 / 0 / 271	1211 / 0 / 81
Final R indices [I>2σ(I)] [a,b]	R_1= 0.0786, wR_2=0.1878	R_1=0 .0558, wR_2=0.1184
R indices (all data)	R_1= 0.1523, wR_2=0.2246	R_1= 0.0818, wR_2=0.1348
Largest diff. peak / hole ($e.A^{-3}$)	1.31 / -0.62	1.02 / -0.66
GoF on F^2	1.041	1.033
Structures were refined on F_o^2 using all data. [a] $R = \Sigma(\|F_o\|-\|F_c\|)/\Sigma\|F_o\|$; [b] $wR_2 = [\Sigma(\|F_o\|-\|F_c\|)^2/\Sigma\|F_o\|^2]^{1/2}$		

Table 3.2: Selected crystallographic details for **3.4** and **3.5**.

3.3 Results and Discussion

Description of the Crystal Structure

The asymmetric unit of **3.4** ({[Cu(4,4'-dipyridyl)$_2$]BF_4}$_n$) contains only one unique copper, Cu(1). The four coordinated nitrogen atoms, from four different 4,4'-dipyridyl molecules, create a distorted tetrahedral environment around Cu(1) (Figure 3.6). The Cu-N bond lengths range from 1.979(5) Å to 2.146(5) Å, which is within the range of acceptable Cu^+-N bond lengths, 2.07 ± 0.07, for pyridine.[29] The structure is extended by the bridging of copper(I) cations via 4,4'-dipyridyl ligands.

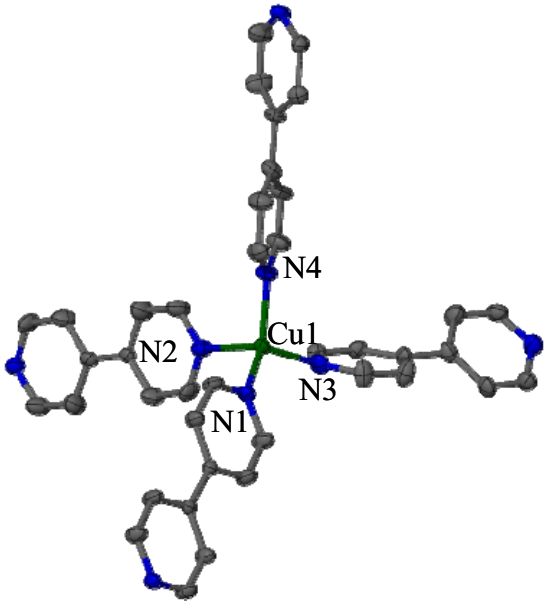

Cu(1) – N(1)	1.979(5) Å	N(1)-Cu(1)-N(2)	107.5(2)°
Cu(1) – N(2)	2.146(5) Å	N(1)-Cu(1)-N(3)	116.9(2)°
Cu(1) – N(3)	2.054(5) Å	N(1)-Cu(1)-N(4)	120.6(2)°
Cu(1) – N(4)	2.034(6) Å	N(3)-Cu(1)-N(2)	99.9(2)°
		N(4)-Cu(1)-N(2)	101.8(2)°
		N(4)-Cu(1)-N(3)	107.1(2)°

Figure 3.6 – Copper coordination environment in **3.4** with selected bond lengths and angles. All atoms are shown as 50% probability thermal ellipsoids. Hydrogen atoms are omitted for clarity.

The extended structure forms cavities in which the BF_4^- anions are located (Figure 3.7). The cavity size is 6 Å x 6 Å based on measurement of the distance between hydrogen atoms on opposite sides of the cavity. The MOF **3.4** is isostructural to that of $\{[Cu(4,4'\text{-dipyridyl})_2]PF_6\}_n$ described previously. The N-Cu-N angles for 4,4'-dipyridyl that make up opposite sides of a cavity are similar (N(1)-Cu(1)-N(2) = 107.5(2)° and N(4)-Cu(1)-N(3) = 107.1(2)°). The comparison of the bond lengths show that the Cu(1)-N(3) and Cu(1)-N(4) are the most similar values (2.054(5) Å and 2.034(6) Å, respectively).

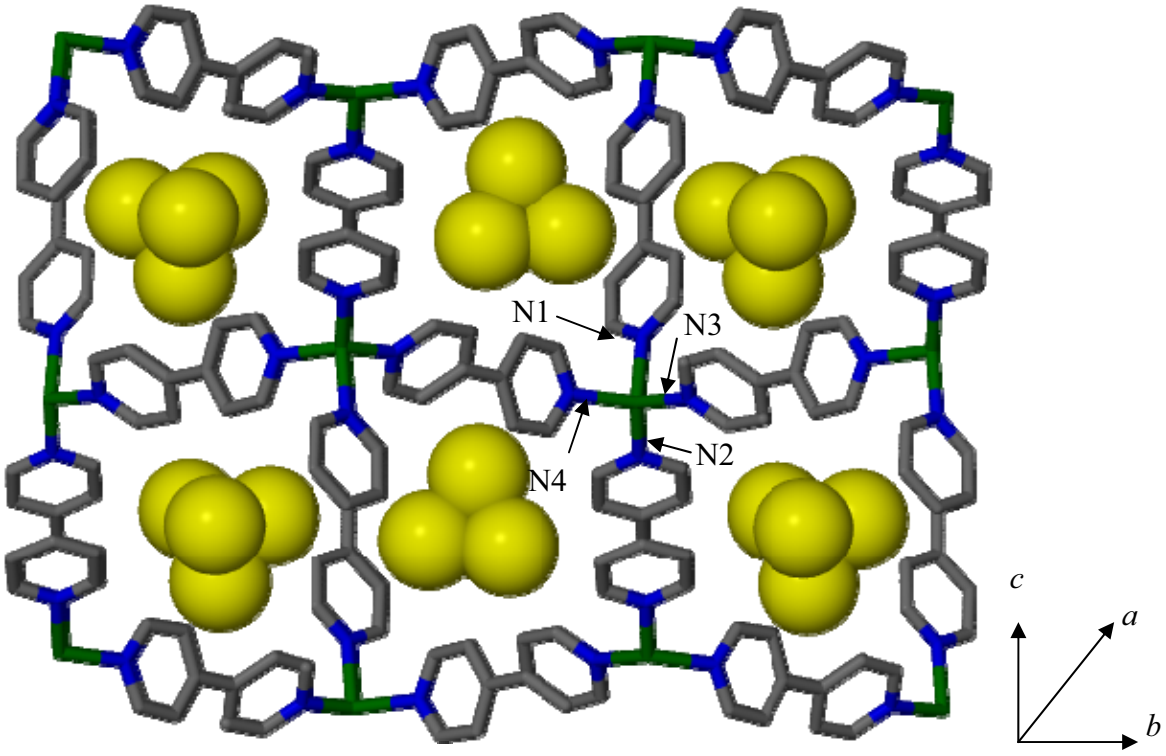

Figure 3.7 – Depiction of the extended structure of 3.4, viewed down the cavities showing the location of the BF_4^- anions. As with the previously reported structure, $\{[Cu(4,4'\text{-dipyridyl})_2]PF_6\}_n$, the structure is three-dimensional. The nitrogen atoms are labeled to provide context for the angles mentioned. The hydrogen atoms are removed for clarity.

As stated the previously reported {[Cu(4,4'-dipyridyl)$_2$]PF_6}$_n$ is isostructural to {[Cu(4,4'-dipyridyl)$_2$]BF_4}$_n$. The similarities can be seen in the N-Cu-N bond angles where the N-Cu-N bond that makes up a corner of a cavity is 111.2º for the {[Cu(4,4'-dipyridyl)$_2$]PF_6}$_n$ case. This is in fact larger than the average N-Cu-N bond angle for the {[Cu(4,4'-dipyridyl)$_2$]BF_4}$_n$ structure, 109.8º. The smaller angle required for the cavity is due to the size difference between the PF_6^- and BF_4^- anions. The 4,4'-dipyridyl molecules that lie on the *c*-axis or the b-axis have similar N-Cu-N bond angles, which are 107º and 106º, for {[Cu(4,4'-dipyridyl)$_2$]BF_4}$_n$ and {[Cu(4,4'-dipyridyl)$_2$]PF_6}$_n$, respectively.

The coordination environment around each Cu atom in **3.5** ({[Cu(4,4'-dipyridyl)$_2$]SO_3CF_3 }$_n$) is similar to that just described for **3.4**. Like the copper(I) coordination for **3.4**, there is only one unique copper atom that is coordinated to four 4,4'-dipyridyl ligands (Figure 3.8). However, there is only one unique nitrogen atom as compared to the four for **3.4**. The reason for the decrease in unique atoms is due to the copper cation sitting directly on the four-fold rotation axis, and the nitrogen atoms are generated from said axis. The previously reported structure had a copper that did not sit on a special position, so all nitrogen atoms were unique. As before, {[Cu(4,4'-dipyridyl)$_2$]SO_3CF_3 }$_n$ is isostructural to the previously reported {[Cu(4,4'-dipyridyl)$_2$]PF_6}$_n$ structure with the PF_6^- anions being replaced by the $SO_3CF_3^-$ anions in the cavities (Figure 3.9). The {[Cu(4,4'-dipyridyl)$_2$]SO_3CF_3 }$_n$ is dissimilar to the {[Cu(4,4'-dipyridyl)$_2$]BF_4}$_n$ and the previously reported {[Cu(4,4'-dipyridyl)$_2$]PF_6}$_n$ when comparing N-Cu-N bond angles. In the {[Cu(4,4'-dipyridyl)$_2$]SO_3CF_3 }$_n$ structure, the smaller N-Cu-N bond angle, 106.88(9)°, make up the corners of each cavity as

compared to the N-Cu-N bond angle for the corner being the largest bong angle(s) the two other structures. The difference in N-Cu-N bond angle is due to the variation in anion's size for all cases.

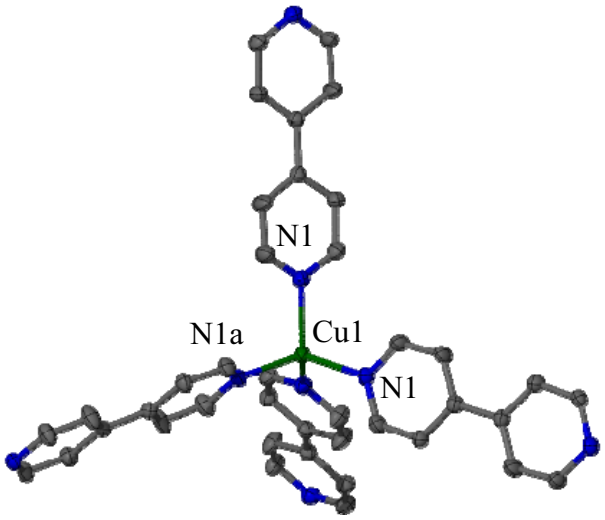

Cu(1)-N(1) 2.051(3)Å	N(1)-Cu(1)-N(1) 106.88(9)°	N(1a)-Cu(1)-N(1) 114.79(8)°

Figure 3.8 – Copper coordination environment in **3.5** with selected bond lengths and angles. All atoms are shown as 50% probability thermal ellipsoids. Hydrogen atoms are omitted for clarity.

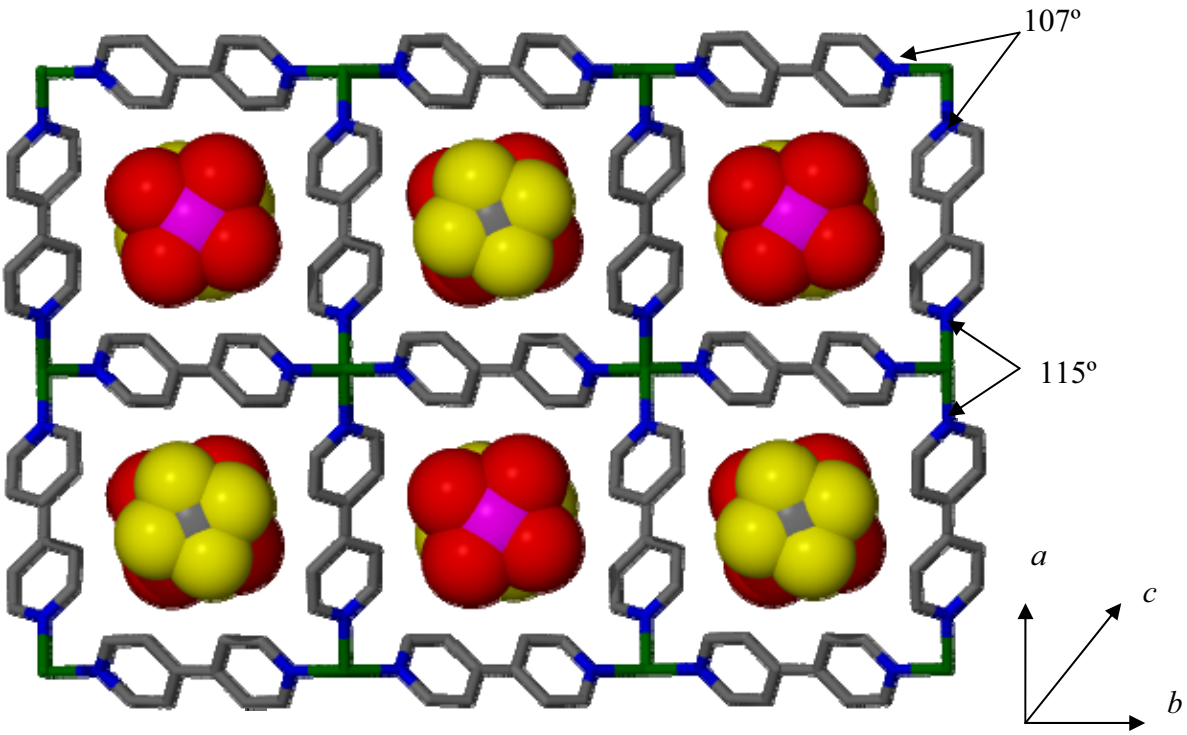

Figure 3.9 – Depiction of the extended structure of **3.5**, viewed down the cavities showing the location of the $SO_3CF_3^-$ anions. The number of O and F on each anion pictured is four instead of three due to the anion sitting on a four-fold rotation axis (site occupancy of each O and F is 0.75). Sulfur is in purple and oxygen in red.

Product Identification

The PXRD patterns for each solid-solid reaction product were compared to the calculated PXRD pattern from the single-crystal data for the four-fold interpenetrating network MOF described. A comparison of each solid-solid reaction's PXRD pattern showed a close match to the calculated PXRD pattern (Figures 3.10, 3.11, and 3.12). From this comparison the solid-solid reaction products, **3.1, 3.2,** and **3.3**, were determined to be the four-fold interpenetrating network MOFs.

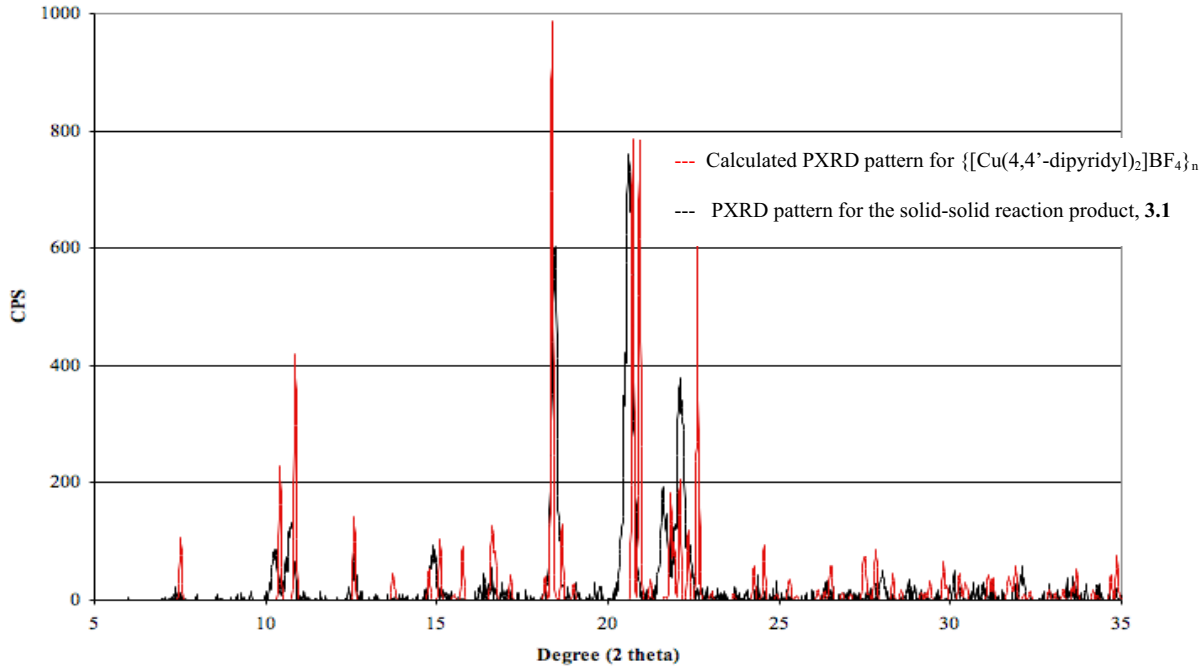

Figure 3.10 – Comparison between the calculated PXRD pattern for {[Cu(4,4'-dipyridyl)$_2$]BF_4}$_n$, in red and the **3.1** PXRD pattern, in black. There are peak shifts to lower angles for **3.1** because of thermal expansion.

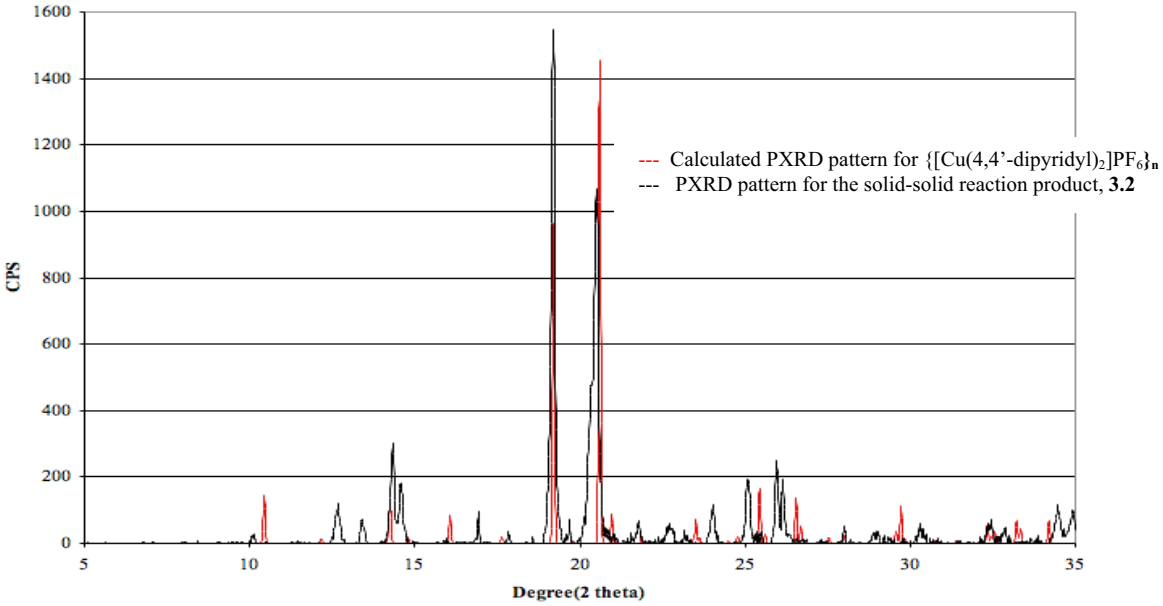

Figure 3.11 – Comparison between the calculated PXRD pattern {[Cu(4,4'-dipyridyl)$_2$]PF_6}$_n$, in red and the experimental PXRD pattern for **3.2** in black. There are peak shifts to lower angles for **3.2** because of thermal expansion.

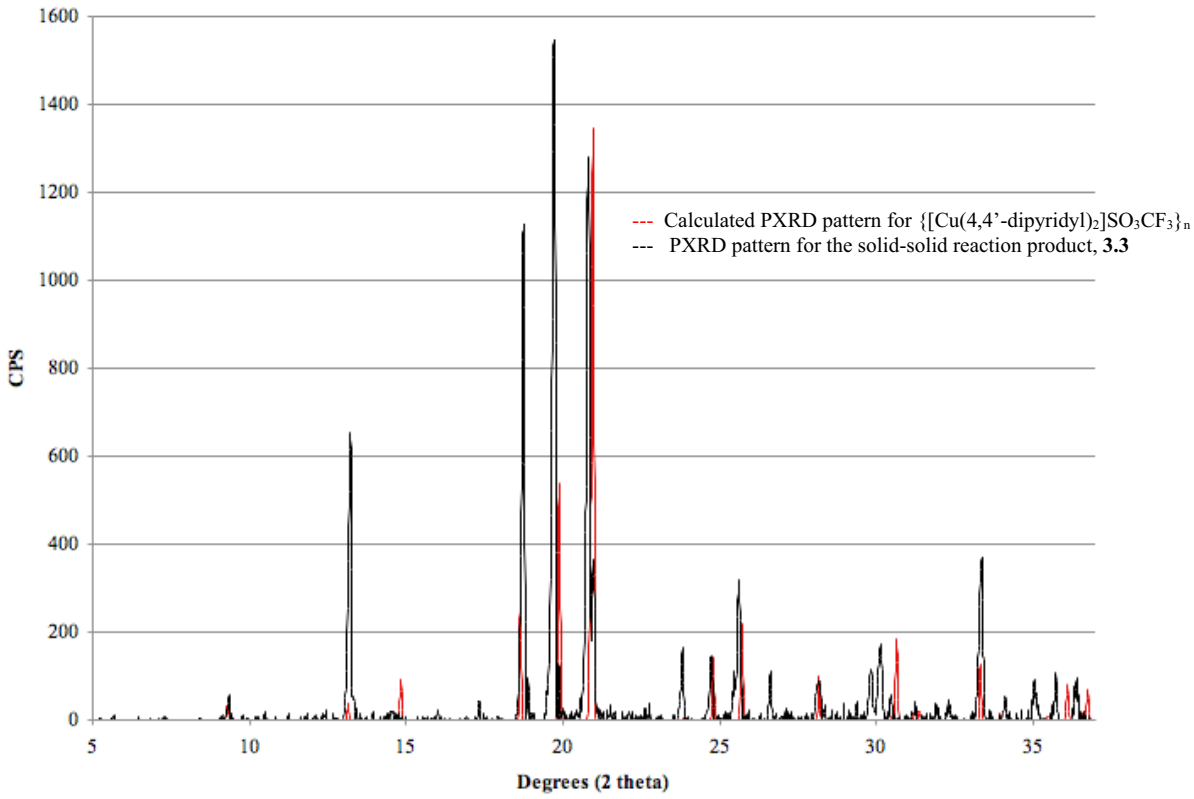

Figure 3.12 – Comparison between the calculated PXRD pattern for {[Cu(4,4'-dipyridyl)$_2$]SO_3CF_3}$_n$ in red, and the experimental PXRD pattern for **3.3** in black. There are peak shifts to lower angles for **3.3** because of thermal expansion.

For both **3.1** and **3.2**, the analysis of the calculated PXRD pattern by both Treor 90 and Dicvol software programs a unit cell solution was not found. Therefore indexing the experimental PXRD pattern prove to be futile. The PXRD pattern for the solid-solid reaction of 4,4'-dipyridyl and [Cu(MeCN)$_4$]SO_3CF_3 was indexed and compared to the calculated PXRD from the {[Cu(4,4'-dipyridyl)$_2$]SO_3CF_3}$_n$ single crystal data (Table 3.3). The results show that the unit cell is close to the parameters obtained at 173 K. The unit cell does not change over temperature as drastically as did the 4,7-phenantholine-containing compounds discussed in Chapter 2.

Name	*a*, Å	*b*, Å	*c*, Å	α, deg.	β, deg.	γ, deg.
3.3 indexed pattern	13.39	13.39	6.08	90	90	90
3.5 single crystal 173 K	13.46(2)	13.46(2)	5.976(1)	90	90	90

Table 3.3 – Treor 90 results for the **3.3** PXRD pattern as compared to $\{[Cu(4,4'\text{-dipyridyl})_2]SO_3CF_3\}_n$ single crystal data.

Monitoring the Reaction

GC-MSD and UV-Vis spectroscopy were performed in order to monitor the progress of the 4,4'-dipyridyl reactions (Figure 3.13). The UV-Vis results for the 4,4'-dipyridyl reactions were similar for **3.1, 3.2,** and **3.3** production. As described in the introduction, the structures formed were four-fold interpenetrating networks. Cavities formed in which the non-coordinating anions were located.

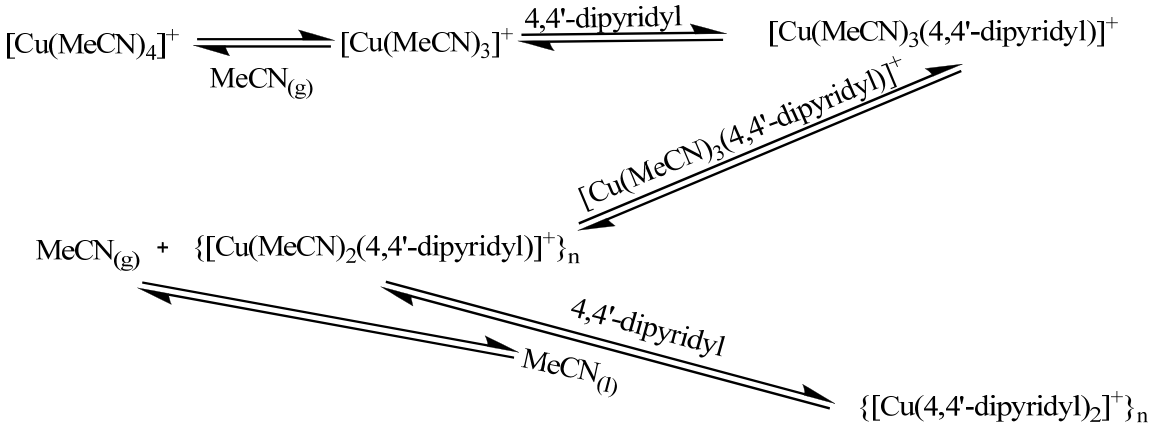

Figure 3.13 – The proposed mechanism between $[Cu(MeCN)_4]X$ and 4,4'-dipyridyl forming the four-fold interpenetrating networks. The anions are located in the cavities that are formed.

A combination of several spectra can be seen with the solid-solid reaction between $[Cu(MeCN)_4]SO_3CF_3$ and 4,4'-dipyridyl (Figure 3.14). These spectrum were selected to describe the general reaction progression.

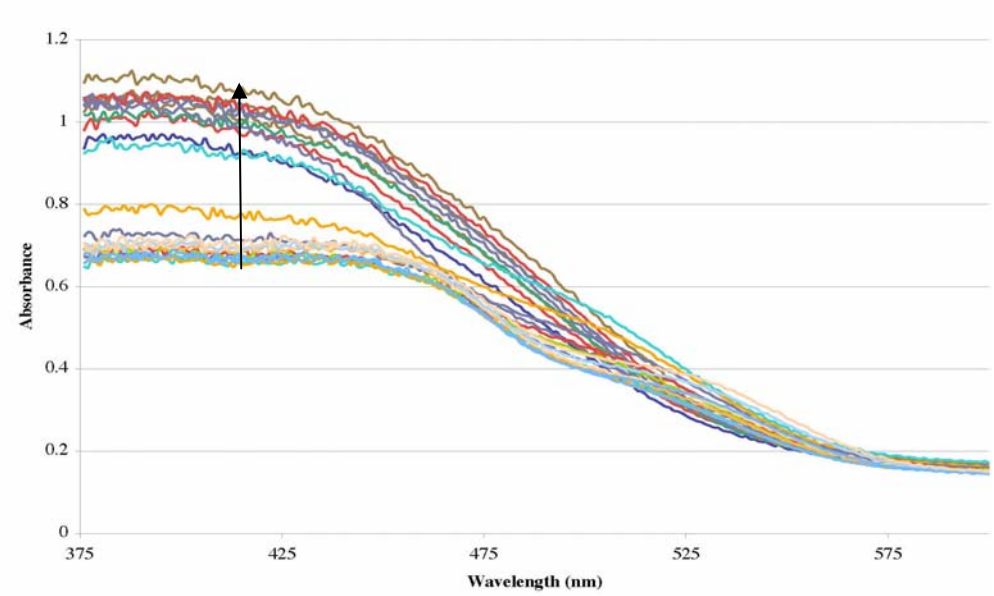

Figure 3.14 – UV-Vis diffuse reflectance spectra taken every half minute for the $[Cu(MeCN)_4]SO_3CF_3$ and 4,4'-dipyridyl reaction. The spectra have been normalized at 750 nm. The arrow indicates the absorbance change, with its tail located at the first spectrum.

The relative time of the spectra is denoted by the order of the color in the visible light spectrum, red (first) to blue (last) (Figure 3.15). An initial yellow species (410 nm) was formed (I). The peak increased until an orange species (525 nm) rapidly developed along with a dramatic decrease of the yellow species (II). The dramatic absorbance change occurs within a minute, strongly suggesting that diffusion is increasing due to the condensation of the MeCN vapor. The MeCN vapor condensation is also indicated by the change in the baseline during (II). At spectrum (III), both the peaks decrease slowly; this indicates that the yellow species is still decreasing. The reason for the absorbance decrease is that the yellow species peak area is a part of the orange species peak area, so if the yellow intermediate's absorbance decreases so would the orange product's.

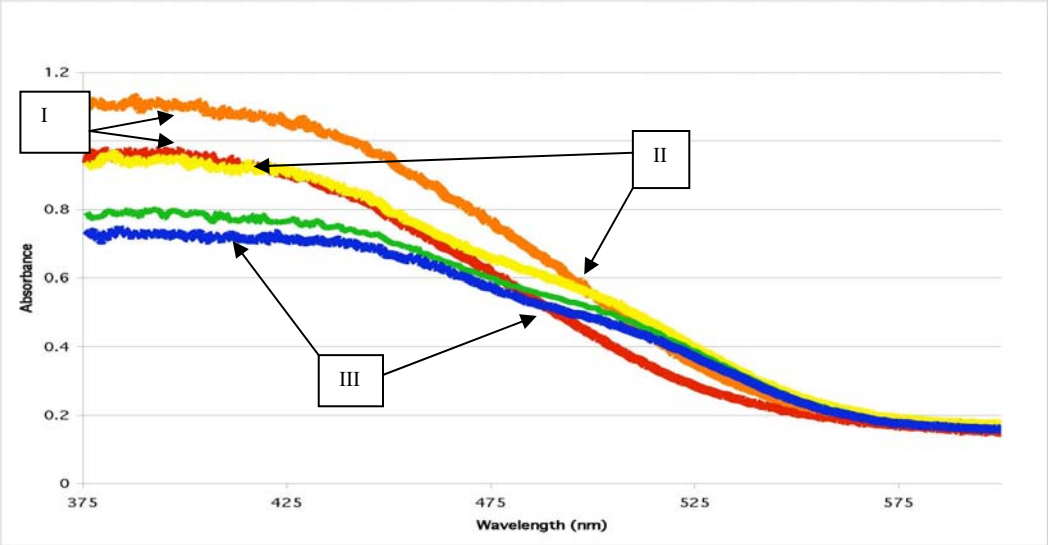

Figure 3.15 – Select UV-Vis diffuse reflectance spectra for the $[Cu(MeCN)_4]SO_3CF_3$ and 4,4'-dipyridyl reaction to show progression of $\{[Cu(4,4'\text{-dipyridyl})_2]SO_3CF_3\}_n$ formation.

The reaction progress indicates that a yellow intermediate species is being created before the diamonoid network is formed (Figure 3.16). The yellow intermediate is probably one in which the copper is being coordinated by two or three 4,4'-dipyridyl based on the yellow color of other structures in which the copper(I) cation has been coordinated by two 4,4'-dipyridyl molecules.[6] The formation of the yellow intermediate allows for acetronitrile molecules to dissociate quicker than that found for the 4,7-phenanthroline study discussed in Chapter 2. This increase in dissociation rate causes the acetronitrile vapor to reach condensation relatively rapidly. The condensation increases diffusion allowing for the formation of the three-dimensional structure (Figure 3.17).

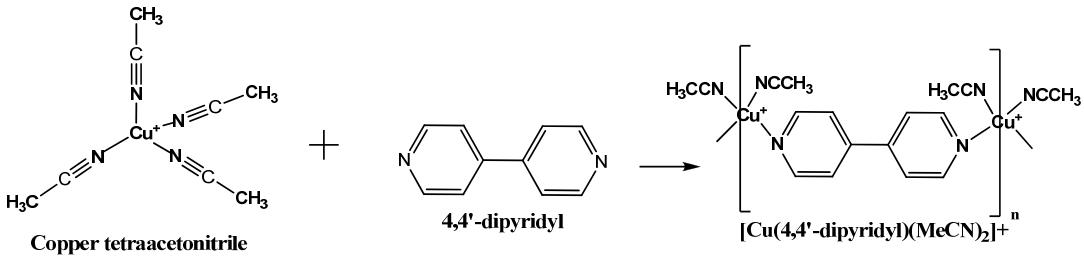

Figure 3.16 – Chemical reaction to produce a proposed intermediate for the 4,4'-dipyridyl and $[Cu(MeCN)_4]X$ ($X=BF_4^-$, PF_6^-, or $SO_3CF_3^-$) solid-solid reaction.

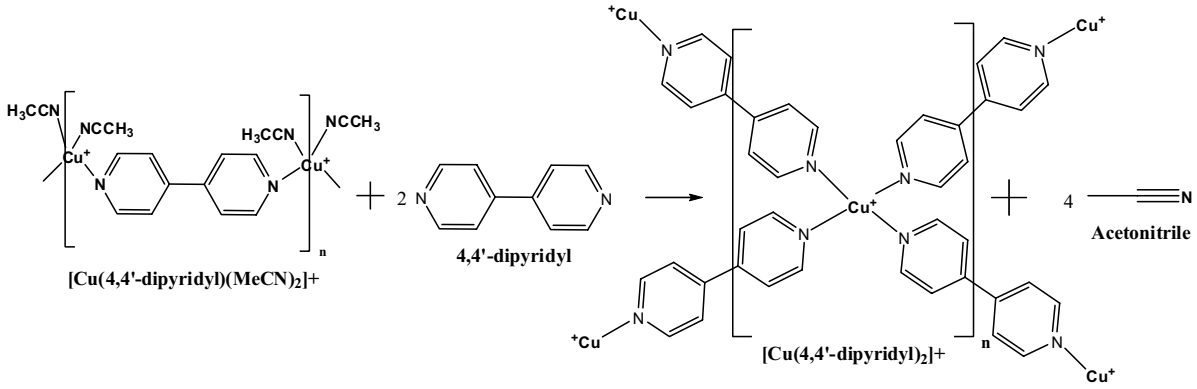

Figure 3.17 – Chemical reaction from a possible yellow intermediate for the 4,4'-dipyridyl and $[Cu(MeCN)_4]X$ ($X=BF_4^-$, PF_6^-, or $SO_3CF_3^-$) solid-solid reaction to the four-fold interpenetrating networks.

The reaction progression for the combination of 4,4'-dipyridyl and $[Cu(MeCN)_4]SO_3CF_3$ becomes apparent when looking at the absorbance taken overtime at 400 nm and 510 nm (Figure 3.18). The 510 nm absorbance increases immediately after the 400 nm absorbance starts to decline relatively rapidly. The absorbance for 510 nm does decrease for a time after the initial increase. However, after the 400 nm absorbance stops decreasing, both wavelengths' absorbance increases at a different rate. As described before, the reason for the absorbance decrease at 510 nm is due to the 410 nm absorbance peak overlapping that of the 510 nm absorbance peak.

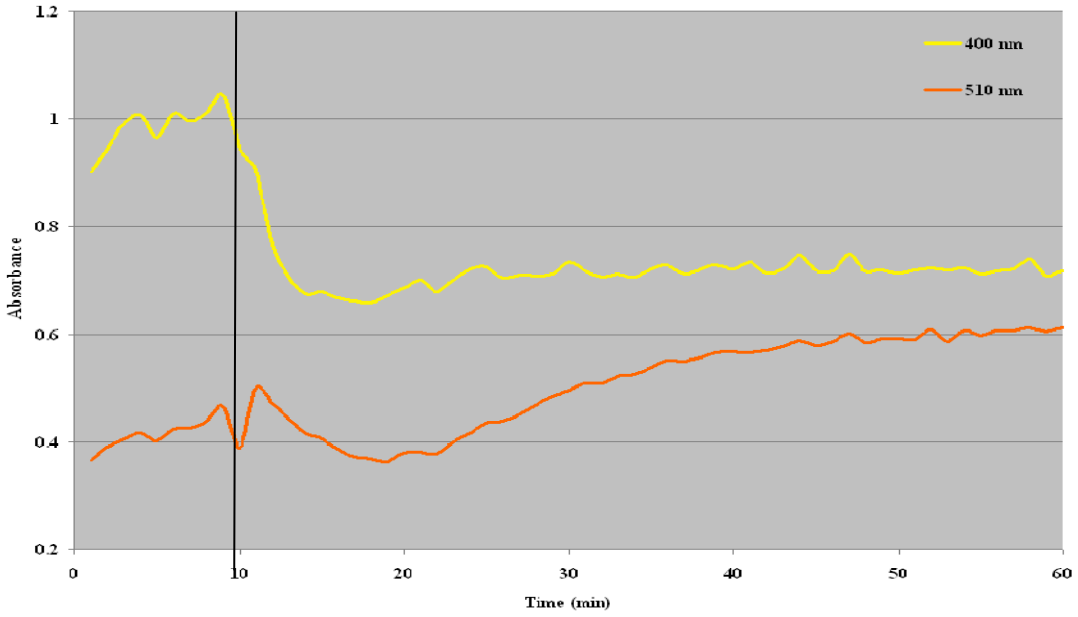

Figure 3.18 – UV-Vis absorbance vs. time for the $[Cu(MeCN)_4]SO_3CF_3$ and 4,4'dipyripyl solid-solid reaction at 510 nm and 400 nm. 400 nm is representative of the yellow transition stage and 510 nm of the four-fold interpenetrating networks MOF. The spectrum is one of two runs performed, with both giving similar results. n = 3.

The transition from yellow intermediate to orange product can also be seen with the reaction of 4,4'-dipyridyl and $[Cu(MeCN)_4]PF_6$ to form $\{[Cu(4,4'\text{-dipyridyl})_2]PF_6\}_n$ (Figure 3.19). Again, the absorbance associated with the product (525 nm) does decrease after the initial increase following the transition due to the peak area overlap with the yellow intermediate's (425 nm) peak area. The absorbance does not recover due to the yellow intermediate absorbance at a relatively high level compared to the orange product.

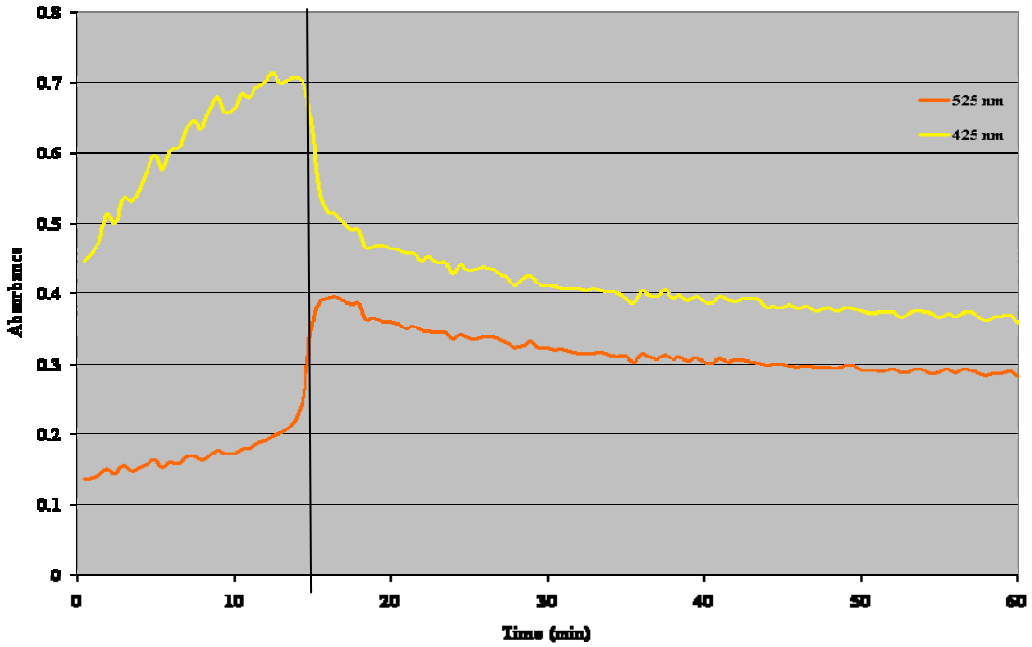

Figure 3.19 – UV-Vis absorbance vs. time for the $[Cu(MeCN)_4]PF_6$ and 4,4'-dipyripyl solid-solid reaction forming **3.2**. Spectra were taken every 30 sec. The absorbance at 510 nm and 425 nm is shown. 425 nm is representative of the yellow transition stage and 510 nm of the four-fold interpenetrating network MOF. The spectrum is one of three runs performed, with all giving similar results. n = 2.

The same transition from yellow intermediate to orange product is seen in the UV-Vis spectrum for the $[Cu(MeCN)_4]BF_4$ and 4,4'-dipyridyl solid-solid reaction (Figure 3.20). Notice that the transition rate by anion occurs in the same order as the reactions in Chapter 2. The transition from the yellow intermediate to the orange product occurs at 4 min, 7 min, and 15 min for reactions containing $SO_3CF_3^-$, BF_4^-, and PF_6^- anions, respectively.

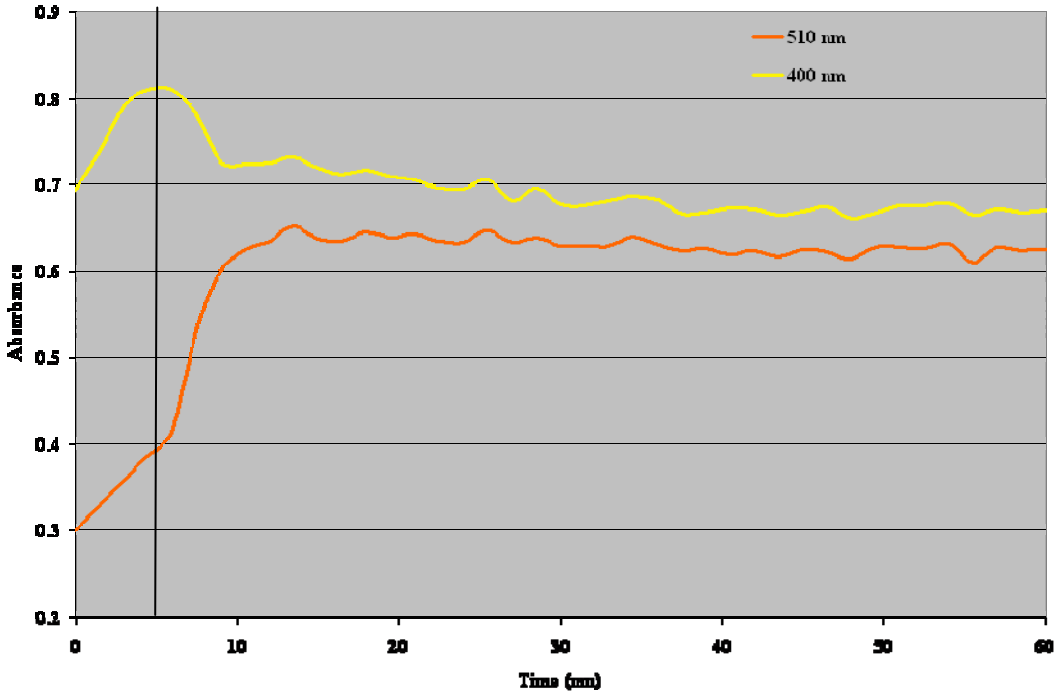

Figure 3.20 – The UV-Vis diffuse reflectance spectra of the $[Cu(MeCN)_4]BF_4$ and 4,4'-dipyripyl solid-solid reaction forming **3.1**. The graph plots UV-Vis absorbance vs. time at 510 nm and 400 nm. 400 nm is representative of the yellow transition stage and 510 nm for $\{[Cu(4,4'dipyridyl)_2]BF_4\}_n$. n = 2.

The GC-MSD analysis was problematic due to the speed at which the reactions occur, and the possibility of supressing the reaction. A normal run took 12 min by that time the reaction had gone to completion. The normal result was an initial relatively low TIC followed by a jump in the TIC value by which time the mixture is orange, indicating the three-dimensional product (Figures 3.21, 3.22, and 3.23). The TIC value remains consistent for each following sample taken. The overall increase in MeCN vapor shows that the reaction is similar to the results for Chapter 2, where the MeCN vapor reaches saturation.

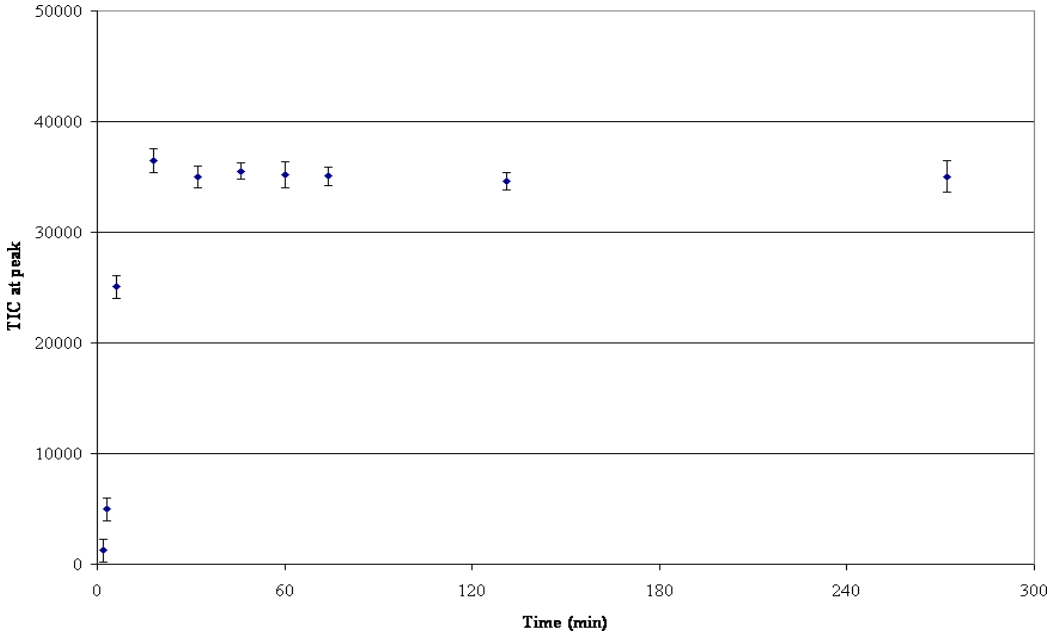

Figure 3.21 – GC-MSD headspace MeCN vapor analysis during the formation of $\{[Cu(4,4'dipyridyl)_2]BF_4\}_n$, **3.1**, formation. Three runs were taken in 15-min increments for each. n = 3 and a standard error of the estimate of ±109.

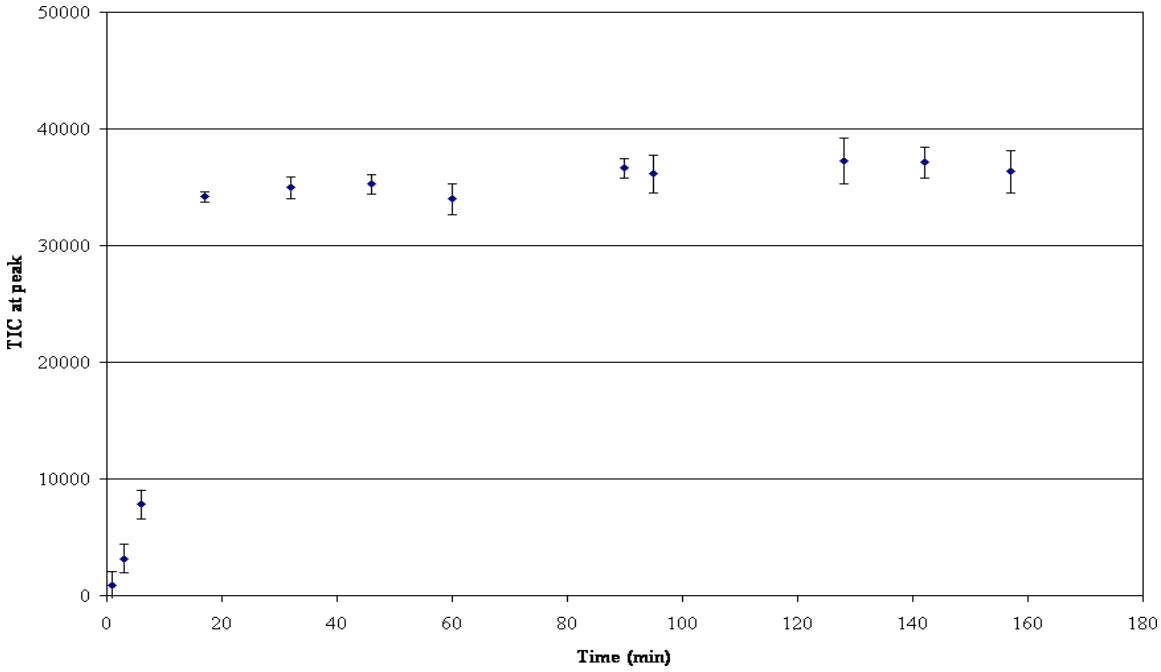

Figure 3.22 – GC-MSD headspace MeCN vapor analysis during the formation of $\{[Cu(4,4'dipyridyl)_2]PF_6\}_n$, **3.2**, formation. Three runs were taken in 15-min increments for each. n = 3 and standard error of the estimate of ±43.

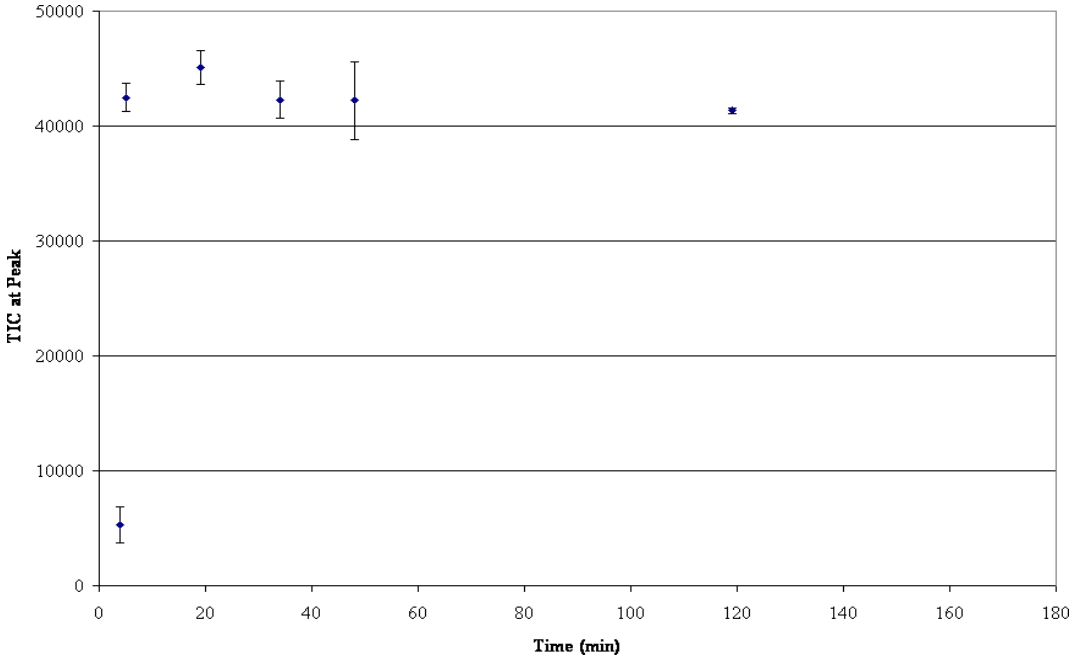

Figure 3.23 – GC-MSD headspace MeCN vapor analysis during the formation of $\{[Cu(4,4'dipyridyl)_2]SO_3CF_3\}_n$, **3.3**, formation. Three runs were taken in 15-minute increments for each. The legend indicates each run by shape and color. n = 3 and a standard error of the estimate of ±218.

When an equimolar ratio was used, the amount of acetonitrile parent ion attains a maximum value and then decreases to an elevated baseline (Figures 3.24 and 3.25). A possibility for this decrease of acetonitrile vapor could be the vapor is being recoordinated to the copper therefore removing it from the headspace. Based on the solution chemistry, this is probably not the case in which an orange powder is produced in abundance. The more likely explanation is that the mixture could be indeed absorbing the acetonitrile vapor. Because there is a decrease in acetonitrile vapor concentration, more research is being conducted, as the material might be a good candidate for gas storage.

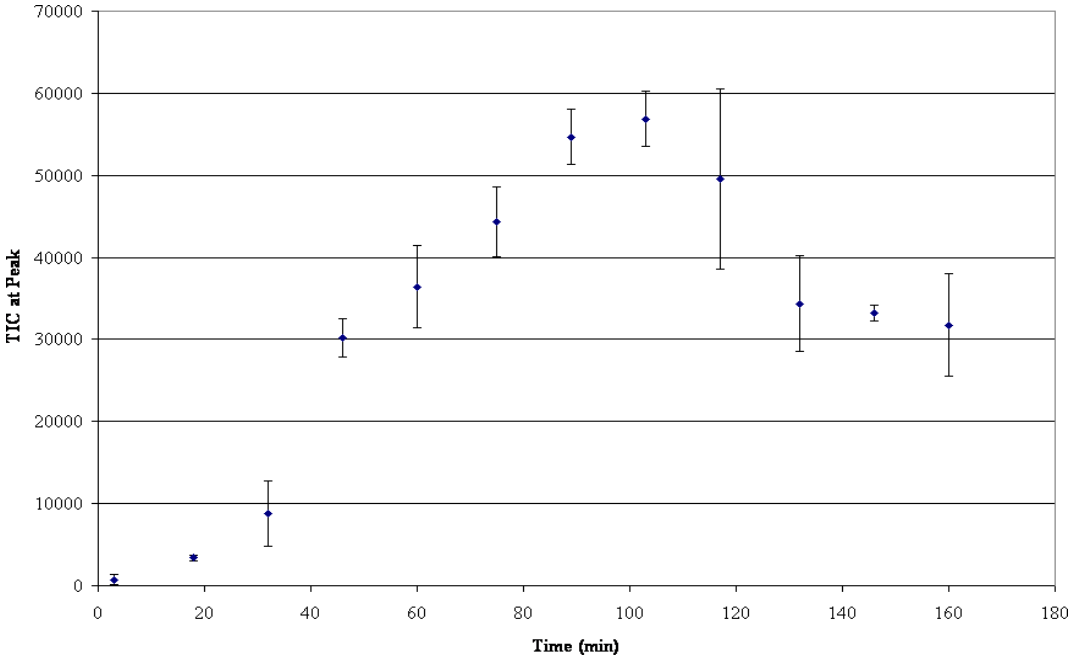

Figure 3.24 – GC-MSD analysis of an equimolar reaction between $\{[Cu(MeCN)_4]SO_3CF_3\}_n$ and 4,4'-dipyridyl. n = 3 and a standard error of the estimate of ±42.

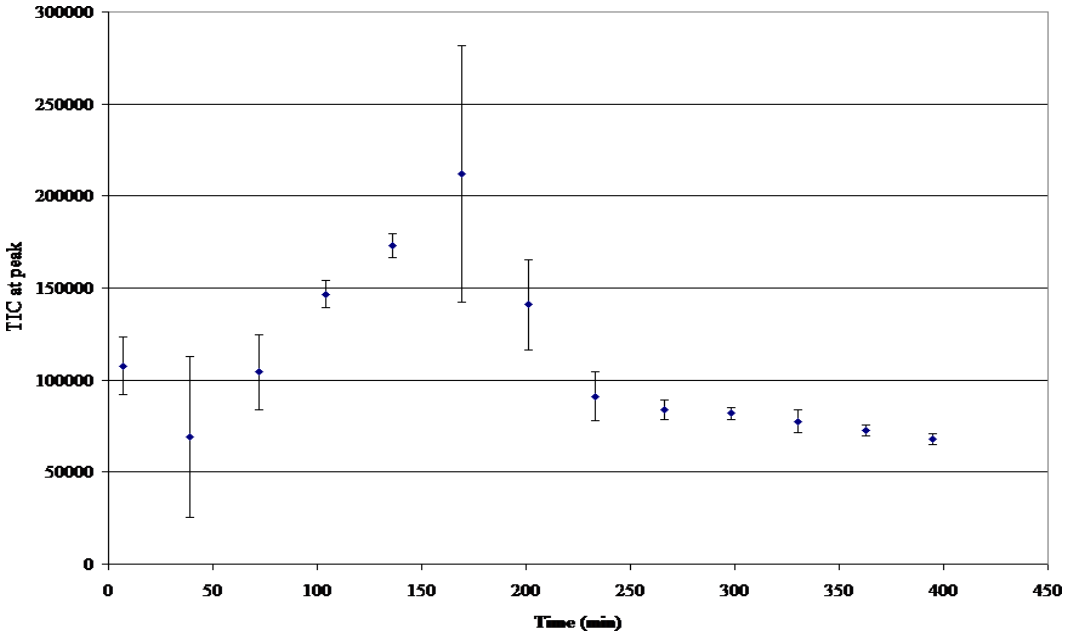

Figure 3.25 – GC-MSD analysis of an equimolar reaction between $[Cu(MeCN)_4]BF_4$ and 4,4'-dipyridyl. The lone point at around 300000 TIC indicates a MeCN vapor spike right before the decrease. The point is also why the error bar is large at that point. n = 3 and a standard error of the estimate of ±265.

Identification of the Yellow Species

The identity of the yellow species was required in order to better understand the mechanism of the solid-solid reactions that produce $\{[Cu(4,4'\text{-dipyridyl})_2]X\}_n$ ($X = BF_4^-$, PF_6^-, or $SO_3CF_3^-$). Unfortunately due to the speed of the reaction in an environment that is saturated with MeCN vapor, the PXRD diffraction monitoring study used with the 4,7-phenanthroline cases could not performed. The yellow species was able to be isolated by grinding together equimolar amounts of $[Cu(MeCN)_4]BF_4$ and 4,4'-dipyridyl. The reaction is suppressed with argon gas by flowing the gas across the top of the mixture thereby removing any acetonitrile vapor that had been released or is going to be released. When acetonitrile liquid is added to this yellow mixture the powder changes to orange indicating the formation of $\{[Cu(4,4'\text{-dipyridyl})_2]BF_4\}_n$.

The yellow species was found to be the one-dimensional linear chain that had been reported previously. The calculated PXRD pattern from the single crystal data for $\{[Cu(4,4'\text{-dipyridyl})(MeCN)_2]BF_4\}_n$ closely matches the yellow product's PXRD pattern (Figure 3.26). This could possibly be the intermediate that is formed before the diamonoid structure. Even though an equimolar ratio was used to isolate the yellow species, there could be local 1:1 stoichiometry with the 2:1 molar ratio reactions, 4,4'-dipyridyl to $\{[Cu(4,4'\text{-dipyridyl})_2]X\}_n$ ($X = BF_4^-$, PF_6^-, or $SO_3CF_3^-$), used for the UV-Vis experiments.

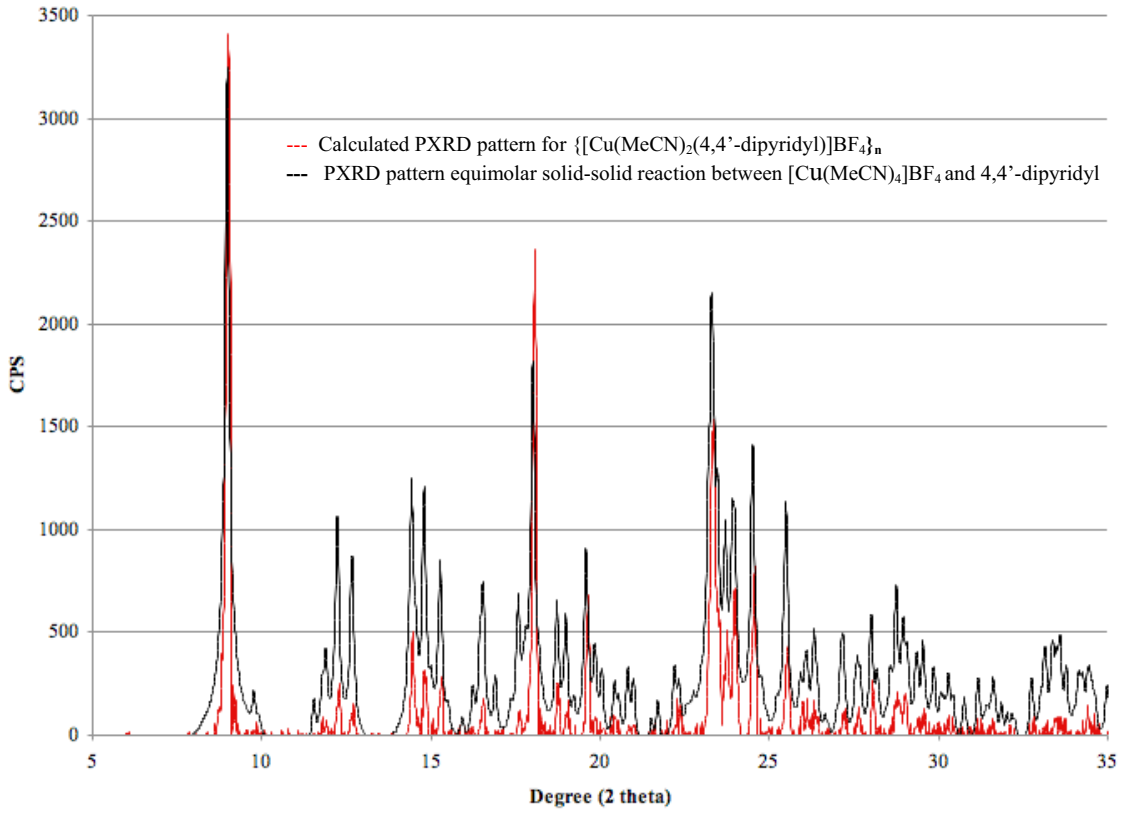

Figure 3.26 – Comparison between the calculated PXRD pattern of $\{[Cu(4,4'\text{-dipyridyl})(MeCN)_2]BF_4\}_n$ and the experimental PXRD pattern for the yellow product of an equimolar solid-solid reaction between $[Cu(MeCN)_4]BF_4$ and 4,4'-dipyridyl.

3.4 Conclusion

This research has shown that the solid-solid reaction progression for 4,4'-dipyridyl is similar to 4,7-phenanthroline in that there is a distinct change in the amount of MeCN vapor headspace concentration over a relatively short time span. The similarity of the reactions suggests that these reactions also need MeCN vapor to condense for the reaction to progress due to the increase in diffusion.

Indication of the reaction progression can easily be seen by UV-Vis spectrophotometry where there is a quick absorbance change at certain wavelengths. Unlike the previously mentioned situation in Chapter 2, the reactions consist of two steps

The first compound produced is a yellow intermediate followed by the orange four-fold three-dimensional network. The refinement of the crystal structures for $\{[Cu(4,4'\text{-dipyridyl})_2]BF_4\}_n$ and $\{[Cu(4,4'\text{-dipyridyl})_2]SO_3CF_3\}_n$ show that the network psuedomorphs with only the anion located in the cavity being different.

The ability to produce three-dimensional coordination networks shows that these solid-solid reactions can be generalized past the simple one-dimensional 4,7-phenanthroline chains described in Chapter 2. Research on the solid-solid reactions with 4,4'-dipyridyl discussed can still be expanded to solidify the yellow intermediates' identities. If the yellow product can be obtained with good purity through these solid-solid reactions then other products are obtainable.

References

(1) Biradha, K.; Sarkar, M.; Rajput, L. *Chem. Commun* **2006**, 4169-4179.

(2) Carlucci, L.; Ciani, G.; Proserpio, D. M.; Sironi, A. *J. Chem. Soc. Dalton Trans* **1997**, *11,* 1801-1804.

(3) Tong, M. L.; Lee, H. K.; Chen, X. M.; Huang, R. B.; Mak, T. C. W. *J. Chem. Soc. Dalton Trans.* **1999**, *21,* 3657-3659.

(4) Park, H. W.; Sung, S. M.; Min, K. S.; Bang, H.; Suh, M. P. *Eur. J. Inorg. Chem.* **2001**, *11*, 2857-2863.

(5) Lin, X. J.; Shen, Z.; Li, Y. Z.; Uno, H.; Song, Y.; Xu, H. J.; You, X. Z. *J. Coord. Chem.* **2005**, *58*, 1139-1144.

(6) Batsanov, A. S.; Begley, M. J.; Hubberstey, P.; Stroud, J. *J. Chem. Soc. Dalton Trans.* **1996**, *9* , 1947-1957.

(7) Lu, C. Z.; Chuan-De Wu, H. H. Z.; Huang, J. S. *Chem. Mater.* **2002**, *14*, 2649-2655.

(8) Cussen, E. J.; Claridge, J. B.; Rosseinsky, M. J.; Kepert, C. J. *J. Am. Chem. Soc.* **2002**, *124*, 9574-9581.

(9) Fletcher, A. J.; Cussen, E. J.; Bradshaw, D.; Rosseinsky, M. J.; Thomas, K. M. *J. Am. Chem. Soc.* **2004**, *126*, 9750-9759.

(10) Wagner, B. D.; McManus, G. J.; Moulton, B.; Zaworotko, M. J. *Chem. Commun* **2002**, *18,* 2176-2177.

(11) Noro, S.; Kitaura, R.; Kondo, M.; Kitagawa, S.; Ishii, T.; Matsuzaka, H.; Yamashita, M.; *J. Am. Chem.* **2002**, *124*, 2568-2583.

(12) Lu, J.; Paliwala, T.; Lim, S. C.; Yu, C.; Niu, T.; Jacobson, A. J. *Inorg. Chem* **1997**, *36*, 923-929.

(13) Gable, R. W.; Hoskins, B. F.; Robson, R. *J. Chem. Soc., Chem. Commun.* **1990**, *23*, 1677-1678.

(14) Fujita, M.; Kwon, Y. J.; Washizu, S.; Ogura, K. *J. Am. Chem. Soc.* **1994**, *116*, 1151-1152.

(15) Tong, M. L.; Ye, B. H.; Cai, J. W.; Chen, X. M.; Ng, S. W. *Inorg. Chem.* **1998**, *37*, 2645-2650.

(16) Yaghi, O. M.; Li, H.; Groy, T. L. *Inorg. Chem.* **1997**, *36*, 4292-4293.

(17) Khaorapapong, N.; Kuroda, K.; Hashizume, H.; Ogawa, M. *Appl. Clay Sci.* **2001**, *19*, 69-76.

(18) Noro, S.; Kitaura, R.; Kondo, M.; Kitagawa, S.; Ishii, T.; Matsuzaka, H.; Yamashita, M. *J. Am. Chem. Soc.* **2002**, *124*, 2568-2583.

(19) MacGillivray, L. R.; Subramanian, S.; Zaworotko, M. J. *J. Chem. Soc. Chem. Commun.* **1994**, *11*, 1325-1326.

(20) Carlucci, L.; Ciani, G.; Proserpio, D. M.; Sironi, A. *J. Chem. Soc. Chem. Commun.* **1994**, *21,* 2755-2756.

(21) Zaworotko, M. J. *Chem. Soc. Rev.* **1994**, *23*, 283-288.

(22) Werner, P. E.; Eriksson, L.; Westdahl, M. *J. Appl. Crystallogr.* **1985**, *18*, 367-370.

(23) Boultif, A.; Louër, D. *J. Appl. Crystallogr.* **2004**, *37*, 724-731.

(24) Yvon, K.; Jeitschko, W.; Parthe, E. *J. Appl. Crystallogr.* **1977**, *10*, 73-74.

(25) Antolasic, F.; Wsearch 32 ed. Melbourne, Victoria, Australia, 2005, p Mass Spec analysis tool.

(26) Bruker Analytical X-ray: 1997.

(27) Sheldrick, G. M.; University of Gottingen, Germany: 1997.

(28) Barbour, L.; University of Missouri-Columbia, Columbia, MO, 2001.

(29) Orpen, A.; Brammer, L.; Allen, F.; Kennard, O.; Watson, D.; Taylor, R. *J. Chem. Soc. Dalton Trans.* **1989**, S1-S83.

Chapter 4

Solid-Solid Reactions between $[Cu(MeCN)_4]BF_4$ and 1,3-dithiane or *trans*-1,2-Bis(4-pyridyl)ethylene

4.1 Introduction

We have used other bridging ligands in order to expand the knowledge base of coordination networks that mimic silicate structures. In this realm, two of the more notable ligands are 1,3-dithiane and *trans*-1,2-bis(4-pyridyl)ethylene (BPE). Both of these ligands have been used by the Keller group and others to fashion coordination networks via solution-based chemistry.[1,2] Both of the aforementioned ligands were used in solid-solid reactions with $[Cu(MeCN)_4]X$ ($X = BF_4^-$, PF_6^-, and $SO_3CF_3^-$) using the same grinding techniques as described in Chapters 2 and 3.

1,3-dithiane was used by the Keller group because of its close resemblance to pyrimidine. As illustrated in Chapter 1, pyrimidine produced a feldspar mimic in addition to other coordination networks. The ligands' molecular structure differ, with 1,3-dithiane containing sulfur atoms at the 1 and 3 positions of the cyclic rings (Figure 4.1). In pyrimidine, nitrogen atoms are located at the 1 and 3 positions and the ligand is aromatic. Pyrimidine's molecular structure allows only one bonding conformation due in part to the nitrogen atom's one unbounded electron pair. Compare this to the eight bonding conformations for 1,3-dithiane from the two electron pairs on each sulfur atom available for bonding, which leads to a larger variety of structural possibilities (Figure 4.2).

pyrimidine 1,3-dithiane

Figure 4.1 – Comparison of the molecular structure of pyrimidine and 1,3-dithiane.

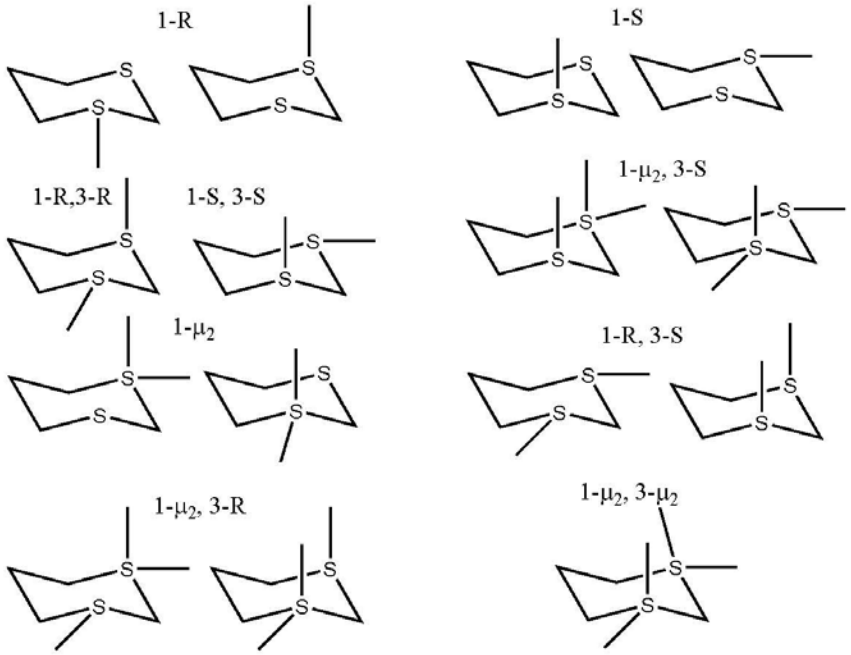

Figure 4.2 – Possible bonding modes of 1,3-dithiane in the chair conformation. This gives 1,3-dithiane a possibility of eight bonding conformations.

The solution based synthesis used molar ratios ranging from 1:1 to 10:1 for 1,3-dithiane:$[Cu(MeCN)_4]BF_4$, however only two of the eight bonding configurations possible were recovered in single crystal form (Figures 4.3, 4.4, and 4.5).[1] Like the reaction with 4,7-phenanathroline and $[Cu(MeCN)_4]BF_4$, the products from equimolar ratio between $[Cu(MeCN)_4]BF_4$ and 1,3-dithiane are one-dimensional chains.

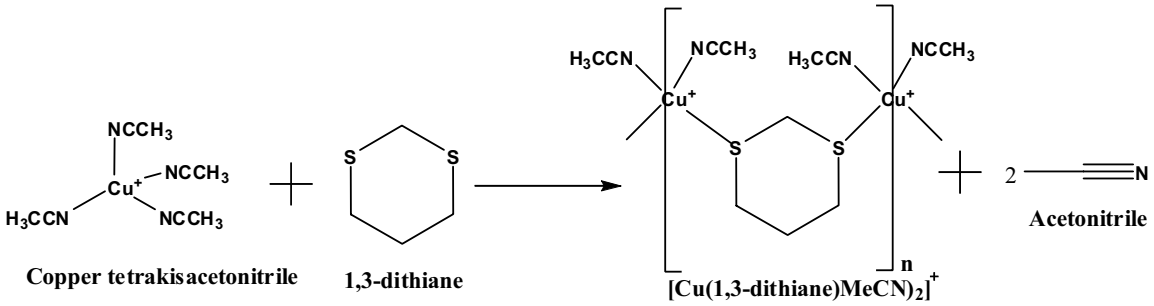

Figure 4.3 – The reaction between 1,3-dithiane and $[Cu(MeCN)_4]BF_4$ to produce one-dimensional chains.

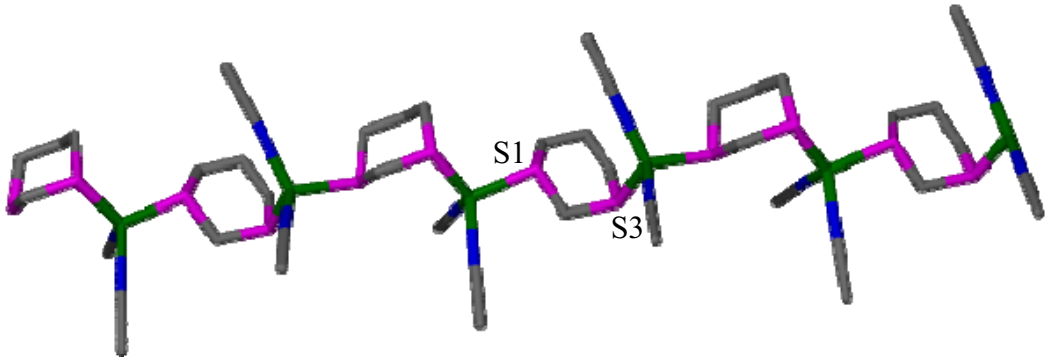

Figure 4.4 – The main chain configuration formed with solution-based chemistry. The stereochemistry around the sulfur is 1-R and 3-R.[1]

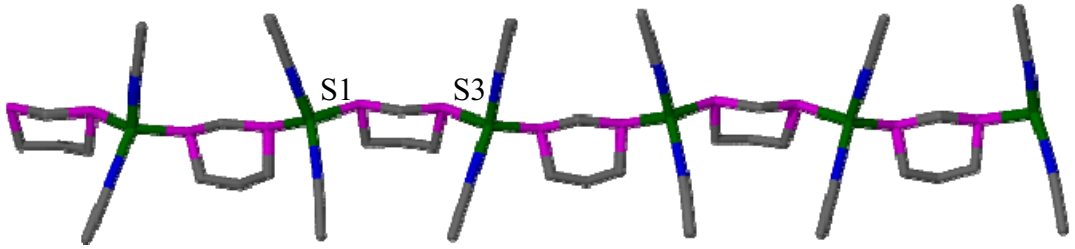

Figure 4.5 – The minor product from the solution-based chemistry in which stereochemistry around the sulfur is 1-R and 3-S. [1]

In addition to the structural comparison between the solution-based versus solid-solid reaction products, a reaction rate comparison between BPE and 4,4'-dipyridyl was performed, due to the ligands' closely related molecular structures (Figure 4.6). Both ligands have nitrogen atoms located at the para position on the pyridyl rings. The BPE

has a longer distance between the nitrogen atoms due to the ethylene linker between the pyridyl rings. The effect of elongating the linker was studied to find out if the solid-solid reaction rate changes when compared to the 4,4'-dipyridyl system.

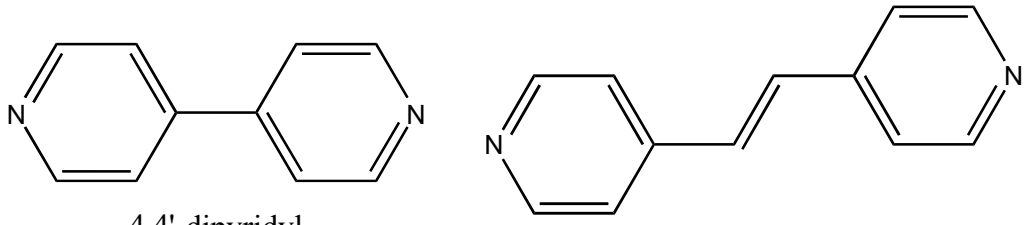

4,4'-dipyridyl

trans-1,2-bis(4-pyridyl)ethylene

Figure 4.6 – Molecular structure comparison between 4,4'-dipyridyl and BPE. BPE is elongated due to the ethylene extension between the pyridine rings.

A previously reported structure of a copper(I)-BPE reaction product was a coordination network similar to the 4,4'-dipyridyl network discussed in Chapter 3. Instead of a four-fold interpenetrating network, a five-fold network was formed (Figure 4.7).[4] Like $\{[Cu(4,4'\text{-dipyridyl})_2]BF_4\}_n$, in the BPE coordination network the BF_4^- anions are located in the cavity, with the addition of free acetonitrile molecules (Figure 4.8). The free acetonitrile was not present in the 4,4'-dipyridyl coordination network, possibly due to the extra cavity space found in $\{[Cu(BPE)_2]BF_4 \bullet MeCN\}_n$ caused by BPE's elongation between pyridine rings.

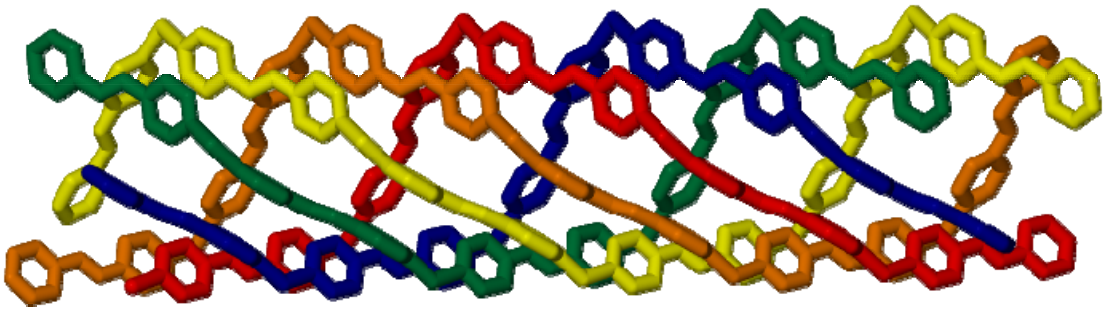

Figure 4.7 – The side on cavity view showing the five interpenetrating networks each in a different color. The hydrogen atoms, anions, and free solvent molecules have been removed for clarity.

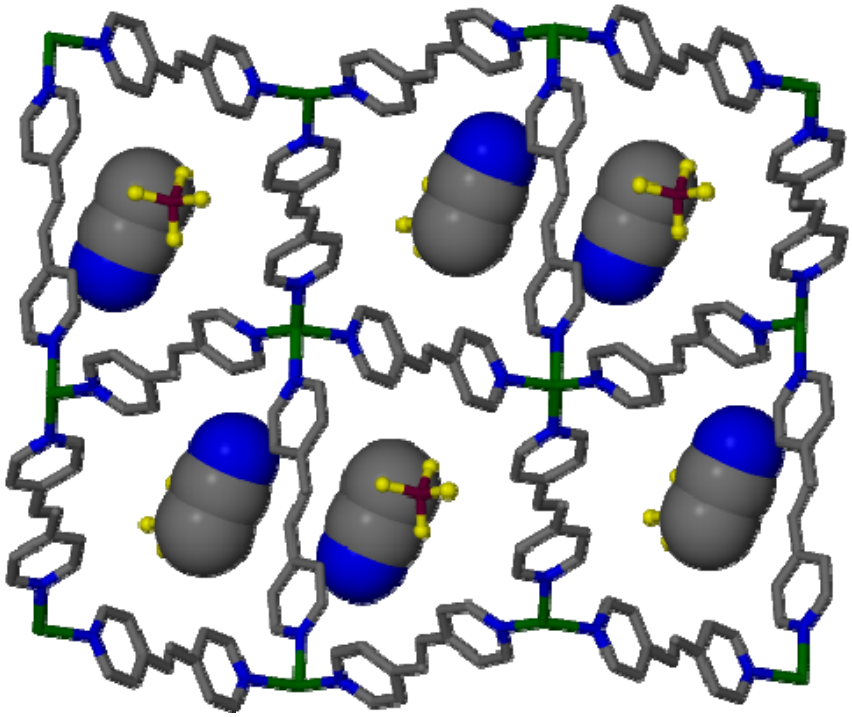

Figure 4.8 – The view down the cavities in which the BF_4^- anions and free acetonitrile molecules reside. The BF_4^- anion is represented in ball-and-stick and the acetonitrile molecule is in space filling forms.

We have reported BPE structures in which the solvent choice changed the dimensionality of the networks produced.[2] In one case, chloroform was used in the synthesis producing a linear coordination network. When chloroform was changed to

dichloromethane a layered polymer formed. The structural dependence on the solvent conditions is of interest since this research covers solid-solid reactions. The lack of an outside solvent (a solvent not produced by one of the reagents during the reaction) leads to the possibility of a different structure forming. However in both of those cases, each copper(I) cation was coordinated by two terminal triphenylphosphine molecules, which prevented more than two BPE molecules from coordinating to the copper(I) cation.

4.2 Experimental

Materials and Methods

Copper(I) oxide (Fisher), tetrafluoroboric acid (Aldrich), hexafluorophosphoric acid (Aldrich), trifluoromethanesulfonic acid (Aldrich), 1,3-dithiane (Aldrich), BPE (Aldrich), acetonitrile (Fisher), and diethyl ether (Fisher) were used without further purification unless otherwise noted in the synthesis. Starting materials **2.1, 2.2,** and **2.3** were synthesized as described in Chapter 2.

Powder X-ray diffraction (PXRD) patterns were collected using a Scintag X2 system at 40 kV and 30 mA for Cu K_α radiation (λ = 1.540562 Å). Continuous scans were taken at 0.60° per min from 5° to 37° 2θ, unless otherwise noted. All patterns were indexed via Treor 90[5] or DICVOL[6] software programs. Single crystal X-ray diffraction (XRD) data of previously solved structures were used in conjunction with LAZY-PULVERIX[7] to generate the calculated powder pattern used for comparison.

UV-Visible (UV-Vis) spectra were recorded using a Cary 3 (Varian, Melrose, Australia) with a diffuse reflectance attachment. The home-built sample holder used a polyethylene gasket with a rubber core between two 40 mm diameter optically inactive

fused silica discs. A Teflon sheet was then inserted to serve as a neutral backing. In order to provide a gas-tight seal the assembly was clamped together via four bolts. Each run was limited to 350-800 nm as a result of the noise beyond those wavelengths. A schematic of the sample holder can be seen in Chapter 2 (Figure 2.8).

Elemental analysis was performed by Desert Analytics Transwest Geochem (Phoenix, AZ). Samples were transferred under nitrogen. The researchers did not observe changes in the color or texture of the samples before or after analysis.

Synthesis of Reaction Products

***catena*-poly[[diacetonitrilecopper(I)-μ-(1,3-dithiane)] tetrafluoroborate], 4.1, ($\{[Cu(1,3\text{-dithiane})(MeCN)_2]BF_4\}_n$)**

With a mortar and pestle, $[Cu(MeCN)_4]BF_4$ (157 mg, 0.5 mmol) was gently ground with 1,3-dithiane (60 mg, 0.5 mmol) for approximately 30 sec until the mixture was of homogeneous particle consistency. The mixture was then placed in a 4 mL vial, sealed with parafilm, and capped. A week later the mixture was analyzed via PXRD.

$[Cu(MeCN)_4]BF_4$ and *trans*-1,2-*bis*(4-pyridyl)ethylene, 4.2

With a mortar and pestle, $[Cu(MeCN)_4]BF_4$ (186 mg, 0.5 mmol) was gently ground with BPE (91 mg, 0.5 mmol) for approximately 30 sec until the mixture was of homogeneous off-white color. The mixture was then placed in a 4 mL vial, sealed with parafilm, and capped. Upon later inspection the off-white color changed to an orange, followed by a slow enveloping encroachment of red. The red product was analyzed by PXRD. Elemental analysis calculated (found) for $CuC_{16}N_4H_{14}BF_4$: C, 46.53 (45.451); H,

3.420 (3.350); N 13.58 (12.34). The chemical formula used for elemental analysis was one in which the copper was coordinated by two BPE molecules and two MeCN molecules.

4.3 Results and Discussion

Structural Determination

The PXRD patterns for the solid-solid reaction product between $[Cu(MeCN)_4]BF_4$ and 1,3-dithiane, **4.1,** matched the calculated PXRD pattern for the major solution-based product, $\{[Cu(MeCN)_2(1,3\text{-dithiane})]BF_4\}_n$ when taking into account thermal expansion and preferred orientation (Figure 4.9). The structure is one in which each copper(I) cation is coordinated by two acetonitrile molecules and two bridging 1,3-dithianes molecules, with stereochemistry S(1)-R and S(3)-R. Interestingly, the only structure present based on the PXRD pattern for the solid-solid reaction product was the major product found in the solution based chemistry. The result of a single structure suggests that solid-solid reactions could be used as a way of eliminating side products.

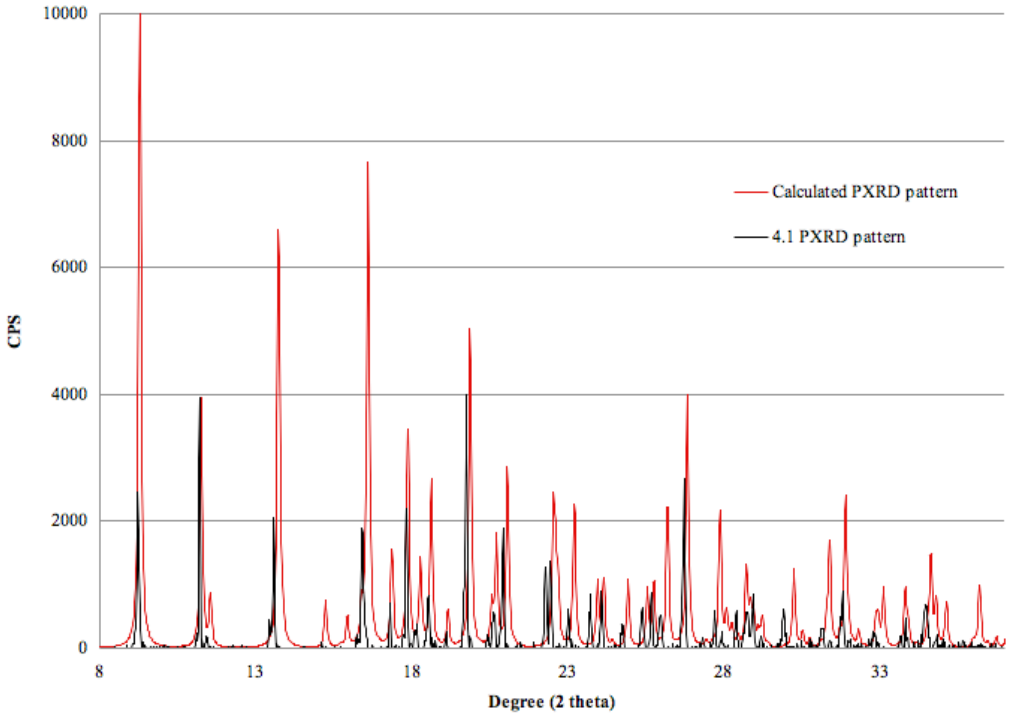

Figure 4.9 – Comparison between the experimental PXRD pattern of **4.1** and calculated PXRD pattern for the S(1)-R and S(3)-R configuration of $\{[Cu(1,3\text{-dithiane})(MeCN)_2]BF_4\}_n$.

The PXRD pattern for the solid-solid reaction product between $[Cu(MeCN)_4]BF_4$ and BPE, **4.2**, did not match the calculated PXRD pattern for the possible structure described in the introduction (Figure 4.10). This is somewhat surprising because the known crystal structure is similar to that of the 4,4'-dipyridyl product containing a three-dimensional coordination network. Both structures contain the BF_4^- anion located in the cavity formed from four or five interpenetrating networks. The BPE three-dimensional coordination network analog however, contains non-coordinated acetonitrile molecules. Even though the structure is not the same for the solid-solid reaction, it is still highly likely that the copper(I) is still coordinated to three or four BPE molecules because of the product's red color. Based on previous results, when looking at the same aromatic

ligand, the more of those ligands coordinated to the copper(I) cation the higher the wavelength for the visible absorption band.

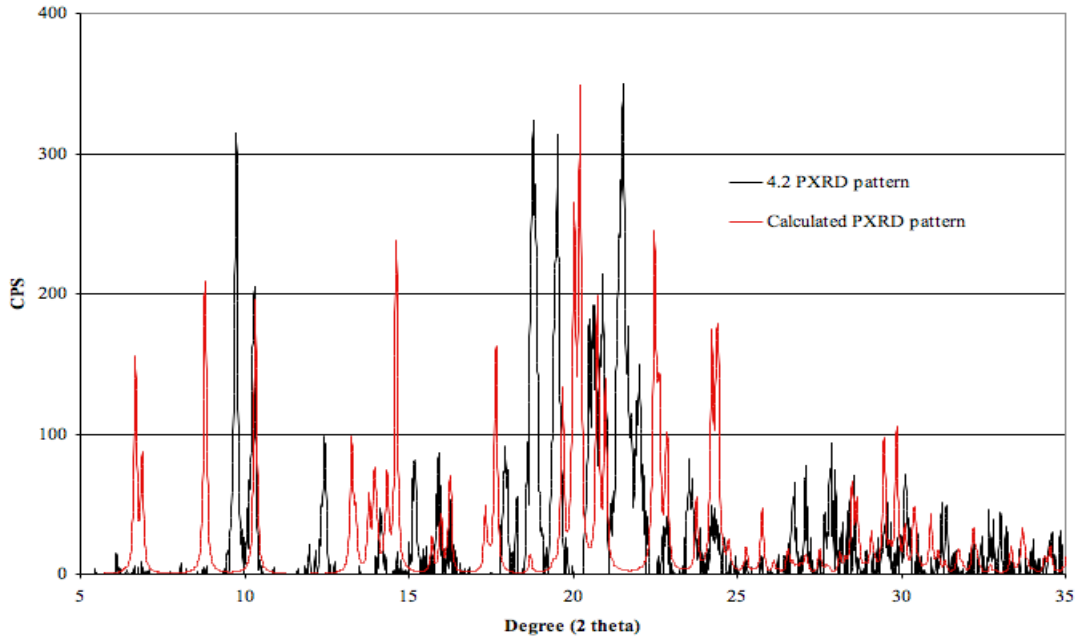

Figure 4.10 – Comparison between the **4.2** PXRD pattern and calculated PXRD pattern for a possible structure, $\{[Cu(BPE)_2]BF_4 \bullet MeCN\}_n$.

Monitoring the Reaction

Only the production of **4.2** from the solid-solid reaction between BPE and $[Cu(MeCN)_4]BF_4$ was monitored via UV-Vis diffuse reflectance because 1,3-dithiane, $[Cu(MeCN)_4]BF_4$, and $\{[Cu(MeCN)_2(1,3\text{-dithiane})]BF_4\}_n$ all absorbed only in the UV region. The Cary 3 UV-Vis was only able to accurately monitor wavelengths between 350 – 800 nm. Interestingly, the visual color progression for the BPE reaction was similar to that of 4,4'-dipyridyl and $[Cu(MeCN)_4]X$ solid-solid reaction. The difference in color progression is that instead of an off-white to yellow to orange color progression, the BPE solid-solid reaction progresses in color from off-white to orange to ruby red. The first absorbance is around 440 nm and the other at 520 nm for the orange

intermediate and red product respectively (Figure 4.11). The UV-Vis diffuse reflectance results do not show a dramatic absorbance change as was seen with 4,4'-dipyridyl reactions. The constrast of UV-Vis results suggests a different mechanism than the one described in Chapter 3.

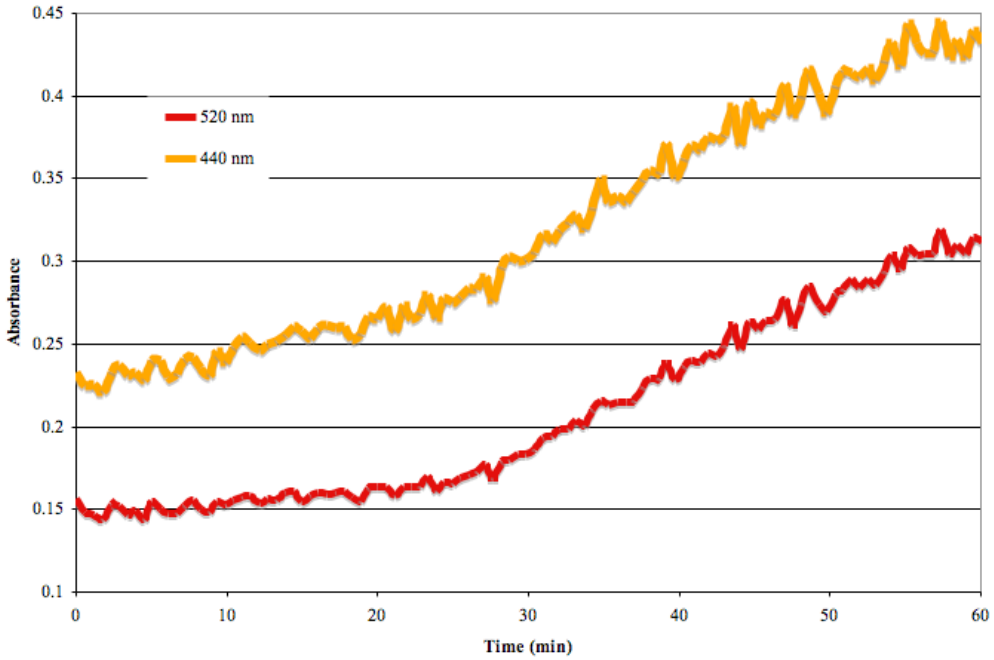

Figure 4.11 – UV-Vis monitoring of the BPE and $[Cu(MeCN)_4]BF_4$ reaction. The 440 nm absorbance represents the orange product and the 520 nm represents the red product.

1,3-dithiane and BPE were also reacted with $[Cu(MeCN)]PF_6$ and $[Cu(MeCN)]SO_3CF_3$ in the solid state. Not surprisingly, the reactions proceeded however their products were not identifiable. This reactivity is based on color and/or difference in PXRD pattern as compared to the starting material. The solid-solid reaction with 1,3-dithiane or BPE and tetraacetonitrilecopper(I) salts further supports the generality of solid-solid reactions.

4.4 Conclusion

The solid-solid reaction of BPE and $[Cu(MeCN)_4]BF_4$ produced a different structure than the previously reported solution product. It is likely that the structure produced via the solid-solid reaction has copper(I) cations that are coordinated to three or four BPE molecules based on the red color of the product. The mechanism of the reaction based on UV-Vis diffuse reflectance is possibly different to that of those discussed in Chapter 3 for 4,4'-dipyridyl.

1,3-dithiane provided additional insight into how the solid-solid reactions compare to the solution-based ones. Quite possibly only one of the solution-based products was formed, therefore eliminating the need for further purification other than removal of excess starting material.

It has been shown that the solid-solid reactions with $[Cu(MeCN)_4]X$ ($X = BF_4^-$, PF_6^-, or $SO_3CF_3^-$) are not limited to nitrogen-contained ligands or ligands of a certain size. This extension shows that these solid-solid reactions can be expanded to a vast range of reactions, therefore providing a green focus to solid-solid reactions used in the development of coordination networks.

References

(1) Knaust, J. M.; Keller, S. W. *Cryst. Eng. Comm.* **2003**, *5*, 459-465.

(2) Knaust, J. M.; Lopez, S.; Keller, S. W. *Inorg Chim. Acta* **2001**, *324*, 81-89.

(3) Lide, D. R. *CRC handbook of chemistry and physics*; 87th ed.; CRC Press: Cleveland, Ohio, 2006-2007.

(4) Batten, S. R.; Harris, A. R.; Jensen, P.; Murray, K. S.; Ziebell, A. *J. Chem. Soc. Dalton Trans.* **2000**, *21*, 3829-3836.

(5) Werner, P. E.; Eriksson, L.; Westdahl, M. *J. Appl. Crystallogr.* **1985**, *18*, 367-370.

(6) Boultif, A.; Louër, D. *J. Appl. Crystallogr.* **2004**, *37*, 724-731.

(7) Yvon, K.; Jeitschko, W.; Parthe, E. *J. Appl. Crystallogr.* **1977**, *10*, 73-74.

Chapter 5

Solid-Solid Reactions with Tetrabenzonitrilecopper(I) Salts

5.1 Introduction

Benzonitrile (BzCN) can be used as a replacement for acetonitrile (MeCN) in the copper(I) salts used as reagents in Chapter 2 and 3.[1] All the acetonitrile molecules have been replaced by benzonitrile molecules in ($[Cu(MeCN)_4]X$, X = BF_4^-, PF_6^-, or $SO_3CF_3^-$). For example, both $[Cu(MeCN)_4]PF_6$ and $[Cu(BzCN)_4]PF_6$ can be made using the same synthesis in which only the nitrile solvent is different. Both reagents are solids under ambient conditions. The molecular variation in benzonitrile is the addition of a phenyl group in place of a methyl group (Figure 5.1).

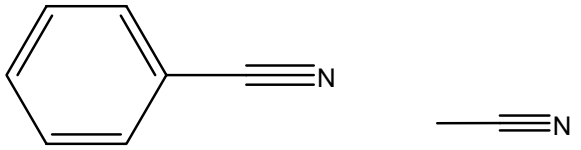

benzonitrile acetonitrile

Figure 5.1 – The molecular structures of benzonitrile and acetonitrile.

The property differences between acetonitrile and benzonitrile are important to note. Both are liquids at room temperature with acetonitrile and benzonitrile having boiling points of 81-82°C and 188-191°C, respectively.[2] The boiling points make acetonitrile and benzonitrile good candidates for comparison in solid-solid reactions. However, their vapor pressures at ambient temperature are 76 mm Hg for acetonitrile and 1 mm Hg for benzonitrile.[3] The vapor pressure difference between the two nitriles is important to consider when monitoring the solid-solid reactions due to the vapor pressure

influencing the headspace vapor concentration.

We have developed coordination networks by using $[Cu(BzCN)_4]BF_4$ or $[Cu(BzCN)_4]PF_6$ with 4,7-phenanthroline and dissolving the reagents in benzonitrile and nitrobenzene and diffusing in tetrahydrofuran.[4] The products formed were $\{[Cu(BzCN)(4,7\text{-phenanthroline})]PF_6\}_n$ or $\{[Cu(BzCN)(4,7\text{-phenanthroline})]BF_4\}_n$, depending on the anion present in the reagent. In both compounds the 4,7-phenanthroline molecules acted as bridging ligands between the copper(I) cations, producing one-dimensional chains. Both products are isostructural with each having two unique copper(I) cations (Figure 5.2).

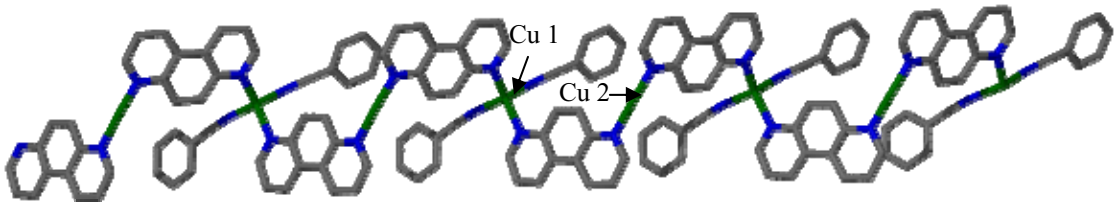

Figure 5.2 – Model of the previously reported structure of $\{[Cu(BzCN)(4,7\text{-phenanthroline})]PF_6\}_n$.[4] The hydrogens and anions are omitted for clarity.

Two benzonitrile molecules and two bridging 4,7-phenanthroline molecules coordinate one copper cation, Cu(1). The other copper cation, Cu(2), is coordinated only by two 4,7-phenanthroline molecules that bridge to the aforementioned copper, Cu(1). These structural results are different from the acetonitrile solution-based analog mentioned in Chapter 2. In the acetronitrile cases each copper cation was four coordinate and the anion influenced the structure. The more important variation for the $\{[Cu(BzCN)(4,7\text{-phenanthroline})]X\}_n$ ($X = BF_4^-$ or PF_6^-) is that the coordination number alternates between the two copper(I) cations. The structural change is due to the bulky phenyl group that is attached and the overall π-π stacking (Figure 5.3).

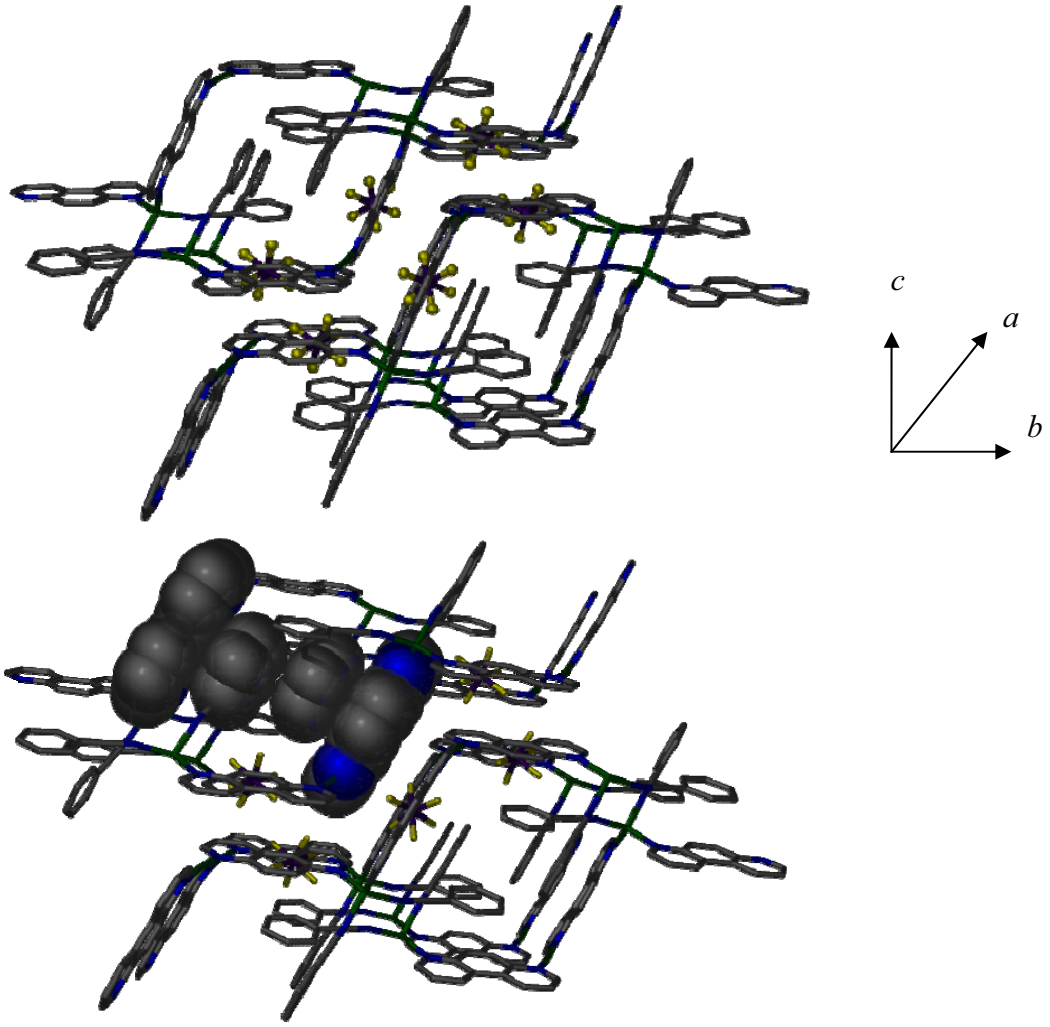

Figure 5.3 – The top picture is one where the one-dimensional chains are viewed side on. Notice how the coppers that are coordinated by only two 4,7-phenanthrolines are in closest contact. The arrangement leads to the π-π ineractions between the chains, pictures on the bottom.[4]

5.2 Experimental

Materials and Methods

Copper(I) oxide (Fisher), tetrafluoroboric acid (Aldrich), hexafluorophosphoric acid (Aldrich), trifluoromethanesulfuric acid (Aldrich), 4,7-phenanthroline (GFS Chemicals and Aldrich), 4,4'-dipyridyl (Aldrich), benzonitrile (Acros), and diethyl ether

(Et_2O)(Fisher) were used without further purification unless otherwise noted in the synthesis. Starting materials **2.1, 2.2,** and **2.3** were synthesized as described in Chapter 2.

Powder X-ray diffraction (PXRD) patterns were collected using a Scintag X2 system at 40 kV and 30 mA for Cu K_α radiation (λ=1.540562 Å). Continuous scans were taken at 0.60° per min from 5° to 37° 2θ, unless otherwise noted. All patterns were indexed via Treor 90[5] or DICVOL[6] software programs. Single crystal X-ray diffraction (XRD) data of previously solved structures were used in conjunction with LAZY-PULVERIX[7] to generate the calculated powder pattern used for comparison.

Gas chromatography mass spectrometry detection (GC-MSD) was performed using an Agilent 6890 (Agilent, San Jose) split-less mode at an oven temperature of 200 °C. A 1-μL gas-tight syringe was used to take 0.2-μL sample size, unless otherwise noted. The samples were taken with an autosampler to ensure the best precision of sample size. Each vial was 2 mL in size and had a Teflon-silicone-Teflon septum. The data were analyzed using WSearch32,[8] where the total ion count (TIC) for the benzonitrile parent ion was taken at the peak of the spectrum.

UV-Visible (UV-Vis) spectra were recorded using a Cary 3 (Varian, Melrose, Australia) with a diffuse reflectance attachment. A home-built sample holder used a polyethylene gasket with a rubber core between two 40 mm diameter optically inactive fused silica discs. A Teflon sheet was then inserted to serve as a neutral backing. In order to provide a gas-tight seal the assembly was clamped together via four bolts. Each run was limited to 350–800 nm as a result of the noise beyond those wavelengths. A schematic of the UV-Vis sample holder can be viewed in Chapter 2 (Figure 2.8).

Elemental analyses were performed by Desert Analytics Transwest Geochem

(Phoenix, AZ). Samples were transferred under nitrogen. The facility researchers did not observe changes in the color or texture of the samples before or after analysis.

Synthesis

The syntheses of $[Cu(BzCN)_4]BF_4$, **5.1** and $[Cu(BzCN)_4]PF_6$, **5.2** are based on previously reported methods.[4] The new structures created are included in the table of selected crystallographic data.

Tetrabenzonitrilecopper(I) tetrafluoroborate, 5.1, ($[Cu(BzCN)_4]BF_4$)

In a 250 mL Erlenmeyer flask, copper(I) oxide (2.00 g, 13.98 mmol) was added to 80 mL of benzonitrile and stirred to form a slurry. Tetrafluoroboric acid was added in 0.5 mL aliquots until a total volume of 2 mL was added with continuous stirring on a warm hotplate. If the temperature is elevated to a high temperature the benzonitrile liquid will change from clear to transparent tan in color. The warm solution was then filtered gravimetrically, removing any residual particulates. The resulting transparent, light-tan solution was removed from the hotplate and allowed to cool to room temperature. The solution was then added drop-wise into a Schlenk flask containing an argon atmosphere and 300 mL of Et_2O, at which time a clumpy tan precipitate formed. The precipitate was allowed to settle and excess Et_2O was decanted from the flask. Chloroform was added dropwise in order to allow the benzonitrile to be more miscible with the solution. The tan precipitate was broken up with a glass stirring rod into smaller particles and then continuously agitated with a stir bar. The powder was triply washed with Et_2O. The precipitate was then dried under vacuum and moved to a 20 mL

scintillation vial, flushed with argon and stored in a desiccator.

A white powder was isolated during the production of **5.1.** Methanol was then added to 20 mg of the powder until the powder dissolved. Two milliliters of the solution were placed into a 4 mL vial. This vial was then placed in a 20 mL scintillation vial that contained 5 mL of Et_2O. The 20 mL vial was then capped. After about 4 days, the Et_2O had diffused into the inner vial, producing transparent, blocky crystals. The single crystal will be referred to as **5.7.**

Tetrabenzonitrilecopper(I) hexafluorophosphate, 5.2, ($[Cu(BzCN)_4]PF_6$)

In a 250 mL Erlenmeyer flask, copper(I) oxide (2.00 g, 13.98 mmol) was added to 80 mL of BzCN and stirred to form a slurry. Hexafluorophosphoric acid was added in 0.5 mL aliquots until a total volume of 2 mL was added with continuous stirring on a warm hotplate. The hot solution was then filtered gravimetrically, removing any residual particulates. The resulting transparent, light-tan solution was removed from the hotplate and allowed to cool to room temperature. The solution was then added drop-wise into a Schlenk flask under an argon atmosphere and 300 mL of Et_2O, at which time a white precipitate formed. The precipitate was allowed to settle and excess Et_2O was decanted from the flask. The white precipitate was triply washed with Et_2O. The precipitate was then dried under vacuum and moved to a 20 mL scintillation vial, flushed with argon and stored in a desiccator.

Reaction Products

$[Cu(BzCN)_4]BF_4$ and 4,7-phenanthroline, 5.3

With a mortar and pestle, $[Cu(BzCN)_4]BF_4$, **5.1** (157 mg, 0.5 mmol) was gently ground with 4,7-phenanthroline (90 mg, 0.5 mmol) for approximately 30 sec until the mixture was of homogeneous off-white color. The mixture was then placed in a 4 mL vial, sealed with parafilm, and capped. After two days the off-white color changed to a bright yellow. Based upon PXRD a +95% yield was accomplished. Elemental analysis calculated (found) for $C_{26}H_{18}BCuF_4N_4$: C, 58.17 (47.56); H, 3.38 (2.870); N 10.44 (8.64). The reason for the difference in calculated versus found is due to the oxidation of the compound that occurred during transportation to analysis. The occurrence of oxidation of the copper was indicated by the green color of the compound on arrival. The oxidation would cause the decrease in perecent due to the coordination of free oxygen or water.

***catena*-poly[[dibenzoitrilecopper(I)-μ-(4,7-phenanthroline)] hexafluorophosphate], 5.4, ($\{[Cu(4,7\text{-phenanthroline})(BzCN)_2]PF_6\}_n$)**

With a mortar and pestle, $[Cu(BzCN)_4]PF_6$ **5.2** (186 mg, 0.5 mmol) was gently ground with 4,7-phenanthroline (90 mg, 0.5 mmol) for approximately 30 sec until the mixture was of homogeneous off-white color. The mixture was then placed in a 4 mL vial, sealed with parafilm, and capped. After a day, the off-white color changed to a bright yellow. Based upon PXRD a +95% yield was accomplished. Elemental analysis calculated (found) for $C_{26}H_{18}Cu_1F_6N_4P$: C, 52.49 (52.41); H, 3.05 (3.010); N 9.42 (9.61).

5.4 (30 mg) was dissolved in 1 mL of benzonitrile and added to a 4 mL vial. The vial was then put into a 20 mL scintillation vial containing 5 mL of Et_2O. The capped

larger vial allowed for the Et_2O to diffuse into the inner vial. After five days pale-yellow plate-like crystals formed. Elemental analysis calculated (found) for $CuC_{16}N_4H_{14}BF_4$: C, 46.53 (45.451); H, 3.420 (3.350); N 13.58 (12.34). The single crystal will be referred to as **5.8** in order to differentiate from polycrystalline **5.4.**

***net*-{[poly[(4,4'-dipyridyl)copper(I)]-*v*-(4,4'-dipyridyl)$_2$] tetrafluoroborate}, 5.5, ({[Cu(4,4'-dipyridyl)$_2$]BF_4}$_n$)**

With a mortar and pestle, $[Cu(BzCN)_4]BF_4$, **5.1** (281 mg, 0.5 mmol) was gently ground with 4,4'-dipyridyl (156 mg, 1.0 mmol) for approximately 30 sec until the mixture was of homogeneous off-white color. The mixture was then placed in a 4 mL vial, sealed with parafilm, and capped. After a day, the off-white color changed to orange. Elemental analysis calculated (found) for $C_{20}H_{16}BCuF_4N_4$: C, 51.91 (56.6); H, 3.49 (3.740); N 12.11 (12.14). The reason for the higher than expected value for carbon is due to the free benzonitrile that was still present in the product that was not evaporated off properly before analysis.

***net*-{[poly[(4,4'-dipyridyl)copper(I)]-*v*-(4,4'-dipyridyl)$_2$] hexafluorophosphate}, 5.6 ({[Cu(4,4'-dipyridyl)$_2$]PF_6}$_n$)**

With a mortar and pestle, $[Cu(BzCN)_4]PF_6$, **5.2** (310 mg, 0.5 mmol) was gently ground with 4,4'-dipyridyl (156 mg, 1.0 mmol) for approximately 30 sec until the mixture was of homogeneous off-white color. The mixture was then placed in a 4 mL vial, sealed with parafilm, and capped. Within 30 min, the off-white color changed to orange. Elemental analysis calculated (found) for $C_{20}H_{16}CuF_6N_4P$: C, 46.12 (48.35); H,

3.10 (3.150); N 10.76 (10.96).

***net*-{[poly[(4,4'-dipyridyl)copper(I)]-*v*-(4,4'-dipyridyl)] hexafluorophosphate} ([Cu(4,4'-dipyridyl)$_{1.5}$]BF_4), 5.9**

5.1 (281mg, 0.5 mmol) was dissolved in 2 mL of benzonitrile and placed in a medium test tube. 4,4'-dipyridyl (78 mg, 0.5 mmol) was dissolved in 2 mL of water and then layered on top of the benzonitrile solution. Et_2O was then layered on top of the previously mentioned solutions. After three weeks, yellow-orange X-ray quality crystals were obtained from the water-benzonitrile interface. The test tube also contained a large amount of orange precipitate.

Crystal Structure Analysis

Single crystals for XRD were placed in inert oil and selected using an optical microscope. Each crystal chosen uniformly extinguished plane polarized light upon rotation of 90°. The selected crystals were then mounted on thin glass fibers with a small amount of silicone grease. Using a Siemens SMART system (Mo(K_α) = 0.71073 Å) with a charge-coupled area detector, a full hemisphere of crystallographic data was collected. Absorption corrections were applied after integration.[9] All structures were solved using SHELXS Direct Methods[10] and refined using a full least squares treatment on F^2.[11] All non-hydrogen atoms were refined with anisotropic thermal parameters. Crystallographic details for **5.7, 5.8**, and **5.9** are listed in Table 5.1.

The high value of R_{int} for **5.9** was due to the reflections' strength. The data was corrected for absorption in SADABS, R_{int} = 0.0661. However, when the corrected data

was loaded into XPREP for space group determination the R_{int} increased to 0.1821, and no other viable options were found with lower R_{int} values. This difference in R_{int} values is likely due to the fact SADABS uses only strong reflections for absorption correction, while XPREP uses the entire data set to determine the space group. The data set is quite weak (less than 20 reflections above 10,000 counts in SMART), determining R_{int} with a small number of strong reflections will result in a much lower value than determination with an entire data set of weak reflections, which will result in a higher value for R_{int}.

	5.7	**5.8**	**5.9**
Empirical formula	$Cu_2C_{56}H_{40}N_8B_2F_8$	$CuC_{26}H_{18}N_4PF_6$	$Cu_2C_{30}H_{24}N_6B_2F_8$
Formula weight (g/mol)	1125.69	594.95	769.25
Crystal system, space group	Monoclinic, $P2_1/n$	Monoclinic, $P2_1/n$	Monoclinic, C2/c
Temperature (K)	173(2)	173(2)	173(2)
Unit cell dimensions (Å, deg)	a = 17.130(1) b = 17.483(1) c = 18.472(1) β = 100.631(1)	a = 11.955(3) b = 12.226(3) c = 19.785(5) β = 91.628(4)	a = 18.390(2) b = 23.534(3) c = 17.421(2) β = 120.797(2)
Volume ($Å^3$)	5437.5(5)	2452.3(12)	6476.6(12)
Z, ρ calc (g/cm^3)	4, 1.375	4, 1.611	8, 1.5776
Absorption coefficient (mm^{-1})	1.375	1.026	1.391
F(000)	2288	1200	3088
Crystal size (mm)	0.3 × 0.2 × 0.2	0.3 × 0.3 × 0.2	0.3 × 0.3 × 0.1
Θ Range for data collection (deg)	2.53 to 26.53	2.43 to 25.98	2.20 to 24.22
Reflections collected/unique	38488/ 11969 [R_{int}=0.0394]	11685 / 3493 [R_{int}=0.0531]	22883 / 7153 [R_{int}=0.1821]
Max. and min. transmission	0.8477 and 0.3889	0.7203 and 0.3813	0.8734 and 0.4003
Data / restraints / parameters	11969 / 0 / 679	3493 / 0 / 343	7153/0/428
Final R indices [I>2σ(I)] [a,b]	R_1= 0.0447, wR_2=0.1021	R_1= 0.1362, wR_2=0.3298	R_1= 0.1540, wR_2=0.4109
R indices (all data)	R_1= 0.0769, wR_2=0.1157	R_1= 0.1476, wR_2=0.3356	R_1= 0.2844, wR_2=0.4695
Largest diff. peak / hole ($e.A^{-3}$)	1.31 / -1.18	2.14 / - 0.91	5.53/-1.05
GoF on F^2	1.022	1.162	1.316
Structures were refined on F_o^2 using all data. [a] $R = \Sigma(\|F_o\|-\|F_c\|)/\Sigma\|F_o\|$; [b] $wR_2 = [\Sigma(\|F_o\|-\|F_c\|)^2/\Sigma\|F_o\|^2]^{1/2}$			

Table 5.1– Selected crystallographic details for **5.7**, **5.8**, and **5.9.**

5.3 Results and Discussion

Description of the Crystal Structure

A new structure for tetrabenzonitrilecopper(I) tetrafluoroborate was found. The unit cell for **5.7** ($[Cu(BzCN)_4]BF_4$) contains two unique copper centers, each having a distorted tetrahedral arrangement of the coordinated benzonitrile molecules (Figure 5.4). The N-Cu-N angles range from 104.64°-117.45°. This variation is due to the packing of each $[Cu(BzCN)_4^+]$ complexes. The arrangement of two $Cu(BzCN)_4^+$, both containing Cu(1), can be described as mirroring each other (Figure 5.5). In this case the N(1) containing only benzonitrile molecules are pointed away from each other, which leads the Cu(1) cations to be positioned toward one another. The other benzonitrile molecules are rotated to adjust for this layout.

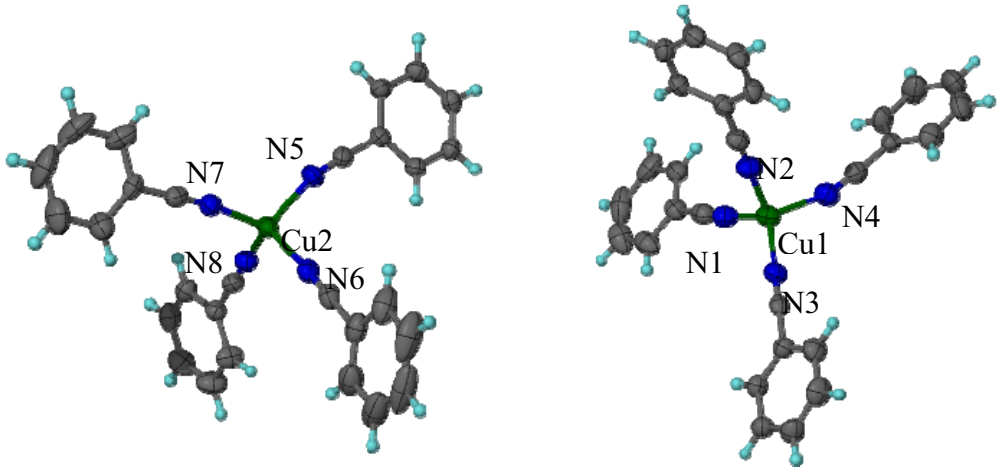

Cu(1)-N(1) 1.984(3)Å	N(1)-Cu(1)-N(2) 108.22(10)°	N(3)-Cu(1)-N(4) 112.37(10)°
Cu(1)-N(2) 2.007(3)Å	N(3)-Cu(1)-N(1) 17.45(10)°	N(3)-Cu(1)-N(2) 106.53(10)°
Cu(1)-N(3) 1.965(2)Å	N(1)-Cu(1)-N(4) 105.80(10)°	N(4)-Cu(1)-N(2) 105.86(11)°
Cu(1)-N(4) 2.006(3)Å		
Cu(2)-N(5) 2.002(2)Å	N(6)-Cu(2)-N(5) 105.75(9)°	N(7)-Cu(2)-N(8) 110.53(9)°
Cu(2)-N(6) 1.993(2)Å	N(7)-Cu(2)-N(5) 116.36(9)°	N(8)-Cu(2)-N(6) 111.24(9)°
Cu(2)-N(7) 1.961(2)Å	N(7)-Cu(2)-N(6) 108.23(9)°	N(8)-Cu(2)-N(5) 104.64(10)°
Cu(2)-N(8) 1.989(2)Å		

Figure 5.4 – Select bond lengths and angles for the **5.7** copper coordination sphere. All non-hydrogen atoms are shown as 50% probability thermal ellipsoids. All bond distances are shorter or within the range of acceptable Cu-N bond lengths, 2.07 ± 0.07, for pyridine.[13]

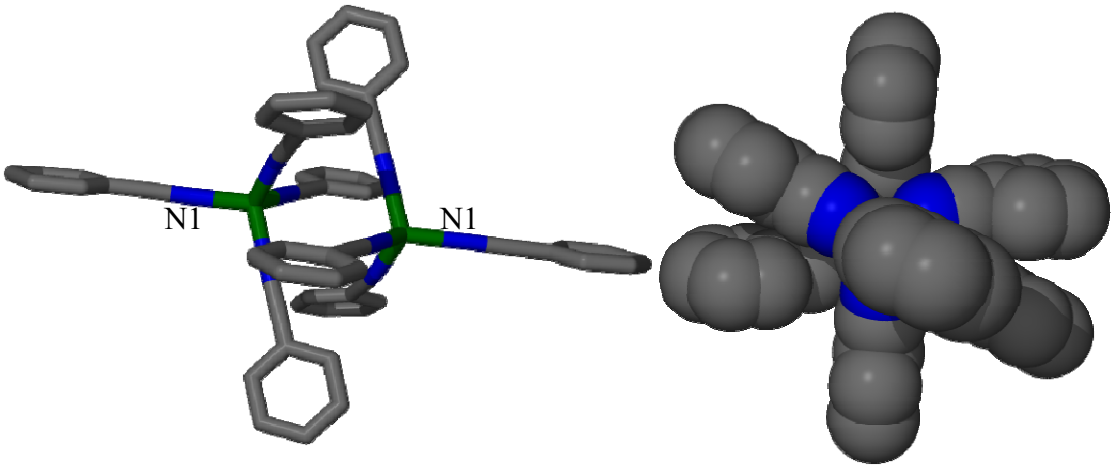

Figure 5.5 – Arrangement of two crystallographically identical $Cu(BzCN)_4^+$ cations in the crystal structure of **5.7**. The image on the left has been rotated 90° to produce the right hand image. The two $Cu(BzCN)_4^+$ cations are related by a two-fold rotation axis.

The previously reported structure for $[Cu(BzCN)_4]BF_4$ has an additional free benzonitrile molecule per each copper(I) (Figure 5.6).[1] This causes a change in the bond angle for $[Cu(BzCN)_4]BF_4$. Although there is no major difference in the N-Cu-N bond angles between the two structures, the tetrahedron for the previously reported structure is somewhat flattened. The flattening can be seen in the C-N-Cu bond angles which are on average closer to 180° for the newly reported structure as compared to the existing structure, 171.9° and 165.8° respectively. The free benzonitrile molecules is indicated by the tinge of tan in the majority of $[Cu(BzCN)_4]BF_4$ starting material, while $[Cu(BzCN)_4]PF_6$ is white, closely resembling the MeCN starting material analog. In addition the $[Cu(BzCN)_4]BF_4$ has a strong benzonitrile odor.

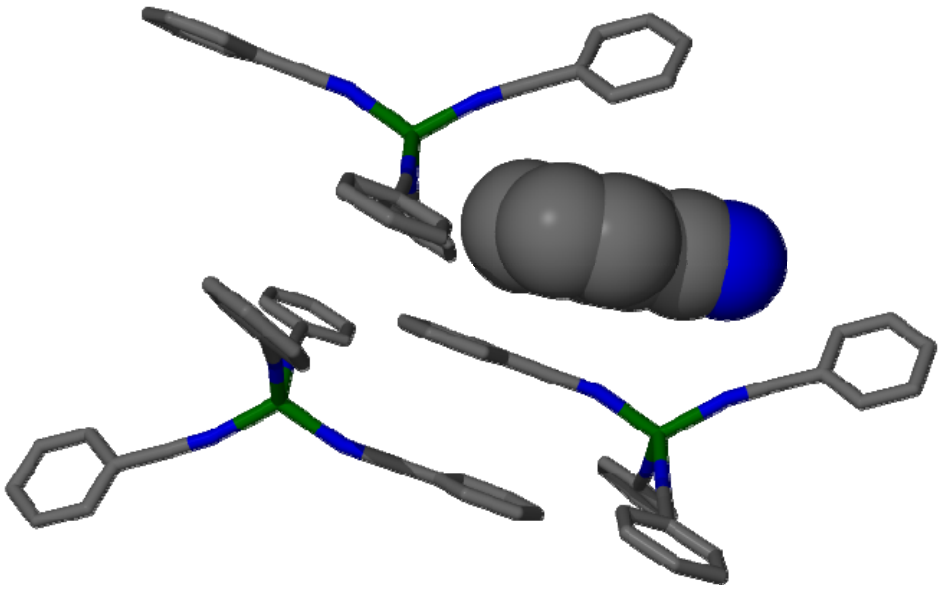

Figure 5.6 – The crystal packing of the previously reported structure for $[Cu(BzCN)_4]BF_4$. The free benzonitrile molecule is indicated with space-filling representation.[1]

Another structure found, was that for $\{[Cu(BzCN)2(4,7\text{-phenathroline})]PF_6\}_n$, **5.8**. The coordination around the only unique copper(I) cation in the **5.8** crystal structure is one in which there are two coordinated benzonitrile molecules and two 4,7-

phenanthroline molecules (Figure 5.7). All of the Cu-N bond lengths are similar, being on average 2.04 Å. The majority of N-Cu-N bond angles are around 103°; the exceptions occur when the nitrogen atoms are a part of the same type of coordinated molecule. For example, the N-Cu-N bond angle between the 4,7-phenanthroline molecules (129.6(5)°) is closer to what would be expected for trigonal planar coordination. In addition, the N-Cu-N bond angle between the two coordinated benzonitrile is 112.8(5)°. These bond angles allow for the π-π stacking of the ligands to continue throughout the structure.

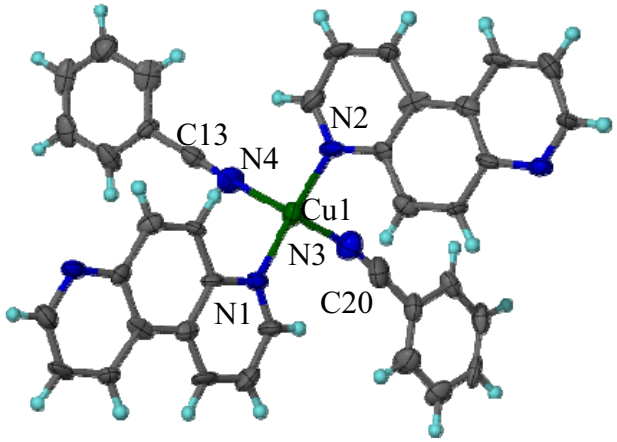

Cu(1)-N(1)	2.05(1)Å	N(4)-Cu(1)-N(3)	112.8(5)°
Cu(1)-N(2)	2.04(1)Å	N(4)-Cu(1)-N(2)	104.5(5)°
Cu(1)-N(3)	2.03(1)Å	N(3)-Cu(1)-N(2)	103.4(5)°
Cu(1)-N(4)	2.03(1)Å	N(4)-Cu(1)-N(1)	103.0(5)°
C(13)-N(4)-Cu(1)	168.2(1)°	N(3)-Cu(1)-N(1)	103.6(5)°
C(20)-N(3)-Cu(1)	166.2(1)°	N(2)-Cu(1)-N(1)	129.6(5)°

Figure 5.7 – Select bond lengths and angles around the copper coordination sphere for **5.8**. All non-hydrogen atoms are shown as 50% probability thermal ellipsoids. All bond distances are within the range of acceptable Cu-N bond lengths, 2.070 ± 0.072, for pyridine.[13]

A chain is formed by 4,7-phenanthroline ligands bridging to neighboring copper cations (Figure 5.8). The orientation of the chain is best described as zigzag, where the 4,7-phenathroline bridges rotate 180º. The structure is different than that previously

reported for {[Cu(4,7-phenanthroline)(BzCN)]PF_6}$_n$.[4] In that case there were two unique copper cations: one copper(I) cation was coordinated by two benzonitrile molecules and two 4,7-phenanthroline molecules and the other copper(I) cation was coordinated only by two 4,7-phenanthroline molecules. The first copper has a similar coordination environment to that of **5.8**. In that case, the larger N-Cu-N bond angles were between the bridging 4,7-phenanthroline molecules (118º) and between the benzonitrile molecules (114º). The N-Cu-N bond angles between different types of ligands is smaller in this case. However, for the copper with only 4,7-phenanthroline molecules attached have a N-Cu-N bond angle of 173°, close to linear. The 4,7-phenanthroline molecules acted as the bridge between the copper(I) cations forming linear chains. Having each of the copper(I) cations coordinated by two benzonitrile molecules has an impact on the structure because it leads to π-π stacking that continue throughout the structure, unlike what is found for the previously reported {[Cu(4,7-phenanthroline)(BzCN)]PF_6}$_n$ structure (Figure 5.9)

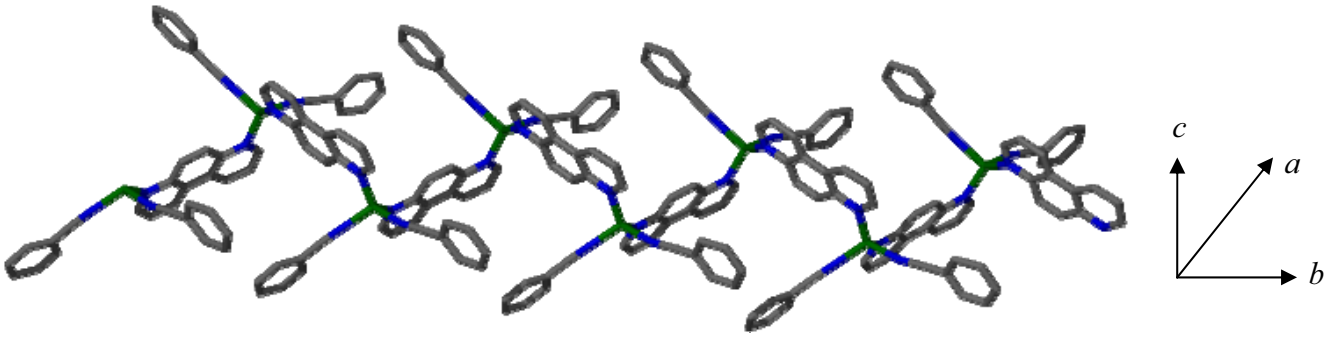

Figure 5.8 – Picture of the one-dimensional linear chains found in **5.8.** From this prospective the 4,7-phenanthroline molecules alternate pointing in and out of the *cb* plane in order to develop a zigzag motif.

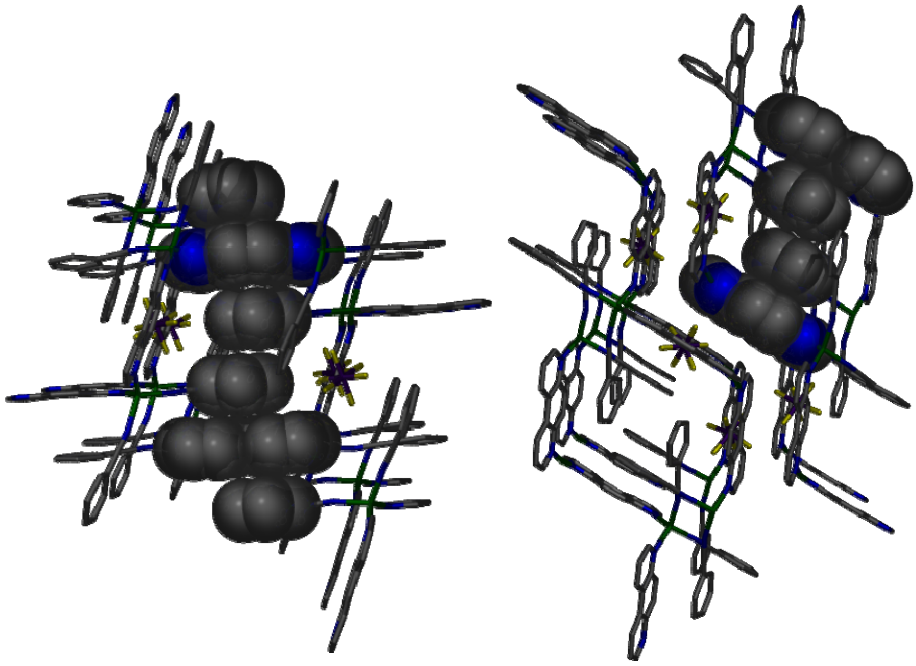

Figure 5.9 – Picture is a comparison of the π-π interaction between the one-dimensional linear chains of $\{[Cu(BzCN)_2(4,7\text{-phenanthroline})]PF_6\}_n$ (left) and $\{[Cu(BzCN)(4,7\text{-phenanthroline})]PF_6\}_n$ (right). The coordination of all the copper cations by two BzCN ligands leads to extended π-π stacking throughout the structure as compared to the isolated π-π stacking for $\{[Cu(BzCN)(4,7\text{-phenanthroline})]PF_6\}_n$.

The similarity between $\{[Cu(4,7\text{-phenanthroline})(BzCN)_2]PF_6\}_n$ and its acetonitrile analog, $\{[Cu(4,7\text{-phenanthroline})(MeCN)_2]PF_6\}_n$, can be seen in Figure 5.10. Besides the coordinated solvents, the only appreciable difference is the orientation of the chains. The structures are close to being mirror images of each other, with the 4,7-phenanthroline molecule's bond on the right hand side going into the page for **5.8**.

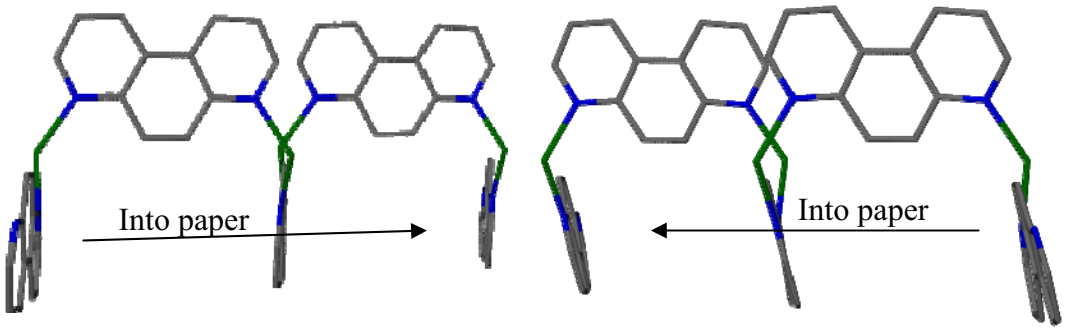

Figure 5.10 – Pictured on the left is the one-dimensional chains of **5.8** with the coordinated benzonitrile molecules removed. On the right is the one-dimensional chains of $\{[Cu(4,7\text{-phenanthroline})(MeCN)_2]PF_6\}_n$ with the coordinated acetonitrile molecules omitted in order to assist in clarity and comparison. In essence they are mirror images of one another.

In the pursuit to isolate any intermediate from the solid-solid reaction of $[Cu(BzCN)_4]BF_4$ and 4,4'-dipyridyl, solution based means were used. From this a new product and structure was found, $\{[Cu(4,4'\text{-dipyridyl})_{1.5}]BF_4\}_n$, **5.9.** Figure 5.11 shows the distorted trigonal planar arrangement environments around the two unique copper centers in **5.9.** Cu(1) is coordinated by three 4,4'-dipyridyl with N-Cu(1)-N angles of 124.1(5)°, 125.5(5)°, and 110.3(5)°. The three 4,4'-dipyridyl coordinated to Cu(2) have N-Cu(2)-N angles of 124.1(6)°, 127.1(5)°, and 108.8(6)°. The same bond angle, 124.1° are attributed to N(3)-Cu(1)-N(2) and N(4)-Cu(2)-N(6). The nitrogen atoms bonded to the same copper are within 1° of being coplanar. However, two of the nitrogen atoms attached to the other copper are above and below this plane. The torsion angles for N(1)-Cu(1)-Cu(2)-N(6) and N(2)-Cu(1)- Cu(2)-N(6) are 66.9° and 67.2°, respectively.

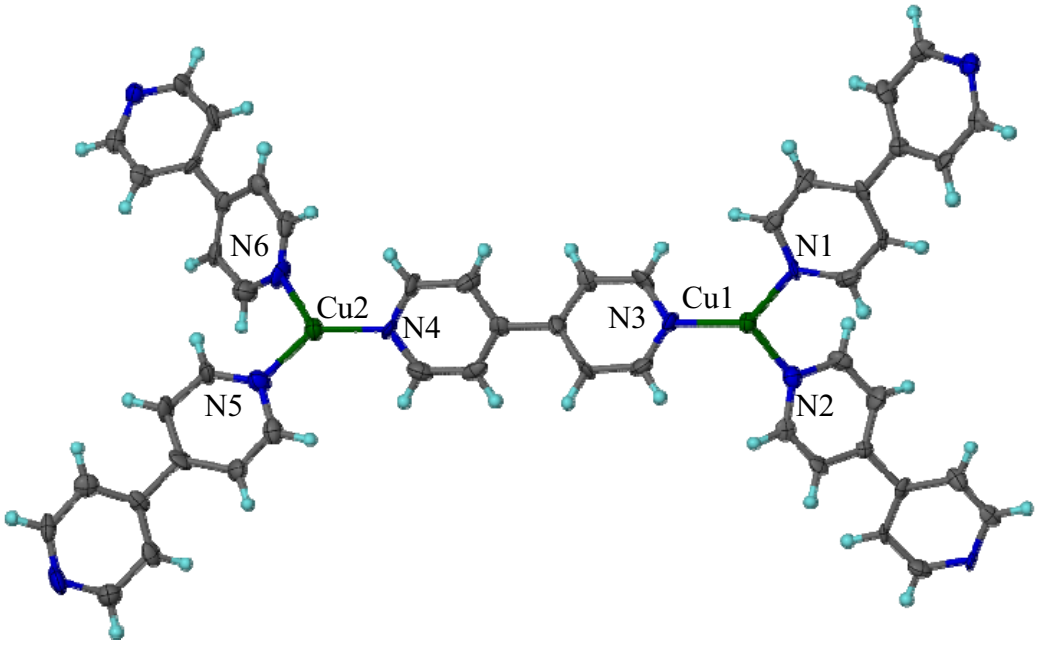

Cu(1)-N(1)	1.980(11)Å	N(3)-Cu(1)-N(2)	124.1(5)°
Cu(1)-N(2)	1.972(12)Å	N(3)-Cu(1)-N(1)	125.5(5)°
Cu(1)-N(3)	1.932(11)Å	N(2)-Cu(1)-N(1)	110.3(5)°
Cu(2)-N(4)	1.947(12)Å	N(4)-Cu(2)-N(5)	127.1(5)°
Cu(2)-N(5)	1.969(13)Å	N(4)-Cu(2)-N(6)	124.1(6)°
Cu(2)-N(6)	1.986(14)Å	N(5)-Cu(2)-N(6)	108.8(6)°
N(1)-Cu(1)-Cu(2)-N(6)	66.9°	N(2)-Cu(1)-Cu(2)-N(6)	67.2°

Figure 5.11 – Shown are select bond distances, angles, and torsion angles for the coordination environment around the two unique copper atoms in **5.9**. All non-hydrogen atoms are shown as 50% probability thermal ellipsoids. All bond distances are shorter or within the range of acceptable Cu-N bond lengths, 2.070 ± 0.072, for pyridine.[13]

An extension of the structure into three dimensions can be seen in Figure 5.12. The formation of the complete structure is accomplished by adding an additional interpenetrating network that is off set slightly lower and to the side. Two more interpenetrating networks are also present in except they are rotated 180° (Figure 5.13).

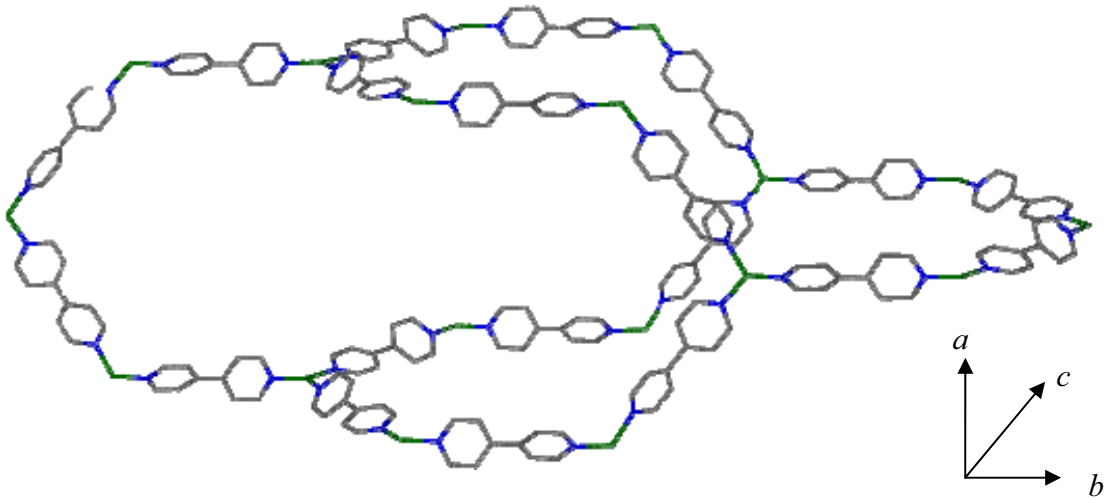

Figure 5.12 – Stick diagram of **5.9.** All copper atoms are coordinated to three 4,4'-dipyridyl ligands.

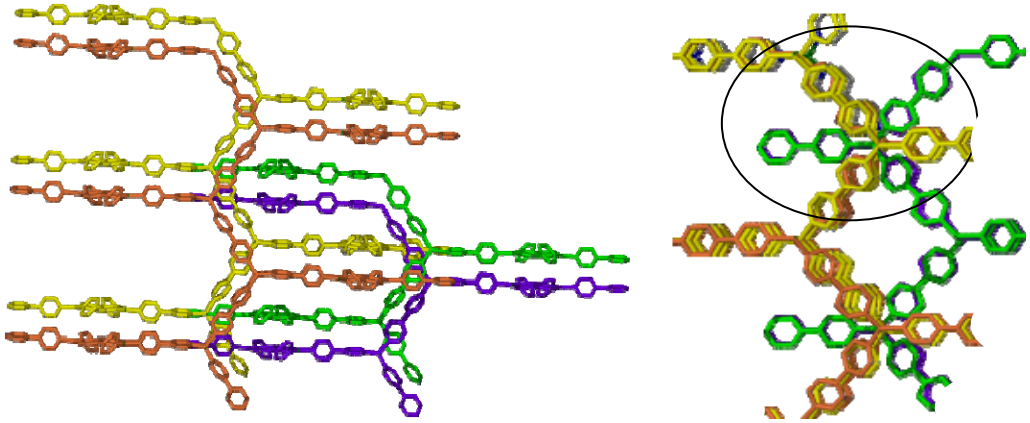

Figure 5.13 – The extended structure of **5.9** there are four interpenetrating networks, each in a different color. On the left, the arrangement of the interpenetrating networks has two networks stacked on each other, with the other two networks shifted to the right half the length of the unit pictured in Figure 5.12.

The extended three-dimensional configuration is isostructural to one previously reported, with the exception of the non-coordinated anion and water molecules.[12] A comparison of the structures N-Cu-N bond angles show the structural similarities, with the N-Cu-N bond angles of 125°**,** 125°, and 108° for the previously reported structure**.** As mentioned in Chapter 2, it is not that unusual for copper(I) to have distorted trigonal planar geometry.

The published case stated that the metal organic framework (MOF) was created via hydrothermal synthesis using a mixture of blue $Cu(NO_3)_2 \cdot 2.5H_2O$, 4,4'-dipyridyl, and 1,3,5-triazine in deionized water. The mixture was placed in a bomb and heated to 140 ºC for 24 h, cooled to 90 ºC, cooled to 70 ºC, and cooled to room temperature. The resultant orange crystals were collected and found to be $\{[Cu(4,4'\text{-dipyridyl})_{1.5}]NO_3 \bullet 1.25H_2O\}_n$. The MOF could not be made at room temperature or by refluxing for 24 h. It was found that the nitrate could be replaced with SO_4^- and BF_4^-, therefore making it a candidate to form an anion exchange medium.

4,7-phenanthroline

The products of tetrabenzonitrilecopper(I) and 4,7-phenanthroline solid-solid reactions were different than previously reported. The reported structures were isostructural, each having two unique coppers (Figure 5.14). One copper(I) cation was coordinated by two benzonitrile molecules and two bridging 4,7-phenanthroline molecules (Figure 5.15). The other unique copper(I) cation was coordinated by two bridging 4,7-phenanthrolines. These two unique copper(I) cations alternate to form a one-dimensional chain.

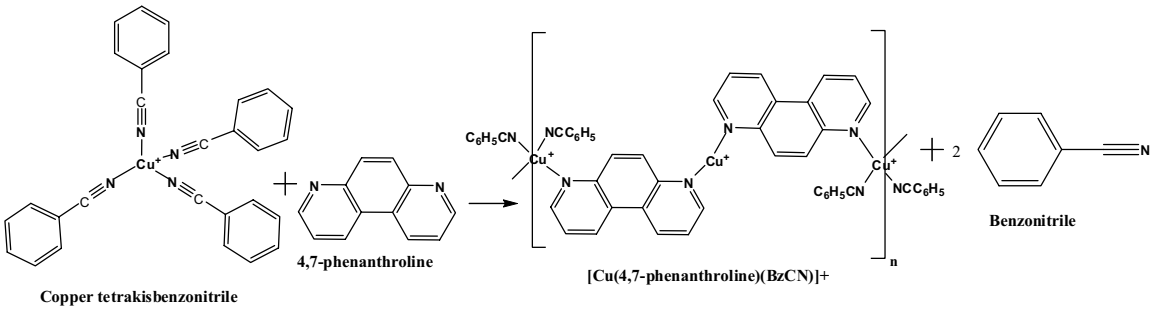

Figure 5.14 – Solution-based chemical reaction for the previously reported $\{[Cu(4,7\text{-phenanthroline})(MeCN)]X\}_n$ (X= BF_4^- or PF_6^-) compounds.[4]

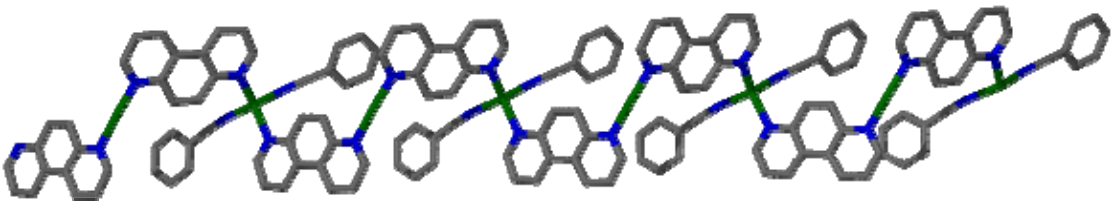

Figure 5.15 – Structure of previously reported $\{[Cu(MeCN)(4,7\text{-phenanthroline})]X\}_n$ (X = BF_4^- or PF_6^-) chains formed with solution-based synthesis.[4]

The finding was that neither of the previously reported structures formed during the solid-solid reaction between $[Cu(BzCN)_4]X$ (X = BF_4^- and PF_6^-) and 4,7-phenanthroline, **5.3** and **5.4**, respectively**.** PXRD patterns did not match the calculated PXRD pattern from the previously reported single crystal data for $\{[Cu(4,7\text{-phenanthroline})(BzCN)]X\}_n$ (X = BF_4^- or PF_6^-) (Figure 5.16). **5.3** was recrystallized by the solvent vapor diffusion of Et_2O into a benzonitrile solution.. The single crystals formed were the previously reported $\{[Cu(4,7\text{-phenanthroline})(BzCN)]BF_4\}_n$. The solvation of **5.3** in benzonitrile caused the solid-solid product's structure and make up to change, converting **5.3** to the solution-based product. The change is important to note because it shows that the solid-solid reaction can produce a different compound than that found by solution-based means. Although we could not solve the crystal structure of solid-solid reaction, it might in fact be related to $\{[Cu(4,7\text{-phenanthroline})(BzCN)_2]PF_6\}_n$ in which all of the copper cations are coordinated to two benzonitrile molecules (Figure 5.17).

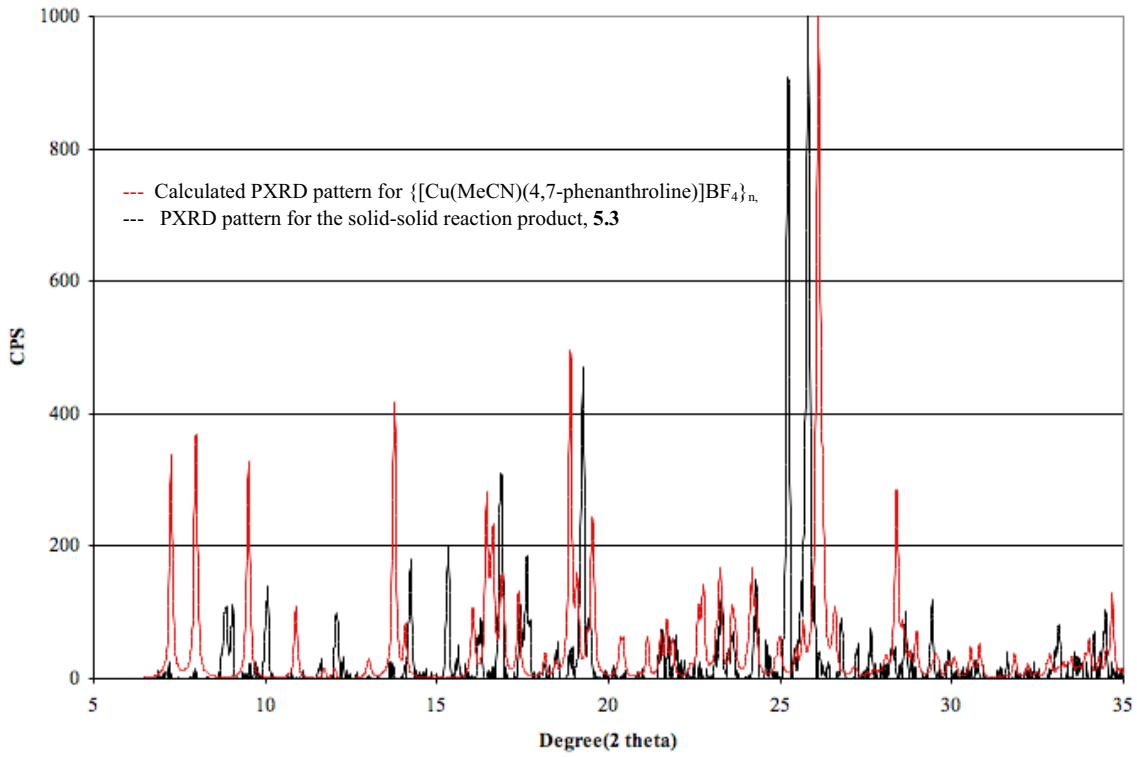

Figure 5.16 – A comparison between $\{[Cu(4,7\text{-phenanthroline})(MeCN)]BF_4\}_n$ calculated PXRD pattern, in red, and the PXRD pattern for the solid-solid reaction product between $[Cu(BzCN)_4]BF_4$ and 4,7-phenanthroline, **5.3**, in black. The patterns do not agree signifying a different crystal structure.

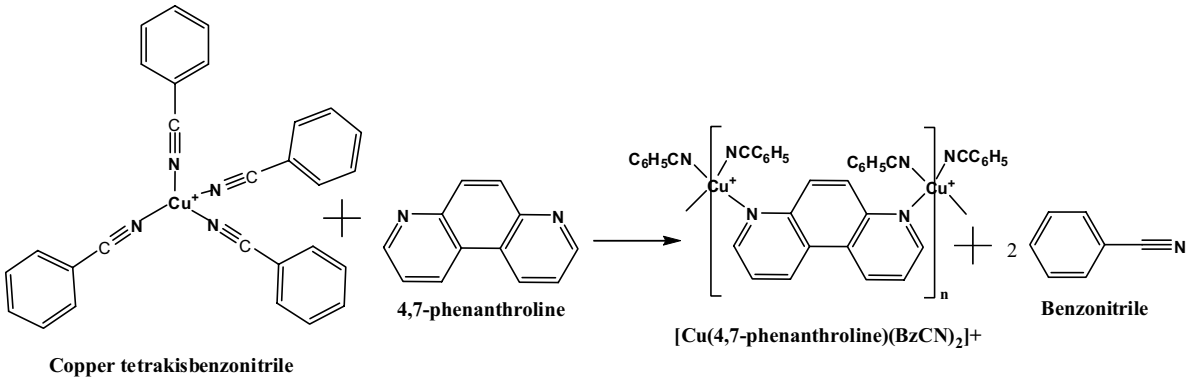

Figure 5.17 – The possible chemical equation for the solid-solid reaction between $[Cu(BzCN)_4]BF_4$ and 4,7-phenanthroline producing the one-dimensional chain. This equation is one for the formation of $\{[Cu(4,7\text{-phenanthroline})(MeCN)_2]PF_6\}_n$.

The product of the reaction between $[Cu(BzCN)_4]PF_6$ and 4,7-phenanthroline was

identified as {[Cu(4,7-phenanthroline)(BzCN)$_2$]PF$_6$}$_n$, **5.4**. **5.4** was determined to be the polycrystalline version of **5.8** based upon comparison of the PXRD patterns (Figure 5.18).

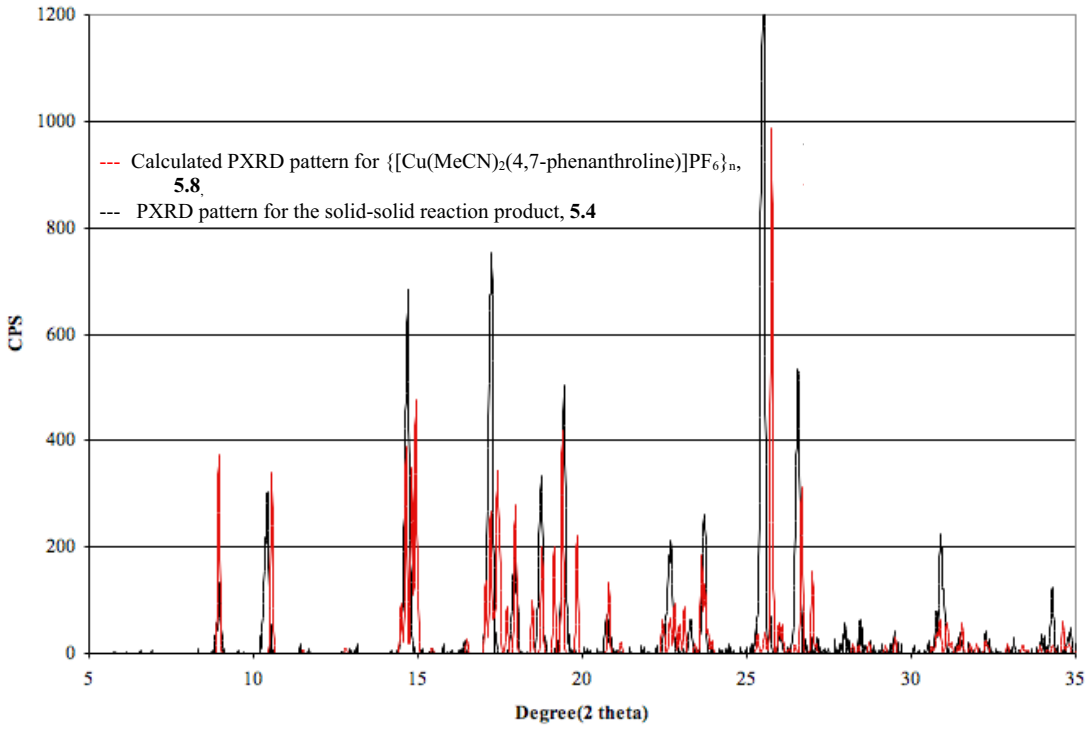

Figure 5.18 – Comparison of experimental PXRD for the solid-solid reaction product between [Cu(BzCN)$_4$]PF$_6$ and 4,7-phenanthroline, **5.4,** and calculated PXRD pattern of {[Cu(4,7-phenanthroline)(MeCN)$_2$]PF$_6$}$_n$, **5.8**.

Monitoring the Reaction

The analysis via GCMS headspace vapor, as mentioned in Chapters 2 and 3, was performed in order to monitor the benzonitrile vapor evolved during the solid-solid reactions. The run conditions had to be adjusted due to the low vapor pressure of benzonitrile. A note should to be made about the difference seen in the TIC for the headspace over the nitrile liquids. Based on the vapor pressures of acetonitrile and benzonitrile, 1 mm Hg and 76 mm Hg respectively, one might expect a factor of 76 to be

the difference between the TIC values. However, the benzonitrile value is 10% the acetonitrile value. The reason for this is two-fold: First, the TIC value is of the mass spectrum at the peak, not the total ions contributed to the vapor over each run time. This means that the results would be relative in nature. Second, only the parent ion amount was taken into account. The acetonitrile molecule fractures off cyanide more easily, making the value for the parent ion and therefore acetonitrile lower overall.

When using 4,7-phenanthroline, $[Cu(BzCN)_4]PF_6$ reacted faster than $[Cu(BzCN)_4]BF_4$ by a wide margin, 6 h and 24 h, respectively. Instead of the non-coordinated benzonitrile found in the starting material assisting in the diffusion, it seemed to be a hindrance. The benzonitrile vapor dramatically increases twice: once at around 1000 TIC and again at 2000 TIC (Figure 5.19). Although the time at which these transitions occur is different for each sample, the trend is consistent for each. The first change in the rate at which benzonitrile is detected is similar for each run, 5.3(4) TIC/min. The dramatic increase is not as similar, 4(1) TIC/min, but in both change are a 5 to 10 times increase in the rate as compared to the slower regions of each run. Interestingly the final slopes are negative being -0.29(7) suggesting that the product maybe absorbing benzonitrile vapor or the benzonitrile is escaping the vial. The basis of the transition time for the second transition cannot be due to the residual heat of grinding. If that were the case, both series 2 and 3 would have the same transition time since the first transition for both occur at the same time The two transitions might be from another phase being formed, however, results from PXRD have been inconclusive. It is unclear whether the PXRD pattern for the $[Cu(BzCN)_4]BF_4$ and 4,7-phenanthroline solid-solid reaction product contained more than a single phase.

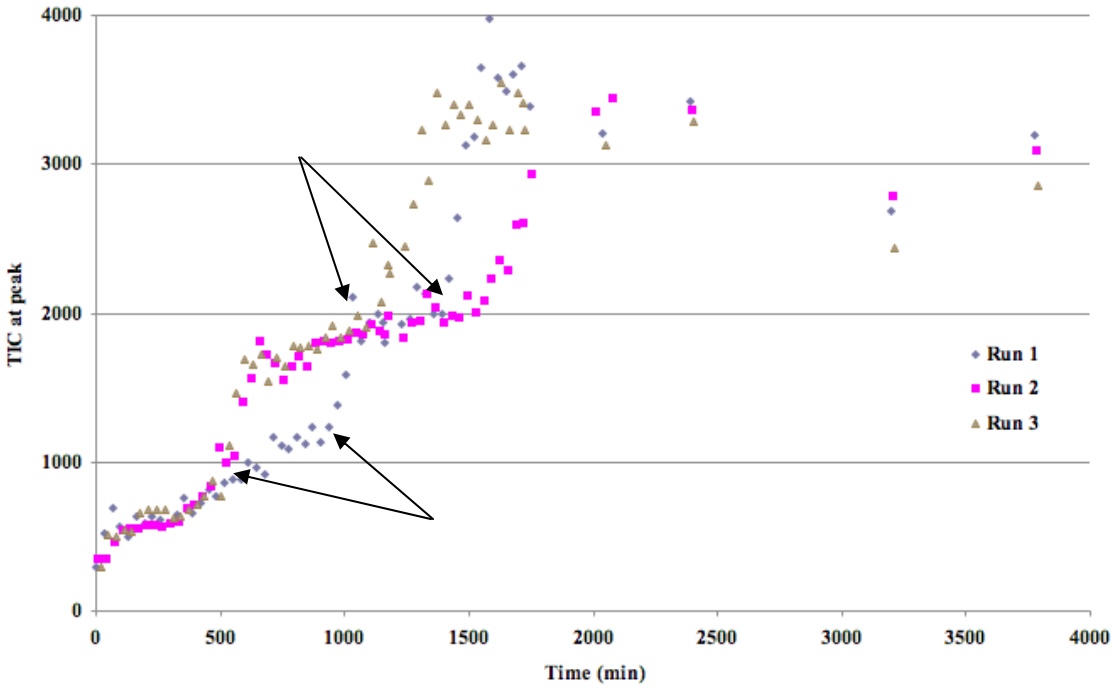

Figure 5.19 – GC-MSD monitoring of BzCN vapor of the **5.3** formation. There are two transitions for each run: one at a TIC of ~1000 and the other ~2000 TIC, as indicated by the arrows. Three runs were performed and are denoted by point shape and color.

The GC-MSD headspace analysis for $\{[Cu(4,7\text{-phenanthroline})(BzCN)_2]PF_6\}_n$ production is different than what is seen for $\{[Cu(4,7\text{-phenanthroline})(MeCN)_2]PF_6\}_n$ and **5.3**. During a run a peak in TIC amount is made and then gradually decreases instead of flattening out (Figure 5.20). This may simply be the product powder absorbing the benzonitrile, in sense acting like clay.

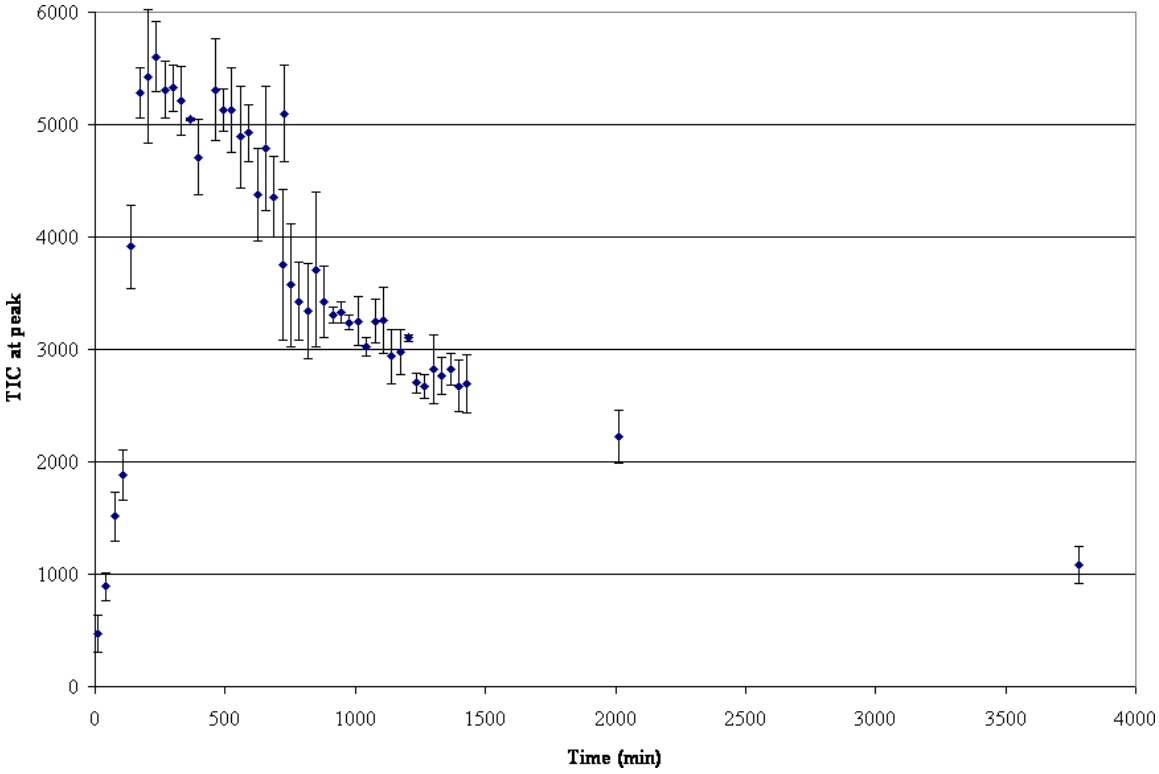

Figure 5.20 – GCMS monitoring of BzCN vapor released during the formation of $\{[Cu(BzCN)_2(4,7\text{-phenanthroline})]PF_6\}_n$, **5.4**. A standard error of the estimate of ±548 and n =3.

The UV-Vis diffuse reflectance results for the solid-solid reaction between $[Cu(BzCN)_4]BF_4$ and 4,7-phenanthroline**,** further validates the GCMS headspace results (Figure 5.21). There are two distinct time ranges in which the spectra change in absorbance dramatically at 410 nm. This too is an unusual result when compared with the $[Cu(MeCN)_4]BF_4$ and 4,7-phenanthroline solid-solid reaction analog. In that case, there is only one transition time range for each run suggesting a different mechanism for the reactions containing BF_4^- verses PF_6^-.

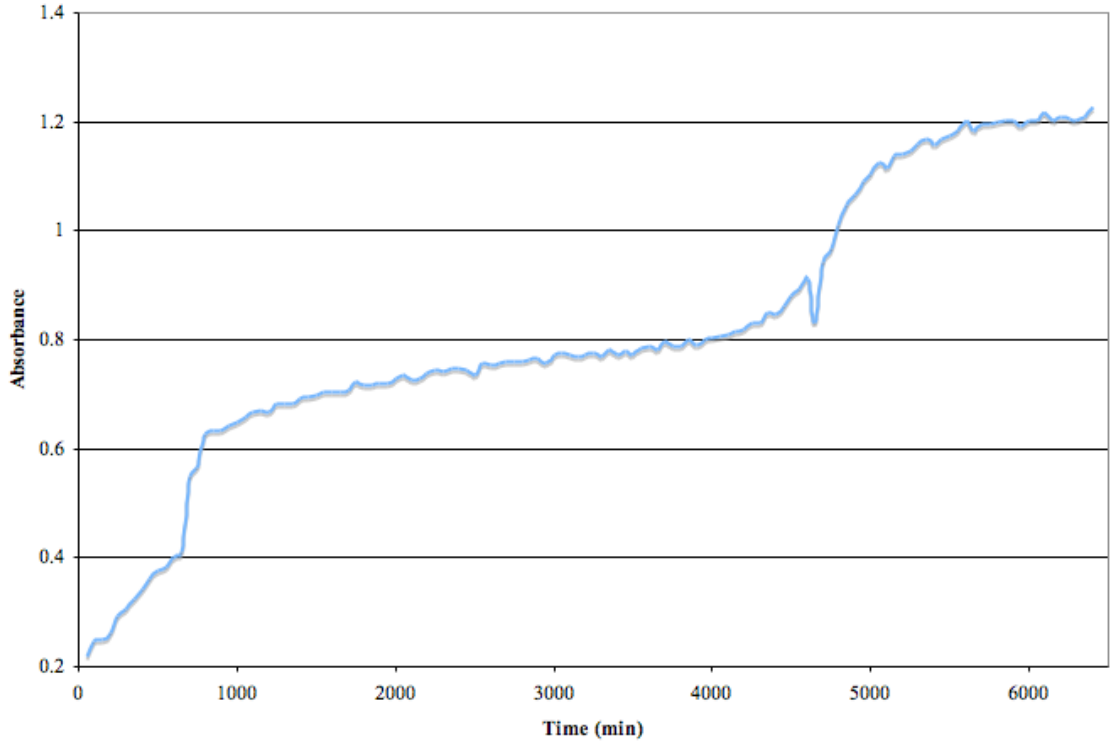

Figure 5.21 – UV-Vis of **5.3** formation over a 2-day period. The graph shows the absorbance at 400 nm vs. time. The difference in time between each spectrum is 50 min. All spectra have been normalized at 750 nm. n =2

The UV-Vis diffuse reflectance findings for the production of **5.4** ({[Cu(4,7-phenanthroline)$(MeCN)_2$]PF_6}$_n$) shows the expected trend of a rapid change in the absorbance around 410 nm (Figure 5.22). However, instead of the increase in absorbance stopping and staying at a relatively constant value, the absorbance decreases, suggesting another species is being produced. When comparing the GC-MSD and UV-Vis results it can be pointed out that the progression is similar in both cases.

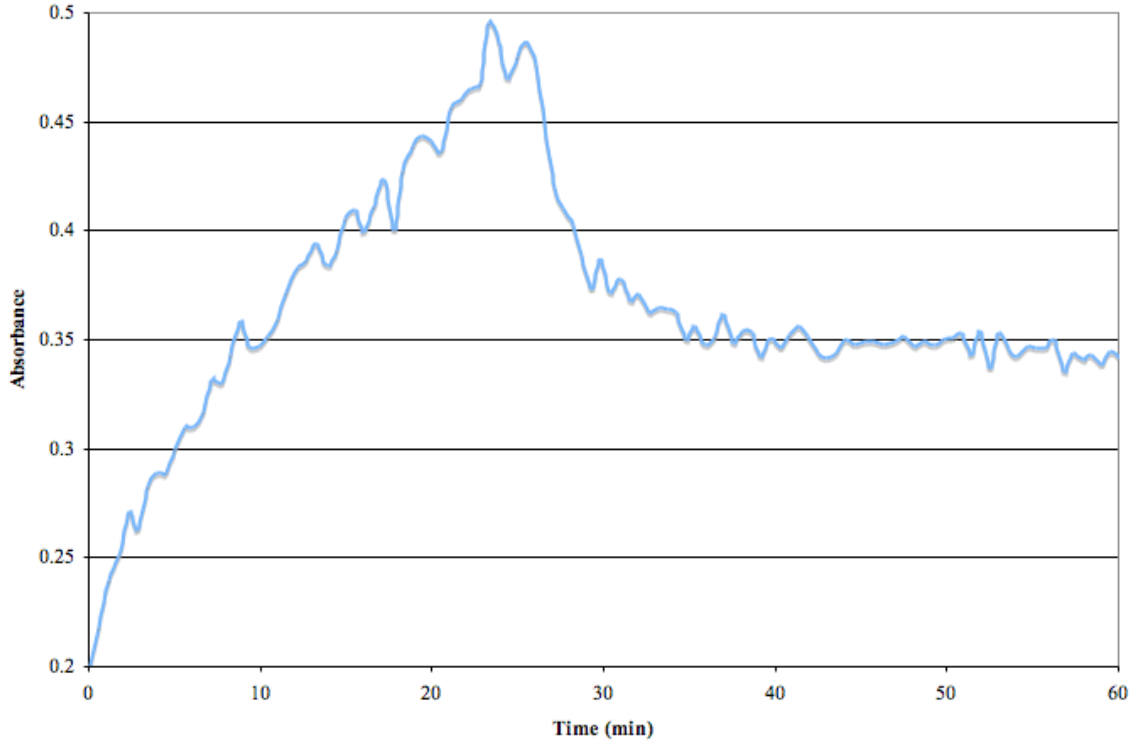

Figure 5.22 – UV-Vis monitoring of **5.4** production. The absorbance is taken at 400 nm over time. The spectra have been normalized at 750 nm. n = 3

4,4'-dipyridyl

As described in Chapter 3, the solid-solid reaction of 4,4'-dipyridyl with $[Cu(MeCN)_4]BF_4$ or $[Cu(MeCN)_4]PF_6$ produced the four-fold interpenetrating diamonoid network. If the mechanism is similar for $[Cu(BzCN)_4]BF_4$ or $[Cu(BzCN)_4]PF_6$, then the structures of **5.5** or **5.6** should be identical (Figure 5.23).

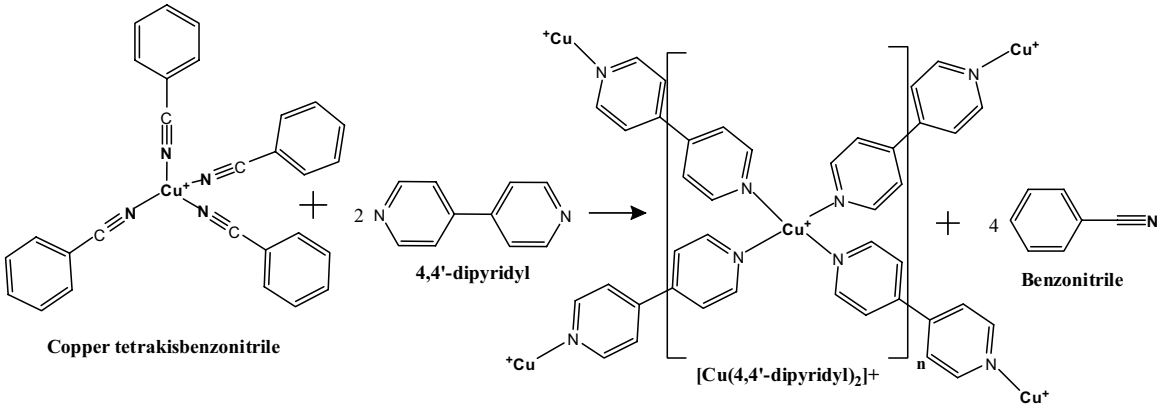

Figure 5.23 – Reaction between 4,4'dipyridyl and tetrabenzonitrilecopper(I) in which all the benzonitrile have been replaced by 4,4'-dipyridyl.

Based on the powder comparison between the benzonitrile and the acetonitrile analogs, both the BF_4^- and PF_6^- cases match (Figures 5.24 and 5.25). This production of identical coordination networks suggests that the formation mechanism is similarly in both cases.

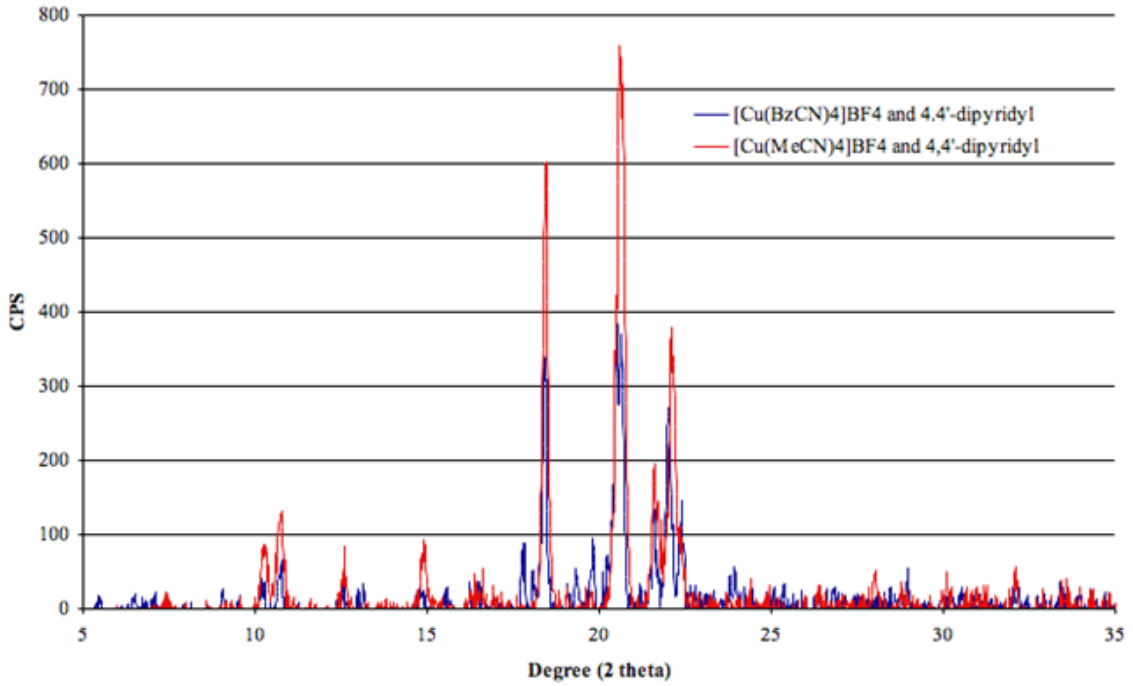

Figure 5.24 – Comparison of the powder patterns for the solid-solid reaction product between $[Cu(BzCN)_4]BF_4$ and 4,4'-dipyridyl, **5.5,** and the acetonitrile solid-solid reaction analog. The PXRD peak positions match; compounds are isostructural.

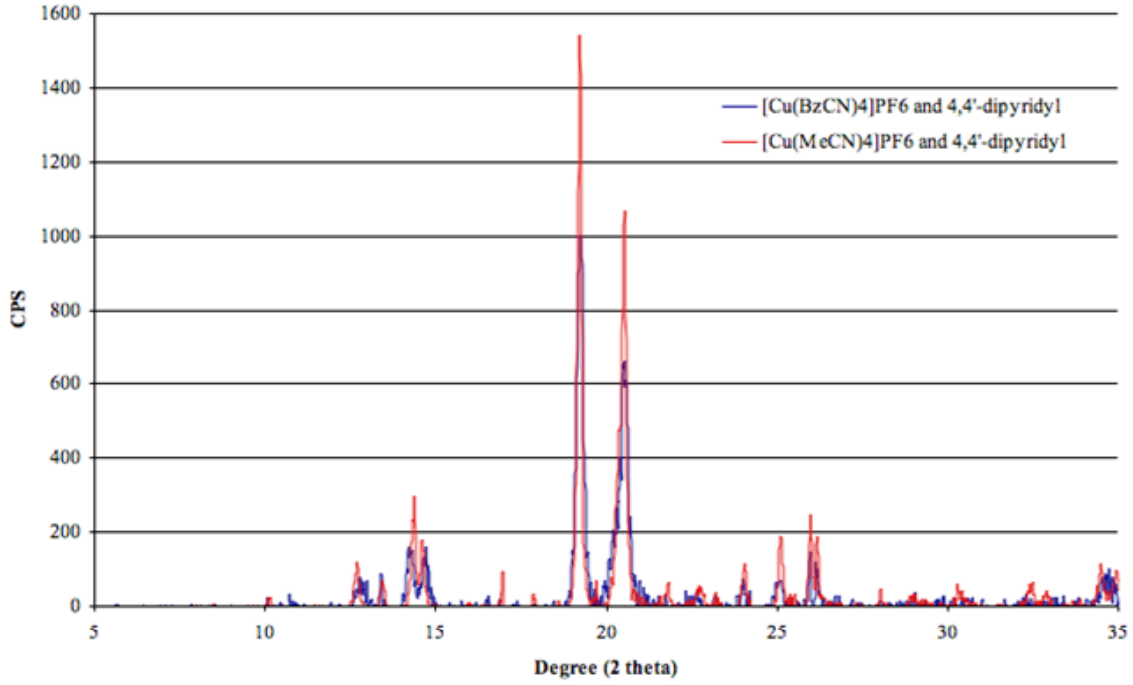

Figure 5.25 – Comparison of the powder patterns for the solid-solid reaction product between $[Cu(BzCN)_4]PF_6$ and 4,4'-dipyridyl, **5.6,** and the acetonitrile solid-solid reaction analog.

The reaction of either $[Cu(BzCN)_4]X$ (X = BF_4 or PF_6) with the 4,4'-dipyridyl proceeded in a similar way as the acetonitrile analog reactions when looking at the UV-Vis spectra. An initial production of a yellow intermediate made during the reaction is followed by a change to $\{[Cu(4,4'\text{-dipyridyl})_2]X$ (X = BF_4 or $PF_6)\}_n$. Figure 5.26 shows the normal mode of spectral change, where the yellow product reaches an absorbance around one at 420 nm, and then a transition to the orange product occurs. The absorbance at 420 nm decreases over time until the reaction reaches completion.

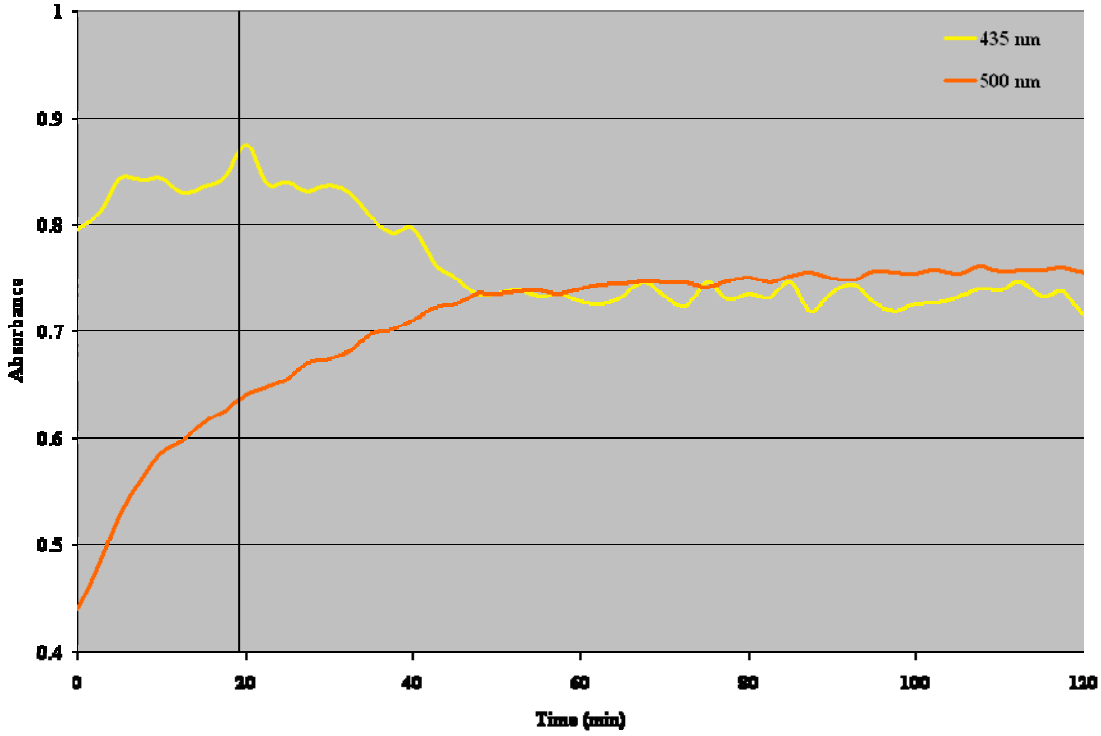

Figure 5.26 – UV-Vis monitoring of the reaction to produce **5.5**. The spectra have been normalized at 750 nm. The absorbance at 420 nm is in yellow and 520 nm in orange

The UV-Vis spectra of **5.6** production is different than the one shown for **5.5** production. The results are close to the 4,7-phenanthroline-MeCN analog solid-solid reaction in that the absorbance keeps increasing instead of the decrease at the transition point (Figure 5.27). This is due to the fact that **5.6** absorbs more strongly than the yellow intermediate. The transition occurs within 2 min, which is why the yellow intermediate's absorbance at 410 nm is only a blip immediately before the orange product forms.

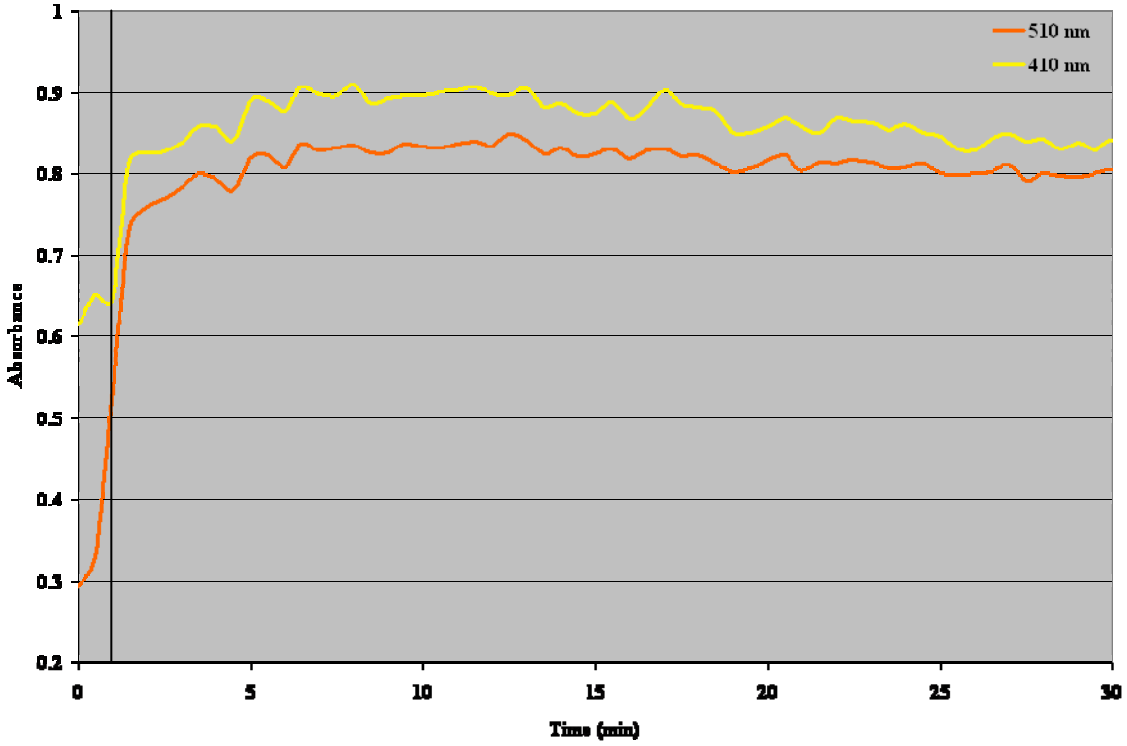

Figure 5.27 – UV-Vis diffuse reflectance monitoring of the reaction to produce **5.6**. The spectra have been normalized at 750 nm. The 410 nm is in yellow and the 500 nm is in orange.

The GC-MSD headspace monitoring for the $[Cu(BzCN)_4]BF_4$ and 4,4'-dipyridyl reaction gave some fascinating results. In the case of the **5.5** production, there was the normal rapid increase followed by a leveling off (Figure 5.28). However, at around 7:12 there is a marked increase followed by a dramatic decrease that again flattens out. This change could be an indication that the transition to **5.5** is occurring at this point agrees with the UV-Vis results. If this is indeed the case the material is absorbing the benzonitrile vapor.

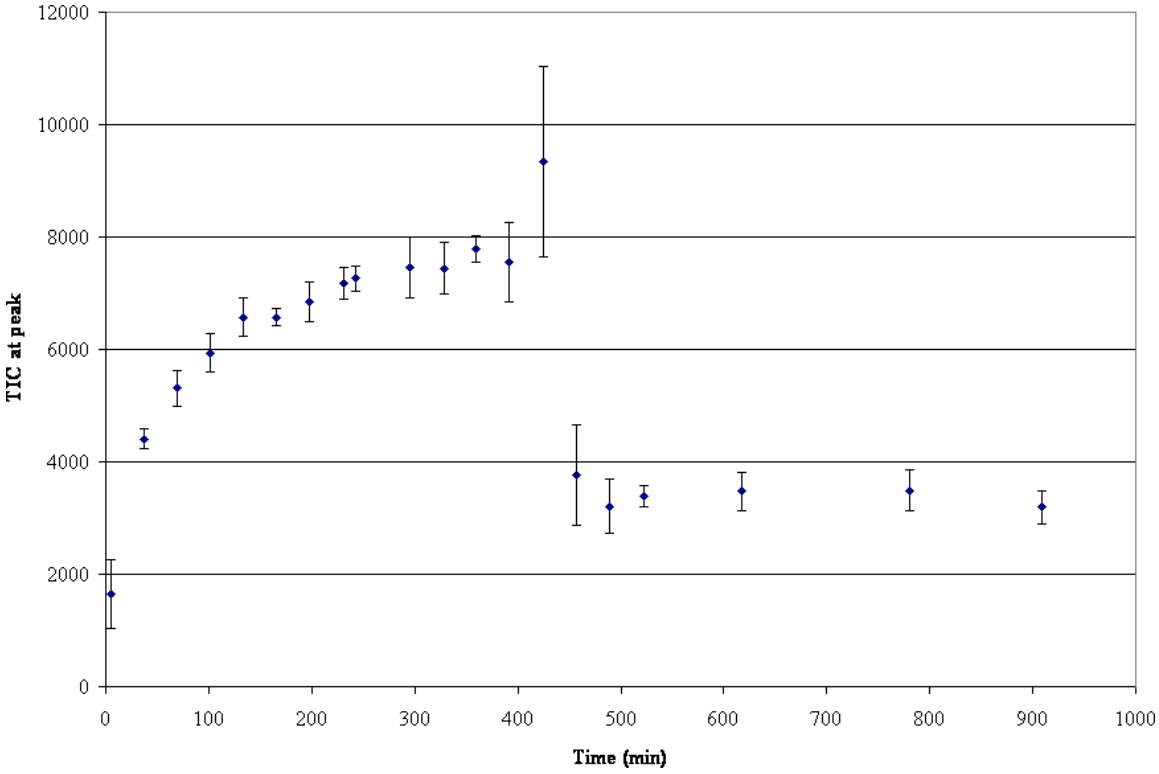

Figure 5.28 – GC-MSD monitoring of BzCN vapor of the reaction to produce $\{[Cu(4,4'\text{-dipyridyl})_2]BF_4\}_n$. A standard error of the estimate of ±222 and n = 3.

Unfortunately, the GC-MSD results for the production of **5.6** were not as informative. In the six experiments that were performed, three at a time, only one showed any appreciable amount of benzonitrile vapor in the headspace, which is why the error for the first point is so great (Figure 5.29). As seen in the UV-Vis, the time of transition is within a minute or two of the collection start time. This could be the reason there is virtually no benzonitrile vapor detected, if in fact it is acting in the same way as **5.5** by absorbing vapor.

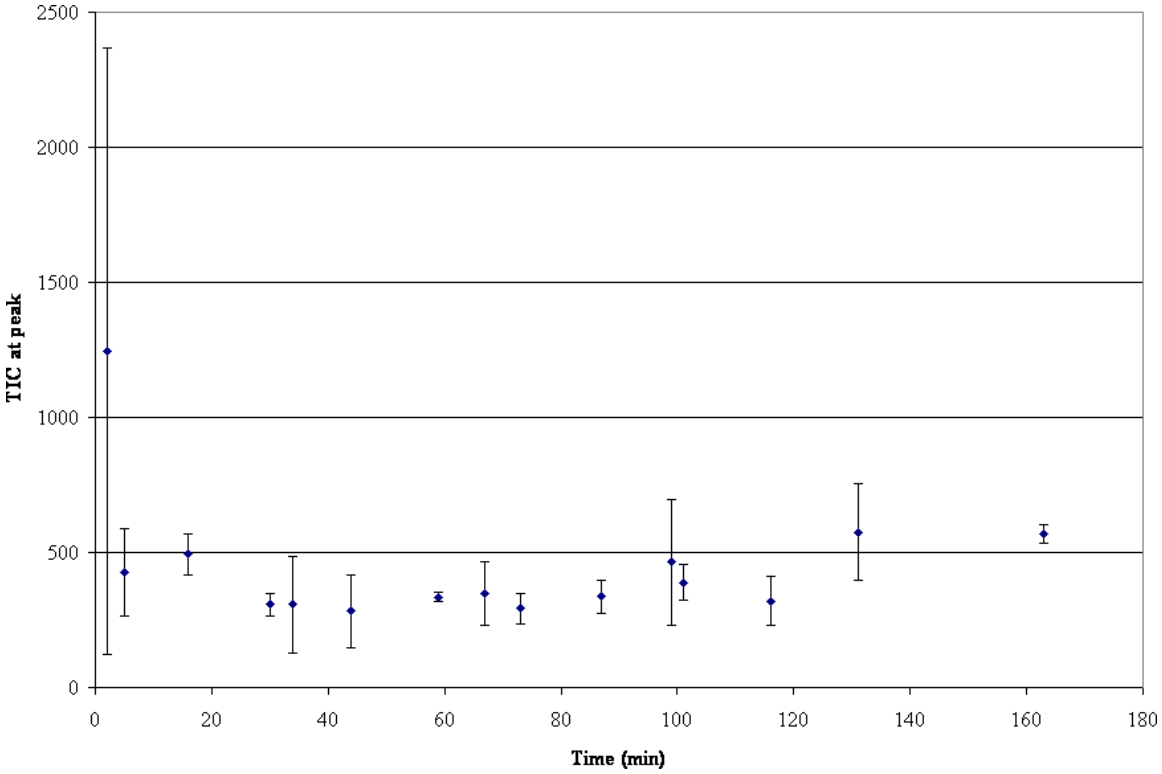

Figure 5.29 – GC-MSD monitoring of BzCN vapor of the reaction to produce $\{[Cu(4,4'\text{-dipyrdyl})_2]PF_6]\}_n$. n = 6 and a standard error of the estimate of ±58.

Identification of the Yellow Intermediate

The yellow intermediate for the solid-solid reaction between $[Cu(BzCN)_4]X$ (X = BF_4^- and PF_6^-) and 4,4'-dipyridyl was to be identified in order to further understand the mechanism of the three-dimensional coordination network formation. Unlike the acetonitrile case, no yellow intermediate could be identified via PXRD. A new crystal structure, $\{[Cu(4,4'\text{-dipyridyl})_{1.5}]BF_4\}_n$, **5.9**, was solved for the yellow crystals formed in a mixture of these reagents. As stated before, it is not known if this is in fact the yellow intermediate.

5.4 Conclusion

This research has shown that the solid-solid reaction between 4,7-phenanthroline or 4,4'-dipyridyl and $[Cu(BzCN)_4]X$ ($X=BF_4$ and PF_6) occurs similarly to the acetonitrile analogs. This observation can potentially be expanded into using different coordinated solvents, such as dimethylsulfoxide.

In the case of the 4,7-phenanthroline, the solid-solid product for $[Cu(BzCN)_4]PF_6$ was more structurally similar to the acetonitrile analog than the solution-based results. In that case, the products have the same amount of coordinated nitrile molecules for each copper. As for the $[Cu(BzCN)_4]BF_4$ case, the solid-solid product was indeed different than the solution-based product. Unfortunately, the structural identification was not accomplished. Perhaps the more important point is that these benzonitrile compounds could not be developed by solution-based synthesis. As stated in Chapter 1, solid-solid reactions can result in products otherwise inaccessible by other synthetic routes.

The structural results for 4,4'-dipyridyl with $[Cu(BzCN)_4]X$ ($X=BF_4$ and PF_6) were three-dimensional diamonoid networks. The GC-MSD headspace results were surprising and suggest that the system needs to be studied further to gain an understanding as to why the vapor decreases or does not change during the reaction progress. This work shows that these solid-solid reactions can be generalized rather easily.

Finally, a new solution-based route was developed to create a previously known structure. The route used reaction conditions at room temperature, unlike before when elevated temperature was needed.

References

(1) Knaust, J. M.; Knight, D. A.; Keller, S. W. *J. Chem. Crystallogr.* **2003**, *33*, 813-823.

(2) Lide, D. R. *CRC Handbook of Chemistry andPphysics*; 86th ed; CRC Press: Cleveland, Ohio **1990**.

(3) Lide, D. R. *CRC Handbook of Chemistry and Physics*; 87th ed.; CRC Press: Cleveland, Ohio, **2006-2007**.

(4) Lopez, S.; Keller, S. W. *Inorg. Chem.* **1999**, *38*, 1883-1888.

(5) Werner, P. E.; Eriksson, L.; Westdahl, M. *J. Appl. Crystallogr.* **1985**, *18*, 367-370.

(6) Boultif, A.; Louër, D. *J. Appl. Crystallogr.* **2004**, *37*, 724-731.

(7) Yvon, K.; Jeitschko, W.; Parthe, E. *J. Appl. Crystallogr.* **1977**, *10*, 73-74.

(8) Antolasic, F.; Wsearch 32 ed. Malbourne, Victoria, Australia, 2005, p Mass Spec analysis tool.

(9) Bruker Analytical X-ray: 1997.

(10) Sheldrick, G. M.; University of Gottingen, Germany: 1997.

(11) Barbour, L.; University of Missouri-Columbia: 2001.

(12) Yaghi, O. M.; Li, H. *J. Am. Chem. Soc.* **1995**, *117*, 10401-10402.

(13) Orpen, A.; Brammer, L.; Allen, F.; Kennard, O.; Watson, D.; Taylor, R. *J. Chem. Soc. Dalton Trans.* **1989**, S1-S83.

Chapter 6

Conclusion

The research performed for this dissertation has shown that solid-solid reactions are a viable way of creating coordination networks. Through the use of $[Cu(RCN)_4]X$ (R= Me or Bz and X = BF_4^-, PF_6^-, or $SO_3CF_3^-$) combined with a ligand, supramolecular networks were formed. The majority of the structures created were identical to solution-based products; however, some structures were divergent from the solution-based results.

The facilitating ligand for this research was 4,7-phenanthroline. The use of this ligand in solid-solid reactions produced linear chains. Two of the resulting structures were previously reported and one structure was new. Through monitoring these reactions, the anion was shown to have a profound effect on the reaction rate. The results from UV-Vis diffuse reflectance spectra and gas chromatography mass spectrometry confirmed that $[Cu(MeCN)_4]SO_3CF_3$ reacted much faster than $[Cu(MeCN)_4]BF_4$ or $[Cu(MeCN)_4]PF_6$. The reaction rate discrepancy was in part due to the difference in the loss of acetonitrile vapor from the tetrasacetonitrilecopper(I) salts under ambient conditions. A mechanistic scheme was developed in which acetonitrile is lost through replacement by 4,7-phenanthroline molecules (Figure 6.1). When enough acetonitrile vapor is present condensation occurs, causing diffusion of the 4,7-phenanthroline to increase dramatically. The increased diffusion allows for the extension of the linear chains. These novel reactions produce crystalline compounds from crystalline reagents with one of the reagents producing a solvent to increase diffusion.

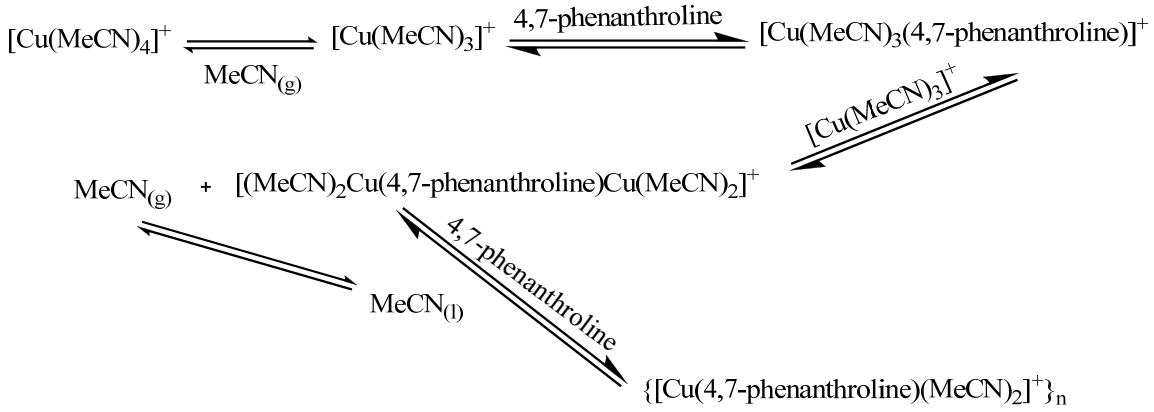

Figure 6.1 – Suggested mechanism of the solid-solid reaction between $[Cu(MeCN)_4]X$ ($X = BF_4^-$ or PF_6^-) and 4,7-phenanthroline.

The dissertation was extended to study 4,4'-dipyridyl in solid-solid reactions due to 4,4'-dipyridyl's substantial use in coordination chemistry. The finding was that the same three-dimensional four-fold interpenetrating network was formed from both solid-solid reactions and solution-based chemistry. The results show solid-solid reactions can easily produce three-dimensional extended networks. Like the 4,7-phenanthroline solid-solid reactions, condensation of the acetonitrile vapor is required for the crystalline product to form (Figure 6.2).

The formation of coordination networks can also be seen in the solid-solid reactions with *trans*-1,2-*bis*(4-pyridyl)ethylene (BPE). However, the solid-solid reaction product's structure was not the same as found in the solution-based chemistry. The structural comparison was performed by comparing powder X-ray diffraction patterns. At present, the product's structure has not been determined. The new structure suggests the possibility of creating new structures that may be accessible only with the use of solid-solid reactions. The reaction rate observed with the BPE solid-solid reactions was slower than the 4,4'-dipyridyl case; the rate difference is possibly due to the elongated

linker between the pyridyl rings for BPE.

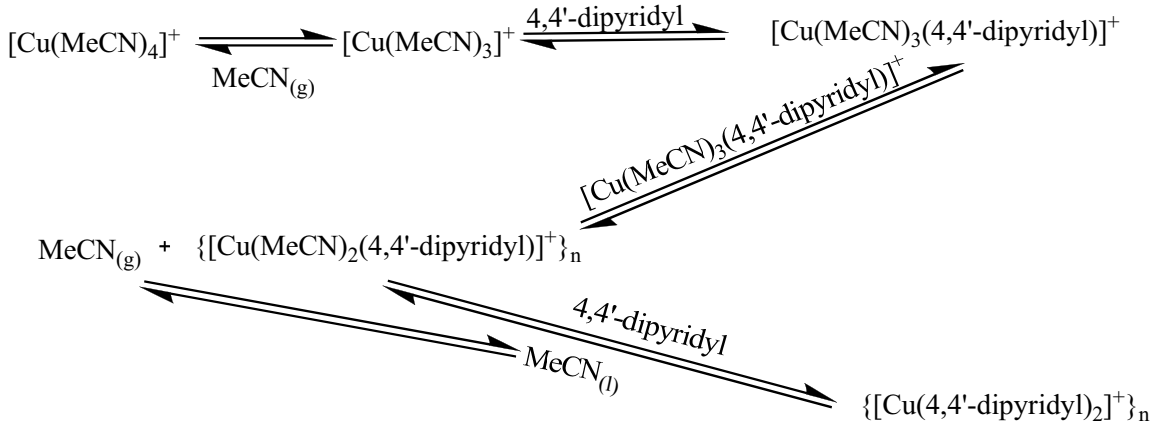

Figure 6.2 – Suggested mechanism of the solid-solid reaction between $[Cu(MeCN)_4]X$ ($X = BF_4^-$ or PF_6^-) and 4,4'-dipyridyl in a one to two ratio.

Another ligand used in solid-solid reactions was 1,3-dithiane. In solution-based chemistry, two similar structures formed with different bonding configurations of the 1,3-dithiane. The solid-solid reactions showed that there is a possibility to isolate the major structure found in solution-based chemistry via solid-solid reactions.

Along with changing the ligand, the coordinated solvent was changed from acetonitrile to benzonitrile. Interestingly, the solid-solid reaction was found to produce a different structure than found through solution in the 4,7-phenanthroline cases. This solidifies the idea that solid-solid reactions can also produce structures that can be reached only by the solid-solid reaction pathway.

These solid-solid reactions address several principles of green chemistry. First, the solvent *waste* is lessened; the only solvent used is one of solvent release during the reaction. With this lowering of solvent content, there is only a small amount of heat needed to drive off the solvent, making the process *energy efficient.* The energy

efficiency of the reactions is also enhanced because they can be run at *ambient temperature and pressure*. In addition, the structural *percent yield* was above 95% for these reactions, producing structures that in some cases are not found in solution. Also, the ability to halt the reaction by removing headspace gas minimizes the *potential for accidents* since reaction control is established.

Comprehensive research on the solid-solid reactions that produce their own solvent can and must be performed. A variety of ways must be used in order to fully grasp the process by which solid-solid reactions produce crystalline products. One important experiment that needs to be done is to perform a solid-solid reaction using single crystals of both reagents. During the reaction, video evidence must first be taken in order to observe the reaction's progression throughout the crystals. At the crystal-crystal interface there should be a noticeable color change signifying product formation. Further analysis can be made by using scanning electron microscopy to obtain a more in-depth idea of the surface interactions between the single crystals.

The solid-solid reaction mechanisms can further be explored by use of ^{13}C- and/or ^{15}N-containing acetonitrile. The acetronitrile would be used to monitor the replacement of coordinated acetonitrile molecules by the ligands with nuclear magnetic resonance (NMR). The question that must be answered is whether the 4,7-phenanthroline bonds to the copper cation before one or two acetonitrile molecules are released. The NMR results would further solidify the mechanism and lead to widespread research possibilities.

In addition to the process by which the release of acetonitrile occurs, the intermediate compound produced during the solid-solid reaction with 4,4'-dipyridyl must be resolved. There are a couple of ways to isolate the compound. The first will be to

remove any free 4,4'-dipyridyl, thus preventing the three-dimensional network from forming. The removal of excess 4,4'-dipyridyl will be accomplished by timing the addition of a solvent so that enough time is given to promote the formation of the intermediate but before the formation of the product. Diethyl ether or chloroform would first be used as a solvent to isolate the intermediate. Other solvents, or a combination thereof, would be used if the intermediate isolation is not accomplished. Column chromatography may be needed to obtain a pure intermediate sample. The intermediate compound could also be found by using methanol as a competitor to acetonitrile in the headspace. The overall reaction conditions would change and might prevent acetonitrile molecules from becoming non-coordinated. Finally, the reaction vessel could be placed under vacuum to essentially remove any free acetonitrile.

The effect of acetonitrile condensation must be studied further. The condensation could be prevented by having a continuous stream of acetonitrile vapor across the reaction medium. The flow would allow for consistent acetonitrile headspace concentration but would eliminate vapor condensation in the headspace. If the solid-solid reaction did indeed continue, the resulting mixture could be analyzed to determine whether the powder mixture absorbed any of the acetonitrile vapor. The absorption could possibly cause condensation in areas of the powder, promoting diffusion.

Along the line of headspace concentration, the reaction vessel parameters need to be studied. Preliminarily, the increase in vial size has halted the solid-solid reactions. The vial size can be adjusted by using a vial with an adjustable volume. If the volume adjustment was performed during the solid-solid reaction, then the vapor pressure could be controlled. The control would also aid in keeping the acetonitrile vapor concentration

consistent. The shape of the reaction vessel also should be explored to determine what effect that would have on the solid-solid reaction.

The tetraacetonitrilecopper(I) salts still need further study in order to clear up the thermogravimetric analysis result presented. The salts need to have isothermal runs at higher temperatures to allow for a shorter time in which the curve becomes more horizontal. The results would further validate the runs performed at 25 °C.

A good start has been made on a way to create a more green process for which coordination networks can and are created. It should be evident at this point that the project scope is wide and varied, with expansion to be made in many areas. For example, ligands containing carboxylic acid functional groups can be studied, which would be of interest because of their use in gas sorption metal organic frameworks. In addition to this, metals such as chromium and nickel could be used instead of copper. In these ways the knowledge base can be broadened.

Appendix 1

Appendix

Atomic coordinates and equivalent isotropic displacement parameters ($Å^2$).

U(eq) is defined as one third of the trace of the orthogonalized Uij tensor.

Anisotropic displacement parameters ($Å^2$). The anisotropic displacement factor

Exponent takes the form: $-2\pi^2 [h^2 a^{*2} U_{11} + \ldots + 2 hka^* b^* U_{12}]$

Hydrogen atomic coordinates and isotropic displacement parameters ($Å^2$).

Table A1
Single Crystal Structure Determinations of
$\{[Cu(4,7\text{-phenanthroline})(MeCN)_2]BF_4\}_n$

Atomic coordinates and equivalent isotropic displacement parameters ($Å^2$) for **2.7**. U(eq) is defined as one third of the trace of the orthogonalized Uij tensor.

Atom Label	x	y	z	U(eq)
Cu(1)	0.55709(4)	0.65029(3)	0.29429(2)	0.02982(16)
F(1)	0.9098(4)	0.6831(2)	0.08677(17)	0.0788(9)
F(2)	0.9385(3)	0.8323(3)	-0.00466(17)	0.0800(9)
F(3)	0.8611(11)	0.8498(3)	0.1338(4)	0.230(5)
F(4)	1.0774(6)	0.8035(5)	0.1166(3)	0.199(3)
N(1)	0.4385(2)	0.57232(19)	0.19232(14)	0.0257(5)
N(2)	0.5747(3)	0.5185(2)	0.39116(16)	0.0387(6)
N(3)	0.7586(3)	0.6658(2)	0.28676(17)	0.0322(5)
N(4)	0.4321(2)	0.72412(18)	-0.16350(14)	0.0256(5)
C(1)	0.3478(3)	0.4962(2)	0.21676(17)	0.0307(6)
C(2)	0.2466(3)	0.4485(2)	0.15809(19)	0.0333(6)
C(3)	0.2382(3)	0.4814(2)	0.06935(19)	0.0312(6)
C(4)	0.3327(3)	0.5615(2)	0.03989(16)	0.0240(5)
C(5)	0.4327(3)	0.6053(2)	0.10307(17)	0.0242(5)
C(6)	0.5337(3)	0.6844(2)	0.07546(17)	0.0274(6)
C(7)	0.5337(3)	0.7201(2)	-0.01163(17)	0.0271(6)
C(8)	0.4302(3)	0.6808(2)	-0.07735(17)	0.0237(5)
C(9)	0.3314(3)	0.6012(2)	-0.05343(17)	0.0251(5)
C(10)	0.2342(3)	0.5624(2)	-0.12030(19)	0.0319(6)
C(11)	0.2386(3)	0.6050(2)	-0.20635(18)	0.0331(6)
C(12)	0.3375(3)	0.6855(2)	-0.22464(18)	0.0298(6)
C(13)	0.8761(4)	0.6550(2)	0.2907(2)	0.0326(6)
C(14)	1.0274(4)	0.6377(3)	0.2954(3)	0.0466(9)
C(15)	0.6454(3)	0.4787(2)	0.44538(19)	0.0330(6)
C(16)	0.7384(4)	0.4315(3)	0.5157(2)	0.0465(8)
B(1)	0.9464(7)	0.7905(4)	0.0808(3)	0.0658(15)

Anisotropic displacement parameters ($Å^2$) for **2.7**. The anisotropic displacement factor exponent takes the form: $-2\pi^2 [h^2 a^{*2} U_{11} + \ldots + 2 hka^* b^* U_{12}]$

Atom Label	U11	U22	U33	U23	U13	U12
Cu(1)	0.0324(2)	0.0353(2)	0.0216(2)	0.00019(13)	-0.00105(14)	0.00363(14)
F(1)	0.117(2)	0.0632(15)	0.0558(14)	-0.0079(12)	-0.0015(15)	-0.0366(16)
F(2)	0.083(2)	0.116(2)	0.0401(12)	0.0231(13)	-0.0043(13)	-0.0175(16)
F(3)	0.482(14)	0.073(3)	0.150(4)	0.026(2)	0.193(7)	0.048(4)
F(4)	0.204(5)	0.300(6)	0.084(2)	0.091(3)	-0.085(3)	-0.198(5)
N(1)	0.0303(12)	0.0271(11)	0.0195(10)	-0.0003(8)	0.0004(9)	0.0035(9)
N(2)	0.0468(16)	0.0433(15)	0.0261(11)	0.0072(11)	0.0049(11)	0.0085(12)
N(3)	0.0327(14)	0.0346(13)	0.0293(12)	-0.0025(9)	0.0016(10)	-0.0020(10)
N(4)	0.0302(12)	0.0267(11)	0.0196(10)	0.0002(8)	-0.0010(9)	-0.0002(9)
C(1)	0.0405(16)	0.0298(14)	0.0221(12)	0.0040(10)	0.0046(11)	0.0047(12)
C(2)	0.0398(16)	0.0299(14)	0.0304(13)	0.0038(11)	0.0046(12)	-0.0041(12)
C(3)	0.0354(15)	0.0286(14)	0.0295(13)	-0.0007(11)	-0.0002(12)	-0.0038(11)
C(4)	0.0292(13)	0.0215(12)	0.0211(12)	-0.0010(9)	-0.0007(10)	0.0024(10)

C(5)	0.0286(14)	0.0233(12)	0.0209(11)	-0.0020(10)	0.0024(10)	0.0022(10)
C(6)	0.0300(14)	0.0289(13)	0.0227(12)	-0.0014(10)	-0.0043(11)	-0.0026(11)
C(7)	0.0299(14)	0.0278(13)	0.0234(12)	-0.0008(10)	-0.0010(11)	-0.0029(11)
C(8)	0.0284(13)	0.0219(12)	0.0206(11)	-0.0013(9)	-0.0015(10)	0.0029(10)
C(9)	0.0316(14)	0.0217(12)	0.0216(12)	-0.0013(10)	-0.0011(11)	0.0007(10)
C(10)	0.0384(16)	0.0276(14)	0.0291(13)	0.0004(11)	-0.0050(12)	-0.0058(12)
C(11)	0.0413(17)	0.0305(14)	0.0263(13)	-0.0004(11)	-0.0112(12)	-0.0053(12)
C(12)	0.0391(16)	0.0283(13)	0.0214(12)	0.0007(10)	-0.0043(11)	-0.0002(12)
C(13)	0.0393(18)	0.0307(14)	0.0278(14)	-0.0001(11)	0.0010(13)	-0.0018(12)
C(14)	0.0351(18)	0.057(2)	0.047(2)	0.0079(15)	-0.0018(15)	0.0004(15)
C(15)	0.0369(16)	0.0341(15)	0.0284(13)	0.0046(11)	0.0060(12)	0.0019(12)
C(16)	0.0348(17)	0.060(2)	0.0444(18)	0.0164(16)	-0.0033(14)	0.0043(15)
B(1)	0.097(4)	0.069(3)	0.0318(19)	0.0012(19)	0.002(2)	-0.046(3)

Hydrogen atomic coordinates and isotropic displacement parameters ($Å^2$) for **2.7**.

Atom Label	x	y	z	U(eq)
H(1)	0.3519	0.4726	0.278	0.037
H(2)	0.1842	0.394	0.1793	0.04
H(3)	0.1694	0.4504	0.0284	0.037
H(6)	0.6017	0.7124	0.1184	0.033
H(7)	0.6027	0.7715	-0.0291	0.033
H(10)	0.1668	0.5078	-0.1064	0.038
H(11)	0.1745	0.5797	-0.2528	0.04
H(12)	0.3378	0.7147	-0.2842	0.036
H(14A)	1.0479	0.56	0.3108	0.07
H(14B)	1.0707	0.6863	0.3418	0.07
H(14C)	1.0652	0.6552	0.2367	0.07
H(16A)	0.8153	0.4833	0.5299	0.07
H(16B)	0.7763	0.3609	0.4947	0.07
H(16C)	0.6861	0.4184	0.57	0.07

Table A2
Single Crystal Structure Determinations of $\{[Cu(4,4'\text{-dipyridyl})_2]BF_4\}_n$

Atomic coordinates and equivalent isotropic displacement parameters ($Å^2$) for **3.4**. U(eq) is defined as one third of the trace of the orthogonalized Uij tensor.

Atom label	X	y	z	U(eq)
Cu(1)	0.4933(3)	0.48830(15)	0.20404(14)	0.0201(5)
N(1)	0.6465(7)	0.4940(3)	0.1200(3)	0.0237(11)
N(2)	0.6854(8)	0.4990(3)	0.3151(3)	0.0262(12)
N(3)	0.3698(7)	0.3772(3)	0.2200(3)	0.0269(12)
N(4)	0.2987(8)	0.5769(3)	0.2136(3)	0.0302(13)
F(1)	0.4455(8)	0.8645(3)	0.0181(3)	0.0671(14)
F(2)	0.4986(10)	0.7287(4)	0.0288(3)	0.102(2)
F(3)	0.1987(9)	0.7735(3)	0.0028(3)	0.0876(18)
F(4)	0.3837(9)	0.7813(3)	-0.0887(3)	0.0736(16)
C(1)	0.7090(10)	0.4254(4)	0.0900(4)	0.0342(16)
C(2)	0.8428(9)	0.4261(4)	0.0416(4)	0.0330(16)
C(3)	0.9238(8)	0.4986(3)	0.0238(3)	0.0197(13)

C(4)	0.8529(9)	0.5691(4)	0.0528(4)	0.0273(14)
C(5)	0.7177(9)	0.5647(4)	0.0998(4)	0.0289(15)
C(6)	0.8296(10)	0.4471(4)	0.3305(4)	0.0351(16)
C(7)	0.9559(10)	0.4449(4)	0.4026(4)	0.0328(16)
C(8)	0.9338(8)	0.4999(3)	0.4614(3)	0.0233(13)
C(9)	0.7806(10)	0.5532(5)	0.4437(4)	0.0408(18)
C(10)	0.6615(10)	0.5509(4)	0.3714(4)	0.0378(17)
C(11)	0.2584(10)	0.3398(4)	0.1613(4)	0.0363(17)
C(12)	0.1328(11)	0.2789(4)	0.1706(4)	0.0382(18)
C(13)	0.1062(9)	0.2585(4)	0.2460(4)	0.0262(14)
C(14)	0.2295(9)	0.2931(4)	0.3076(4)	0.0259(14)
C(15)	0.3578(9)	0.3517(4)	0.2936(4)	0.0268(14)
C(16)	-0.0364(9)	0.1959(4)	0.2585(4)	0.0294(15)
C(17)	-0.0673(9)	0.1253(4)	0.2135(4)	0.0309(15)
C(18)	0.2687(9)	0.6428(4)	0.1706(4)	0.0323(16)
C(19)	0.1380(10)	0.7030(4)	0.1804(4)	0.0334(16)
C(20)	0.1962(9)	0.5694(4)	0.2707(4)	0.0353(16)
B(1)	0.3865(14)	0.7894(5)	-0.0101(5)	0.042(2)

Anisotropic displacement parameters ($Å^2$) for **3.4**. The anisotropic displacement factor exponent takes the form: $-2\pi^2 [h^2 a^{*2} U_{11} + \ldots + 2 hka^* b^* U_{12}]$

Atom Label	U11	U22	U33	U23	U13	U12
Cu(1)	0.0164(9)	0.0244(8)	0.0214(11)	-0.0047(7)	0.0085(8)	-0.0028(6)
N(1)	0.022(3)	0.023(3)	0.029(3)	-0.001(2)	0.013(2)	-0.002(2)
N(2)	0.027(3)	0.027(3)	0.025(3)	-0.002(2)	0.008(2)	0.004(2)
N(3)	0.024(3)	0.034(3)	0.025(3)	0.002(2)	0.012(2)	-0.005(2)
N(4)	0.029(3)	0.032(3)	0.032(3)	0.002(2)	0.014(3)	0.007(2)
F(1)	0.082(4)	0.056(3)	0.070(3)	-0.017(2)	0.032(3)	-0.031(3)
F(2)	0.131(6)	0.082(4)	0.073(4)	0.012(3)	-0.036(4)	0.015(4)
F(3)	0.086(4)	0.076(4)	0.107(5)	-0.023(3)	0.037(4)	-0.029(3)
F(4)	0.123(5)	0.067(3)	0.034(3)	0.004(2)	0.023(3)	0.001(3)
C(1)	0.037(4)	0.028(3)	0.043(4)	-0.005(3)	0.023(3)	-0.001(3)
C(2)	0.037(4)	0.023(3)	0.044(4)	-0.009(3)	0.021(3)	-0.002(3)
C(3)	0.018(3)	0.023(3)	0.017(3)	-0.002(2)	0.002(2)	0.001(2)
C(4)	0.029(4)	0.021(3)	0.036(4)	0.000(3)	0.018(3)	-0.003(3)
C(5)	0.036(4)	0.024(3)	0.031(4)	-0.004(3)	0.016(3)	0.004(3)
C(6)	0.043(4)	0.035(4)	0.026(4)	-0.014(3)	0.001(3)	0.003(3)
C(7)	0.033(4)	0.037(4)	0.029(4)	0.000(3)	0.004(3)	0.014(3)
C(8)	0.020(3)	0.026(3)	0.026(3)	-0.003(3)	0.010(2)	-0.002(3)
C(9)	0.032(4)	0.054(5)	0.033(4)	-0.014(3)	0.000(3)	0.008(4)
C(10)	0.034(4)	0.047(4)	0.032(4)	-0.008(3)	0.004(3)	0.015(3)
C(11)	0.039(4)	0.047(4)	0.022(3)	0.005(3)	0.003(3)	-0.013(3)
C(12)	0.049(5)	0.037(4)	0.028(4)	-0.005(3)	0.006(3)	-0.014(3)
C(13)	0.023(4)	0.029(3)	0.029(4)	-0.003(3)	0.010(3)	-0.011(3)
C(14)	0.031(4)	0.028(3)	0.021(3)	-0.003(3)	0.011(3)	-0.001(3)
C(15)	0.027(4)	0.027(3)	0.025(3)	0.002(3)	0.004(3)	0.000(3)
C(16)	0.021(4)	0.041(4)	0.026(3)	0.000(3)	0.006(3)	-0.005(3)
C(17)	0.023(4)	0.037(4)	0.035(4)	-0.002(3)	0.011(3)	-0.010(3)
C(18)	0.031(4)	0.030(4)	0.040(4)	0.001(3)	0.018(3)	-0.003(3)
C(19)	0.037(4)	0.028(4)	0.039(4)	0.007(3)	0.016(3)	0.008(3)
C(20)	0.031(4)	0.037(4)	0.042(4)	0.009(3)	0.019(3)	0.007(3)

B(1)	0.059(7)	0.033(4)	0.035(5)	0.002(4)	0.011(4)	-0.016(4)

Hydrogen atomic coordinates and isotropic displacement parameters ($Å^2$) for **3.4**.

Atom label	X	y	z	U(eq)
H(1)	0.659	0.3741	0.1024	0.041
H(2)	0.8791	0.3759	0.0206	0.04
H(4)	0.8984	0.6213	0.0402	0.033
H(5)	0.673	0.6144	0.1186	0.035
H(6)	0.848	0.4095	0.2906	0.042
H(7)	1.0565	0.406	0.4113	0.039
H(9)	0.7579	0.5919	0.4821	0.049
H(10)	0.5575	0.5881	0.3615	0.045
H(11)	0.2656	0.3561	0.1091	0.044
H(12)	0.0644	0.2507	0.1259	0.046
H(14)	0.2264	0.2767	0.3602	0.031
H(15)	0.4413	0.3752	0.3373	0.032
H(17)	0.0005	0.116	0.172	0.037
H(18)	0.3404	0.6502	0.1301	0.039
H(19)	0.1179	0.7487	0.1456	0.04
H(20)	0.215	0.5213	0.3025	0.042

Table A3
Single Crystal Structure Determinations of
$\{[Cu(4,4'\text{-dipyridyl})_2]SO_3CF_3\}_n$

Atomic coordinates and equivalent isotropic displacement parameters ($Å^2$) for **3.5**. U(eq) is defined as one third of the trace of the orthogonalized Uij tensor.

Atom Label	X	y	z	U(eq)
Cu(1)	0.75	0.25	0	0.0217(3)
F(1)	0.3359(5)	0.2163(7)	-0.3585(10)	0.123(3)
S(1)	0.25	0.25	0.0234(6)	0.1035(16)
O(1)	0.2736(6)	0.1436(6)	0.0785(12)	0.108(3)
N(1)	0.6604(2)	0.1581(2)	0.1849(5)	0.0233(7)
C(1)	0.6959(3)	0.0937(3)	0.3368(7)	0.0260(8)
C(2)	0.6362(3)	0.0311(3)	0.4624(7)	0.0253(9)
C(3)	0.5336(3)	0.0324(3)	0.4341(6)	0.0232(8)
C(4)	0.4971(3)	0.0995(3)	0.2757(8)	0.0327(10)
C(5)	0.5615(3)	0.1592(3)	0.1587(7)	0.0298(9)
C(6)	0.25	0.25	-0.273(2)	0.087(5)

Anisotropic displacement parameters ($Å^2$) for **3.5**. The anisotropic displacement factor exponent takes the form: $-2\pi^2 [h^2 a^{*2} U_{11} + \ldots + 2 hka^* b^* U_{12}]$

Atom label	U11	U22	U33	U23	U13	U12
Cu(1)	0.0193(3)	0.0193(3)	0.0264(5)	0	0	0
F(1)	0.138(6)	0.157(7)	0.073(4)	0.007(5)	0.044(4)	-0.008(6)
S(1)	0.142(3)	0.142(3)	0.0255(16)	0	0	0
O(1)	0.086(5)	0.155(7)	0.081(5)	0.062(5)	-0.008(4)	-0.017(5)
N(1)	0.0215(16)	0.0244(16)	0.0242(17)	0.0000(14)	0.0023(14)	-0.0022(12)
C(1)	0.0186(18)	0.029(2)	0.030(2)	0.0027(17)	-0.0012(16)	-0.0025(14)
C(2)	0.0221(18)	0.0246(18)	0.029(2)	0.0044(16)	0.0002(16)	-0.0012(14)

C(3)	0.0228(18)	0.0216(18)	0.025(2)	-0.0006(15)	0.0016(15)	-0.0010(15)
C(4)	0.0176(18)	0.040(2)	0.040(2)	0.014(2)	-0.0017(18)	-0.0025(16)
C(5)	0.023(2)	0.033(2)	0.033(2)	0.0129(19)	-0.0006(18)	-0.0008(16)
C(6)	0.108(8)	0.108(8)	0.045(8)	0	0	0

Hydrogen atomic coordinates and isotropic displacement parameters ($Å^2$) for **3.5**.

Atom label	X	y	z	U(eq)
H(1)	0.7657	0.091	0.3593	0.031
H(2)	0.6654	-0.0128	0.5681	0.03
H(4)	0.4277	0.1038	0.2489	0.039
H(5)	0.5343	0.204	0.0524	0.036

Table A4
Single Crystal Structure Determinations of $[Cu(BzCN)_4]BF_4$

Atomic coordinates and equivalent isotropic displacement parameters ($Å^2$) for **5.7**. U(eq) is defined as one third of the trace of the orthogonalized Uij tensor.

Atom Label	X	y	z	U(eq)
Cu(1)	0.02425(2)	0.971106(19)	0.12454(2)	0.04572(11)
Cu(2)	0.944717(17)	0.757643(17)	0.235313(18)	0.03585(10)
F(1)	1.06161(10)	0.85712(10)	0.71349(9)	0.0613(5)
F(2)	1.03757(11)	0.79585(10)	0.60380(9)	0.0612(5)
F(3)	1.06124(10)	0.72788(10)	0.70940(10)	0.0607(5)
F(4)	1.16092(10)	0.79279(12)	0.67492(12)	0.0739(6)
F(5)	0.44625(9)	-0.03187(9)	0.25873(10)	0.0510(4)
F(6)	0.43159(10)	0.08877(9)	0.21518(9)	0.0578(5)
F(7)	0.32579(9)	0.02438(10)	0.24200(10)	0.0577(5)
F(8)	0.42377(14)	0.06417(12)	0.33371(10)	0.0799(6)
N(1)	0.05064(15)	0.96625(14)	0.23360(15)	0.0497(6)
N(2)	0.10622(15)	1.03608(14)	0.08919(14)	0.0505(6)
N(3)	0.02010(14)	0.87405(13)	0.07030(13)	0.0436(6)
N(4)	-0.07792(16)	1.02974(15)	0.10056(15)	0.0542(6)
N(5)	0.88227(13)	0.85452(13)	0.23444(14)	0.0450(6)
N(6)	0.89195(12)	0.69843(13)	0.14765(12)	0.0378(5)
N(7)	1.05737(13)	0.76893(12)	0.22974(12)	0.0380(5)
N(8)	0.93276(13)	0.70574(13)	0.32845(13)	0.0406(5)
C(1)	0.06133(17)	0.96950(16)	0.29631(19)	0.0451(7)
C(2)	0.07644(15)	0.97501(16)	0.37572(16)	0.0407(6)
C(3)	0.09851(18)	0.91036(18)	0.41859(19)	0.0552(8)
C(4)	0.1155(2)	0.9163(2)	0.4932(2)	0.0675(10)
C(5)	0.108127(17)	0.977533(17)	0.530403(18)	0.0821(13)
C(6)	0.08703(18)	1.0494(2)	0.48545(19)	0.0635(10)
C(7)	0.07021(16)	1.04516(17)	0.40852(17)	0.0473(7)
C(8)	0.15307(17)	1.07151(16)	0.06762(15)	0.0424(6)
C(9)	0.21258(15)	1.11637(15)	0.04115(15)	0.0370(6)
C(10)	0.28161(16)	1.13593(15)	0.09007(15)	0.0404(6)
C(11)	0.33881(16)	1.17912(16)	0.06530(16)	0.0452(7)
C(12)	0.32745(16)	1.20181(16)	-0.00779(17)	0.0477(7)
C(13)	0.25884(16)	1.18207(17)	-0.05632(16)	0.0472(7)
C(14)	0.20097(16)	1.13932(16)	-0.03237(15)	0.0434(7)

C(15)	0.01985(15)	0.81896(16)	0.03719(15)	0.0384(6)
C(16)	0.01950(14)	0.74822(14)	-0.00374(14)	0.0353(6)
C(17)	0.03502(14)	0.67980(15)	0.03455(14)	0.0345(6)
C(18)	0.03301(15)	0.61249(16)	-0.00428(15)	0.0417(6)
C(19)	0.01749(17)	0.61316(18)	-0.08007(16)	0.0494(7)
C(20)	0.00360(18)	0.68086(19)	-0.11833(16)	0.0530(8)
C(21)	0.00374(17)	0.74962(17)	-0.08055(16)	0.0466(7)
C(22)	-0.12385(18)	1.07817(18)	0.08835(16)	0.0460(7)
C(23)	-0.177573(17)	1.142113(17)	0.073533(18)	0.0381(6)
C(24)	-0.214673(17)	1.158813(17)	0.000933(18)	0.0532(8)
C(25)	-0.2601(2)	1.2216(2)	-0.0117(2)	0.0709(10)
C(26)	-0.2712(2)	1.2680(2)	0.0443(3)	0.0780(12)
C(27)	-0.2368(2)	1.2512(2)	0.1162(2)	0.0786(12)
C(28)	-0.18937(19)	1.18742(19)	0.13167(17)	0.0569(8)
C(29)	0.83224(15)	0.89605(15)	0.23858(15)	0.0372(6)
C(30)	0.76610(14)	0.94424(14)	0.24517(14)	0.0324(5)
C(31)	0.77659(15)	1.02208(14)	0.26023(14)	0.0350(6)
C(32)	0.71138(15)	1.06585(15)	0.26765(14)	0.0382(6)
C(33)	0.63690(15)	1.03256(15)	0.26068(14)	0.0377(6)
C(34)	0.62670(15)	0.95544(15)	0.24589(14)	0.0363(6)
C(35)	0.69096(14)	0.91067(15)	0.23751(14)	0.0363(6)
C(36)	0.86674(15)	0.66334(16)	0.09673(16)	0.0386(6)
C(37)	0.83657(15)	0.61996(18)	0.03114(15)	0.0452(7)
C(38)	0.82358(18)	0.6582(2)	-0.03635(17)	0.0643(10)
C(39)	0.7999(2)	0.6160(4)	-0.0991(2)	0.0938(16)
C(40)	0.7891(2)	0.5380(4)	-0.0962(3)	0.0971(18)
C(41)	0.8006(2)	0.5013(3)	-0.0291(3)	0.0836(13)
C(42)	0.82528(18)	0.5420(2)	0.03571(19)	0.0600(9)
C(43)	1.12205(16)	0.76805(14)	0.22288(14)	0.0342(6)
C(44)	1.20416(14)	0.76544(15)	0.21509(13)	0.0345(6)
C(45)	1.24442(18)	0.83319(18)	0.20822(16)	0.0515(8)
C(46)	1.3242(2)	0.8301(2)	0.20429(19)	0.0717(12)
C(47)	1.3627(2)	0.7612(3)	0.2076(2)	0.0774(13)
C(48)	1.32256(19)	0.6943(2)	0.21369(19)	0.0680(10)
C(49)	1.24268(17)	0.69543(18)	0.21738(16)	0.0499(7)
C(50)	0.92822(15)	0.67031(15)	0.37933(15)	0.0364(6)
C(51)	0.92383(15)	0.62505(15)	0.44349(14)	0.0354(6)
C(52)	0.95978(15)	0.65088(17)	0.51285(15)	0.0429(7)
C(53)	0.95708(17)	0.60567(19)	0.57353(16)	0.0516(8)
C(54)	0.9189(2)	0.53604(18)	0.56582(17)	0.0551(8)
C(55)	0.8823(2)	0.51139(18)	0.49716(17)	0.0561(8)
C(56)	0.88412(18)	0.55530(16)	0.43546(15)	0.0460(7)
B(1)	1.08040(19)	0.79363(18)	0.67524(18)	0.0400(7)
B(2)	0.40727(19)	0.03694(17)	0.26299(16)	0.0381(7)

Anisotropic displacement parameters ($Å^2$) for **5.7**. The anisotropic displacement factor exponent takes the form: $-2\pi^2 [h^2 a^{*2} U_{11} + \ldots + 2 hka^* b^* U_{12}]$

Atom Label	U11	U22	U33	U23	U13	U12
Cu(1)	0.0525(2)	0.0374(2)	0.0502(2)	0.00132(16)	0.01716(17)	-0.00088(15)

Cu(2)	0.03181(16)	0.03608(18)	0.0407(2)	0.00650(14)	0.00946(13)	0.00290(13)
F(1)	0.0706(12)	0.0578(11)	0.0495(11)	-0.0185(9)	-0.0040(9)	0.0214(9)
F(2)	0.0899(13)	0.0495(10)	0.0378(10)	-0.0071(8)	-0.0049(9)	-0.0012(9)
F(3)	0.0555(11)	0.0558(11)	0.0712(13)	0.0220(9)	0.0125(9)	0.0037(8)
F(4)	0.0456(10)	0.0884(15)	0.0934(16)	-0.0294(12)	0.0273(10)	-0.0189(10)
F(5)	0.0415(9)	0.0422(9)	0.0672(11)	-0.0005(8)	0.0048(8)	0.0069(7)
F(6)	0.0734(12)	0.0492(10)	0.0484(10)	0.0132(8)	0.0055(9)	-0.0129(9)
F(7)	0.0418(9)	0.0658(11)	0.0666(12)	0.0102(9)	0.0129(8)	0.0111(8)
F(8)	0.1273(18)	0.0744(13)	0.0362(11)	-0.0177(9)	0.0106(11)	-0.0136(12)
N(1)	0.0571(16)	0.0423(14)	0.0521(17)	0.0026(12)	0.0164(13)	-0.0054(11)
N(2)	0.0599(16)	0.0462(15)	0.0482(15)	0.0050(12)	0.0172(12)	-0.0071(12)
N(3)	0.0527(14)	0.0351(13)	0.0436(14)	0.0049(11)	0.0103(11)	-0.0004(11)
N(4)	0.0582(16)	0.0491(16)	0.0568(17)	-0.0019(13)	0.0141(13)	0.0049(13)
N(5)	0.0391(13)	0.0363(13)	0.0599(16)	0.0064(11)	0.0099(11)	0.0060(11)
N(6)	0.0390(12)	0.0412(13)	0.0337(13)	0.0094(10)	0.0076(10)	-0.0010(10)
N(7)	0.0342(12)	0.0383(13)	0.0416(13)	0.0053(10)	0.0077(10)	0.0008(9)
N(8)	0.0443(13)	0.0389(13)	0.0398(14)	0.0043(11)	0.0110(10)	-0.0026(10)
C(1)	0.0452(16)	0.0376(16)	0.055(2)	0.0037(14)	0.0164(14)	0.0002(12)
C(2)	0.0375(14)	0.0432(16)	0.0442(17)	0.0077(13)	0.0148(12)	0.0005(12)
C(3)	0.0540(18)	0.0491(18)	0.068(2)	0.0143(16)	0.0244(16)	0.0058(14)
C(4)	0.062(2)	0.091(3)	0.055(2)	0.026(2)	0.0238(17)	0.0138(19)
C(6)	0.0452(18)	0.091(3)	0.057(2)	-0.0275(19)	0.0163(15)	-0.0208(17)
C(5)	0.044(2)	0.154(4)	0.047(2)	0.019(3)	0.0056(16)	0.001(2)
C(7)	0.0400(15)	0.0486(18)	0.054(2)	0.0062(14)	0.0112(13)	-0.0010(13)
C(8)	0.0519(17)	0.0407(16)	0.0351(16)	0.0029(12)	0.0096(13)	0.0016(13)
C(9)	0.0387(14)	0.0351(14)	0.0390(16)	0.0064(12)	0.0118(12)	0.0033(11)
C(10)	0.0466(16)	0.0400(15)	0.0341(15)	0.0057(12)	0.0062(12)	0.0082(12)
C(11)	0.0381(15)	0.0456(17)	0.0500(18)	-0.0006(14)	0.0034(13)	0.0027(12)
C(12)	0.0382(15)	0.0455(17)	0.063(2)	0.0135(15)	0.0172(14)	0.0049(13)
C(13)	0.0462(16)	0.0567(18)	0.0411(17)	0.0192(14)	0.0144(13)	0.0091(14)
C(14)	0.0397(15)	0.0524(17)	0.0374(16)	0.0090(13)	0.0051(12)	0.0040(13)
C(15)	0.0374(14)	0.0412(16)	0.0372(16)	0.0109(13)	0.0083(12)	-0.0005(12)
C(16)	0.0331(13)	0.0389(15)	0.0343(14)	-0.0011(11)	0.0072(11)	-0.0016(11)
C(17)	0.0337(13)	0.0403(15)	0.0299(14)	-0.0005(11)	0.0066(11)	-0.0001(11)
C(18)	0.0423(15)	0.0389(15)	0.0431(17)	-0.0016(12)	0.0060(12)	0.0004(12)
C(19)	0.0505(17)	0.0516(18)	0.0452(18)	-0.0129(14)	0.0063(14)	0.0018(14)
C(20)	0.0566(18)	0.072(2)	0.0291(16)	-0.0055(15)	0.0052(13)	-0.0011(16)
C(21)	0.0496(17)	0.0518(18)	0.0381(16)	0.0094(14)	0.0074(13)	-0.0015(14)
C(22)	0.0494(17)	0.0480(18)	0.0412(17)	-0.0020(13)	0.0100(13)	-0.0058(14)
C(23)	0.0396(14)	0.0383(15)	0.0364(15)	0.0002(12)	0.0072(12)	-0.0032(12)
C(24)	0.0554(19)	0.067(2)	0.0376(18)	-0.0017(15)	0.0079(14)	-0.0019(16)
C(25)	0.063(2)	0.083(3)	0.061(2)	0.021(2)	-0.0037(18)	0.010(2)
C(26)	0.064(2)	0.054(2)	0.108(4)	0.007(2)	-0.003(2)	0.0171(18)
C(27)	0.073(2)	0.069(2)	0.087(3)	-0.033(2)	-0.003(2)	0.019(2)
C(28)	0.061(2)	0.063(2)	0.0402(18)	-0.0120(15)	-0.0062(14)	0.0081(16)
C(29)	0.0367(14)	0.0333(14)	0.0409(16)	0.0043(12)	0.0054(12)	-0.0017(12)
C(30)	0.0345(13)	0.0313(13)	0.0311(14)	0.0036(11)	0.0056(11)	0.0046(10)
C(31)	0.0357(13)	0.0344(14)	0.0342(14)	-0.0004(11)	0.0051(11)	-0.0029(11)
C(32)	0.0455(15)	0.0314(14)	0.0380(16)	-0.0034(11)	0.0087(12)	0.0021(12)
C(33)	0.0379(14)	0.0423(16)	0.0331(15)	-0.0023(12)	0.0069(11)	0.0077(12)

C(34)	0.0323(13)	0.0430(16)	0.0334(15)	0.0007(11)	0.0059(11)	-0.0029(11)
C(35)	0.0377(14)	0.0322(14)	0.0390(15)	0.0012(11)	0.0070(11)	-0.0005(11)
C(36)	0.0329(14)	0.0473(17)	0.0371(16)	0.0100(13)	0.0102(12)	0.0047(12)
C(37)	0.0296(14)	0.069(2)	0.0372(16)	-0.0065(14)	0.0076(11)	0.0016(13)
C(38)	0.0456(18)	0.109(3)	0.0378(19)	0.0065(18)	0.0070(14)	-0.0074(18)
C(39)	0.051(2)	0.192(6)	0.038(2)	-0.012(3)	0.0064(16)	-0.007(3)
C(40)	0.044(2)	0.182(5)	0.064(3)	-0.067(3)	0.0036(19)	0.014(3)
C(41)	0.049(2)	0.098(3)	0.098(3)	-0.054(3)	-0.002(2)	0.015(2)
C(42)	0.0479(18)	0.070(2)	0.058(2)	-0.0198(17)	0.0006(15)	0.0134(16)
C(43)	0.0390(15)	0.0363(14)	0.0268(13)	0.0009(11)	0.0046(11)	-0.0033(11)
C(44)	0.0293(13)	0.0499(16)	0.0246(13)	-0.0029(11)	0.0056(10)	-0.0082(11)
C(45)	0.0585(19)	0.0553(19)	0.0465(18)	-0.0169(14)	0.0245(14)	-0.0219(15)
C(46)	0.064(2)	0.093(3)	0.066(2)	-0.038(2)	0.0357(18)	-0.048(2)
C(47)	0.0357(17)	0.146(4)	0.053(2)	-0.026(2)	0.0139(15)	-0.018(2)
C(48)	0.0432(18)	0.101(3)	0.063(2)	0.006(2)	0.0190(16)	0.0199(19)
C(49)	0.0451(17)	0.0574(19)	0.0506(19)	0.0104(15)	0.0178(14)	0.0034(14)
C(50)	0.0364(14)	0.0350(15)	0.0378(16)	-0.0013(12)	0.0072(11)	-0.0034(11)
C(51)	0.0389(14)	0.0364(14)	0.0319(14)	0.0024(11)	0.0092(11)	-0.0002(11)
C(52)	0.0400(15)	0.0471(16)	0.0407(17)	-0.0052(13)	0.0052(12)	-0.0028(12)
C(53)	0.0523(18)	0.071(2)	0.0286(16)	0.0007(15)	0.0011(13)	0.0075(16)
C(55)	0.083(2)	0.0426(17)	0.048(2)	0.0058(14)	0.0232(17)	-0.0094(16)
C(54)	0.075(2)	0.058(2)	0.0355(18)	0.0148(15)	0.0169(15)	0.0101(17)
C(56)	0.0638(19)	0.0451(16)	0.0307(15)	-0.0016(12)	0.0131(13)	-0.0099(14)
B(1)	0.0414(17)	0.0388(17)	0.0389(18)	-0.0029(14)	0.0050(14)	-0.0004(14)
B(2)	0.0492(18)	0.0363(17)	0.0278(16)	0.0002(13)	0.0042(13)	0.0006(14)

Hydrogen atomic coordinates and isotropic displacement parameters ($Å^2$) for **5.8**.

Atom Label	x	y	z	U(eq)
H(3)	0.1017	0.8621	0.3957	0.066
H(4)	0.1344	0.8717	0.5202	0.081
H(5)	0.1155	0.9775	0.5826	0.099
H(6)	0.0852	1.0973	0.5094	0.076
H(7)	0.0549	1.0894	0.3796	0.057
H(10)	0.2893	1.1197	0.14	0.048
H(11)	0.3859	1.1933	0.0983	0.054
H(12)	0.3671	1.2312	-0.0247	0.057
H(13)	0.2516	1.198	-0.1063	0.057
H(14)	0.1538	1.1256	-0.0655	0.052
H(17)	0.0469	0.6795	0.0869	0.041
H(18)	0.0424	0.5653	0.0213	0.05
H(19)	0.0163	0.5663	-0.1063	0.059
H(20)	-0.0061	0.6806	-0.1707	0.064
H(21)	-0.0067	0.7965	-0.1065	0.056
H(24)	-0.2039	1.1240	-0.0323	0.064
H(26)	-0.3029	1.3127	0.0339	0.094
H(25)	-0.285	1.2337	-0.0607	0.085
H(27)	-0.2459	1.2837	0.155	0.094
H(28)	-0.1656	1.175	0.1809	0.068
H(31)	0.8278	1.0447	0.2653	0.042
H(32)	0.7176	1.119	0.2776	0.046
H(33)	0.5925	1.0631	0.2661	0.045

H(34)	0.5755	0.9331	0.2415	0.044
H(35)	0.6841	0.8577	0.2267	0.044
H(38)	0.831	0.7119	-0.0387	0.077
H(39)	0.7907	0.641	-0.1456	0.113
H(40)	0.7738	0.5096	-0.1403	0.117
H(41)	0.7917	0.4478	-0.0271	0.1
H(42)	0.8341	0.5168	0.0821	0.072
H(45)	1.2176	0.8809	0.2062	0.062
H(46)	1.3524	0.876	0.1993	0.086
H(47)	1.4177	0.7597	0.2057	0.093
H(48)	1.3499	0.6469	0.2154	0.082
H(49)	1.2147	0.6492	0.2214	0.06
H(52)	0.9859	0.699	0.5184	0.051
H(53)	0.9818	0.6227	0.6211	0.062
H(54)	0.9179	0.505	0.6079	0.066
H(55)	0.8554	0.4636	0.4922	0.067
H(56)	0.8587	0.5381	0.3882	0.055

Table A5
Single Crystal Structure Determinations of $\{[Cu(4,7\text{-phenanthroline})(BzCN)_2]PF_6\}_n$

Atomic coordinates and equivalent isotropic displacement parameters ($Å^2$) for **5.8**. U(eq) is defined as one third of the trace of the orthogonalized Uij tensor.

Atom Label	X	Y	z	U(eq)
Cu(1)	0.75427(15)	0.48270(14)	0.10317(10)	0.0314(6)
P(1)	0.4379(3)	0.2580(3)	0.2513(2)	0.0352(10)
F(1)	0.3516(9)	0.3364(11)	0.2849(11)	0.120(7)
F(2)	0.5240(9)	0.1779(12)	0.2172(11)	0.123(7)
F(3)	0.4764(18)	0.2222(12)	0.3347(8)	0.135(7)
F(4)	0.3479(8)	0.1617(8)	0.2448(7)	0.068(3)
F(5)	0.3978(17)	0.2905(12)	0.1668(9)	0.133(7)
F(6)	0.5252(9)	0.3525(10)	0.2570(7)	0.073(3)
N(1)	0.6110(9)	0.5484(10)	0.1472(7)	0.030(3)
N(2)	0.8926(9)	0.4237(10)	0.1625(7)	0.034(3)
N(3)	0.6984(12)	0.3519(12)	0.0386(8)	0.044(3)
N(4)	0.8132(11)	0.6051(12)	0.0339(7)	0.043(3)
C(1)	0.5170(11)	0.5089(13)	0.1200(10)	0.039(4)
C(2)	0.4120(13)	0.5484(13)	0.1377(10)	0.041(4)
C(3)	0.4070(11)	0.6381(13)	0.1864(9)	0.038(4)
C(4)	0.5020(11)	0.6854(12)	0.2143(8)	0.028(3)
C(5)	0.6070(10)	0.6410(12)	0.1945(8)	0.029(3)
C(6)	0.7071(10)	0.6877(11)	0.2248(8)	0.027(3)
C(7)	0.7087(12)	0.7790(12)	0.2707(8)	0.032(3)
C(8)	1.0958(11)	0.3360(12)	0.2148(10)	0.036(4)
C(9)	0.9989(11)	0.2811(13)	0.2375(8)	0.034(4)
C(10)	0.8956(11)	0.3301(11)	0.2089(8)	0.026(3)
C(11)	1.0914(12)	0.4298(13)	0.1737(10)	0.044(4)
C(12)	0.9883(12)	0.4685(13)	0.1467(9)	0.038(4)
C(13)	0.8545(12)	0.6812(13)	0.0068(9)	0.034(4)

C(14)	0.9045(11)	0.7746(11)	-0.0299(8)	0.027(3)
C(15)	1.0168(14)	0.7849(14)	-0.0234(8)	0.043(4)
C(16)	1.0660(15)	0.8770(14)	-0.0582(10)	0.048(4)
C(17)	1.0016(17)	0.9480(13)	-0.1042(8)	0.047(5)
C(18)	0.8888(16)	0.9356(13)	-0.1115(10)	0.048(4)
C(19)	0.8405(14)	0.8465(14)	-0.0763(10)	0.047(4)
C(20)	0.6474(15)	0.2817(14)	0.0101(10)	0.048(4)
C(21)	0.5792(14)	0.1981(12)	-0.0269(9)	0.038(4)
C(22)	0.4662(13)	0.2024(14)	-0.0239(9)	0.044(4)
C(23)	0.4025(14)	0.1217(14)	-0.0639(9)	0.044(4)
C(24)	0.4537(15)	0.0425(11)	-0.1055(9)	0.042(4)
C(25)	0.5666(15)	0.0380(12)	-0.1076(8)	0.040(4)
C(26)	0.6338(13)	0.1158(12)	-0.0701(8)	0.037(4)

Anisotropic displacement parameters ($Å^2$) for **5.8**. The anisotropic displacement factor exponent takes the form: $-2\pi^2 [h^2 a^{*2} U_{11} + \ldots + 2 hka^* b^* U_{12}]$

Atom label	U11	U22	U33	U23	U13	U12
Cu(1)	0.0376(11)	0.0223(10)	0.0346(10)	-0.0007(8)	0.0061(7)	-0.0027(8)
P(1)	0.026(2)	0.040(2)	0.040(2)	-0.0044(18)	0.0054(16)	0.0006(17)
F(1)	0.041(6)	0.072(9)	0.245(19)	-0.090(11)	0.012(8)	0.006(6)
F(2)	0.029(6)	0.112(11)	0.231(18)	-0.110(12)	0.017(8)	-0.001(6)
F(3)	0.27(2)	0.073(9)	0.062(8)	0.020(7)	-0.049(11)	-0.027(11)
F(4)	0.049(6)	0.043(6)	0.112(9)	-0.014(6)	0.025(6)	-0.017(5)
F(5)	0.225(19)	0.083(10)	0.086(10)	0.021(8)	-0.073(11)	-0.068(11)
F(6)	0.059(7)	0.077(8)	0.082(8)	-0.012(6)	0.005(6)	-0.027(6)
N(1)	0.021(6)	0.031(7)	0.038(7)	0.006(6)	0.008(5)	0.000(5)
N(2)	0.017(6)	0.037(7)	0.047(7)	-0.020(6)	0.008(5)	-0.001(5)
N(3)	0.054(9)	0.038(8)	0.039(8)	-0.005(7)	0.007(6)	-0.004(7)
N(4)	0.043(8)	0.049(9)	0.037(7)	0.018(7)	0.020(6)	-0.002(7)
C(1)	0.015(7)	0.035(9)	0.067(11)	-0.008(8)	0.006(7)	-0.005(6)
C(2)	0.040(9)	0.034(9)	0.049(10)	-0.004(7)	-0.002(7)	-0.017(7)
C(3)	0.013(7)	0.047(10)	0.056(10)	0.024(8)	0.008(6)	-0.006(7)
C(4)	0.023(7)	0.034(8)	0.025(7)	0.010(6)	-0.002(6)	-0.004(6)
C(5)	0.012(7)	0.035(8)	0.039(8)	0.011(7)	-0.004(6)	-0.004(6)
C(6)	0.014(6)	0.028(8)	0.039(8)	-0.005(6)	0.003(6)	0.005(6)
C(7)	0.031(8)	0.038(9)	0.027(7)	0.001(7)	0.002(6)	-0.008(7)
C(8)	0.019(7)	0.029(8)	0.060(10)	0.001(8)	0.008(7)	0.003(6)
C(9)	0.026(8)	0.049(10)	0.029(8)	-0.030(7)	0.018(6)	-0.013(7)
C(10)	0.025(7)	0.021(7)	0.031(8)	-0.009(6)	0.006(6)	0.005(6)
C(11)	0.018(8)	0.044(10)	0.072(12)	-0.022(9)	0.023(7)	-0.012(7)
C(12)	0.035(9)	0.033(9)	0.048(9)	-0.007(7)	0.010(7)	-0.011(7)
C(13)	0.026(8)	0.041(9)	0.036(8)	0.003(7)	0.004(6)	0.009(7)
C(14)	0.024(7)	0.026(7)	0.030(7)	0.003(6)	0.002(6)	-0.008(6)
C(15)	0.068(12)	0.049(10)	0.014(7)	0.007(7)	0.008(7)	-0.003(9)
C(16)	0.048(10)	0.045(10)	0.053(10)	-0.012(9)	0.004(8)	-0.010(8)
C(17)	0.094(15)	0.028(9)	0.020(8)	-0.001(7)	0.013(8)	-0.008(9)
C(18)	0.070(13)	0.033(9)	0.042(10)	-0.001(8)	0.017(9)	0.016(9)
C(19)	0.048(10)	0.045(10)	0.049(10)	0.015(8)	0.019(8)	0.020(8)
C(20)	0.063(11)	0.029(9)	0.053(10)	0.011(8)	0.000(9)	0.007(9)
C(21)	0.055(10)	0.021(8)	0.038(9)	-0.002(7)	-0.003(7)	0.001(7)

C(22)	0.047(10)	0.043(10)	0.043(9)	-0.009(8)	0.022(7)	-0.003(8)
C(23)	0.046(10)	0.049(10)	0.038(9)	0.003(8)	0.018(7)	-0.014(8)
C(24)	0.077(13)	0.016(8)	0.032(8)	0.004(6)	-0.011(8)	-0.012(8)
C(25)	0.069(12)	0.023(8)	0.028(8)	-0.004(6)	-0.009(7)	0.004(8)
C(26)	0.045(9)	0.035(9)	0.032(8)	0.002(7)	0.005(7)	0.017(7)

Hydrogen atomic coordinates and isotropic displacement parameters ($Å^2$) for **5.8**.

Atom label	x	y	z	U(eq)
H(1)	0.5203	0.4479	0.0851	0.047
H(2)	0.346	0.5146	0.1168	0.049
H(3)	0.3365	0.667	0.2005	0.046
H(6)	0.7761	0.6539	0.2126	0.032
H(7)	0.7779	0.8091	0.2893	0.038
H(8)	1.1668	0.3058	0.2291	0.043
H(11)	1.1579	0.4691	0.1632	0.053
H(12)	0.9873	0.5323	0.1143	0.046
H(15)	1.0612	0.7315	0.0038	0.052
H(16)	1.1437	0.8906	-0.05	0.058
H(17)	1.0367	1.0064	-0.1312	0.057
H(18)	0.8444	0.9873	-0.1403	0.058
H(19)	0.7625	0.834	-0.0838	0.057
H(22)	0.4306	0.2591	0.0047	0.053
H(23)	0.3232	0.1227	-0.0616	0.053
H(24)	0.41	-0.0106	-0.1336	0.05
H(25)	0.6008	-0.02	-0.1355	0.048
H(26)	0.7129	0.1138	-0.0732	0.045

Table A6
Single Crystal Structure Determinations of $\{[Cu(4,4'\text{-dipyridyl})_{1.5}]BF_4\}_n$

Atomic coordinates and equivalent isotropic displacement parameters ($Å^2$) for **5.9**. U(eq) is defined as one third of the trace of the orthogonalized Uij tensor.

Atom label	X	y	z	U(eq)
Cu(1)	0.10808(12)	0.10954(7)	0.24477(12)	0.0279(6)
Cu(2)	0.11008(13)	-0.35592(8)	0.25311(13)	0.0337(6)
F(1)	0.3697(11)	0.1633(7)	0.7095(11)	0.116(6)
F(2)	0.3370(15)	0.1485(10)	0.8120(12)	0.173(9)
F(3)	0.4010(12)	0.0846(8)	0.7883(14)	0.153(8)
F(4)	0.2755(11)	0.1052(10)	0.6894(12)	0.171(9)
F(5)	0.1800(12)	0.1608(7)	0.0230(10)	0.133(7)
F(6)	0.1983(8)	0.1258(6)	0.1479(7)	0.082(4)
F(7)	0.1980(11)	0.0790(7)	0.0361(11)	0.120(6)
F(8)	0.0833(10)	0.0996(8)	0.0171(8)	0.116(6)
N(1)	0.0197(7)	0.1614(5)	0.1572(8)	0.025(3)
N(3)	0.1005(7)	0.0276(5)	0.2440(8)	0.024(3)
N(4)	0.1048(8)	-0.2733(5)	0.2535(8)	0.029(3)
N(2)	0.2049(7)	0.1535(5)	0.3368(8)	0.026(3)
N(5)	0.1071(8)	-0.4084(6)	0.3395(9)	0.034(3)
N(6)	0.1158(9)	-0.4011(6)	0.1601(10)	0.040(4)
C(1)	0.1147(9)	-0.0013(7)	0.3165(10)	0.028(4)

C(2)	0.1168(9)	-0.0596(6)	0.3225(9)	0.026(3)
C(3)	0.1030(9)	-0.0928(6)	0.2478(10)	0.026(3)
C(4)	0.0900(9)	-0.0621(6)	0.1733(10)	0.026(3)
C(5)	0.0872(10)	-0.0032(7)	0.1728(10)	0.031(4)
C(6)	0.1030(10)	-0.1542(6)	0.2492(10)	0.027(3)
C(7)	0.1614(9)	-0.1840(7)	0.3242(9)	0.030(4)
C(8)	0.1609(10)	-0.2432(7)	0.3246(10)	0.036(4)
C(9)	0.0466(9)	-0.2451(6)	0.1799(10)	0.027(4)
C(10)	0.0435(9)	-0.1844(7)	0.1755(9)	0.029(4)
C(11)	-0.0446(8)	0.1411(6)	0.0781(9)	0.024(3)
C(12)	-0.1050(9)	0.1758(6)	0.0144(10)	0.027(4)
C(13)	-0.1019(9)	0.2341(6)	0.0303(9)	0.020(3)
C(14)	-0.0393(9)	0.2550(6)	0.1096(9)	0.025(3)
C(15)	0.0207(9)	0.2178(7)	0.1718(10)	0.032(4)
C(16)	-0.1710(8)	0.2736(6)	-0.0381(9)	0.020(3)
C(17)	-0.2044(9)	0.2608(7)	-0.1251(10)	0.033(4)
C(18)	-0.1979(9)	0.3202(6)	-0.0138(9)	0.025(3)
C(19)	0.2320(9)	0.2021(7)	0.3108(10)	0.027(4)
C(20)	0.2418(8)	0.1458(6)	0.4253(9)	0.021(3)
C(21)	0.1263(10)	-0.3903(7)	0.4225(11)	0.033(4)
C(22)	0.1296(9)	-0.4250(6)	0.4856(10)	0.029(4)
C(23)	0.1177(10)	-0.4847(7)	0.4676(10)	0.033(4)
C(24)	0.0974(11)	-0.5049(6)	0.3848(11)	0.038(4)
C(25)	0.0965(11)	-0.4649(6)	0.3253(10)	0.035(4)
C(26)	0.1165(10)	-0.5241(6)	0.5353(10)	0.027(4)
C(27)	0.1701(10)	-0.5133(6)	0.6233(10)	0.031(4)
C(28)	0.0615(9)	-0.5718(6)	0.5063(10)	0.030(4)
C(29)	0.1711(12)	-0.4475(7)	0.1882(11)	0.045(5)
C(30)	0.0659(9)	-0.3930(6)	0.0739(11)	0.031(4)
B(1)	0.3476(11)	0.1265(9)	0.7506(13)	0.035(5)
B(2)	0.1566(12)	0.1252(9)	0.0567(11)	0.032(4)

Anisotropic displacement parameters ($Å^2$) for **5.9**. The anisotropic displacement factor exponent takes the form: $-2\pi^2 [h^2 a^{*2} U_{11} + \ldots + 2 hka^* b^* U_{12}]$

Atom label	U11	U22	U33	U23	U13	U12
Cu(1)	0.0367(11)	0.0180(10)	0.0291(10)	-0.0010(8)	0.0169(8)	0.0009(8)
Cu(2)	0.0471(13)	0.0210(10)	0.0343(11)	0.0003(9)	0.0218(10)	-0.0044(9)
F(1)	0.157(15)	0.115(13)	0.096(11)	0.023(10)	0.080(12)	-0.010(11)
F(2)	0.25(2)	0.21(2)	0.110(14)	-0.047(14)	0.130(17)	0.018(19)
F(3)	0.158(17)	0.082(12)	0.160(17)	0.053(12)	0.039(14)	0.030(12)
F(4)	0.092(12)	0.23(2)	0.118(15)	-0.080(15)	0.003(11)	-0.057(14)
F(5)	0.187(17)	0.106(12)	0.076(10)	0.020(9)	0.045(11)	-0.078(12)
F(6)	0.089(9)	0.115(11)	0.027(6)	-0.013(6)	0.018(6)	0.023(8)
F(7)	0.122(13)	0.113(14)	0.125(13)	-0.038(11)	0.063(11)	-0.018(11)
F(8)	0.110(12)	0.168(16)	0.043(7)	-0.009(9)	0.020(8)	-0.065(11)
N(1)	0.029(7)	0.010(6)	0.029(7)	0.008(5)	0.009(6)	0.002(5)
N(2)	0.024(7)	0.024(7)	0.031(7)	0.002(5)	0.014(6)	0.004(5)
N(3)	0.031(7)	0.015(6)	0.027(7)	-0.009(5)	0.014(6)	-0.001(5)
N(4)	0.051(8)	0.018(7)	0.025(7)	-0.014(6)	0.024(6)	-0.014(6)
N(5)	0.046(8)	0.028(8)	0.032(7)	0.004(6)	0.023(7)	0.007(6)

N(6)	0.045(9)	0.022(7)	0.050(9)	-0.014(6)	0.023(8)	0.004(6)
C(1)	0.030(9)	0.032(9)	0.020(8)	-0.011(7)	0.011(7)	-0.011(7)
C(2)	0.049(9)	0.015(7)	0.018(7)	0.008(6)	0.021(7)	0.002(7)
C(3)	0.024(8)	0.019(8)	0.027(8)	0.004(6)	0.008(7)	0.002(6)
C(4)	0.035(9)	0.026(8)	0.031(8)	0.000(7)	0.026(7)	0.005(7)
C(5)	0.042(10)	0.031(9)	0.028(9)	0.016(7)	0.023(8)	0.002(7)
C(6)	0.039(9)	0.027(9)	0.027(8)	0.000(7)	0.026(7)	0.000(7)
C(7)	0.029(8)	0.047(11)	0.021(8)	-0.013(7)	0.018(7)	-0.013(7)
C(8)	0.036(9)	0.045(11)	0.023(8)	0.008(7)	0.012(7)	0.009(8)
C(9)	0.033(9)	0.012(7)	0.034(9)	-0.007(6)	0.015(7)	0.001(6)
C(10)	0.024(8)	0.034(9)	0.024(8)	-0.010(7)	0.008(7)	0.001(7)
C(11)	0.023(8)	0.027(8)	0.029(8)	-0.009(7)	0.019(7)	-0.013(6)
C(12)	0.016(7)	0.026(9)	0.035(8)	-0.010(7)	0.011(7)	-0.002(6)
C(13)	0.028(8)	0.015(7)	0.030(8)	0.009(6)	0.023(7)	0.002(6)
C(14)	0.035(9)	0.007(7)	0.030(8)	-0.003(6)	0.016(7)	0.001(6)
C(15)	0.031(9)	0.041(10)	0.021(8)	-0.008(7)	0.010(7)	-0.008(7)
C(17)	0.027(8)	0.028(9)	0.041(9)	0.010(7)	0.017(8)	0.013(7)
C(18)	0.027(8)	0.023(8)	0.025(8)	-0.009(6)	0.014(7)	-0.015(6)
C(19)	0.028(8)	0.036(9)	0.028(8)	0.007(7)	0.021(7)	0.003(7)
C(20)	0.018(7)	0.023(8)	0.031(8)	-0.001(6)	0.018(6)	0.006(6)
C(21)	0.035(9)	0.025(9)	0.042(10)	0.003(7)	0.021(8)	0.003(7)
C(22)	0.030(8)	0.027(9)	0.032(8)	-0.002(7)	0.017(7)	-0.010(7)
C(23)	0.037(9)	0.028(9)	0.024(8)	0.015(7)	0.009(7)	0.017(7)
C(24)	0.070(12)	0.015(8)	0.045(10)	-0.007(7)	0.040(10)	-0.002(8)
C(25)	0.063(11)	0.018(8)	0.030(9)	0.000(7)	0.029(8)	-0.011(8)
C(26)	0.040(9)	0.024(8)	0.031(8)	0.006(7)	0.027(8)	0.011(7)
C(27)	0.042(9)	0.017(8)	0.042(10)	0.007(7)	0.028(8)	0.010(7)
C(28)	0.031(9)	0.032(9)	0.032(8)	-0.003(7)	0.020(7)	0.005(7)
C(29)	0.058(11)	0.039(11)	0.032(9)	0.002(8)	0.018(9)	0.007(9)
C(30)	0.027(8)	0.017(8)	0.051(10)	-0.003(7)	0.020(8)	0.000(6)
B(1)	0.030(10)	0.034(11)	0.041(11)	0.010(9)	0.019(9)	0.001(9)
B(2)	0.036(11)	0.045(12)	0.018(8)	-0.007(8)	0.018(8)	-0.007(9)

Hydrogen atomic coordinates and isotropic displacement parameters ($Å^2$) for **5.9**.

Atom label	X	y	z	U(eq)
H(1)	0.1239	0.0198	0.3672	0.034
H(2)	0.1274	-0.0776	0.376	0.031
H(4)	0.0829	-0.0817	0.1223	0.032
H(5)	0.0753	0.0163	0.1199	0.038
H(7)	0.2022	-0.1639	0.3758	0.036
H(8)	0.2015	-0.2627	0.3769	0.043
H(9)	0.0063	-0.2663	0.1295	0.033
H(10)	0.0018	-0.1654	0.1233	0.035
H(11)	-0.0477	0.1014	0.0668	0.029
H(12)	-0.1487	0.1604	-0.0404	0.032
H(14)	-0.0365	0.2944	0.1223	0.03
H(15)	0.0643	0.2327	0.2271	0.039
H(17)	-0.1864	0.2282	-0.1432	0.039
H(18)	-0.1733	0.3289	0.0478	0.03
H(19)	0.2073	0.2103	0.249	0.033

H(20)	0.2241	0.1144	0.446	0.026
H(21)	0.1379	-0.351	0.4363	0.04
H(22)	0.1396	-0.4102	0.5409	0.035
H(24)	0.0847	-0.5438	0.3691	0.046
H(25)	0.0876	-0.4787	0.2698	0.042
H(27)	0.2061	-0.481	0.642	0.037
H(28)	0.0239	-0.5796	0.4447	0.036
H(29)	0.2096	-0.4535	0.2501	0.054
H(30)	0.0297	-0.3608	0.0556	0.038

VITA

EDUCATION

Ph.D. in Chemistry, University of Missouri-Columbia, May 2008;
Advisor: Dr. Steven W. Keller

BS in Chemistry and Biology, College of the Ozarks,
Point Lookout, MO, May 2001;
Minor: Mathematics

TEACHING

University of Missouri-Columbia
Lab Instructor Winter 2007
Physical Chemistry Lab (1 section). Multiple experiments were run during the same section, so a working knowledge of each experiment was needed.

Course Instructor Summer 2006
Chemistry 1100: Atoms and Molecules (1 section). Taught the course aimed at the non-chemistry major. Captured, rendered, and uploaded lecture video to be downloaded as a podcast using iTunes.

Head Graduate Teaching Assistant Winter 2006
General Chemistry III (1 section). Taught one lab section and acted as a guest lecturer. Captured, rendered, and uploaded lecture video to be viewed via web streaming or to be downloaded as a podcast.

Head Graduate Teaching Assistant 2002-2005
Inorganic Chemistry Lab (2 sections). Developed innovative assignments in conjunction with existing labs.

Lab Instructor Winter 2005
Physical Chemistry Lab (1 section). Multiple experiments were run during the same section, so a working knowledge of each experiment was needed.

Westminster College, Fulton, MO Fall 2004
Adjunct Instructor
Taught General Chemistry Lab section including recitation where the curriculum and grading were developed with my assistance.

University of Missouri-Columbia 2001-2004
Graduate Teaching Assistant
General Chemistry Lab (2-3 sections a semester). The course included recitation.